



Faculteit wetenschappen
Departement Chemie

Faculté des Sciences
Département de Chimie

Plasma kinetics modelling of nitrogen fixation

Ammonia synthesis in dielectric barrier discharges with catalysts

Proefschrift voorgelegd tot het behalen van de graad Doctor in de wetenschappen aan de Universiteit Antwerpen en Doctor in de wetenschappen chemie aan de Université libre de Bruxelles te verdedigen door

Kevin Christiaan van 't Veer

Academiejaar 2021-2022

Promotors:

Professor Annemie Bogaerts (University of Antwerp)

Professor François Reniers (Université libre de Bruxelles)

Summary

Ammonia (NH_3) synthesis is crucial for the production of artificial fertilizer, which enables sustaining the nutritional demands of the ever increasing world population. Ammonia synthesis is carried out through the Haber-Bosch process and is a form of artificial nitrogen fixation in which value-added products are made from the normally inert nitrogen that is available in the atmosphere.

Artificial nitrogen fixation disturbs the earth's natural nitrogen cycle, increasing the amount of fixed nitrogen on earth and increasing the amount of fixed nitrogen that eventually returns to the atmosphere through denitrification. During this denitrification process, nitrous oxide (N_2O) can be produced, which is a greenhouse gas with 300 times more negative impact than CO_2 .

In addition, with an energy consumption of 30 GJ/t- NH_3 and the emission of 2 kg- CO_2 /kg- NH_3 , ammonia created through the Haber-Bosch process is the chemical with the largest environmental footprint.

Increasing awareness of climate change and the need for a more sustainable future, aims to make green and renewable energy universally available, such that small-scale, regional infrastructures and responsible production and consumption patterns with improved management of chemicals and their lifecycle become possible.

However, ammonia synthesis through the current Haber-Bosch process operates under high pressure and high temperature conditions, making it only suitable for large scale. Alternative technologies thus need to be developed. One such technology that can enable a more sustainable future through more regional and greener ammonia production is plasma technology. Plasma technology can be deployed on a small scale, is electrically driven, and excellently compatible with the intermittency of green energy.

Dielectric barrier discharges are a popular plasma source, due to the already widespread industrial adoption and the ease of operation. Furthermore, a catalyst is easily

incorporated into the reactor. The effects of plasma and catalyst and their synergy can circumvent the harsh reaction conditions of the Haber-Bosch process, that are required to break the strong triple bond of nitrogen.

In this thesis a zero-dimensional plasma kinetics modelling approach is used to gain insight into the mechanisms of plasma-catalytic ammonia synthesis in a dielectric barrier discharge. Specifically, a systematic modelling approach has been developed that enables the description of various experimental dielectric barrier discharge setups, that is with and without a catalytic packing material in the reactor bed.

In this modelling approach, special attention is given to the instantaneous plasma power absorbed by the electrons (see Chapter 4). The electrons absorb power during the strong filamentary microdischarges, but can also absorb small amounts of power due to a weaker uniform plasma contribution. In addition, the relevant fraction of the microdischarges and the corresponding discharge volumes in which the power is deposited to the electrons are specifically considered as well.

The importance of vibrational excitation is investigated by distributing the plasma power of the strong filamentary microdischarges and the weaker uniform plasma components in Chapter 5. It was found that vibrational excitation can occur in both the microdischarges and the uniform plasma component. Depending on the exact discharge conditions, it was found that both the strong microdischarges and vibrational excitation can be simultaneously important for the ammonia yield.

The temporal behavior of filamentary dielectric barrier discharges was explicitly taken into account, making it possible to assess the temporal reaction mechanisms as explained in Chapter 6. It was found that ammonia is decomposed during the microdischarges due to electron impact dissociation. At the same time the electron impact collisions also create atomic nitrogen and other excited species. Those reactive species recombine to ammonia in the afterglow through various elementary Eley-Rideal and Langmuir-Hinshelwood surface reaction steps with a net ammonia gain until a

steady state is reached. Once in steady state, the ammonia production is balanced with electron impact dissociation even in the weaker uniform plasma.

Finally, in Chapter 7, an empirical relationship for the fraction of microdischarges was confirmed. In addition, the concept of the fraction of microdischarges was generalized. This concept takes into account the temporal and spatial non-uniformity of a dielectric barrier discharge. It directly represents the efficiency with which the applied electric power is transferred to each individual particle in the plasma reactor. It is argued that any type of spatial or temporal non-uniformity of the plasma will cause unequal treatment of the gas molecules in the reactor, corresponding to a lower efficiency at which the power is transferred to the gas molecules. Some molecules can then receive a lot of plasma power, while others receive very little power.

All of those insights (the role of vibrational excitation and the reaction mechanisms in plasma-catalytic ammonia synthesis, and the generalized implications of temporal and spatial non-uniform characteristics of plasma) aid in an increased understanding of plasma-catalytic ammonia synthesis as a potential green chemistry solution to the synthesis of ammonia on small scale.

Samenvatting (Dutch summary)

De synthese van ammoniak (NH_3) is cruciaal voor de productie van kunstmest. Het gebruik van kunstmest maakt het mogelijk om te voorzien in de voedingsbehoefte van de steeds groeiende wereldbevolking. Ammoniaksynthese wordt uitgevoerd via het Haber-Bosch proces en is een vorm van kunstmatige stikstoffixatie waarbij chemicaliën met toegevoegde waarde worden gemaakt vanuit de stikstof die in de atmosfeer aanwezig is en normaal gesproken inert is.

Kunstmatige stikstoffixatie verstoort de natuurlijke stikstofkringloop op aarde, waardoor de hoeveelheid gefixeerde stikstof op aarde toeneemt. Ook de hoeveelheid gefixeerde stikstof die uiteindelijk via denitrificatie terugkeert naar de atmosfeer neemt toe. Tijdens dit denitrificatieproces kan distikstofoxide (N_2O) worden geproduceerd, een broeikasgas met een 300 keer zo grote negatieve impact dan CO_2 .

Bovendien is ammoniak geproduceerd via het Haber-Bosch proces met een energieverbruik van 30 GJ/t- NH_3 en een uitstoot van 2 kg- CO_2 /kg- NH_3 de chemische stof met de grootste ecologische voetafdruk.

Door het vergrote bewustzijn van klimaatverandering en de bewustwording van de noodzaak van een duurzamere toekomst, is er tot doel gesteld dat groene en hernieuwbare energie universeel beschikbaar moet zijn. Deze universele beschikbaarheid van groene energie staat kleinschalige en regionale infrastructuren en verantwoorde productie- en consumptiepatronen toe met verbeterd beheer van chemicaliën en hun levenscyclus.

De synthese van ammoniak via het huidige Haber-Bosch proces werkt echter onder hoge druk en hoge temperatuur, waardoor het proces alleen geschikt is voor grote schaal. Er moeten dus alternatieve technologieën worden ontwikkeld. Een van die technologieën die een duurzamere toekomst mogelijk kan maken door meer regionale en groenere ammoniakproductie is plasmatechnologie. Plasmatechnologie is

kleinschalig inzetbaar, elektrisch aangedreven en uitstekend te combineren met het onregelmatige karakter van groene stroom.

Vooraf diëlektrische barrièreontladingen zijn een populaire plasmabron, vanwege de huidige industriële toepassingen en het gebruiksgemak. Verder kan een katalysator gemakkelijk in de reactor worden opgenomen. De effecten van plasma en katalysator en hun synergie kunnen de hoge temperatuur en druk van het Haber-Bosch-proces omzeilen die nodig zijn om de sterke drievoudige binding van stikstof te verbreken.

In dit proefschrift wordt een nuldimensionaal plasmakineticmodel gebruikt om inzicht te krijgen in de mechanismen van plasma-katalytische ammoniaksynthese in een diëlektrische barrière ontleding. In het bijzonder is een systematische modelleringsaanpak ontwikkeld die het mogelijk maakt om verschillende diëlektrische barrière ontladingen te beschrijven, met en zonder een katalytisch materiaal in de reactor.

In deze methode wordt speciale aandacht besteed aan het ogenblikkelijke plasmavermogen dat door de plasma-elektronen wordt geabsorbeerd (zie Hoofdstuk 4). De elektronen absorberen vermogen tijdens de sterke filamentaire microontladingen, maar kunnen ook kleine hoeveelheden vermogen absorberen vanwege een zwakkere uniforme plasmabijdrage. Daarnaast wordt specifiek gekeken naar de relevante fractie van de microontladingen en de bijbehorende ontladingsvolumes waarin het aangebrachte vermogen wordt overgebracht op de elektronen.

Het belang van vibrationele excitatie wordt onderzocht in Hoofdstuk 5, door het plasmavermogen over de filamentaire microontladingen en het zwakkere uniforme plasma te verdelen. Vibrationele excitatie kan optreden in zowel de microontladingen als het uniforme plasma. Afhankelijk van de exacte ontladingscondities werd gevonden dat zowel de sterke microontladingen als de vibrationele excitatie tegelijkertijd van belang kunnen zijn voor de ammoniakopbrengst.

In Hoofdstuk 6 wordt het tijdsafhankelijke gedrag van filamentaire diëlektrische barrièreontladingen expliciet in rekening genomen, waardoor het mogelijk is om de tijdsafhankelijke reactiemechanismen te onderzoeken. Er werd gevonden dat ammoniak wordt afgebroken tijdens de microontladingen als gevolg van dissociatie geïnduceerd door elektronen. Tegelijkertijd creëren de botsingen met elektronen ook atomaire stikstof en andere geëxciteerde deeltjes. Al die reactieve deeltjes recombineren buiten de microontladingen om tot ammoniak via verschillende elementaire Eley-Rideal en Langmuir-Hinshelwood oppervlaktereacties, met een netto ammoniakwinst als gevolg totdat een stabiele toestand is bereikt. Eenmaal in de stabiele toestand, wordt de ammoniakproductie in evenwicht gebracht met dissociatie van elektronenimpact, zelfs in het zwakkere uniforme plasma.

Ten slotte wordt in Hoofdstuk 7 een empirische relatie voor de relevante fractie van de microontladingen bevestigd. Bovendien werd het concept van de fractie van microontladingen veralgemeend. Dit concept houdt rekening met de tijdelijke en ruimtelijke niet-uniformiteit van een diëlektrische barrièreontlading. Het geeft direct de efficiëntie weer waarmee het toegepaste elektrische vermogen wordt overgebracht naar elk afzonderlijk deeltje in de plasmareactor. Er wordt gesteld dat elke afwijking van een volledig uniform plasma zal leiden tot een ongelijke behandeling van de gasmoleculen in de reactor, wat overeenkomt met een lagere efficiëntie waarmee het aangebrachte vermogen wordt overgedragen aan de gasmoleculen. Sommige moleculen kunnen dan veel plasmavermogen krijgen toegespeeld, terwijl andere deeltjes heel weinig vermogen krijgen toegespeeld.

Al deze inzichten (de rol van vibrationele excitatie en de reactiemechanismen in plasma-katalytische ammoniaksynthese, en de algemene implicaties van een niet-uniform plasma) helpen bij een beter begrip van plasma-katalytische ammoniaksynthese als een potentiële groene oplossing voor de synthese van ammoniak op kleine schaal.

Contents

Part I. Introduction	15
Chapter 1. Introduction and thesis outline.....	17
1.1. Nitrogen fixation: Our growing nutritional demands and our impact on the nitrogen cycle.....	17
1.2. Climate change: A wakeup call towards a more sustainable future.....	19
1.3. Plasma as an enabling technology	21
1.4. Plasma-catalytic ammonia synthesis: a literature overview	23
1.4.1. Performance and characteristics	23
1.4.2. Computational studies.....	24
1.4.3. Computational studies: zero-dimensional modelling.....	26
1.4.4. Reaction mechanisms	27
1.5. Thesis outline	29
Part II. Theory & Computational details.....	31
Chapter 2. Describing plasma	33
2.1. Plasma: An exciting collection of particles.....	33
2.1.1. Ground state atoms: Electron configurations and their notations.....	34
2.1.2. Ground state molecules: Electron configurations and their notations ...	37
2.1.3. Electronically excited atoms and molecules	40

2.1.4. Ionization	42
2.1.5. Molecules: Vibrational and rotational excitation	44
2.1.6. Nitrogen: The complete picture.....	46
2.1.7. Harnessing plasma for nitrogen fixation.....	49
2.2. Plasma: A too large collection of particles.....	50
2.2.1. The Boltzmann equation and number densities.....	51
2.2.2. Zeroth moment of the Boltzmann equation: The continuity equation ...	53
2.2.3. Probabilities and (common) distributions functions	55
2.3. Concluding remarks	57
Chapter 3. Describing chemical reactors	59
3.1. Deriving the continuity equation: Plug flow and related reactors	59
3.2. Distinctions between time and residence time dependencies: Continuously stirred tank reactors	62
3.3. Concluding remarks	65
Chapter 4. Plasma kinetics modelling of dielectric barrier discharges	67
4.1. Plasma kinetics modelling: The continuity equation	67
4.1.1. Rate coefficients and the kinetics	68
4.1.2. Rate coefficients for electron impact collisions: Electric field and plasma power	69
4.1.3. Calculations at constant pressure.....	71
4.2. Capturing the average behavior of dielectric barrier discharges	72
4.2.1. Instantaneous plasma power and its average characteristics.....	74

4.2.2. The fraction of microdischarges	76
4.2.3. The maximum and minimum power, and the microdischarge and uniform power contributions.....	78
4.2.4. Discharge volumes	79
4.2.5. Comments on model iterations	81
4.3. Concluding remarks	83
Part III. Results & Discussion	85
Chapter 5. The role of vibrational kinetics in ammonia synthesis.....	87
5.1. Brief model description and model input	88
5.1.1. Kinetics description.....	88
5.1.2. Plasma power and model input.....	89
5.1.3. Describing packed bed DBDs	92
5.2. Species density evolution and steady-state densities	93
5.3. Reaction mechanisms	98
5.4. Reduced electric field and vibrational temperatures	100
5.5. Conclusions	104
Chapter 6. Reaction mechanisms: Role of the microdischarges and their afterglows	107
6.1. Brief model description and model input	108
6.2. Surface Coverages and Plasma Species Densities in the microdischarges and Their Afterglows.....	111

6.3. Production and Destruction of Plasma Radicals, Adsorbed Species and NH ₃ in the microdischarges and Their Afterglows	116
6.4. NH ₃ Formation: Reaction Rates and Determination of the Rate-Limiting Step	120
6.5. N ₂ Dissociation Rates in the Plasma.....	123
6.6. NH ₃ Formation Reaction Scheme for the microdischarges and Their Afterglows	125
6.7. Conclusions	135
Chapter 7. Microdischarges from the perspective of molecules.....	137
7.1. Methods.....	138
7.1.1. Particle tracing	138
7.1.2. Monte Carlo calculations	140
7.1.3. Experiments	142
7.1.4. Plasma kinetics model.....	144
7.2. Particle tracing results	145
7.2.1. Particle trajectories through an axial cylindrical packed bed reactor ...	145
7.2.2. Residence time distribution in an empty and packed bed DBD reactor	147
7.2.3. Gas distribution in an empty and packed bed DBD reactor	149
7.3. Monte Carlo calculations	151
7.3.1. Microdischarge distribution and “hits” in the empty and packed bed reactor.....	151
7.3.2. Determination of the fraction of microdischarges to which the gas molecules are exposed	157

7.3.3. Empirical relationship for the fraction of microdischarges	158
7.4. Experimentally observed microdischarge distributions	160
7.5. Experimental and calculated plasma-catalytic NH ₃ yield.....	162
7.6. Generalization of the concept: Fraction of plasma power transferred to the gas molecules.....	166
7.7. Conclusions	167
Part IV. Conclusion & Outlook	169
Chapter 8. Overall conclusions	171
Chapter 9. Final thoughts and outlook.....	175
Appendix.....	177
Appendix A. Kinetics	179
A.1. Gas phase kinetics tables.....	179
A.2. Gas phase: Vibrational kinetics.....	185
A.3. Surface kinetics.....	187
Appendix B. Plasma current, gas voltage and instantaneous power	193
Appendix C. Supplementary Information of Chapter 6	197
C.1. Surface Coverages and Gas Phase Concentrations in the microdischarge...	197

C.2. Calculated Plasma Parameters	199
C.3. NH ₃ Formation: Detailed Analysis of the Reaction Rates and Determination of the Rate-Limiting Step	200
C.4. N ₂ Dissociative Adsorption Compared Against N Atom Direct Adsorption ..	211
C.5. Data Used in the Assessment of the Reaction Mechanisms.....	211
C.6. Influence of Langmuir-Hinshelwood Reactions and Alternative Reaction Mechanisms	216
Bibliography	219
List of publications and conference contributions	237
Acknowledgements	241

Part I.

Introduction

Chapter 1.

Introduction and thesis outline

1.1. Nitrogen fixation: Our growing nutritional demands and our impact on the nitrogen cycle

Modern day society is characterized by large growths in population. From 2 billion people in 1930, the population grew to 7.7 billion in 2019, and a growth up to 10.9 billion people in 2100 is predicted [1]. Cultivating enough food to sustain this population is a major challenge and has been made possible by the green revolution. During this time period (ca. 1960-1980s [2]), synthetic fertilizers (such as ammonium nitrate, NH_4NO_3) were introduced. Those fertilizers significantly increased crop yields, and enabled sustaining the growing world population in terms of nutritional needs. However, the introduction of those nitrogen-based fertilizers is accompanied by two fundamental problems [3]: The disturbance of the natural nitrogen cycle and the energy costs and greenhouse gas emissions associated with the production of those fertilizers.

The main constituent of earth's atmosphere is nitrogen (78 %), followed by oxygen (21 %) and argon (0.9 %). However, most of this nitrogen is not available to the various life forms on earth. The circulation of nitrogen in its different forms throughout the atmosphere, land, plants, animals and bacteria is called the nitrogen cycle and occurs through a series of processes:

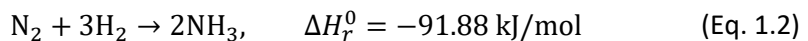
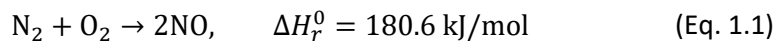
- Nitrogen in the atmosphere is fixed into earth's soil by bacteria (nitrogen fixation).
- The resulting nitrates (NO_3^-) and ammonium (NH_4^+) can be absorbed by plants (assimilation).
- Organic waste from plants and animals is converted back to ammonium by soil bacteria and fungi (ammonification).

- The ammonium is further converted by bacteria to nitrites (NO_2^-) and nitrates (nitrification).
- The final bacterial-driven process is the conversion of nitrates back to nitrogen in the atmosphere (denitrification).

The complexity of this cycle, involving nitrogen fixation, assimilation, ammonification, nitrification and denitrification processes, indicates a delicate natural balance [4].

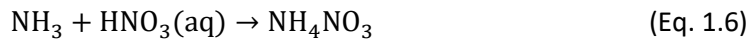
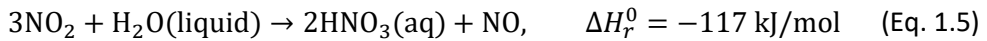
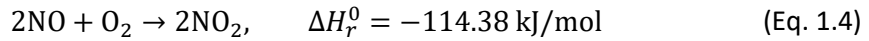
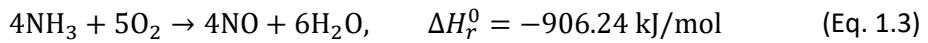
To produce synthetic fertilizer, extra nitrogen is fixed artificially. This is problematic because introducing more artificially fixed nitrogen, in the form of fertilizer, into the nitrogen cycle also increases the nitrogen released back into the atmosphere (denitrification) due to inefficient fixation and/or utilization of the fixed nitrogen. Nitrous oxide (N_2O) is one possible product of denitrification and is actually a greenhouse gas, which has approximately 300 times more negative impact on climate change than carbon dioxide (CO_2) [5]–[7]. The agriculture section is responsible for 6 million metric ton of nitrous oxides released into the atmosphere [8], which doubles the approximately 6 million metric ton of nitrous oxide that is already released from natural soils [8]. More efficient fertilizer thus needs to be developed [9].

Artificial nitrogen (N_2) fixation is the conversion of nitrogen into nitrogen oxides (NO_x) and/or ammonia (NH_3) or related compounds, through industrial processing [10]. The formation of nitric oxide follows the Zeldovich mechanism (Eq. 1.1), while ammonia is formed in the Haber-Bosch process (Eq. 1.2), which is the focus of this thesis.

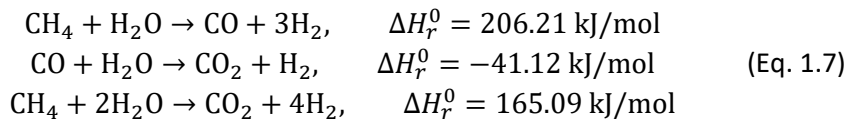


Currently, the Haber-Bosch (HB) process forms the basis of ammonium nitrate synthesis for the use in fertilizers. Specifically, the Haber-Bosch process produces ammonia (NH_3 , Eq. 1.2) from nitrogen and hydrogen (H_2). The ammonia is oxidized to nitrogen dioxide (NO_2 , Eq. 1.3 and 1.4), which is used to form nitric acid (HNO_3 , Eq. 1.5) by adding water,

in the Ostwald Process. Ammonia and nitric acid are combined to create the ammonium nitrate, which is used in fertilizer [11].



Haber-Bosch (Eq. 1.2) operates under high pressure and high temperature conditions (around 200 atm and 500 °C). This inherently makes the process only suitable for large industrial scale, and it relies heavily on fossil energy fuels [12]. In addition, the process relies on H₂, which is obtained through steam reforming (of methane, CH₄, Eq. 1.7).



The Haber-Bosch process (Eq. 1.2) and the subsequent synthesis of ammonium nitrate (Eq. 1.3 – 1.6) are exothermic processes, releasing heat. However, it requires high activation energy to break the nitrogen triple bond. In addition, the Haber-Bosch process relies on H₂ feed gas, which is produced through endothermic processes (Eq. 1.7). Ammonia, synthesized through Haber-Bosch, is the chemical with the highest associated energy consumption (ca. 30 GJ/t-NH₃) and greenhouse gas emissions in the form of carbon dioxide (CO₂) (ca. 2 kg-CO₂/kg-NH₃) [13].

1.2. Climate change: A wakeup call towards a more sustainable future

Over the recent years we have become more and more aware of climate change due to the emission of greenhouse gases. There have been various agreements to combat climate change by reducing greenhouse gas emissions. Agreements/negotiations were made in 1992, 1997, 2007, 2012, 2015 and 2021 [14]. The 2021 Glasgow and 2015 Paris

agreements are the most recent ones. The Paris agreement aimed to limit global warming to an average of 1.5 to 2 °C maximum [15], [16]. Our awareness of the need for change towards a sustainable future even surpasses combatting climate change, as reflected in the 17 Sustainable Development Goals (SDGs) also agreed upon in 2015 by the United Nations (UN) to be achieved by 2030 [17].

For example, SDG #7 focusses on affordable and clean energy by ensuring universal access to renewable energy. SDG #9 addresses industry, innovation and infrastructure with a focus on developing reliable, sustainable and resilient regional infrastructures. SDG #12 aims to achieve responsible consumption and production patterns, including improved management of chemicals and their life cycle [18]. All of those target goals can be related to the nitrogen cycle, our impact on it and the role therein of the fossil fuel-driven, large scale Haber-Bosch process – indicating a need for improvement [19], [20].

In terms of the nitrogen cycle and agricultural use of fertilizer, technology is needed that enables local, small scale, self-sufficient and closed life cycles of chemical use, such as nitrogen and all its relevant compounds. This technology should also be based on renewable energy sources, rather than to be reliant on fossil fuels. Plasma technology is one of the technologies that potentially answers all those criteria and offers excellent compatibility with the intermittency of renewable energy sources [21], [22].

When making the distinction between the synthesis of ammonia from H_2 (Eq. 1.2) and the production of this required H_2 (Eq. 1.7), it is clear that improvements towards making the process more sustainable should originate from this H_2 production (Eq. 1.7), which is actually the only endothermic reaction described in section 1.2, and it produces CO_2 . There exist many strategies to improve the current Haber-Bosch process. For example, the fossil fuel based hydrogen production could potentially be based on electrolysis instead, which also enables the use of renewable electrical energy instead of fossil energy sources. At the same time, the ammonia synthesis itself can be improved, either by improving the current Haber-Bosch process (for example, through

improvements in catalysts) or by alternative technologies. However, while improvements to the existing Haber-Bosch process could alleviate the harsh reaction conditions, operation significantly above atmospheric pressure is still required. In turn, this means that alternative technologies with the potential for small-scale and decentralized ammonia production should also be investigated [23].

1.3. Plasma as an enabling technology

Plasma technology is vital for the modern society and is already used in numerous industries. For example, plasma treatment is widely used in the optics, glass, plastics and textile industries for functionalization of surfaces. In the medicine and hygiene sector, plasma is used for sterilization. Plasma is also used for water treatment. A lot of research is performed for applications in cancer treatment and wound healing [24], [25]. Welding is often plasma-based and is very important for the aerospace and automotive industry. Plasma is crucial in the manufacturing of semiconductor devices. Those examples form only a small handful of the possible applications of plasma [26]. The vast range of applications corresponds to a vast range of different and unique plasmas.

Plasma is often considered to be the fourth state of matter. It is estimated that up to 99 % of the visible universe is in the plasma state, for example: The sun is one of the strongest plasmas in the universe, having an extremely high temperature (ca. 10^7 K) and very high (charged) particle density (ca. 10^{30} m^{-3}) [27]. But of course, plasma technology is not based on excavating small pieces of the sun and using those on earth.

Plasma can also be obtained by supplying large amounts of energy to a gas. This energy can be supplied in the form of electrical energy. When enough energy is supplied to ionize the gas, free electron-ion pairs are created. The free electrons are able to induce a variety of electron impact processes, in turn creating a variety of reactive plasma species, which are not found in the same proportions in a normal gas. Plasmas can generally be classified by the ionization degree, gas temperature and electron temperature. High ionization degree (towards 100 %) plasmas are different from low

ionization degree plasmas (e.g. below 1 %). The electron and gas temperature is equal to each other in thermal plasmas, while in cold and warm plasma, the electron temperature (a few eV, corresponding to a few ten thousand Kelvins) is (significantly) higher than the gas temperature. Cold plasma can operate at room temperature, while warm plasma still has elevated gas temperatures (a few thousand Kelvins) [28].

Before the Haber-Bosch process was widely adopted (ca. 1930), the Birkeland-Eyde process had reached commercial scale (ca. 1900) [29]. The Birkeland-Eyde process was actually based on a thermal arc plasma [30]. Unfortunately, the capital investment and operational costs, as well as the energy cost of the produced NO_x , phased out the Birkeland-Eyde process in favor of the Haber-Bosch process. However, the increased availability of green energy and the need for more resilient, small scale infrastructures and the increased understanding of plasmas has caused a renewed interest in plasma technology for green nitrogen fixation. This is especially true because plasma processes are excellently compatible with the intermittency of green energy. The renewed research interests explore a variety of plasma types (e.g. microwaves, arcs and dielectric barrier discharges) as a possible enabler of future green fertilizer synthesis processes [11].

Dielectric barrier discharges are popular plasma sources for the synthesis of ammonia from nitrogen and hydrogen feed gases, due to their (operational) simplicity and already widespread adoption in industry. To increase process yields and efficiencies, catalytic packing materials have been introduced in the reactors [23].

Modelling and simulation of plasma, and the improvements therein that took place over the past few years, are an important driving force in the continuous research development and research interests of plasma-driven technologies [31], [32].

This thesis focusses on plasma kinetics modelling, specifically, modelling of dielectric barrier discharges for plasma-catalytic ammonia synthesis. Plasma kinetics models by so-called zero-dimensional models, also often called global models, do not intrinsically

capture real spatial dimensions of a plasma or the associated species transport. Instead, such models only capture the time dependence. Those restrictions, compared to higher dimensional approaches in computational fluid dynamics calculations, do allow to focus on the detailed plasma kinetics taking place. Such kinetics descriptions can contain a large number of species and a large number of reactions, with each species described by one differential equation. The number of differential equations that are typically needed causes full spatial models to be unfeasible due to computational costs. Plasma kinetics modelling thus has an important role in understanding plasma chemistry.

1.4. Plasma-catalytic ammonia synthesis: a literature overview

1.4.1. Performance and characteristics

In literature, many variations of catalytic material, support and loading arrangements can be found for NH₃ synthesis in DBD reactors. Product yields mostly range from 0.1 % to 5 % or higher for more complex configurations [33]–[44].

Bai et al. used a powdered catalyst, smeared on the electrode of a DBD, and achieved an NH₃ yield of up to 0.5 %. With increased discharge area, they found higher NH₃ concentrations [36]. Later, they reached a yield of 1.25 % in a micro-gap, at a reduced electric field of around 300 Td¹. The yield increased with power density, applied voltage and gas temperature. In addition, the discharge frequency was shown to be an important parameter in process optimization [38]. Mizushima and coworkers used a metal-loaded membrane-like structure as catalyst. A N₂ conversion of up to 2.4 % was reported. When the catalyst was loaded, the NH₃ concentration increased with applied voltage. Without a catalyst, this increase was significantly less [39], [40]. Gómez-Ramírez et al. reported their highest N₂ conversion as 2.7 %, corresponding to the smallest discharge gap at constant residence time. They indicate N₂⁺ to play an important role in the formation of NH in the gas phase. In addition, electron impact

¹ The Townsend (Td), is a unit of the reduced electric field (V·m²), defined as 1 Td = 10⁻²¹ V·m². The reduced electric field is given by the electric field (V/m) over the gas number density (m⁻³).

dissociation of NH_3 was indicated as a possible source of NH [41]. Later, they found a N_2 conversion of 7 % and further argued the importance of both the N_2^+ ions and electron impact dissociation of NH_3 [42]. Barboun et al. reported NH_3 yields up to 2.7 %, depending on the metallic catalyst and the residence time. Higher concentrations were achieved for longer residence times. They separately investigated the influence of bulk gas temperature and plasma input power, and found that a higher input power was more effectively enhancing the plasma-catalytic NH_3 yield than the bulk gas temperature [43]. Peng et al. reached up to 3.7 % NH_3 yield, depending on the discharge frequency, applied voltage, flow rate and gas composition [44]. By optimizing the catalyst support, catalyst material and their manufacturing, as well as the plasma power and electrode configuration, Akay and Zhang reported an NH_3 concentration of 16 % [35].

1.4.2. Computational studies

Packed reactors show beneficial, but complex behavior. This complexity is due to simultaneous and synergistic effects that can hardly be separated from each other in experimental studies, indicating the need for modeling [45]. Due to the nature of a packed bed (PB) DBD, ideally three-dimensional modeling is required. However, the computational cost of the latter makes that modeling studies often resort to two-dimensional (2D) or even one-dimensional (1D) geometrical representations to study the plasma physics. As in any chemical process, the chemistry is also an important aspect subject to modeling studies. The potential complexity of the actual molecular chemistries involved again limits the possibilities of 1D and 2D numerical studies due to the computational cost. Instead, such studies are often performed with zero-dimensional (0D) plasma kinetic models (see section 1.4.3).

Babaeva, Kushner and co-workers performed 2D modeling of single and multiple solid particles obstructing the discharge propagation path in humid air mixtures [46]–[49]. Within the same research group, Kruszelnicki et al. reported a reduced version of the same chemistry set for 2D modeling, describing a truer PB configuration [50]. Kang et

al. studied the impact of various dielectric barrier arrangements, including a PB reactor in 2D for simple dry air [51], using the methods of Kulikovsky [52]. Similar studies were performed by Russ et al. [53]. Takaki et al. performed both computations and experiments for a N₂ discharge in a PB reactor. They used an analytical description of the electron density and electric field based on 1D approximations [54]. The computed species densities as a function of applied voltage were in agreement with experiments. They also reported the measured vibrational temperature to be constant (around 2250 K) with increasing applied voltage. Thus, they concluded that the additional power at higher applied voltage does not go to vibrational excitation [55], [56]. Mehta et al. also measured significant vibrational temperatures (around 2700 K) in a N₂/H₂ DBD. They suggest that vibrationally excited molecules can play an important role in plasma-catalytic NH₃ synthesis [57], and this was later substantiated by Rouwenhorst et al. [58]. Van Laer and Bogaerts performed several modeling studies of PB reactors for various configurations and conditions, operated with helium [45], [59], [60]. Wang et al. developed a model for dry air, focusing on streamer propagation in between the packing beads [61].

Most of the above modeling studies focused on the plasma physics rather than the plasma chemistry. The latter was kept simple and did for instance not include excitation to individual vibrationally excited states.

In some of those studies, various kinds of discharges were observed in PB reactors, such as filamentary discharges and surface ionization waves [50], [61]. Some modeling studies tried to relate single features to specific current peak characteristics [59]. However, experimental current characteristics of PB reactors, with often a far greater number of packing beads compared to modeling configurations, exhibit a complexity not allowing for a distinction between the various kinds of microdischarges based on the electrical current characteristics [62], [63]. Indeed, the conversion and product yield in PB DBDs are, in general, affected by the various plasma and process parameters (e.g. the type of dielectric barrier and its thickness, the packing beads, the discharge

frequency, the flow rate) and their combinations in complex ways [62], even in reactors without any packing material [63]–[65].

1.4.3. Computational studies: zero-dimensional modelling

Several numerical studies have focused on the plasma chemistry in filamentary discharges using zero-dimensional modeling, in which filaments were described as sharply peaked power density pulses [66]–[73]. However, the number of microdischarge pulses in the model and the time between the pulses were chosen rather arbitrary, with motivations based on the discharge frequency alone or in combination with an effective filament discharge volume. In addition, the pulse magnitudes were chosen to mimic the total specific energy input, corresponding to the total plasma power, for the sum of all pulses in the model, despite the transient characteristics of filaments. The plasma power in between the pulses was effectively chosen to be zero. In particular, the importance of the interpulse duration was acknowledged [72]. When applied to long time scale simulations, a large number of pulses, in the order of 10 thousand to 1 million, was mentioned to occur in the 0D model, corresponding to gas residence times in the order of 1 to 10 s. An agreement with experiments was found, when a power transfer efficiency, effectively corresponding to a reduction in power, was introduced [66]. Overall, the 0D models could achieve good agreement with experiments. The inclusion of vibrational kinetics in a 0D CO₂ DBD model was reported to yield slightly different values, but the overall trends were the same [73].

Colonna et al. performed 0D plasma kinetic studies of repetitive nanosecond pulsed discharges in H₂ [74], and this kinetic description was later used in a similar N₂/H₂ pulsed plasma [75]. The nanosecond pulse repetition was in the order of microseconds. These models included detailed state-to-state kinetics of vibrational levels, or even represented complete collisional-radiative models, in case of H₂. Reduction of the vibrational resolution in their models, when compared to the full state-to-state models, showed clearly different vibrational distribution functions [74], [75]. Teramoto and Kim

experimentally investigated two consecutive discharge pulses in N_2 [76]. Their results indicate that vibrational excitation in the first pulse influences the second pulse, if it occurs within 300 microseconds of the first pulse.

Hong et al. reported on detailed kinetic modeling of NH_3 production related to experimental measurements in a PB DBD, with emphasis (among others) on the vibrational kinetics. The plasma conditions were constant, averaged values, derived from the electrical characteristics. No spatial or temporal behavior of their PB DBD, mimicking the microdischarges, was captured in the model. The electron temperature was in the order of 1 to 1.5 eV. A reasonable agreement with experiments was found [77]–[79]. Shah et al. studied NH_3 synthesis in a low pressure radio-frequency plasma and successfully used the same chemistry set to elucidate the underlying reaction mechanisms [80].

In order to capture the characteristics of a filamentary DBD in 0D plasma kinetics models, various authors have adopted a certain microdischarge frequency [66], [70]–[73], and later specifically applied a so-called volume-corrected microdischarge frequency [67], [81]. The latter takes into account that a molecule does not experience all the microdischarges due to the stochastic behavior of these microdischarges [82]. This quantity was defined as the microdischarge volume over the reactor volume [67], [81].

1.4.4. Reaction mechanisms

Starting late 1960, the synthesis of NH_3 in plasma systems has been attributed to ‘wall effects’, i.e. the reactor walls and/or electrodes appear to have a (catalytic-like) contribution to the NH_3 formation [37]. The packing support material and the catalytic material applied on the support, in actual plasma-catalytic setups, influence the discharge characteristics [61] and reaction kinetics. In addition, the discharge characteristics and reaction kinetics, especially in the plasma itself, are closely tied to each other. The radicals or excited molecules created in the plasma can, in turn, either influence the physical properties of the catalytic surface [83] or steer the surface

reaction kinetics [57], [58]. This causes a complexity that is difficult to resolve with experimental studies only. Hence, modelling studies are helpful, allowing to disentangle the different effects. At the same time, the sheer amount of choice for catalytic and support materials and their intrinsic properties, in combination with the lack of data in literature on the catalytic reaction rates, makes it difficult to capture in detail the full complexity of plasma catalysis in a single model. Therefore, the combination of individual modelling and experimental studies with properly set boundaries can increase our understanding of plasma-catalytic mechanisms. Particularly, NH_3 synthesis from N_2/H_2 feed gas is an important case study due to the simplicity of the reaction (i.e. only NH_x as reaction products).

Mehta *et al.* proposed that vibrational excitation of N_2 can increase the NH_3 synthesis rate by decreasing the dissociative adsorption energy barrier [57]. Rouwenhorst *et al.* confirmed by additional experiments that vibrational excitation in the plasma helps to overcome this barrier and that further hydrogenation towards NH_3 happens on the catalytic surface [58]. However, the specific energy input (SEI) of the DBD plasma was relatively low when compared to typical DBD values, as reported in [33]. Many researchers observed an increasing NH_3 synthesis rate with increasing plasma power (or SEI) [35], [38], [43], [84], [85]. Aihara *et al.* proposed that NH_3 synthesis occurred through the adsorption of electronically excited N_2 with further hydrogenation on the surface, based on a direct correlation between the NH_3 synthesis rate and electronically activated N_2 [84]. Zhu *et al.* also hypothesized that electronically excited metastable N_2 aids in the adsorption processes [86]. Bai *et al.* assumed ionization to be detrimental for the NH_3 formation [38]. Akay *et al.* argued that NH plasma radicals are most likely created between N and H_2 , and that NH_3 can be formed by further hydrogenation reactions in the gas phase. At the same time, they also reported NH_3 formation due to hydrogenation on the surface, starting with N_2 and H_2 adsorption, but the gas phase and surface reaction pathways were not linked to each other [35]. Peng *et al.* reported the stepwise hydrogenation on the surface as the faster pathway [85]. Hong *et al.* performed a detailed kinetic analysis with and without a catalytic surface. They found

that the surface-adsorbed N atoms (i.e. N(s)) were formed mainly by dissociative adsorption of ground state N₂ molecules, followed by the first vibrational level and direct adsorption of N atoms. H(s) was also mainly formed by dissociative adsorption from ground state H₂ molecules, but followed by direct adsorption of H atoms, and only then by dissociative adsorption from the first vibrational level. The rate of H(s) formation was four orders of magnitude higher than that of N(s). The authors did not only consider stepwise hydrogenation on the surface, but also reactions between gas phase radicals and surface-adsorbed species (so-called Eley-Rideal reactions), and they actually found that the reaction of gas phase NH₂ with H(s) was more important in the formation of NH₃ [77].

1.5. Thesis outline

This thesis consists of 4 parts. After this introduction (Part I), **Part II** presents the theoretical background and consists of Chapters 2, 3 and 4:

Chapter 2 goes into more detail of plasma and related theory, with a special focus on the type of species that can be found in plasma and how plasma itself can be described, in order to understand the basis of plasma kinetics modelling.

Chapter 3 discusses how chemical reactors and plasma reactors can be described, and what the underlying assumptions are.

Chapter 4 presents the computational details of the plasma kinetics modelling, as well as the specific considerations made to describe a dielectric barrier discharge in a global kinetics model.

Part III (Chapter 5, 6 and 7) presents the results and discussion and is based on the peer-reviewed publications made during this doctorate. Each Chapter aims to answer specific research questions.

In **Chapter 5**, the importance of vibrational excitation in (packed bed) dielectric barrier discharges is evaluated to complement experimental reports in literature that indicated

high vibrational temperatures in dielectric barrier discharges. *The specific research questions answered are:*

- What is the importance of vibrational excitation in packed bed dielectric barrier discharges in view of (experimental) reports in literature?
- How can the differences between a packed bed dielectric barrier discharge and an empty (non-packed) dielectric barrier discharge be captured?

In **Chapter 6**, the reaction mechanisms behind plasma-catalytic ammonia synthesis in a dielectric barrier discharge are discussed, while explicitly considering the temporal behavior and characteristics of those plasmas. *The specific research question that will be answered is:*

- What are the reaction mechanics of plasma-catalytic ammonia synthesis when considering the temporal plasma behavior?

In **Chapter 7**, the assumptions underlying our modelling method to describe dielectric barrier discharges are substantiated by various computational and experimental analyses. *The specific research questions answered are:*

- *Can the concept of the fraction of microdischarges be substantiated?*
- *What are the implications of the (spatial and temporal) non-uniformity of a given plasma?*

Finally, **Part IV** presents the overall conclusions by summarizing the main findings of this thesis (**Chapter 8**) and gives final thoughts and recommendations concerning plasma kinetics modelling, and its role in a faster adoption of plasma-driven industrial applications, as an outlook to the future (**Chapter 9**).

Part II. Theory & Computational details

Part II serves as general background for this thesis. Detailed concepts might be presented, which are not used directly in plasma kinetics modelling. However, those concepts do form an important basis and do underlie plasma modelling and plasma kinetics. This is by no means an extensive account; instead *key terms* are indicated as such, to aid in more detailed investigations of those concepts outside of this thesis.

Chapter 2.

Describing plasma

2.1. Plasma: An exciting collection of particles

As mentioned in the introduction; a plasma is a highly energetic gas and there are many varieties of plasmas, which can generally be characterized by the electron temperature, gas temperature and ionization degree. Based on the temperatures, two distinct plasma types can be defined: Thermal and non-thermal plasma.

In thermal plasma, all particles have the same temperature, the plasma is thus in thermal equilibrium. In non-thermal plasma, the electron temperature is (significantly) higher than the gas temperature. Non-thermal plasma can be further divided in warm and cold plasma. In warm plasma, the gas temperature is significantly elevated compared to room temperature, while cold plasma can exist even at room temperature.

The ionization degree reflects the fraction of charged particles, or electron-ion pairs, in the plasma. Those charged particles make plasma conductive, while a normal gas is not conductive. The electrons typically induce a wide range of kinetic processes through electron impact collisions. Those processes include: Excitation, ionization, attachment and dissociation. Excitation can lead to rotationally, vibrationally or electronically excited gas molecules or electronically excited gas atoms. Ionization leads to positive (atomic or molecular) ions, while attachment leads to negative ions. Upon dissociation, molecules are separated into atoms or smaller molecules. Another iconic characteristic of plasma is the emission of light (photons) from excited states. This emission often occurs at specific wavelengths (colors), depending on the gas.

Thus a plasma typically represents a collection of neutral and charged particles with different degrees of excitation. This is achieved because of the energy that is put into the gas/plasma. Especially in the case of non-thermal plasma, non-equilibrium conditions are created: The various reactive plasma species (electrons, ions and

molecules and atoms with specific excitations) thus occur in quantities larger than what would be found under equilibrium conditions. If it would be possible to harness those non-equilibrium conditions, we potentially enter a very exciting chemical world – but, what are excited molecules and atoms, and ions exactly?

2.1.1. Ground state atoms: Electron configurations and their notations

Let's first consider a single atom in its ground state. The electron cloud that surrounds the atomic nucleus can be seen as the space in which the electron(s) can be found. The exact location of an electron cannot be pinned down (*uncertainty principle*). The "shape" of the electron cloud is obtained by solving the *Schrödinger equation* and actually represents the probability of finding an electron at a certain location in the electron cloud. The solutions to this equation depend on various quanta; the quantum numbers. The quantum numbers that describe the electron clouds are:

- The *principal quantum number* n , which can take any positive integer value starting with 1. The principal quantum number describes the main shells that can hold up to $2n^2$ electrons.
- The *orbital quantum number* l , which for a given n , can take positive integer values starting with 0 up to $n - 1$. The orbital quantum number describes the subshells for every shell n , which hold up to $2(2l + 1)$ electrons.
- The *magnetic quantum number* m_l , which for a given l , can take integer values ranging from $-l$ to $+l$, including 0. The magnetic quantum number describes the specific orbital for every subshell l , which can hold up to two electrons each. A set of quantum numbers n , l and m_l completely describes the electron orbitals. See Table 2.1 (at the end of section 2.1) for a graphical representation of those orbitals.

In addition, the *spin quantum number* m_s indicates the intrinsic spin of an electron and has a value of $+1/2$ or $-1/2$. Those values are often referred to as *spin up* (\uparrow) and *spin*

down (\downarrow), respectively. Each specific orbital labelled with m_l can hold one spin up and one spin down electron (*Pauli exclusion principle*).

When an atom (or molecule) is in its ground state, the electron configuration is such that the principal and orbital quantum numbers, n and l , are minimal: The shells are filled in order of increasing $n + l$, followed by increasing n . Those two quantum numbers and the associated *electron configuration* are typically represented with the *spectroscopic notation*. For example, the nitrogen atom (N) has the electron configuration $1s^2 2s^2 2p^3$. The normal integer numbers represent the principal quantum number n . The letters s and p, represent the orbital quantum number l , where $l = 0, 1, 2, 3$ correspond to the lowercase letters s, p, d and f, respectively. Those letters stand for sharp, principal, diffuse, and fundamental, respectively. This convention has its origin in *spectroscopy*. The exponents indicate the number of electrons in the specified subshell. This notation is often abbreviated as $[\text{He}]2s^2 2p^3$, because the ground state of helium (He) has all $n = 1$ shells completely filled. Sometimes, even $[\text{He}]$ is dropped completely in abbreviated notations.

The atomic number of nitrogen is 7, there are thus 7 electrons, which does correspond to the $1s^2 2s^2 2p^3$ notation ($2 + 2 + 3 = 7$). If we consider the $n = 2$ shell of nitrogen, we see that it has $2 + 3 = 5$ electrons, while the shell can be filled with $2 \cdot 2^2 = 8$ electrons. The 2s subshell, can hold $2(2 \cdot 0 + 1) = 2$ electrons and is thus filled completely. The 2p subshell is the last shell in which the remaining 3 electrons have to be placed and can hold $2(2 \cdot 1 + 1) = 6$ electrons.

The exact configuration of the 3 electrons in the 2p subshell over the 6 available vacancies, is specified with the magnetic and spin quantum numbers, m_l and m_s . For the 2p subshell $l = 1$, meaning that $m_l = -1, 0, +1$ and each m_l has place for an electron with $m_s = +\frac{1}{2}$ and $m_s = -\frac{1}{2}$.

The 3 electrons (in case of N) in the 2p subshell thus all have principal quantum number $n = 2$ and orbital quantum number $l = 1$, but the values of m_l and m_s are different for

each of those electrons. Those latter values can also be described with the *total orbital quantum number* L and the *total spin quantum number* S , respectively. L and S are simply given by the sum of all m_l and m_s , respectively. The total angular momentum effects, due to both the orbital angular momentum and the spin angular momentum, are given by the *total angular momentum quantum number* J , which can take values from $J = |L - S|$ till $J = L + S$ with increments of 1.

The ground state configuration can be found using *Hund's rules*, which states that the minimum energy configuration is given for the largest possible S and L values. The electrons should thus be unpaired and prioritize spin up as much as possible. The electrons are first placed in the largest m_l orbitals. Similarly electron pairs are first completed in the largest m_l orbitals. The ground state of the N atom thus corresponds to $S = +\frac{1}{2} + \frac{1}{2} + \frac{1}{2} = +\frac{3}{2}$ and $L = +1 + 0 - 1 = 0$. Those quantum numbers are summarized in the *term symbol*. The term symbol is given by ^{2S+1}L , where $L = 0,1,2,3$ is indicated with capital letters S, P, D and F, respectively. Thus for N, the term symbol is 4S .

Determining the ground state configuration in terms of the total angular momentum quantum number J , also follows from Hund's rules. However it is slightly more complicated as it depends on whether or not the subshell (l) is more or less than half filled. Furthermore, for the purpose of the kinetic models discussed in this thesis (see Chapter 4), J is not resolved in the kinetics considered. Different J causes only relatively small energy differences (order of 0.01 eV). Still, the term symbol including J is given by $^{2S+1}L_J$. For the N atom, this is $^4S_{3/2}$, as $L = 0$, such that $J = S$ and only a single value is possible.

Finally, the parity P , which can be considered a measure for the symmetry of *the wave function* (resulting from the Schrödinger equation), is given by $P = (-1)^{\sum l}$ and can also be included in the term symbol. The parity can be odd (-1) or even ($+1$). The complete notation is then either $^{2S+1}L_J^P$ or $^{2S+1}L_{J,P}$. For the N atom the parity is odd, as $P =$

$(-1)^{(1+1+1)} = (-1)^3 = -1$. The first notational convention, which is most common for atoms, then gives ${}^4S_{3/2}^o$. In this notation, only odd parity is explicitly stated with a lowercase letter o. The second notational convention would give ${}^4S_{3/2,u}$. In this case, lowercase letters u (*ungerade* – German) and g (*gerade*) are used for odd and even parity, respectively.

The above considerations are summarized in Table 2.1 (at the end of section 2.1).

2.1.2. Ground state molecules: Electron configurations and their notations

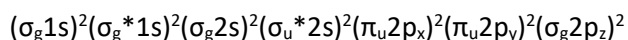
When two atoms approach each other, their electron clouds can overlap. In other words, their electron orbitals can overlap, forming *molecular orbitals*. The molecular orbital can be a *bonding orbital* or an *anti-bonding orbital* in case of homonuclear molecules. In general, *non-bonding orbitals* are also possible when there is no overlap between the atomic electron orbitals.

The molecular orbitals are indicated with the quantum number λ , given by $\lambda = |m_l|$. In homonuclear diatomic molecules, each λ corresponds to one bonding and one anti-bonding orbital, the latter is indicated with an asterisk (*). The orbitals $\lambda = 0,1,2,3$ are indicated with the Greek lowercase letters: $\sigma, \pi, \delta, \phi$. Each orbital can again hold one spin up and one spin down electron (spin quantum number m_s). Bonding orbitals are less energetic and those bonds are formed first – electrons first occupy the vacancies of the bonding orbitals. The exact order of orbitals when λ reaches above 1, can quickly become convoluted.

The molecular term symbol is given by ${}^{2S+1}\Lambda_p^{(+/-)}$, where $\Lambda = |M_L|$ and $M_L = \sum m_l$ describes the orbital angular momentum of the molecule. $\Lambda = 0,1,2,3$ is indicated with the capital Greek letters $\Sigma, \Pi, \Delta, \Phi$. S is the total spin quantum number, also notated as M_S for molecules. The parity P is again indicated with u (odd) or g (even). The parity is odd when an odd number of electrons are in odd molecular orbitals, and the parity is even when an even number of electrons are in odd molecular orbitals. The parity of the

individual molecular orbitals is also often notated with u and g, and can be determined by inspection of the molecular orbitals (see Table 2.1). How the electrons of the individual atoms occupy the molecular orbitals is often presented in a molecular orbital diagram (see Figure 2.1). The + or – sign in the molecular term symbol, indicates the reflection symmetry (symmetric and antisymmetric, respectively), and is only relevant for Σ states ($\Lambda = 0$).



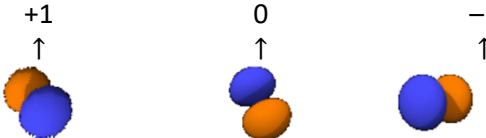
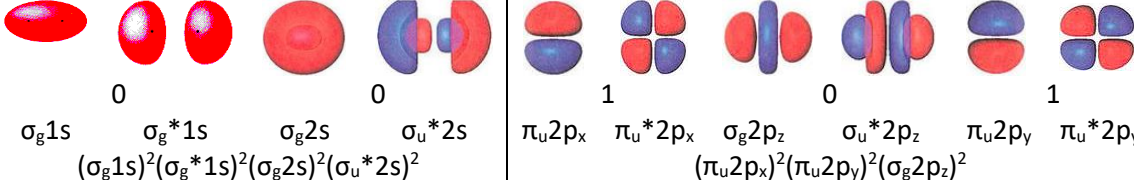
For molecular nitrogen (N_2), the electron configuration is given by:



Analogous to the atomic case, to determine the term symbol, only the 2p orbitals have to be considered, as 2p is not filled completely. It follows that $M_L = +1 + 1 - 1 - 1 + 0 + 0 = 0$, as p_x corresponds to $m_l = +1$, p_z to $m_l = 0$ and p_y to $m_l = -1$. Λ is notated with Σ ($\Lambda = |M_L| = 0$). The total spin quantum number is $M_S = +\frac{1}{2} - \frac{1}{2} + \frac{1}{2} - \frac{1}{2} + \frac{1}{2} - \frac{1}{2} = 0$, thus $2S + 1 = 2 \cdot 0 + 1 = 1$. In total there are 4 electrons in u-orbitals (all of which π_u), thus the parity is even (indicated with g). Including the reflection symmetry, the term symbol becomes $^1\Sigma_g^+$. In addition, ground state molecular term symbols are often labeled with a capital X: $X^1\Sigma_g^+$.

The above considerations are summarized in Table 2.1.

Table 2.1. Summary of the quantum numbers associated with the filled electron shells/orbitals of the nitrogen atom and molecule, including the electronic configurations, graphic representations of the orbitals and term symbol.²

Ground state nitrogen atom, N			
n	1	2	2
l	0	0	1
Vacancies	2	2	6
Electron configuration	$1s^2$	$2s^2$	$2p^3$
m_l	0	0	0
m_s	$\uparrow\downarrow$	$\uparrow\downarrow$	\uparrow
Orbital			
S, L, J, P			$+3/2, 0, 3/2, -1$
Term symbol			$4S_{3/2}^0$
Ground state nitrogen molecule, N ₂			
Molecular orbital			
λ	0	0	1
Orbital notation	$\sigma_g 1s$	$\sigma_g^* 1s$	$\sigma_g 2p_z$
Electron configuration	$(\sigma_g 1s)^2 (\sigma_g^* 1s)^2 (\sigma_g 2s)^2 (\sigma_u^* 2s)^2 (\pi_u 2p_x)^2 (\pi_u 2p_y)^2 (\sigma_g 2p_z)^2$		
m_s	$\uparrow\downarrow$	$\uparrow\downarrow$	$\uparrow\downarrow$
M_S, M_L, Λ, P			$0, 0, 0, +1$
Term symbol			$X^1\Sigma_g^+$

² The orbital illustrations were obtained from Orbital Viewer by David Manthey (<https://www.orbitals.com/orb>) [178]. The molecular orbital illustrations for $n = 1$ were obtained from the "General Chemistry Help" made by the Bodner Group at Purdue University [179]. The molecular orbital illustrations for $n = 2$ were obtained from the Chemistry Libretexts [180].

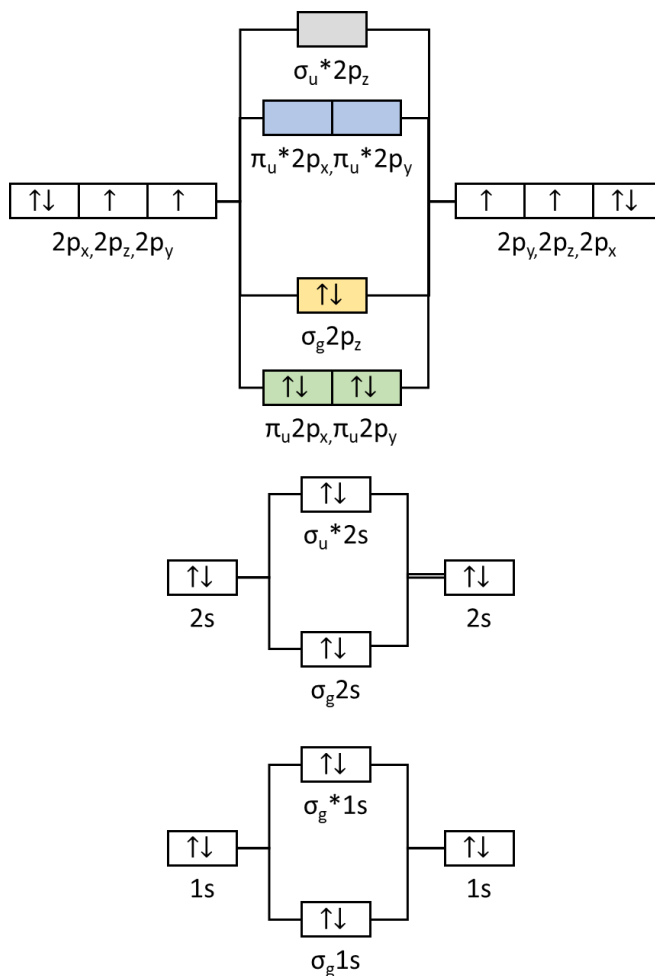


Figure 2.1. Molecular orbital diagram of nitrogen in the ground state. The colors correspond to Table 2.1.

2.1.3. Electronically excited atoms and molecules

In sections 2.1.1 and 2.1.2 electron configurations for atoms and molecules were described. Specifically, the nitrogen atom and molecule in its ground state was taken as an example (see Table 2.1 and Figure 2.1). When atoms or molecules are in the ground state, the electrons occupy the electron vacancies corresponding to the lowest energy, which involve the lowest quantum numbers (n, l) or are determined using Hund's rules (m_l, m_s).

In terms of the electron cloud, those electron configurations can be considered to be such that the electrons are closest to the atomic nuclei. In an electronically excited state,

electrons move further away from the nucleus. This means that the electrons occupy different states, described by possible changes in the various quantum numbers.

Electronic excitation can typically happen upon collision. For example, when a free electron has a certain *kinetic energy* (corresponding to a certain velocity) and collides with an atom, it can transfer part of its energy to the electron in the outer shell of the atom, which is then able to occupy a state that requires a higher energy. The atom thus *gains potential energy*.

For example, as discussed in section 2.1.1 in case of the nitrogen atom, the outer shell is specified with $2p^3(^4S)$, where 4S specifies the configuration in terms of the spin quantum number m_s in each orbital m_l . In the ground state, all three orbitals m_l contain one spin up electron. Upon collision it is possible for an electron to gain enough energy to transfer to another orbital (m_l). This electron can still occupy the spin down vacancies of the other m_l orbitals that already contain a spin up electron. This means that the spectroscopic notation ($2p^3$) does not necessarily have to change for an excited state. Two examples of this are given in Table 2.2 for electronically excited nitrogen atoms [$N(^2D)$ and $N(^2P)$].

The electronically excited states described in Table 2.2 already have an energy of a few eV (ca. 2 to 3) above the ground state configuration. Of course, it is also possible for the quantum number n and l to change. Those changes in electron configuration correspond to even larger energies. For example, nitrogen in the $2s^22p^2(^3P)3s(^4P)$ state has an energy of ca. 10 eV.

The National Institute of Standards and Technology (NIST) offers a detailed overview of all atomic states and their energy levels in their Atomic Spectra Database (www.nist.gov/pml/atomic-spectra-database).

Electronic excitation in molecules follows the same principles as in the atomic case. Electrons can occupy molecular orbitals different from the ground state configuration. An example is given in Table 2.3.

Table 2.2. Electron configurations and determination of the term symbols for nitrogen atoms in the ground state (a – see Table 2.1 for more details) and electronically excited states (b and c), in which an electron has changed the orbital it occupies (indicated with red m_s values [arrows]).

Electron configuration	$2p^3$	$2p^3$	$2p^3$
m_l	+1 0 -1	+1 0 -1	+1 0 -1
m_s	↑ ↑ ↑	↑↓ ↑	↑ ↑↓
S	+ 3/2	+1/2	+1/2
L	0	+2	+1
J	3/2	5/2, 3/2	1/2, 3/2
P	-1	-1	-1
Term symbol(s)	$4S_{3/2}^0$	$2D_{5/2}^0, 2D_{3/2}^0$	$2P_{1/2}^0, 2P_{3/2}^0$
	(a)	(b)	(c)

The term symbol of electronically excited molecules also uses an empirical notation. As mentioned in section 2.1.2, the ground state is labelled with a capital X. The electronically excited states are labelled alphabetically with increasing energy. Both capital and lowercase letters are used. This generally depends on the *spin multiplicity*, given by the $2S + 1$ term. The capital letters are mostly reserved for the states with spin multiplicity identical to the ground state. However, it is also common to always give *triplet states* (which have spin multiplicity 3) capital letter labels.

2.1.4. Ionization

Ionization of atoms occurs when an electron in one of the atomic orbitals gains enough energy to completely detach itself from the nucleus. Ionization thus creates an ion and a free electron. Similar to excitation, this can be caused by electron impact collisions induced by free electrons. Ionization is very important, as this process itself results in those free electrons. Ionization is at the basis of the ionization degree in a plasma, and it causes the *electron avalanches* that are responsible for a gas *breakdown*: When a gas transitions to a plasma.

Table 2.3. Electron configurations and determination of molecular nitrogen in the ground state (see Table 2.1) and an electronically excited state, in which an electron has changed the molecular orbital it occupies (indicated with red m_s values [arrows]). Including the determination of the term symbol and the molecular orbital diagram of the excited state (see Figure 2.1 for the full ground state molecular orbital diagram).

m_l	+1	0	-1
λ	1	0	1
Orbital notation	$\pi_u 2p_x$	$\pi_u^* 2p_x$	$\sigma_g 2p_z$
			$\sigma_u^* 2p_z$
			$\pi_u 2p_y$
			$\pi_u^* 2p_y$
Electron configuration	Ground state:		
m_s	$(\pi_u 2p_x)^2 (\pi_u 2p_y)^2 (\sigma_g 2p_z)^2$		
	$\uparrow\downarrow$	$\uparrow\downarrow$	$\uparrow\downarrow$
Electron configuration	Electronically excited state example:		
m_s	$(\pi_u 2p_x) (\pi_u 2p_y)^2 (\sigma_g 2p_z)^2 (\pi_u^* 2p_x)$		
	\uparrow	\uparrow	$\uparrow\downarrow$
M_S			+1
M_L			0
Λ			0
P			-1
Term symbol			$A^3\Sigma_u^+$
Molecular orbital diagram:			

Because ions have one (or more) electron(s) less, the description just starts from a different electron configuration. Realizing this, ions also have ground states and electronically excited states that follow the same rules as described in section 2.1.1 through 2.1.3. Atoms and molecules can also be doubly ionized; in which case two electrons are detached from the nuclei, etc.

The atomic nitrogen ion N^+ has electron configuration: $[He]2s^22p^2$. The corresponding ground state term symbol is: 3P . The Atomic Spectra Database (nist.gov/pml/atomic-spectra-database) also offers a detailed overview of all atomic ionic states and their energy levels. Atoms and ions are indicated with I's, N I corresponds to the neutral atom N, while N II and N III correspond to N^+ and N^{2+} , respectively.

Molecular ions can simply be considered as the combination of one atom and one atomic ion. For example, N_2^+ can be formed by N and N^+ . Determining the (ground state) electron configuration of such a molecular ion is completely analogous to considering the combination of two N atoms. The ground state term symbol of N_2^+ is: $X^2\Sigma_g^+$, corresponding to the electron configuration $(\pi_u2p_x)^2(\pi_u2p_y)^2(\sigma_g2p_z)$.

2.1.5. Molecules: Vibrational and rotational excitation

Up to now (section 2.1.1 through 2.1.4) the electrons and their location relative to the atomic nuclei have been discussed. Those discussions thus described the electron as a quantum mechanical system. However, molecules consist of multiple atomic nuclei, which also have a position relative to each other. In addition, those systems are not necessary symmetrical (over every coordinate). Those considerations introduce two additional modes of excitation: Vibrational and rotational excitation, respectively.

In diatomic molecules, the two atomic nuclei can move relative to each other, as if connected by a *spring*. This oscillatory movement is called vibration (see the bottom of the next page for a schematic illustration). Applying the Schrödinger equation to this system gives the *quantum harmonic oscillator* from which it follows that multiple discrete modes of vibration are possible. This is often indicated with the *vibrational*

quantum number ν . Analogous to the quantum numbers describing the electron orbitals (see section 2.1.1 through 2.1.4), a higher vibrational number ν can be thought of as a larger distance between the two atomic nuclei, which intuitively corresponds to a more energetic state of the molecule. The lower the vibrational quantum number, the lower the energy of the molecule. Molecules in the ground state thus have $\nu = 0$. When also considering vibrational excitation, the nitrogen molecule ground state can be indicated by: $\text{N}_2(X^1\Sigma_g^+, \nu = 0)$. Vibrational excitation can in principle also occur for electronically excited states.

Molecules can also rotate, over a rotation axis such that the molecule does end up in a different location in a fixed reference frame. This is illustrated in Figure 2.2. This system, in isolation, can be approximated as a *rigid rotor*. Solving the Schrödinger equation for this system also results in discrete solutions, introducing the *rotational quantum number* J , which can be considered similarly to ν (see above). The ground state can thus be indicated with: $\text{N}_2(X^1\Sigma_g^+, \nu = 0, J = 0)$.

The kinetics used in this thesis are described in Appendix A, and include various excited states in the reactions.

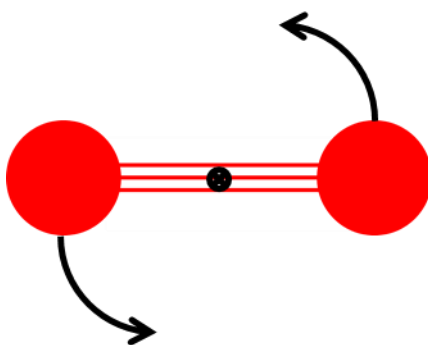


Figure 2.2. Schematic drawing of the rotation of a diatomic molecule.



2.1.6. Nitrogen: The complete picture

The Schrödinger equation has been mentioned a few times and many quantum numbers and complex notations have been introduced in sections 2.1.1 through 2.1.5. Even though those descriptions work well, only the hydrogen atom can be described analytically by the Schrödinger equation, as it is a single electron system – a single particle system. The *time-independent Schrödinger equation* is given by:

$$\left[-\frac{\hbar^2}{2m} \nabla^2 + U \right] \Psi = E\Psi \quad (2.1)$$

The first term in the [] brackets correspond to the kinetic energy; \hbar is the *reduced Planck constant* and m is the mass of the particle under investigation. The second term, U , is the *potential energy* of the system. Those terms together are known as the *Hamiltonian*. E is the energy of the system and Ψ is the wave function, which is solved for, together with the relevant boundary conditions of a system. The wave function causes the various quantum numbers to be introduced. E can generally be expressed in terms of those quantum numbers.

Throughout sections 2.1.1 to 2.1.5, three distinct quantum mechanical systems have actually been discussed. In order to describe those systems, the potential energy of the system have to be used in the Schrödinger equation.

Section 2.1.1 through 2.1.4. describe the electrons in atoms and molecules. As mentioned here, the Schrödinger equation can be solved analytically for a single electron system such as the hydrogen atom. For this system the potential is given by:

$$U(r) = -\frac{e^2}{4\pi\epsilon_0} \frac{1}{r} \quad (2.2)$$

This potential only depends on the radius r (in *spherical coordinates*), the elementary charge e and the vacuum permittivity ϵ_0 .

In section 2.1.5, the quantum harmonic oscillator was mentioned in relation to vibrational excitation. For this system the potential is:

$$U(x) = \frac{1}{2}kx^2 \quad (2.3)$$

Finally, the rigid rotor was mentioned in relation to rotational excitation. For that system $U = 0$.

Thus, in order to describe a system, the potential energy description of the system should be known. For complex molecules, the situation quickly becomes very convoluted. In Figure 2.3 the potential energy curves of molecular nitrogen are shown, which directly reflect the complexity of the system.

For example, in order to study vibrational excitation and the corresponding quantized energies, the *quantum harmonic oscillator* is a very simple approximation of the potential shown in Figure 2.3. Common other descriptions of those potential curves are the *Lennard-Jones* potential and the *Morse* potential.

In literature there are various techniques to describe systems of such complexity; such as *first order perturbation theory* [87], *quasi-classical trajectory calculations* [88] and *analytical non-perturbative methods* [89].



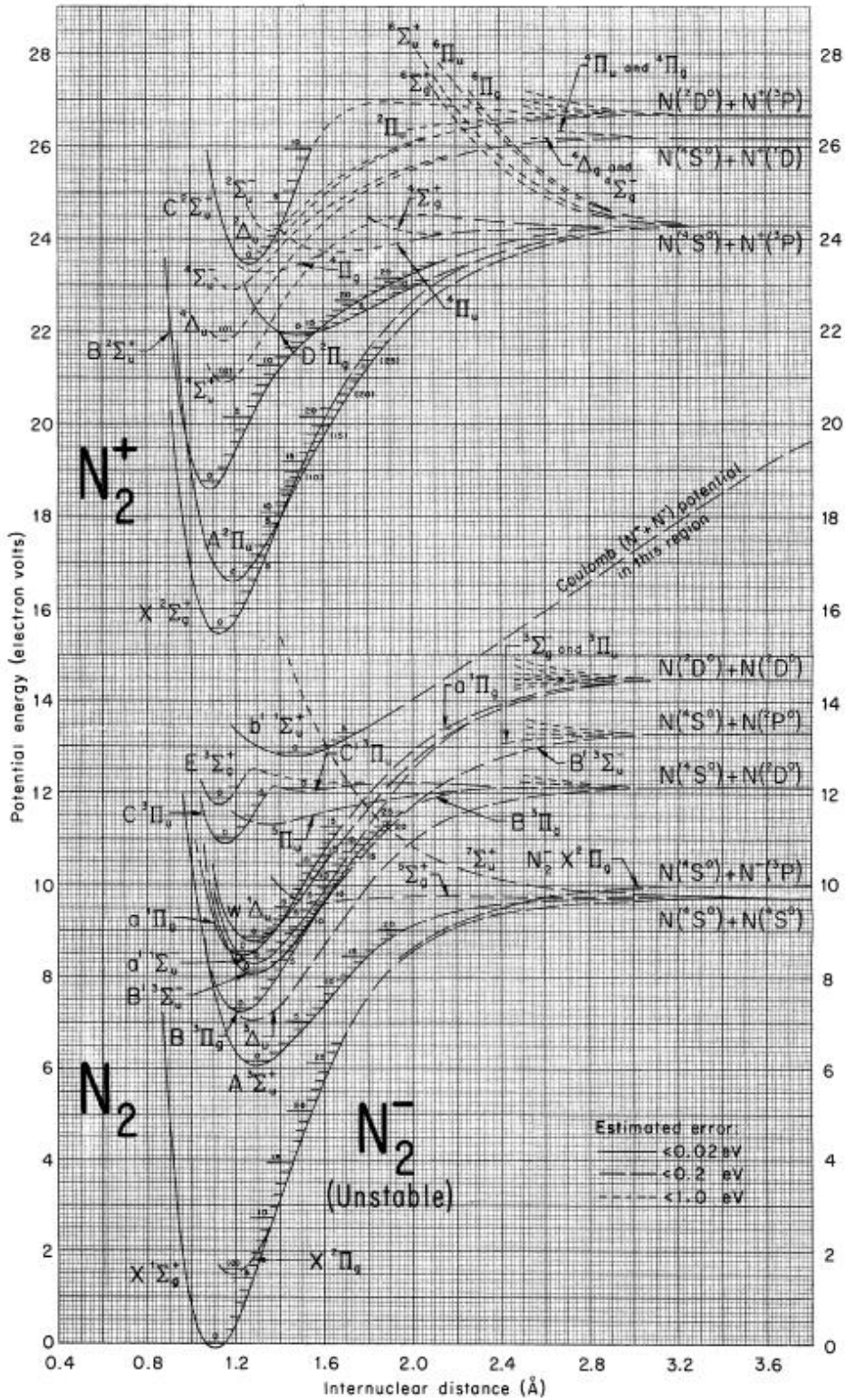


Figure 2.3. The potential energy curves for N_2 [90]. This diagram indicates how atoms and their excited states come together to form different (electronically excited) states of the N_2 molecule, as well as the ion N_2^+ . Vibrational levels are also indicated (small horizontal markings in the potential curves).

2.1.7. Harnessing plasma for nitrogen fixation

Finally, before we continue, we will use the descriptions of the preceding sections in order to briefly discuss why artificial nitrogen fixation is so energy-intensive and why plasma might be used for this purpose.

In Figure 2.1, the molecular orbital diagram of nitrogen shows that three bonding orbitals are completely filled. The *bond order* is thus 3. The nitrogen molecule N_2 has a triple bond: $N\equiv N$. Compared to oxygen and hydrogen, which have a double and single bond respectively, this is a very strong bond. As can be seen in Figure 2.3, it takes 9.8 eV in order to dissociate N_2 (*dissociation energy*). The potential energy curve of $N_2(X^1\Sigma_g^+)$ until $N(^4S^0) + N(^4S^0)$, indicates the reaction barrier that needs to be overcome in order for dissociation to occur. From the same curve it is clear that a vibrationally excited level significantly reduces the energy difference between the N_2 molecule and the dissociation products. Vibrational excitation thus helps to overcome the dissociation reaction barrier more easily. Similarly, electronic excitation is also linked to reduced dissociation barriers. See for example the potential energy curve of $N_2(B^3\Pi_g)$ to $N(^4S^0) + N(^4D^0)$.

Thus, if in a plasma the vibrational and/or electronic excitation degrees can be increased, it is possible to increase the dissociation reaction rate, which in turn makes it possible to reach dissociation degrees beyond the *thermal chemical equilibrium*. Such equilibrium that can be obtained in plasma is sometimes referred to as a *partial chemical equilibrium* [91].

2.2. Plasma: A too large collection of particles

As discussed in section 2.1, a plasma is a collection of many types of particles; neutral gas atoms and molecules, positive (and negative) ions and electrons. On top of that, the atoms, molecules and ions can occur in many different states (see section 2.1.1 through 2.1.6) due to vibrational and electronic excitation (as well as rotational excitation).

In plasma kinetics modelling, we describe how all those different species interact with each other in a plasma environment. While there can be a large variety of species, the absolute number of particles is even larger. For example, the *Loschmidt constant* gives the number of particles in an ideal gas at atmospheric pressure and 0 °C. Its value is: $2.687 \times 10^{25} \text{ m}^{-3}$. Clearly it is not very feasible to describe and keep track of in the order of 26,870,000,000,000,000,000,000 particles in a plasma. Even in a small plasma volume, such as 1 cm³ or 1 mm³ instead of 1 m³, the number of particles is still cumbersome large.

The Loschmidt constant gives a particle density. It gives the number of particles that can be found in a certain volume. Due to the large number of particles, the same quantity is used in plasma kinetic modelling. However, despite the units of ‘per volume’, such *number densities* do actually describe the number density in a specific point. Number densities specify that it is possible to find a certain number of particles per unit volume at a certain point. A point very close to it, does not need to have the same number density due to slight changes in pressure and/or temperature (even within a unit of volume).

The total number density, in a specific point, is a sum of all number densities of the individual species, in that same point.

2.2.1. The Boltzmann equation and number densities

As discussed, due to the large number of particles in a plasma, a macroscopic description is needed. In such a macroscopic description, also known as a *hydrodynamic description*, the plasma is effectively considered as a (continuous) fluid. However, how does such a description relate to the individual particles?

Let's consider many particles of a single kind of species. The particles are thus identical. However, we distinguish them by their actual position $\mathbf{r} = (x, y, z)$ and velocity $\mathbf{v} = (v_x, v_y, v_z)$. The particles are thus in a *six-dimensional phase space*. A *distribution function* $f(\mathbf{r}, \mathbf{v}, t)$ describes the locations and velocities of all the particles in this phase space at any moment in time.

In Figure 2.4 the two x components of this phase space are drawn. If we consider a small element, we can write down the changes that take place [92]:

$$\text{change in time: } [f(x, v_x, t + dt) - f(x, v_x, t)]dv_x dx = df dv_x dx$$

$$\begin{aligned} \text{change in velocity direction: } [f(x, v_x, t)dx - f(x, v_x + dv_x, t)dx]dv_x \\ = -a_x df dx dt \end{aligned}$$

$$\begin{aligned} \text{change in space direction: } [f(x, v_x, t)dv_x - f(x + dx, v_x, t)dv_x]dx \\ = -v_x df dv_x dt \end{aligned}$$

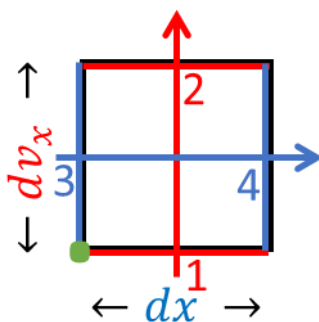


Figure 2.4. Schematic drawing of a small element in two-dimensional phase space (the two x components of six-dimensional phase space). It indicates the reference point $[f(x, v_x, t)]$, green, and how particles with different velocity and position enter this small element (across face 1 and 3, respectively), and how particles with the correct velocity and position leave this small phase space element (across face 2 and 4, respectively). A change in velocity has to be caused by an (de-)acceleration ($a = dv/dt$). In order to change position, a velocity is required ($v = dx/dt$).

In the above expressions the acceleration $a_x = dv_x/dt$ was used, as changes in velocity (change in velocity direction) correspond to accelerations. Similarly, $v_x = dx/dt$ was used for changes in the space direction. If we keep track of all particles with the distribution function f , and collisions are neglected, then the sum of all those terms should be equal to 0:

$$dfdv_x dx = -a_x dfdv_x dt - v_x df dx dt \quad (2.4)$$

Dividing by $dx dv_x dt$ and rearranging gives:

$$\frac{\partial f}{\partial t} + v_x \frac{\partial f}{\partial x} + a_x \frac{\partial f}{\partial v_x} = 0 \quad (2.5)$$

Generalizing this approach over the whole phase space gives:

$$\frac{\partial f}{\partial t} + \mathbf{v} \cdot \nabla_{\mathbf{r}} f + \mathbf{a} \cdot \nabla_{\mathbf{v}} f = 0 \quad (2.6)$$

This is the *collisionless Boltzmann equation*. If collisions (subscript c) do take place, it is possible for particle to appear and disappear:

$$\frac{\partial f}{\partial t} + \mathbf{v} \cdot \nabla_{\mathbf{r}} f + \mathbf{a} \cdot \nabla_{\mathbf{v}} f = \left. \frac{\partial f}{\partial t} \right|_c \quad (2.7)$$

This is the *Boltzmann equation*. The exact form of the *collision term* can be rather complex [93].

Solving the Boltzmann equation, gives the distribution function $f(\mathbf{r}, \mathbf{v}, t)$. From this function, which describes all particles and their location, macroscopic quantities can be derived, including the total number of particles:

$$N = \iint f(\mathbf{r}, \mathbf{v}, t) d^3x d^3v \quad (2.8)$$

And the number density:

$$n(\mathbf{r}, t) = \int f(\mathbf{r}, \mathbf{v}, t) d^3v \quad (2.9)$$

The second integral (Eq. 9) effectively counts all particles at a certain location \mathbf{r} , no matter their velocity, while the first integral counts all particles in the volume given by d^3x .

2.2.2. Zeroth moment of the Boltzmann equation: The continuity equation

Similar to integrating the distribution function f over velocity space to obtain macroscopic quantities, each term in the Boltzmann equation itself can also be integrated over velocity space [92]. The *zeroth moment of the Boltzmann equation* gives the *continuity equation*.

The average velocity is given by:

$$\langle \mathbf{v} \rangle = \frac{1}{n} \int \mathbf{v} f(\mathbf{r}, \mathbf{v}, t) d^3v \quad (2.10)$$

This concept can be generalized to taking the average of a hypothetical quantity A :

$$\langle A \rangle = \frac{1}{n} \int A f(\mathbf{r}, \mathbf{v}, t) d^3v \quad (2.11)$$

Performing such integrations for each term in the (collisionless) Boltzmann equation gives³:

$$\int A \frac{\partial f}{\partial t} d^3v = \frac{\partial}{\partial t} (n \langle A \rangle) \quad (2.12)$$

$$\int A (\mathbf{v} \cdot \nabla_{\mathbf{r}} f) d^3v = \nabla_{\mathbf{r}} (n \langle \mathbf{v} A \rangle) \quad (2.13)$$

$$\int A (\mathbf{a} \cdot \nabla_{\mathbf{v}} f) d^3v = -\nabla_{\mathbf{v}} (n \langle \mathbf{a} A \rangle) \quad (2.14)$$

³ Each time the product rule is used to expand the integrand. For example, for Eq. 2.14, $y(x) \equiv A \mathbf{a} f$, $\frac{dy}{dx} \equiv y' = A' \mathbf{a} f + A \mathbf{a}' f + A \mathbf{a} f'$ such that the integrand $A (\mathbf{a} \cdot \nabla_{\mathbf{v}} f) = \nabla_{\mathbf{v}} \cdot (A \mathbf{a} f) - (\mathbf{a} \cdot \nabla_{\mathbf{v}}) f A - A f (\nabla_{\mathbf{v}} \cdot \mathbf{a})$. The last term evaluates to zero if $\mathbf{a} \neq \mathbf{a}(\mathbf{v})$ is assumed. In this specific case, the first term evaluates to zero after using the *divergence theorem*: $\int \nabla_{\mathbf{v}} \cdot (A \mathbf{a} f) d^3v = \oint A \mathbf{a} f dS_{\mathbf{v}}$, where $dS_{\mathbf{v}}$ is the surface boundary of the velocity space, where $\mathbf{v} \rightarrow \infty$ and thus $f \rightarrow 0$, evaluating the integral to 0, which is a consequence of considering all particles and possible velocities.

For the n th velocity moment, the quantity $A \propto \mathbf{v}^n$. If we fill in $A = 1$ ($n = 0$, and proportionality constants neglected) and evaluate the above expressions, the zeroth moment of the Boltzmann equation follows:

$$\frac{\partial n}{\partial t} + \nabla_{\mathbf{r}} \cdot (n\langle\mathbf{v}\rangle) = 0 \quad (2.15)$$

This is the continuity equation, representing *mass conservation*. If we again generalize this to include collisions, then:

$$\frac{\partial n}{\partial t} + \nabla_{\mathbf{r}} \cdot (n\langle\mathbf{v}\rangle) = G \quad (2.16)$$

Where G specifies the generation (or loss) of particles due to collisions.

Similar to the above; the first moment ($A \propto \mathbf{v}$) would give an equation for the *conservation of momentum* and the second moment ($A \propto \mathbf{v}^2$) would give an equation for the *conservation of energy*. The momentum balance equation is often used to find an expression for the particle fluxes ($\mathbf{\Gamma} = n\langle\mathbf{v}\rangle$). Especially in case of plasma modelling, for transport of charged particles, the *drift-diffusion* approximation is often used. However, those concepts will not be discussed in detail as the plasma kinetics modelling approach used in this thesis does not rely on them.

Indeed, as mentioned in the introduction, plasma kinetics (zero-dimensional) modelling neglects spatial dependencies. This means that the second term in the continuity equation, which describes the flux of particles, is not taken into account in plasma kinetics modelling.

In addition, this derivation is for a single kind of species. However, in a plasma there are many different kinds of species, all of which interact with each other through the collision term (G). The continuity equation then becomes:

$$\frac{\partial n_s}{\partial t} = G_s \quad (2.17)$$

Where n_s and G_s are the number density and generation term, respectively, for the specific species s .

2.2.3. Probabilities and (common) distributions functions

A reoccurring theme in this chapter is that of probabilities and distributions.

In section 2.1., electron configurations and electron clouds were discussed.

Electron clouds are described by wave functions, obtained by solving the Schrödinger equation. Those are only a measure for the likelihood of finding an electron at a certain location. The exact location is thus not known.

When considering the rotational, vibrational and electronic excitations, the associated electron configurations and corresponding potential energy, it is clear that a gas consists of particles which all can have different energies. This situation can be described in two ways: Each individual state is considered as a unique kind of species, or the gas is described with a distribution function over the various internal energy states. In this thesis the former approach is followed; the various vibrational and electronically excited levels are treated as separate species (see section 4.1.1).

Commonly used practical distribution functions are for example *vibrational distribution functions*, which give the probability of finding a molecule in a certain vibrational level. Such a distribution function can be constructed from the absolute number densities of the individual levels (*state-to-state approach*). The distribution can also be calculated using the *Fokker-Planck equation*, which is a *continuum approach* [94].

There are a few analytical distribution functions. Under thermal equilibrium, the vibrational distribution will follow a *Boltzmann distribution*, which depends on the gas temperature. Non-equilibrium situations can also correspond to a Boltzmann distribution, at a vibrational temperature above the gas temperature. The *Treanor distribution* is another analytical form, which does capture non-equilibrium behavior and is based on both a gas and vibrational temperature. However, most often, actual non-equilibrium distribution functions require numerical calculations.

Number densities, introduced in section 2.2.1, also forgo the exact spatial information of the individual species. Section 2.2.1 showed that the connection between the spatial information and the number density is given by distribution functions of positions and velocities. Velocity can directly be related to the *kinetic energy* ($E = \frac{1}{2}mv^2$).

Depending on the collisions taking place, and their frequency, the Boltzmann equation can result in the *Maxwell-Boltzmann (velocity or energy) distribution function*. This can hypothetically be used to describe any of the species in a plasma. However, it does correspond to an equilibrium, which can for example be readily achieved if there are only elastic collisions between the specific species themselves, which equilibrate the energies between the individual particles.

The Maxwell-Boltzmann distribution function can also be derived based on *statistical mechanics* in various *canonical ensembles*.

Especially for the electrons such distribution functions are important. The (kinetic) energy of the electrons greatly determines the electron impact collisions that can take place (such as [de-]excitation, ionization, attachment and dissociation). Not all electrons have the same energy, and tracking each individual electron is unfeasible. Thus, the electrons are described with an *electron energy distribution function* (EEDF). While it is possible for the EEDF to be Maxwellian, it greatly depends on various factors, such as the (elastic) collision frequency between electrons themselves, as described above, and the plasma conditions which impose forces on the electrons. For example, electrons are accelerated by the electric fields that are present in plasma. EEDFs are thus often calculated numerically from the electron Boltzmann equation (see section 4.1.2) [93].

2.3. Concluding remarks

The aim of this chapter was to familiarize the reader with important concepts that underlie plasma kinetics modelling.

The main points of interests are:

- The meaning of individual excited states (and ions) and how those concepts relate to a large collection of particles – a gas.
- The challenges in artificial nitrogen fixation: Breaking the nitrogen triple bond and how a plasma can aid in this objective.
- The use and interpretation of number densities, in order to describe a large collection of particles.
- The derivation of the Boltzmann equation, its relation to a macroscopic description of a gas/plasma.
- The continuity equation and how it follows from the Boltzmann equation.
- The relationship between number densities and distribution functions, including the use and interpretation of distribution functions.

In Chapter 3, chemical reactors and their description will be considered, as well as how that description relates to the above.

Chapter 4 takes the concepts from Chapter 2 and 3 and applies them to plasma kinetics modelling specifically.

Chapter 3.

Describing chemical reactors

3.1. Deriving the continuity equation: Plug flow and related reactors

Most plasma experiments use a continuous flow. The corresponding (chemical) reactors are thus continuous flow reactors. In Figure 3.1, a schematic of a tubular reactor is given.

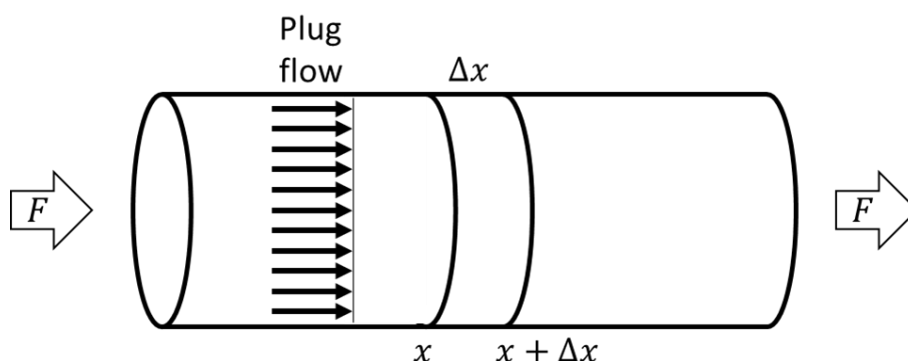


Figure 3.1. Schematic of a tubular continuous flow reactor, indicating the molar in and out flow, a reactor segment and a uniform plug flow.

The mass balance for such a reactor can be described as:

$$\text{accumulation} = \text{inflow} - \text{outflow} + \text{generation} \quad (3.1)$$

The generation term accounts for the rate of production or consumption of different species in the system due to (chemical) reactions.

We can also consider a small reactor segment Δx . The simplest flow is a plug flow, which assumes that the flow velocity in the reactor is uniform in the radial direction. Following the above description, the mass balance equation for the small reactor segment becomes:

$$\frac{dN}{dt} = F(x, t) - F(x + \Delta x, t) + G \quad (3.2)$$

Where N is the number of particles in moles, F is the molar flow rate, and G is the generation term: The number of moles created per second per unit volume of the reactor segment ($A\Delta x$, where A is the cross sectional area of the reactor). This can be rewritten and rearranged:

$$\frac{d}{dt}cA\Delta x = vAc(x, t) - vAc(x + \Delta x, t) + RA\Delta x \quad (3.3)$$

$$\frac{dc}{dt} = \left[\frac{vc(x, t) - vc(x + \Delta x, t)}{\Delta x} \right] + R \quad (3.4)$$

$$\frac{\partial c(x, t)}{\partial t} = -\frac{\partial}{\partial x}vc(x, t) + R \quad (3.5)$$

This results in the (continuity) equation for a *plug flow reactor* (PFR). $F = vAc$, $N = cV$ and $G = RV$ was used, with v the flow velocity, c the molar concentration, V the volume of the reactor segment and R the rate of reaction in mol/m³s. The reactor segment Δx is taken to be infinitesimally small in order to arrive at the differential equation (Eq. 3.5).

The plug flow reactor is very similar to a *laminar flow reactor*. In the latter, the velocity $v = f(r)$, depends on the radius r , thus such a system is normally solved in cylindrical coordinates. The equivalent derivation is a bit more complicated and won't be discussed. The plasma kinetics models in this thesis are based on the plug flow reactor approach.

The Avogadro constant N_A can be used to convert the molar concentration to number densities ($n = cN_A$). Furthermore, there can be many different kinds of species s in the reactor, that interact with each other through collisions. Each species thus has a generation term G_s due to collisions/reactions – here, the units are 1/m³s. The above continuity equation can thus be written as:

$$\frac{\partial n_s(x, t)}{\partial t} = v\frac{\partial n_s(x, t)}{\partial x} + G_s \quad (3.6)$$

Solving this equation gives the number densities of each species over the whole reactor length L such that $x \in [0, L]$, and as a function of time $t \in [0, \infty)$. The residence time is given by $\tau_{res} = L/v$. Of course, a steady state might be reached long before $t \rightarrow \infty$. A specific relation between reaching steady state and the residence time is not guaranteed. The time to reach steady state depends on the reactions taking place and the flow (rate/velocity). There is thus a significant distinction between the residence time τ_{res} and the time t . The latter can be considered as the operational time of the reactor.

The plug flow reactor can also be considered in steady state; then $\partial n_s / \partial t = 0$. However, using $v = dx/dt$ to rewrite $v \partial n / \partial x$, the steady state plug flow reactor can be written as:

$$\frac{dn_s}{dt} = G_s \tag{3.7}$$

When considering a plug flow reactor in this way, it is very important to realize the steps that led to this equation. The equation ends up stating $dn_s/dt \neq 0$, while the underlying assumption was a steady state. Because the velocity and position was used to obtain the current time dependency, the relevant time scale is now only $t \in [0, \tau_{res}]$. Going back to Figure 3.1, this approach corresponds to a small volume (see ∂x in Eq. 3.6) moving throughout the reactor (with velocity v , see Eq. 3.6). This volume starts with the initial feed gas. The speciation then evolves as it moves through the reactor because of the reactions (G_s) taking place. This description is only valid if the small volume that moves through the reactor does not influence the (steady state) conditions in the reactor, such that a second volume moving through the reactor does not experience different conditions. In other words, there should not be an interaction between the flowing gas and the fixed reactor walls (e.g. plasma-surface interactions, as in plasma catalysis), or similar.

This approach is often used in ‘quasi-1D modelling’ where this time dependence ($t \in [0, \tau_{res}]$) is converted back to a positional dependence ($x = vt$) in order to describe the reactor conditions as a function of position throughout the reactor.

The above continuity equation also corresponds directly to a *batch reactor*, which can be compared to baking a cake – or Surinamese Bojo⁴ for that matter – in an oven. The reagents are placed in a reactor without in or out flow and the reaction is allowed to take place for a certain residence time.

Finally, this exact continuity equation can be recognized from section 2.2.2 (Eq. 2.17), where it was derived starting with the Boltzmann equation.

3.2. Distinctions between time and residence time dependencies: Continuously stirred tank reactors

By initially considering a reactor segment Δx in section 3.1, the (axial) spatial dimension of the reactor was explicitly considered. The reactor as a whole can also be considered as a continuously stirred (tank) reactor (CSTR). In such reactors perfect mixing is assumed. A portion of the gas that flows in the reactor is instantly able to flow out of the reactor, because the gas that enters the reactor is assumed to be instantly evenly mixed/distributed over the whole reactor. The corresponding continuity equation can be written as:

$$\frac{dn_s}{dt} = + \frac{1}{\tau_{res}} n_{s,0} - \frac{1}{\tau_{res}} n_s + G_s \quad (3.8)$$

Where $n_{s,0}$ is the initial number density of species s . In this description the number density n_s is also only a function of time, again $t \in [0, \infty)$, as the spatial information is lost due to how the in and out flow terms are resolved (based on perfect mixing).

⁴ Mix ca. 1 kg of grated cassava, 0.3 kg sugar, 0.2 kg grated coconut, 0.005 l vanilla essence, 0.005 l almond essence, 0.02 kg cinnamon powder, 0.1 kg (white) raisins (optional), 0.4 l milk, 0.4 l coconut milk and 0.15 kg melted butter until a smooth and even mass and place it in your batch reactor at ca. 444 K for ca. 5400 s – your mileage may vary.

Considering the outflow term ($-n_s/\tau_{res}$) and that perfect mixing was assumed, then it is clear that $n_s(t)$ directly represents what comes out of the reactor.

If the reactor is divided into N CSTR reactors, each with a residence time $\tau_{res,N} = \tau_{res}/N$ and if the above equation is solved for each of those reactors, then a set of differential equations, with appropriate inflow terms, can be written:

$$\begin{aligned} \frac{dn_{s,1}}{dt} &= + \frac{1}{\tau_{res,N}} n_{s,0} - \frac{1}{\tau_{res,N}} n_{s,1} + G_s \\ \frac{dn_{s,n}}{dt} &= + \frac{1}{\tau_{res,N}} n_{s,n-1} - \frac{1}{\tau_{res,N}} n_{s,n} + G_s, \quad n \in [1, N] \\ \frac{dn_{s,N}}{dt} &= + \frac{1}{\tau_{res,N}} n_{s,N-1} - \frac{1}{\tau_{res,N}} n_{s,N} + G_s \end{aligned} \quad (3.9)$$

This effectively corresponds to the full plug flow reactor description (Eq. 3.6). Each differential equation gives the density at a specific point along the reactor length:

$$n_{s,n}(t) = n_s(x, t), \quad x = n \frac{L}{N} \quad (3.10)$$

Of course, solving so many differential equations is unpractical. However, from those considerations it is clear that a large number of CSTRs in series, approaches a plug flow reactor.⁵

The different reactor descriptions and the differences therein are very important, as the specific descriptions also directly influence the conversion that is obtained. The various approaches discussed in this chapter are summarized in Table 3.1. In Figure 3.2, the conversions in a plug flow reactor (Eq. 3.7) and a CSTR (Eq. 3.8) as a function of (residence) time are compared for a simple first order irreversible reaction.

If the reaction is given by $A \rightarrow \text{products}$, with rate coefficient k , then Eq. 3.7 becomes:

$$\frac{dn_A}{dt} = -kn_A \quad (3.11)$$

⁵ More rigorous derivations/proofs are available in literature, involving for example the *design equations* for each reactor, which characterize their performance in terms of conversion [181].

Which can be solved, resulting in:

$$n_A(t) = n_{A,0} \exp(-kt) \quad (3.12)$$

Thus the conversion χ is given by:

$$\chi_A(t) = 1 - \exp(-kt) \quad (3.13)$$

Similarly, for Eq. 3.8:

$$\frac{dn_A}{dt} = \frac{1}{\tau_{res}}(n_{A,0} - n_A) - kn_A \quad (3.14)$$

$$n_A(t) = \frac{n_{A,0}}{k\tau_{res} + 1} [1 - \exp(-k't)], \quad k' = \frac{1}{\tau_{res}} + k \quad (3.15)$$

$$\chi_A(t) = \frac{k\tau_{res}}{k\tau_{res} + 1} + \exp(-k't) \quad (3.16)$$

In steady state ($t \rightarrow \infty$), this equation gives:

$$\chi_A(\tau_{res}) = \frac{k\tau_{res}}{k\tau_{res} + 1} \quad (3.17)$$

Table 3.1. Summary of the various reactor descriptions.

Reactor	Equation	Result	Domain
PFR ∞ CSTRs in series	Eq. 3.6 Eq. 3.9	$n_s(x, t)$	$x \in [0, L], t \in [0, \infty)$
PFR in steady state Batch reactor	Eq. 3.7	$n_s(t)$	$t \in [0, \tau_{res})$
CSTR	Eq. 3.8	$n_s(t)$	$t \in [0, \infty)$

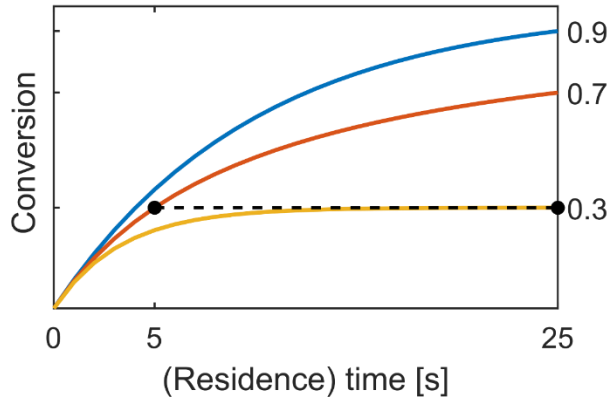


Figure 3.2. Illustration of the different conversion characteristics (based on a simple first order irreversible reaction with $k = 0.1$) for the different reactor descriptions. A plug flow reactor in steady state, which operates as a function of time until a certain desired residence time is reached, reaches relatively high conversion (blue line, 0.9, Eq. 3.13). A CSTR is characterized by a certain residence time and operates as a function of time (yellow line, 0.3, Eq. 3.16, with $\tau_{res} = 5$ s). CSTRs that have reached steady state, reach relatively low conversions (red line, 0.7, Eq. 3.17), compared to equivalent plug flow reactors.

3.3. Concluding remarks

The aim of this chapter was to introduce the reader to the different ways in which a (chemical) reactor can be described. However, many concepts, such as the *design equations* and *residence time distribution functions*, have not been discussed, as they are out of the scope of the calculations presented in this thesis. Nevertheless, they do play a crucial role in understanding and modelling (chemical) reactors.

The main points of interests discussed in this chapter are:

- The derivation of the plug flow reactor model (continuity equation), and the domain over which that description operates.
- The assumptions and implications of a plug flow reactor in steady state, and its correspondence to a batch reactor.
- The difference between residence time and (operation) time.
- The description of a continuously stirred tank reactor, perfect mixing, and its correspondence to a plug flow reactor.

- The different conversion characteristic of plug flow reactors and continuously stirred tank reactors.

Chapter 4 will present how a specific plasma reactor – a dielectric barrier discharge – has been modelled in this work. Amongst others, the generation term G_s will be specified.

Chapter 4.

Plasma kinetics modelling of dielectric barrier discharges

4.1. Plasma kinetics modelling: The continuity equation

The Zero-Dimensional Plasma Kinetics modelling platform ZDPlasKin [95] has been used to solve the continuity equation (Eq. 2.17), representing a batch reactor (or a plug flow reactor in steady state, Eq. 3.7). As discussed in the introduction (section 1.3), plasma kinetics modelling does not capture explicitly the spatial dimensions or spatial variations in species concentrations and the associated transport phenomena (see Eq. 2.16). This significantly reduces the computational costs and allows plasma kinetics models to describe detailed chemistries.

The continuity equation is given by:

$$\frac{dn_s}{dt} = G_s \quad (4.1)$$

Where n_s is the number density of species s , and G_s is the corresponding generation term, or source term, which represents the change in n_s due to reactions. The source term is given by:

$$G_s = \sum_r c_{r,s} R_r \quad (4.2)$$

$$R_r = k_r \prod_{q_r} n_{q_r} \quad (4.3)$$

Where $c_{r,s}$ is the stoichiometry of species s in reaction r , which can be negative (when s is a reactant), positive (when s is a product) or zero, R_r is the rate of reaction r , k_r is the corresponding rate coefficient and q_r represents all reactants in reaction r .

4.1.1. Rate coefficients and the kinetics

The rate coefficients k_r , typically depend on the temperature, more specifically, the gas temperature and/or electron temperature for reactions involving the (neutral) gas particles and electrons, respectively.

The rate coefficients as a function of gas temperature are typically taken from literature. The gas temperature itself can be calculated self-consistently (based on the *enthalpies of reaction*) or its value can be set to describe the relevant plasma conditions. The calculations in this thesis assume fixed gas temperatures.

Using a constant gas temperature to describe the average plasma temperature is assumed to be a valid approach, even though ammonia formation is an exothermic process (Eq. 1.2). Based on experimental experience, a significant temperature increase throughout the whole reactor is not always observed. This can be explained by the typically low flow rates at which a DBD operates and cooling of the gas at the reactor walls. However, at the same time, microdischarges are sometimes observed to have elevated temperatures (increased by a few 100 K [96]).

In total, the kinetics used to describe (plasma-catalytic) ammonia synthesis from nitrogen and hydrogen feed gases involve:

- Electron impact reactions (see also section 4.1.2)
- Neutral-neutral reactions, including with excited states and three-body reactions
- Ion-neutral reactions, involving positive ions
- Negative-positive ion recombination of H^-
- Vibrational kinetics, including electron impact vibrational (de-)excitation, vibrational-translational relaxation and vibrational-vibrational relaxation

- Surface kinetics, including wall relaxation, direct (radical) adsorption, Eley-Rideal and Langmuir-Hinshelwood elementary reaction steps and dissociative adsorption

The kinetics are presented in detail in Appendix A. The species that are considered in the kinetics are listed in Table 4.1.

Table 4.1. The species taken into account in the plasma and surface kinetics. Surface adsorbed species are indicated by (s). See Figure 2.3 and section 2.1 for additional context on the various excited nitrogen species.

	Nitrogen	Hydrogen
Ground states	N_2 N	H_2 H
	NH, NH_2, NH_3	
Vibrationally excited states	$N_2(V)$	$H_2(V)$
Electronically excited states	$N_2(A^3\Sigma_u^+), N_2(B^3\Pi_g),$ $N_2(a'^1\Sigma_u^-), N_2(C^3\Pi_u)$ $N(^2D^0), N(^2P^0)$	$H_2(b^3\Sigma_u^+), H_2(B^1\Sigma_u^+),$ $H_2(c^3\Pi_u), H_2(a^3\Sigma_g^+)$
Ions	N^+, N_2^+, N_3^+, N_4^+ $NH^+, NH_2^+, NH_3^+, NH_4^+, N_2H^+$	H^+, H_2^+, H_3^+ H^-
Surface adsorbed species	$N(s)$ $NH(s), NH_2(s)$	$H(s)$

4.1.2. Rate coefficients for electron impact collisions: Electric field and plasma power

Rate coefficients for electron impact processes depend on the electron temperature (or the electron energy). The electron temperature can be set directly⁶, or it can be calculated. In this thesis the latter approach is followed. It is assumed that the electrons

⁶ In the modelling platform ZDPlasKin, directly setting the electron energy enforces a Maxwellian electron energy distribution function. This approach is not used in this thesis.

are heated by a given plasma power P . This process is described as *Joule heating* or *Ohmic heating* [92]:

$$\frac{dP}{dV} = \mathbf{J} \cdot \mathbf{E} = \sigma E^2 \quad (4.4)$$

The power adsorbed by the electrons in a small volume dV is given by the current density $\mathbf{J} = \sigma \mathbf{E}$ and the electric field E . The conductivity σ is given by:

$$\sigma = en_e \mu_e \quad (4.5)$$

Where e is the elementary charge, n_e the electron density and μ_e the electron mobility.

From a known power that is supplied to the electrons, i.e. the plasma power, the electric field can be calculated if uniform power deposition and adsorption is assumed over the volume.

$$E = \sqrt{\frac{p}{\sigma}} \quad (4.6)$$

Where p is the power density defined as $p \equiv P/V$.

In the Boltzmann equation (Eq. 2.7), there is an acceleration (\mathbf{a}) term. A force can cause acceleration: $\mathbf{F} = m\mathbf{a}$. The Lorentz force gives the force exerted on charged particles by electric fields (and magnetic fields – which are neglected here as they are not relevant in this work); $\mathbf{F} = q\mathbf{E}$, where q is the charge of the particle ($-e$ for electrons). The Boltzmann equation for electrons can thus be written as:

$$\frac{\partial f}{\partial t} + \mathbf{v} \cdot \nabla_{\mathbf{r}} f - \frac{e}{m} \mathbf{E} \cdot \nabla_{\mathbf{v}} f = \frac{\partial f}{\partial t} \Big|_c \quad (4.7)$$

Calculating the electric field from Eq. 4.6 and using it in Eq. 4.7, only leaves the collision term as unknown. The collisions term is given based on the specific collision type (elastic, [de-]excitation, ionization, attachment, dissociation) and the associated cross sections. The cross sections $[\sigma(\varepsilon)]$ give the probability of the specific collisions to occur. Those probabilities, the cross sections, are a function of the electron energy ε .

Thus, having the electric field and cross sections, Eq. 4.7 can be solved (numerically) to obtain the electron energy distribution function (EEDF). ZDPlasKin is coupled to BOLSIG+ [93], which numerically solves the time-independent electron Boltzmann equation (Eq. 4.7 with $\partial f/\partial t = 0$). Once BOLSIG+ obtains the EEDF at the specified electric field, for the specified collisions (cross sections) and the current gas phase composition, it derives other properties from this distribution. From the EEDF and for each cross section, the corresponding rate coefficient $k(\varepsilon)$ is calculated. In addition, the mobility μ_e and mean electron energy $\bar{\varepsilon}$ are calculated. The rate coefficients and mobility values that are used (in Eq. 4.1 and Eq. 4.6, respectively) are evaluated at this mean energy.

The electron impact cross sections that are used in this thesis are listed in Appendix A (Table A.1).

To summarize, a plasma power is specified from which the electric field is calculated (Eq. 4.6). At this specified field, BOLSIG+ calculates an EEDF and the corresponding mean electron energy, at which the rate coefficients for electron impact processes (such as ionization and dissociation, amongst others) are calculated. The plasma power thus determines the behavior of the electrons. The plasma power allows capturing the behavior of specific plasma sources, such as dielectric barrier discharges – as will be discussed in the section 4.2.

4.1.3. Calculations at constant pressure

In the used kinetic modelling approach, i.e. solving the continuity equation in the form of Eq. 4.1, there is no intrinsic conservation of pressure. This is because the equation itself does not capture explicit in and out flow of the gas, which can regulate the pressure (see for example Eq. 3.8).

In the followed modelling approach, the total number density of gas phase species can increase with time, e.g. due to dissociation, in turn increasing the pressure. To account for this, after each time progression, we modify all gas phase species densities to return the set (atmospheric) pressure. This changes the mass density such that it is no longer

the initial value. For any calculation involving initial densities and new densities (after modification), the new densities are normalized to the initial value such that the mass density is the same. Both the modification and normalization are assumed linear, i.e. an equal multiplication factor is applied for all gas phase species.

In a 'quasi-1D' modelling approach (section 3.1) the velocity can be adjusted based on a recalculated mass flow rate. This thesis however, focusses only on results in function of time as there is no strong spatial dependency of the (average) plasma conditions.

4.2. Capturing the average behavior of dielectric barrier discharges

Dielectric barrier discharges (DBDs) are electrical discharges driven by an AC (alternating current) applied voltage between two opposing electrodes. Typically, at least one of those electrodes is covered by a dielectric barrier. The (applied) voltage $V(t)$ across the gaseous gap increases until the electric field is strong enough for a breakdown to occur. Charges that built up on the dielectric barrier limit this electric field from building up further. The discharge will continue at the burning voltage U_b , until the electric field becomes too weak to maintain the discharge due to a reduction in the applied voltage and due to the charges build up on the dielectric. This process repeats itself every half cycle of the applied voltage (which is most commonly sinusoidal). When the discharge is active, the gas is conductive and a current $i(t)$ is able to pass through the gaseous gap from electrode to electrode. DBDs typically operate in the filamentary regime, causing pulsed current characteristics corresponding to small plasma filaments in the discharge. This is summarized in Figure 4.1.

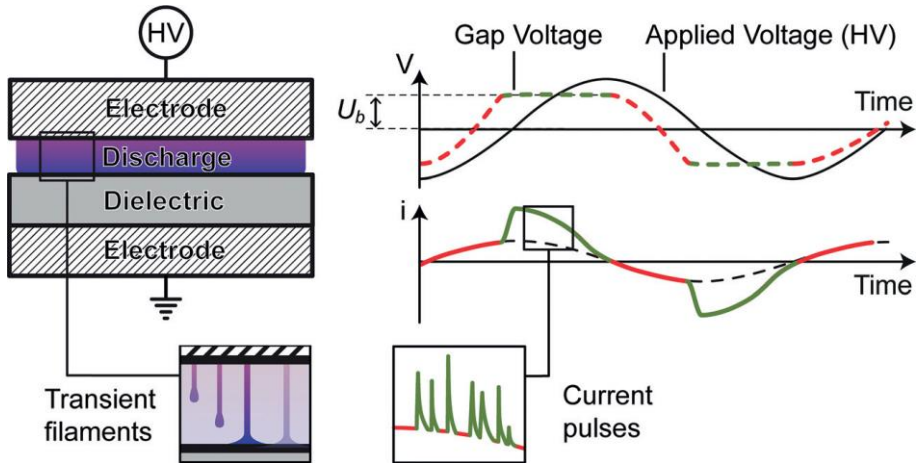


Figure 4.1. Schematic drawing and summary of the working principles of a DBD operating in a filamentary regime [97].

As discussed in section 4.1, the plasma behavior can be captured through the gas temperature and the electron temperature/energy. The latter is calculated from the power density (see section 4.1.2.). The plasma power thus needs to be known. The instantaneous power is given by $P(t) = V(t)i(t)$. However, due to the dielectric barrier, the measured current and voltage do not directly represent the plasma current and gaseous voltage drop (see Appendix B).

The current and voltage characteristics that are measured over the gaseous gap of the DBD can be considered to describe the average behavior of the plasma. That is, the current and voltage characteristics describe, for example, the number of filaments in the discharge, but not their location. Similarly, plasma kinetics modelling does not capture true spatial information, thus we need to describe the average behavior. More specifically, the average behavior as would be ‘observed’ by individual molecules in the plasma. To achieve this, we pay special attention to:

- The (instantaneous) power characteristics of the actual plasma (see section 4.2.1 and 4.2.3).

- The ‘fraction of microdischarges’, which takes into account that the filamentary microdischarges happen throughout the whole reactor, and thus, individual molecules can’t observe all filamentary microdischarges (see section 4.2.2).
- The appropriate discharge volume in which the measured power is deposited (see section 4.2.4).

4.2.1. Instantaneous plasma power and its average characteristics

It is common to characterize a DBD, and other plasma sources, with the average power \bar{P} . For AC driven discharges, or other periodic discharges, this averaging needs to occur over full discharge periods T_D :

$$\bar{P} = \frac{1}{T_D} \int_0^{T_D} V(t)i(t) \quad (4.8)$$

However, the instantaneous power itself also contains a lot of information, such as the number of microdischarges and their strength, reflected as current peaks of different height.

The calculation of the plasma current, gas voltage, and dissipated power is based on Peeters et al. [98]. Peeters et al. also considered that not the whole electrode is participating in the discharge due to the filamentary nature of the plasma. Those considerations are also taken into account when calculating the plasma current and voltage characteristics, and is presented in Appendix B in more detail for the actual current and voltage characteristics as used in Chapter 6.

In order to capture the characteristics of a DBD in our model, the average behavior of the instantaneous power profiles is described. However, this is not based on a single value (\bar{P}). The concepts of an average pulse width (given by the microdischarge lifetime τ_{MD}), average pulse height (P_{max}), and average minimum power (P_{min}) are introduced instead. We base those values on the actual plasma-dissipated power P_{diss} , which in

turn is based on the plasma current $i_{plasma}(t)$ and gas voltage $V_{gas}(t)$, to ensure that only the power that is actually deposited in the gaseous gap is considered (Appendix B).

In the model we consider the pulses in the instantaneous power characteristics as triangular pulses. Such a (periodic) function can be defined with:

$$P(t) = (P_{max} - P_{min}) \times \frac{2}{\tau_{MD}} \times \max \left[\left(\frac{\tau_{MD}}{2} - |t_{mod}(t) - t_0| \right), 0 \right] + P_{min} \quad (4.9)$$

In Eq. 4.9, the second line gives a triangle with height 1 and width τ_{MD} , centered around $t_0 = T_P/2$, where T_P is the pulse period, calculated from the discharge frequency T_D and the number of microdischarges per discharge half cycle N_{MD} : $T_P = T_D/2N_{MD}$. The time dependency is actually $t_{mod}(t) = t \bmod T_P$, to ensure the periodicity of the function.

A fraction of microdischarges η_{MD} is introduced to reduce the number of microdischarges that we consider in the model; see section 4.2.2. for the motivation of this parameter and its determination.

Effectively, η_{MD} is used to increase the pulse period to $T_P^\eta = T_P/\eta_{MD}$. This change propagates to t_0^η , t_{mod}^η and eventually the instantaneous $P^\eta(t)$, which is described analogous to Eq. 4.9.

The above ideas are summarized in Figure 4.2.

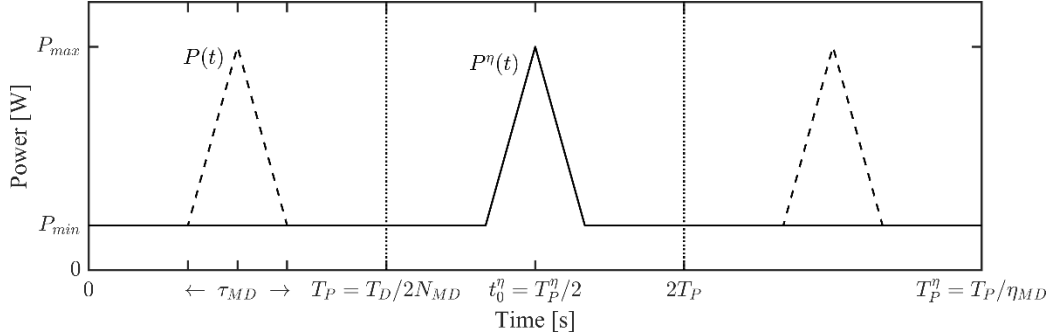


Figure 4.2. Definition of the instantaneous power pulses in time (Eq. 4.9), with P_{max} and P_{min} being the maximum power in the pulse and the (minimum) power in between the pulses, respectively, τ_{MD} the microdischarge life time, N_{MD} the number of microdischarges per half cycle, η_{MD} the fraction of microdischarges to which molecules are exposed (depicted here as $\eta_{MD} = 1/3$), T_D the discharge period, T_P the pulse period based on all microdischarges that occur throughout the whole reactor, t_0^n the pulse location and T_P^n the pulse period corresponding to the microdischarges to which individual molecules are exposed to (on average) (see also section 4.2.2).

First the concept of the fraction of microdischarges η_{MD} is substantiated in section 4.2.2. Expressions for the maximum and minimum power that ensure that the exact plasma power is used are given in section 4.2.3. There, the implications of η_{MD} on the plasma power will also be discussed.

4.2.2. The fraction of microdischarges

One of the most important considerations in the created methodology to model DBDs with a plasma kinetics modelling approach is the fraction of microdischarges η_{MD} . During typical residence times at which DBDs operate, there can be millions of microdischarges taking place throughout the gaseous gap of the reactor. However, those microdischarges are randomly distributed over the reactor. Thus a gas molecule that only just entered the reactor will not be exposed to a microdischarge that takes place at the end of the reactor.

The first conceptualization was based on the gas flow (velocity v). If it takes multiple discharge periods T_D for a gas molecule to pass through the reactor (with length L) and if all microdischarges are distributed uniformly, then the gas molecules can only be exposed to $\eta_{MD} = vT_D/L$ of the microdischarges. This idea is schematically shown in Figure 4.3.

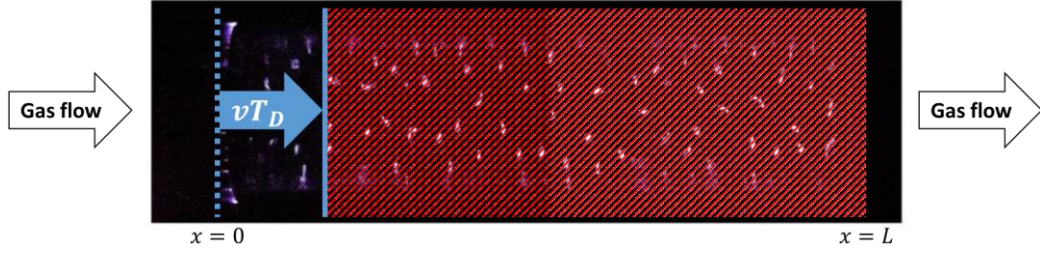


Figure 4.3. Conceptualization of the fraction of microdischarges η_{MD} . During a given discharge period T_D , the gas with velocity v is only able to traverse part of the reactor (vT_D). Only the microdischarges (white 'dots') in the traversed reactor section are relevant.

When considering this expression, $\eta_{MD} = vT_D/L$, the reduced pulse period (see section 4.2.1) reduces to: $T_P^\eta = T_P/\eta_{MD} = \tau_{res}T_P/T_D = \tau_{res}/2N_{MD}$. This means that with this approach, the number of microdischarges per discharge cycle is simply evenly distributed over the residence time. If the residence time changes, while the discharge parameters (i.e. the number of microdischarges) remain the same, then only the interpulse time will change.

The above approach is used in Chapter 5 and 6. In Chapter 5, various number of microdischarge values are used.

In Chapter 7, we investigate the fraction of microdischarges by employing various modelling techniques, based on which we confirmed an empirical relationship for the fraction of microdischarges: $\eta_{MD} = V_{MD}/V_R$, that is, the fraction of microdischarges corresponds to the microdischarge volume of the reactor (gaseous) volume. Following this approach, the number of microdischarges that are described in our model does increase with the residence time.

Sometimes it is useful to (directly) speak in terms of microdischarge frequencies. The total microdischarge frequency in the reactor is given by: $2N_{MD}f_D$, and the reduced microdischarge frequency is given by: $\eta_{MD}2N_{MD}f_D$, where f_D is the discharge frequency.

4.2.3. The maximum and minimum power, and the microdischarge and uniform power contributions

In order to find expressions for P_{max} and P_{min} we can integrate Eq. 4.9, in order to calculate the average power (\bar{P} , see Eq. 4.8, or equivalently, P_{diss} , see Appendix B):

$$P_{diss} = \frac{1}{T_P} \int_0^{T_P} P(t) dt = (P_{max} - P_{min}) \frac{\tau_{MD}}{2T_P} + P_{min} \quad (4.10)$$

$$P_{diss} = [(1 - \gamma)N_{MD}f_D\tau_{MD} + \gamma]P_{max} \quad (4.11)$$

Where $T_P = 1/2N_{MD}f_D$ was used and $P_{min} \equiv \gamma P_{max}$ is defined. $\gamma \in [0,1]$ is a distribution factor, which defines the eventual minimum and maximum instantaneous power values (in the model). The maximum power is given by:

$$P_{max} = \frac{P_{diss}}{(1 - \gamma)N_{MD}f_D\tau_{MD} + \gamma} \quad (4.12)$$

The maximum instantaneous power P_{max} is considered to represent the microdischarges (subscript MD), while the minimum instantaneous power P_{min} is considered to correspond to a uniform plasma contribution (subscript U) that is present throughout the whole reactor. The total plasma power is thus:

$$P_{diss} = P_{MD} + P_U \quad (4.13)$$

The fraction of microdischarges only reduces the power attributed to the microdischarges, the effective total power P^η is given by:

$$P^\eta = P_{MD}^\eta + P_U = \eta_{MD}P_{MD} + P_U \quad (4.14)$$

Thus, in principle, in our model description we do not consider the total plasma power that is dissipated in the reactor (Eq. 4.13). Only the power deposited into the same gas molecules (Eq. 4.14) is considered (see also section 4.2.2).

The two power contributions can be calculated with:

$$P_{MD} = \left[\frac{(1 - \gamma)N_{MD}f_D\tau_{MD}}{(1 - \gamma)N_{MD}f_D\tau_{MD} + \gamma} \right] P_{diss} \quad (4.15)$$

$$P_U = \left[\frac{\gamma}{(1 - \gamma)N_{MD}f_D\tau_{MD} + \gamma} \right] P_{diss} \quad (4.16)$$

Those relationships can be used to determine the fraction of power attributed to the microdischarges and the uniform plasma component, respectively.

The plasma conditions of Chapter 6 are presented in Appendix B. The power distribution factor γ was chosen as 0.1 for those conditions. Together with $N_{MD}f_D\tau_{MD} = 25 \times 23.5 \text{ kHz} \times 200 \text{ ns} = 0.1175$ (see Appendix B), Eq. 4.15 and 4.16 result in 51 % and 49 % of the power assigned to the microdischarges and the uniform plasma component, respectively. Note that Figure 5.1 in Chapter 5 describes different values. This is discussed in Section 4.2.5.

4.2.4. Discharge volumes

As discussed in section 4.1.2, the power density is what is actually required to calculate the electric field based on Joule heating (Eq. 4.6). Thus, appropriate discharge volumes have to be chosen.

The model description of the instantaneous power (cf. the red line in Figure B.3) consists of microdischarge pulses and a constant, minimum, power value. We assign the latter to a uniform plasma component that is also present in between the microdischarges. We thus need to define a discharge volume for both the microdischarges and the uniform plasma. The uniform power component is thought of as a weak plasma contribution that is present in the whole reactor. We assign the following volume to the uniform plasma:

$$V_U = \beta(1 - \alpha_{packing})V_R \quad (4.17)$$

The uniform discharge volume V_U , is the reactor volume V_R , corrected for packing with the packing factor $\alpha_{packing}$, as well as corrected for partial discharging of the plasma reactor through β (see Appendix B).

Packing factors of ca. 0.5 to 0.68 are recommended. The latter value is based on a body-centered cubic structure, which is not the most optimal packing, but more likely to occur in practice. The hexagonal close packed structure with $\alpha_{packing} = 0.74$ (the most optimal packing) is unlikely. The former value (ca 0.5) was obtained numerically by Uytendhouwen et al. [99].

Furthermore, because we are considering packed bed reactors, we attributed the size of typical voids in the assumed packed bed structure to the discharge volume of individual microdischarges, such that the microdischarge volume V_{MD} depends on the packing bead radius r_{bead} :

$$V_{MD} = \frac{4}{3}\pi(0.29r_{bead})^3 \tag{4.18}$$

Kruszelnicki et al. have clearly shown that microdischarges take place between the packing beads in a packed bed reactor. See Figure 4.4.

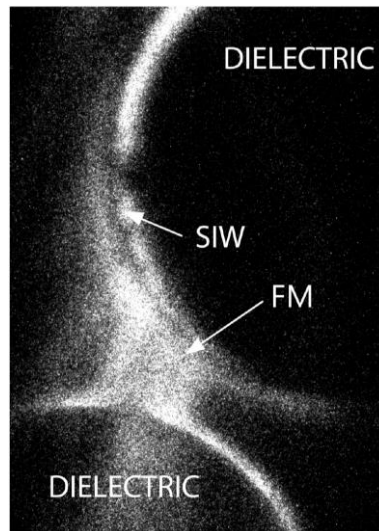


Figure 4.4. Experimental imaging by Kruszelnicki et al. [50], of a filamentary microdischarge (FM) and a surface ionization wave (SIW) in a two-dimensional packed bed reactor. Adopted from [50].

4.2.5. Comments on model iterations

Throughout this doctorate (3.5 years), improvements have been made to the modelling approach of dielectric barrier discharges in plasma kinetics modelling, as presented in this chapter.

The results and discussions are presented in Chapters 5, 6 and 7, based on the peer-reviewed publications produced during the doctorate.

In this chapter, mainly the latest approaches and insight were reported (corresponding to Chapter 6).

In the modelling for Chapter 5 and 6, the fraction of microdischarges was based on the gas velocity (see Figure 4.3). In Chapter 7, we have changed this approach to an empirical relationship (microdischarge volume over reactor volume). The latter approach allows the number of microdischarges to scale with the residence time, which can be considered more intuitive than the former approach. However, different residence times were not studied, and the fraction of microdischarge values obtained from the two methods are typically of the same order of magnitude.

In Chapter 5, the instantaneous plasma power was not yet explicitly considered. Instead, only the average plasma power was considered, which commonly is the only metric reported to describe experimental conditions. Still, the modelling approach followed is still very much the same. The modelled instantaneous power followed the same relationships as described here (Eq. 4.9 – 4.16).

However, considering only the average plasma power did influence our choice of discharge volumes. The average plasma power, which is determined over one discharge period, was considered to be most significantly deposited into all the microdischarges taking place during that discharge cycle: $V_{discharge} = 2N_{MD}V_{MD}$. Those considerations also meant that we did not consider a separate discharge volume for the uniform plasma component, which was still present and can in this case be considered as a weaker plasma representing the local afterglow of the microdischarges. In that study

(Chapter 5), the number of microdischarges per half cycle ranged from 50 to 500 based on [63]. Eventually, the choice of V_{MD} is very approximate, as well as counting the number of microdischarges successfully, which depends greatly on the discharge gas and electrical setup of the experiments.

Finally, because only one discharge volume was chosen, the power distribution factor γ (see Eq. 4.11) was actually called the power density distribution factor (see Chapter 5). In this case, the naming is actually ambiguous; the power can be distributed first, then divided by one discharge volume, or vice versa. However, due to using only the microdischarge volume to determine the power density, the relevant values of γ followed a logarithmic scale (i.e., $10^{-6}, 10^{-5}, 10^{-4}, 10^{-3}, 10^{-2}, 10^{-1}, 10^0$). In contrast, with the two discharge volume approach, the recommended values for the power – not power density – distribution factor γ are close to 0.1 ... 1. Also in this regard, the approaches were ambiguous. The eventual power density values are still of the same order of magnitude, as the order of magnitude difference in γ cancels out against the order of magnitude difference in the uniform discharge volume (Eq. 4.17) and the microdischarge volume (Eq. 4.18).

Specific differences can only be found when calculating the percentage of power that is assigned to the microdischarge or the uniform plasma. As mentioned, Eq. 4.15 and 4.16 are valid for both approaches. However, this does mean that the ratio of power assigned to the (modelled) microdischarges over the total power is a function of gamma: $P_{MD}^{\eta}/P_{diss} = f(\gamma)$. This function is the same for both approaches ($O(\gamma) \sim 10^{-6}$ vs $O(\gamma) \sim 0.1$), thus calculated percentages can differ when describing similar plasma conditions (power densities) in the two approaches. However, this difference does not influence the calculated results from the plasma kinetics model itself, as the plasma conditions are still similar in both approaches (see discussion above).

4.3. Concluding remarks

In this chapter the general plasma kinetics modelling approach was summarized, as well as the specific concepts and ideas used to capture the characteristics of dielectric barrier discharges in such models.

Specifically:

- The generation/source term in the continuity equation has been specified.
- The calculation of electron impact rate coefficients has been explained, requiring the electric field, which is calculated from the plasma power density.
- The plasma power (density) and how it allows capturing specific plasma characteristics was discussed.
- The concepts that allow us to more systematically capture the characteristics of dielectric barrier discharges were discussed: Considering the average maximum and minimum power and average microdischarge lifetime instead of just the average plasma power, the fraction of microdischarges and the appropriate choice of discharge volumes.

In Part III those concepts are used to gain insight into the role of vibrational excitation (Chapter 5), to investigate the temporally resolved reaction mechanisms (Chapter 6) and to consider the implications of spatially and temporally non-uniform plasma (Chapter 7).

Part III.
Results
&
Discussion

Chapter 5.

The role of vibrational kinetics in ammonia synthesis⁷

Abstract

The developed zero-dimensional plasma kinetics model, which includes both surface and gas phase kinetics, as explained in Chapter 4, is used to determine the role of vibrationally excited states in plasma-catalytic ammonia synthesis. We distribute the plasma power over the filamentary microdischarges and a uniform plasma component to scale the modelled plasma conditions from filamentary to uniform plasma. If vibrational excitation is included in the plasma chemistry, such that vibrational-translation non-equilibrium can be described, those different conditions yield an ammonia density that is only varying within one order of magnitude. When there is a clear non-zero uniform plasma component, a model neglecting vibrational excitation does not result in adequate amounts of ammonia. The model thus suggests that vibrational kinetic processes can be of importance in (packed bed) DBDs. Vibrational excitation takes place in both the uniform plasma, in between the filamentary microdischarges, and in the strong microdischarges itself, and is responsible for an increased N₂ dissociation rate.

⁷ This chapter is based on:

Zero-dimensional modelling of unpacked and packed bed dielectric barrier discharges: The role of vibrational kinetics in ammonia synthesis.

K. van 't Veer, F. Reniers and A. Bogaerts
Plasma Sources Sci. Technol., 29, 045020 (2020)

<https://doi.org/10.1088/1361-6595/ab7a8a>

5.1. Brief model description and model input

5.1.1. Kinetics description

As explained in Chapter 4, we used the zero-dimensional plasma kinetics solver ZDPlasKin [95], coupled to the BOLSIG+ numerical solver of the steady state Boltzmann equation for electrons [93]. The plasma kinetics solver solves the continuity equations (Eq. 4.1) for the various species in the plasma (Table 4.1). BOLSIG+ is used to calculate the electron energy distribution function (EEDF), which in turn is used to calculate the rate coefficients of electron impact processes. The calculation of the EEDF requires an electric field value. The electric field we derive from the plasma power (density), which allows us to capture the characteristics of a dielectric barrier discharge (see Chapter 4).

N_2 , H_2 , their corresponding atoms, ions and vibrationally and electronically excited states, as well as various compound species, empty surface sites and surface adsorbed species, are considered in the plasma chemistry, as listed in Table 4.1. We have used a 75/25% N_2/H_2 ratio as input gas. It should be noted that this ratio does not correspond to the stoichiometry of NH_3 . Indeed, in plasma catalysis, the use of more N_2 can be beneficial for NH_3 synthesis because N_2 is more difficult to dissociate compared to H_2 , requiring more than twice the electron energy, i.e., the threshold for electron impact dissociation of N_2 is ~ 9.8 eV, while it is 4.5 eV for H_2 [100].

The reactions involving only N_2 related species are reported in Appendix A. It includes a detailed description of the vibrational kinetics of N_2 , considering 24 vibrational states (based on resonant vibrational excitation cross sections available from the Phys4Entry database [101]) and describing the N_2 - N_2 vibrational-vibrational (VV) exchanges, N_2 - N_2 vibrational-translational (VT) relaxations [89], and N_2 -N VT relaxations, with single and multi-quantum transitions [88].

The reactions involving only H_2 and both N and H components used in this chapter are directly adopted from Hong et al. [77]. They also include the vibrational states of H_2 , considering 3 levels, and H_2 - N_2 , H_2 - H_2 , H_2 -N and H_2 -H VT relaxations, as well as H_2 - H_2 and N_2 - H_2 VV exchanges (involving the first 8 vibrational levels of N_2).

The surface kinetics are also adopted from Hong et al. [77], which are based on Carrasco et al. [102], and include direct adsorption, dissociative adsorption, recombination desorption, elementary Eley-Rideal and Langmuir-Hinshelwood reaction steps, and surface relaxation of excited states. The calculated rate coefficients represent a metallic surface, but we do not consider different materials in this study. Indeed, we do not consider here the influence of the catalytic material, i.e. the surface kinetics model is based on sticking probabilities and their values are not known for a wide variety of materials. This was indeed not the focus of this paper and would require other type of modelling (i.e., microkinetics modelling based on transition state theory and density functional theory data [57]). In contrast, in this paper we investigate the role of vibrational excitation in a DBD applied to a plasma-catalytic process, for which we simply assume a metallic surface (without further specification). A detailed description of the surface kinetics model is given in Appendix A.3. The sticking probabilities in the model are specific for the different vibrationally excited states, where applicable.

5.1.2. Plasma power and model input

In our model, we defined the power density as a function of time. This function allows us to include the concept of microdischarges in the 0D model. A proper translation of experimentally observed microdischarges allows us to systematically describe the plasma conditions found in both packed bed (PB) and non-packed DBD reactors. The term microdischarges is used rather than filaments, because experimental current characteristics do not reveal the specific type of discharge that took place [62]. We model the individual microdischarges as triangular power density pulses with a certain duration (i.e. width or life time). Such power density pulses have already been shown to return electron avalanches [70], [72]. (See also section 4.2.1.)

DBDs typically operate with low gas flow rates (order of 100 mL/min). We consider the residence time of molecules in the reactor to be greater than a single discharge period. Thus, it takes multiple discharge cycles for the molecules to pass through the reactor. During one half discharge period, we can count the number of microdischarges, e.g.

from the measured current characteristics [63]. If we assume that those microdischarges are distributed uniformly throughout the whole plasma reactor, it is obvious that, within one discharge period, the molecules entering the reactor cannot have seen all microdischarges that took place, simply because the molecules have not crossed the whole reactor yet. In other words, during a certain residence time, millions of microdischarges can occur throughout the reactor, but it is impossible for a single molecule to be exposed to all of them. This means that the plasma power deposited into the plasma reactor through the microdischarges is not deposited to every single molecule in the reactor. Thus in our model, we do not by definition consider the total experimental plasma power, because we do not consider all microdischarges that occur throughout the whole reactor within a certain residence time. (See also section 4.2.2.)

In addition, we introduce the concept of a uniform plasma component. By doing so, we distinguish between power deposited by the microdischarges (i.e. strong plasma, temporally and spatially isolated in nature) and power deposited by a uniform or homogenous plasma (i.e. weaker plasma that is always present, throughout the whole reactor and continuous through time). Typically, both in experiments and modelling, it is assumed that all power is deposited by the microdischarges [62], [66]–[73]. In our present model, we scale the plasma from a filamentary to a uniform plasma. To do this, we have introduced a power density distribution factor, γ , when defining our time-dependent power density function. This parameter is used to set the minimum power density p_{min} based on the maximum power density p_{max} , i.e. $p_{min} = \gamma p_{max}$. (See also section 4.2.)

Figure 5.1 shows the power included in this specific model, due to the microdischarges alone and the total power, as a function of γ . We consider 200 microdischarges per discharge half cycle (i.e. the original value from the adopted plasma parameters used in our model [81]) as well as 50 microdischarges (i.e. a reduced number, because the number of microdischarges in N_2 is typically lower than in other reactive gases).

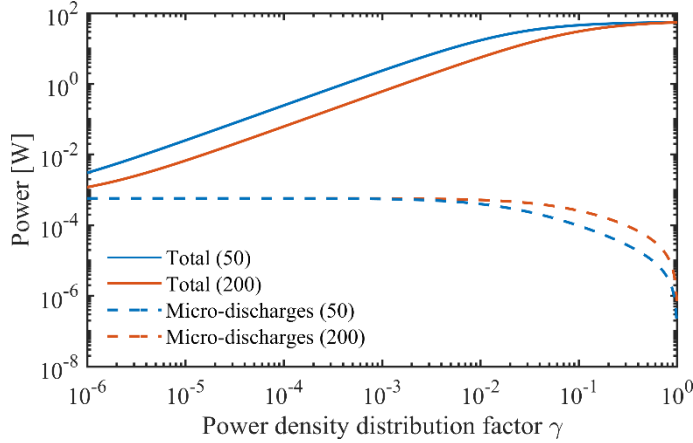


Figure 5.1. Total power and power due to the microdischarges used in the model based on 55 W of plasma power determined from experiments [63], as a function of the power density distribution factor γ , both for 200 and 50 microdischarges per half cycle (indicated in brackets in the legend). See Eq. 4.15 and Eq. 4.16.

We apply our model to a plasma power of 55 W, a discharge frequency of 28.6 kHz and a microdischarge life time of 15.6 ns, adopted from experiments [63]. We assume a constant gas temperature of 400 K and atmospheric pressure. We consider 200 microdischarges per half cycle [81], as well as 50, for which the microdischarges occur every 16 ms and 66 ms, respectively (based on a residence time of 3.33 s).

It should be noted that the power values reported in Figure 5.1 have to be considered with caution. Section 4.2.5 discussed how the modelling approach has changed. In this chapter only the average plasma power was initially considered, while in Chapter 6 and forward, the instantaneous plasma power was considered more directly. Eventually, the power density (i.e., the values of Figure 5.1 divided by the discharge volume, discussed below) is what determines the plasma conditions in the model. Those plasma conditions are still correctly representative of the conditions that follow from the improved modelling approach (see section 4.2.5 and Chapter 6).

In order to calculate the maximum and minimum power densities in the pulse, the relevant discharge volume V needs to be chosen. We assume the latter to be equal to: $V = 2N_{MD} \cdot 10^{-5} \text{ cm}^3$. The latter value (10^{-5} cm^3) was chosen based on calculations of single filament volumes ($1.6 \cdot 10^{-5} \text{ cm}^3$ in [81]) and approximated volumes of single

voids in a DBD reactor packed with spherical beads, because various kinds of local microdischarges are known to occur in between the packing material [61]. Using the void sphere radii and the bead sizes studied in [45], values for single void volumes in the order of 10^{-3} to 10^{-7} cm³ were retrieved. (See also section 4.2.4 and 4.2.5.)

As an example, for 50 microdischarges per half cycle, after the above considerations, the power density ranges from a minimum value, p_{min} , of 2.5 W/cm³ and a maximum value, p_{max} , of 2.5×10^6 W/cm³ as used in the most filamentary plasma ($\gamma = 10^{-6}$), to a constant value of 5.5×10^4 W/cm³ in the fully uniform plasma ($\gamma = 1$).

5.1.3. Describing packed bed DBDs

One motivation for the development of this new model approach (Chapter 4), is to be able to describe a PB reactor. Being able to systematically describe an unpacked and packed reactor, and distinguish them from each other, in OD plasma chemistry modelling is of high interest. As a summary, accounting for PB DBDs in our model is achieved in multiple ways. First, through the introduction of the fraction of microdischarges η_{MD} , which can be based on the gas velocity, the flow rate or residence time. In PB reactors, the gas volume in the reactor may be different for different packing configurations (and they are also smaller than for unpacked reactors), thus flow rates are different for equal residence times, or vice versa, the residence time is different for equal flow rates [62]. Those quantities are systematically taken into account. The use of η_{MD} also returns a number of microdischarges in the model, which is found to correspond directly to the actual (experimentally) measured number of microdischarges. The number of microdischarges has also been shown to change upon introducing a packing material under the same experimental conditions [62]. Second, in calculating the discharge volume (for the microdischarges), the size of a single void between the spheres can be used, meaning that the actual bead size is taken into account. In calculating the (V/A) ratio (for use in the surface kinetics in OD plasma kinetic solvers, in units of cm⁻³ instead of cm⁻² – see Appendix C.3), the surface area A should also depend on the actual packing [77], [80]. Finally, the distinction between a

filamentary and uniform plasma component (Eq. 4.14 in Chapter 4) has a clear physical meaning. In this work we differentiate between the two through a power density distribution factor γ . 2D modelling has shown that, depending on the dielectric constant of the packing material, the electric field is enhanced near the surface of the beads, giving rise to mainly local filamentary discharges (at low values of the dielectric constant) or mainly surface discharges (at high values of the dielectric constant) or a combination of both (at intermediate values) [61]. While the predominance of local filamentary discharges corresponds to small values of γ , higher values of γ would refer to the presence of surface discharges.

5.2. Species density evolution and steady-state densities

Initially we consider three types of models:

- (i), the full model, including vibrational kinetics with the full triangular power (density) pulses (see Figure 4.2);
- (ii), the same model without vibrational excitation (i.e., neglecting processes that involve vibrational levels);
- (iii), the full model of (i), but considering only the uniform power density component, i.e., assuming no microdischarges, but simply the uniform DBD plasma (that is, neglecting the triangular power density pulses on top of the constant value). For this model the power density distribution factor thus represents uniform plasma of various intensity.

The various models and conditions (which are all derived from the same plasma power) provide a somewhat different calculated NH_3 density time evolution, as illustrated in Figures 5.2 – 5.4, which mainly focusses on 50 microdischarges per discharge half cycle. The distinct conditions (i.e. the various power density distribution factors, γ) are reported in Figures 5.2, 5.3 and 5.4 with unique and consistent colors.

Figure 5.2 shows the full model results. The more uniform plasma (larger γ) reaches steady state NH_3 densities very quickly (i.e. after 16 ms for $N_{MD} = 50$, $\gamma = 10^{-3}$) or almost immediately (i.e. after 0.53 ms for $N_{MD} = 50$, $\gamma = 10^{-1}$), but the most uniform plasma ($\gamma = 10^{-1}$) reaches a lower steady state value. The more filamentary plasma ($\gamma = 10^{-4}$ and 10^{-6}) reaches a steady state on much longer time scales, and not necessarily within the gas residence time (3.33 s). Generally, a steady state NH_3 density is reached earlier when the plasma becomes more uniform ($N_{MD} = 50$, $\gamma = 10^{-4}$ compared to $N_{MD} = 50$, $\gamma = 10^{-6}$). In addition, more microdischarges ($N_{MD} = 200$, $\gamma = 10^{-4}$ vs. $N_{MD} = 50$, $\gamma = 10^{-4}$) yield higher NH_3 densities and steady state is reached later. The latter is attributed to the shorter inter-pulse times. Indeed, this makes it more likely for a pulse to be influenced by the previous pulse, because of a relatively large number of created radicals still being present. The steady state value is in principle determined by the surface reactions and electron impact dissociation of NH_3 , which is an important NH_3 loss process (see section 5.4). Finally, the most pronounced filamentary plasma, that reaches steady state slowly ($N_{MD} = 50$, $\gamma = 10^{-6}$) can reach higher steady state NH_3 densities than the more uniform plasmas ($N_{MD} = 50$, $\gamma = 10^{-3}$ and 10^{-1}).

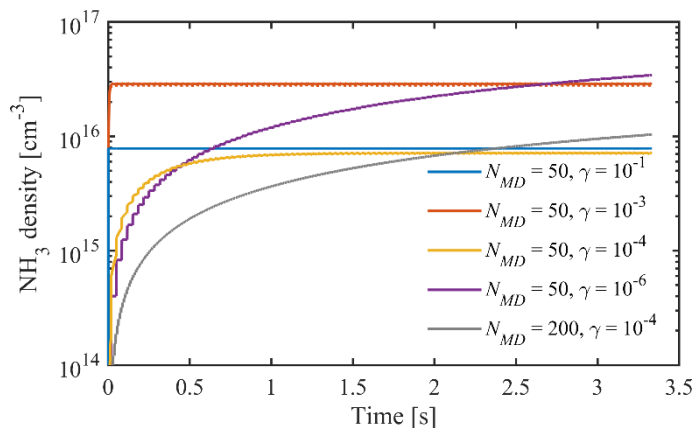


Figure 5.2. NH_3 density evolution as a function of time for selected conditions of γ and N_{MD} , obtained with the full model (i).

Figure 5.3 compares the full model (model (i)) with the model neglecting vibrational excitation (model (ii)). The most filamentary plasma can reach the highest NH_3 density if vibrational excitation is present ($N_{MD} = 50, \gamma = 10^{-6}$; compare (i) vs. (ii)). Those conditions did not yet reach steady state in the full model (i), whereas a lower steady state NH_3 density is already reached if vibrational excitation is not included (model ii). When the plasma becomes only slightly less filamentary ($\gamma = 10^{-5}$ compared to $\gamma = 10^{-6}$), the NH_3 density cannot reach an adequate steady state value anymore without vibrational excitation (model (ii): $N_{MD} = 50, \gamma = 10^{-5}$ compared to $\gamma = 10^{-6}$). When comparing the number of microdischarges in model (ii) ($N_{MD} = 200, \gamma = 10^{-5}$ against $N_{MD} = 50, \gamma = 10^{-5}$), we observe in Figure 5.3, similar to Figure 5.2, that a larger number of microdischarges can surpass the steady state NH_3 density obtained with less microdischarges for the same γ value. Finally, by comparing models (i) and (ii) for $N_{MD} = 50, \gamma = 10^{-5}$, the results further indicate that vibrational excitation yields a higher steady state NH_3 density. Thus, Figure 5.3 demonstrates that vibrational excitation does contribute towards reaching high NH_3 yields in filamentary plasma ($\gamma = 10^{-6}$ and $\gamma = 10^{-5}$).

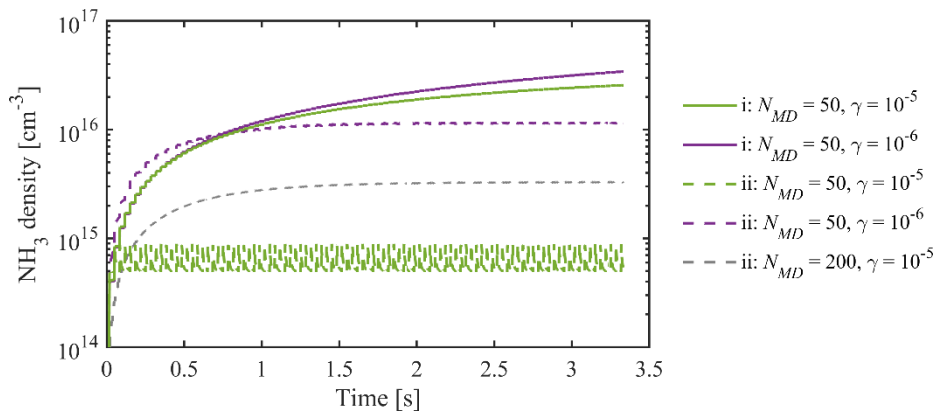


Figure 5.3. NH_3 density evolution as a function of time for selected conditions and comparison of the full model (model (i), solid lines) and the model neglecting vibrational excitation (model (ii), dashed lines).

Figure 5.4 compares the full model (model (i)) with the model neglecting the microdischarges (model (iii)), assuming 50 microdischarges per discharge half cycle. For $\gamma = 10^{-3}$, both models overlap, indicating that the microdischarges in model (i) were

not strong enough to influence the NH_3 formation. For the most filamentary plasma ($\gamma = 10^{-6}$), the strong microdischarges are very important for the formation of NH_3 . In intermediate plasma ($\gamma = 10^{-4}$), the microdischarges only slightly elevate the NH_3 yield. Thus, based on Figure 5.4 we can consider $\gamma \geq \sim 10^{-3}$ as uniform plasma and $\gamma = 10^{-6} \dots \sim 10^{-4}$ as filamentary plasma.

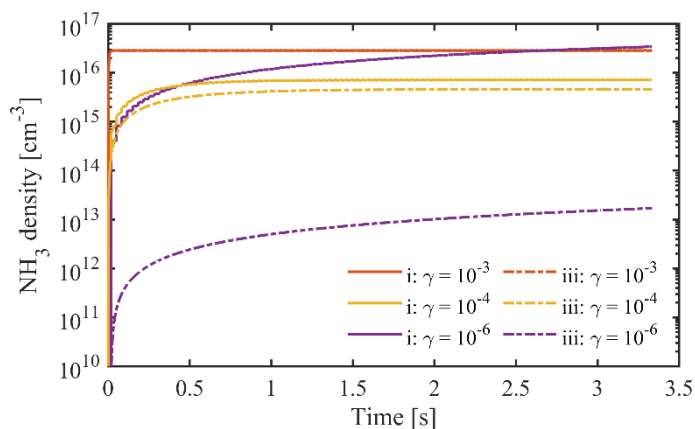


Figure 5.4. NH_3 density evolution as a function of time for selected conditions, and comparison of the full model (model (i), solid lines) and the model neglecting the microdischarges (model (iii), dashed lines). All data is from calculations assuming 50 microdischarges per discharge half cycle (N_{MD}). The results of model (i) and (iii) for $\gamma = 10^{-3}$ overlap each other.

Combining the comparisons made in Figure 5.3 and 5.4, we can conclude that despite being in the filamentary regime ($\gamma = 10^{-6} \dots \sim 10^{-4}$), both the microdischarges (cf. Figure 5.4) and the vibrationally excited states (cf. Figure 5.3) actively contribute to the NH_3 formation.

In Figure 5.5, we plot the final NH_3 density resulting from the three models, for 50 microdischarges, over the full range of filamentary, intermediate and uniform plasma (i.e. as a function of γ). In the full model, we observe a slight drop in the NH_3 density at $\gamma = 10^{-4}$. Similar behavior was also observed for the other number of microdischarges (not shown). After comparing models (i) and (iii) in Figure 5.5, we attribute this behavior to a possible change in mechanisms that govern the steady state, because the microdischarges do not influence the NH_3 density evolution beyond $\gamma = 10^{-3}$ (cf. model (i) and (iii) in Figure 5.4).

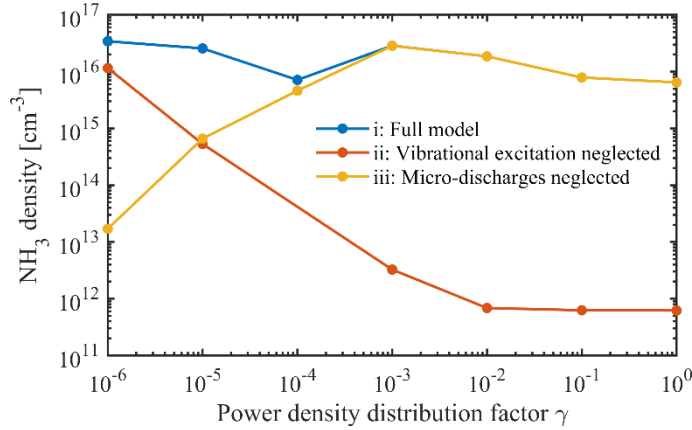


Figure 5.5. Final (steady state) NH_3 density as a function of γ , for 50 microdischarges per discharge half cycle, as calculated in the full model (i), when neglecting vibrational excitation (model (ii)), and when neglecting microdischarges (model (iii)).

Clearly, in the filamentary range ($\gamma = 10^{-6} \dots \sim 10^{-4}$), there is a synergistic effect between the microdischarges and vibrational excitation, because the sum of the results of model (ii) and (iii) is less than model (i). This can be understood because in model (iii) the N formation is enhanced through a higher effective rate coefficient of N_2 dissociation, due to the vibrationally excited states compared to dissociation from the ground state, while in model (ii) the N formation is enhanced through a higher electron density, due to the microdischarges compared to a uniform plasma (see also Section 5.4, Figure 5.6). As these two effects are combined in model (i), it yields a more than linear increase relative to model (ii) and (iii).

In addition, it should be noted that the final NH_3 density obtained in model (i) does not significantly vary (i.e. less than an order of magnitude) for all conditions, despite significantly different plasma conditions being used in the model (cf. Figure 5.1). This observation potentially explains why Hong et al. found reasonable agreement with PB DBD experiments for their OD model that included the interactions of the vibrational states, but assumed a uniform plasma [77] (i.e. corresponding to $\gamma = 10^0 = 1$ in the present study).

The NH_3 yield (defined here as the final calculated NH_3 density divided by the theoretical NH_3 density if 100% of the initial gas would be converted to the product) in the most filamentary case ($\gamma = 10^{-6}$) is calculated as 1.11 %. Compared to literature, where NH_3 yields between 0.1 and 5 % were reported for plasma-catalytic NH_3 synthesis in PB DBDs (cf. the overviews in [33], [34], [37]), 1.11 % is a reasonable value, but can be considered on the lower side. However, not all models reached steady state already, at the considered residence time of 3.33 s, and thus the maximum possible yield might not have been reached (especially for the full model (i), cf. Figure 5.2). Still, our calculated values are in the same order of magnitude as in the experiments from literature, suggesting that our model could provide a reasonable description of NH_3 synthesis in a (packed bed) DBD, and stressing again the importance of including vibrational excitation. (See also the literature review in section 1.4.1.)

5.3. Reaction mechanisms

A reaction analysis did not reveal clear differences between the actual reactions taking place for the different model assumptions and conditions. However, we gained some global insights. In Figure 5.6 and 5.7, the species densities, both in the plasma phase (electrons, N, H, NH, NH_2 , NH_3 , $\text{N}_2(\text{V})$), and at the surface (N(s), H(s), NH(s) and $\text{NH}_2(\text{s})$) are plotted as a function of time. The surface-adsorbed species represent the surface coverages of these species. We present the results of the full model (i), with 50 microdischarges per half cycle and the most filamentary plasma (i.e. $\gamma = 10^{-6}$). Generally, we see that the microdischarges, because of their ns time scale, cause pulsed behavior in the neutral and surface-adsorbed species densities, with pulses of ms widths. This is true for most species, including the vibrationally excited states of N_2 , for which the density rises by approximately one order of magnitude (see further discussion below).

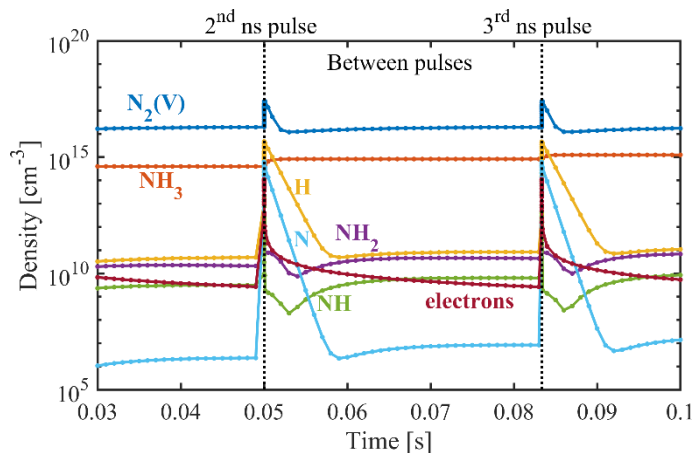


Figure 5.6. Gas phase species density evolution with time, for the 2nd and 3rd microdischarge pulse, obtained for 50 microdischarges per half cycle in the full model (i) and the most pronounced filamentary plasma ($\gamma = 10^{-6}$). The two ns microdischarge pulses are indicated, but are not resolved in detail on this long time scale.

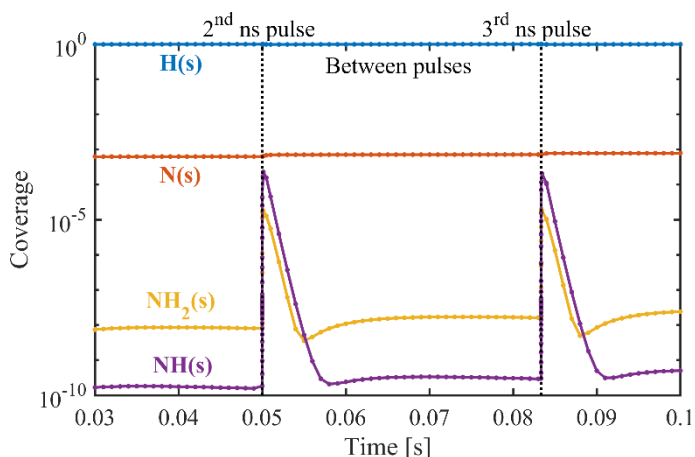


Figure 5.7. Surface coverages, calculated from the surface species densities, as a function of time, over the 2nd and 3rd microdischarge pulse, obtained for 50 microdischarges per half cycle in the full model (i) and the most pronounced filamentary plasma ($\gamma = 10^{-6}$). The two ns microdischarge pulses are indicated, but are not resolved in detail on this long time scale.

In our model we see that the surface quickly becomes covered with H(s), due to dissociative adsorption of H₂. In the microdischarges, the electron density increases rapidly due to ionization of both N₂ and H₂, and in addition N₂ and H₂ are dissociated by electron impact. The dissociation products have a relatively long lifetime until after the microdischarge (cf. Figure 5.6). During the uniform plasma in between the microdischarges, we observed the formation of NH₃, basically by a two-step process,

starting after the microdischarge. First NH(s) is formed through an Eley-Rideal mechanism (reaction of N with H(s)). Then, NH_3 is formed through an additional Eley-Rideal step (reaction of NH(s) with H_2). During the microdischarges, NH_3 is actually lost due to electron impact dissociation. The main dissociation products are NH and NH_2 , which also remain present until after the microdischarge. NH reacts with H(s) (Eley-Rideal step) into $\text{NH}_2(\text{s})$, and subsequently NH_3 can be formed (Langmuir-Hinshelwood step with H(s)). In addition, also NH_2 reacts with H(s) into NH_3 (Eley-Rideal). H atoms created from electron impact dissociation of H_2 in the microdischarges are converted back to H_2 after the microdischarge by desorption (i.e. Eley-Rideal step with H(s)).

Clearly, the observed mechanisms are dictated by the quick surface coverage by H(s) . It should however be noted that our surface kinetics model (Appendix A.3) contains several input data subject to uncertainties, so the above analysis is only qualitative. A more detailed quantitative examination of the various reaction steps would require micro-kinetics modelling based on transition state theory and density function theory calculations, which is beyond the scope of present study.

A more detailed assessment of the reaction mechanisms is performed in Chapter 6 and Appendix C.

5.4. Reduced electric field and vibrational temperatures

To gain more insight into the various electron impact processes, we plot in Figure 5.8 the electron energy loss fractions for vibrational excitation, dissociation and ionization of N_2 as a function of the reduced electric field (E/N). Vibrational excitations are the main electron impact processes at a weak reduced electric field ($E/N = 1$ to 30 Td). However, the tail of this process does not fall off sharply upon rising E/N , and vibrational excitation is still present towards $E/N = 100$ Td.

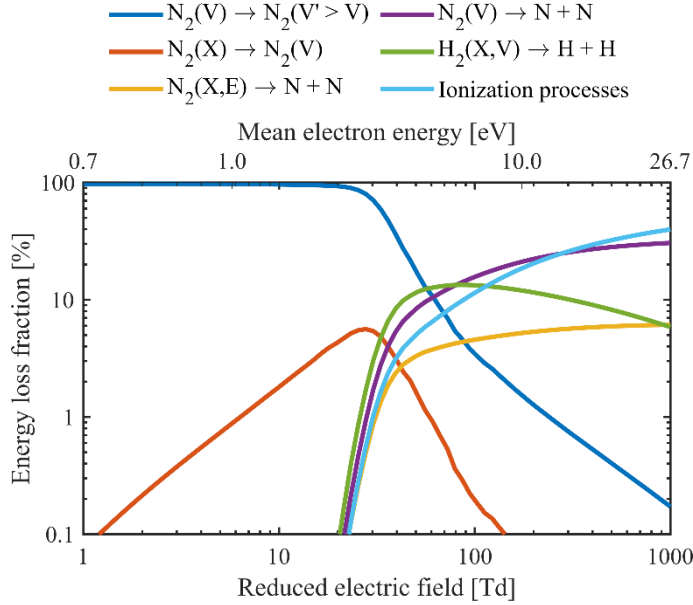


Figure 5.8. Fractions of electron energy transferred to various important electron impact collisions (i.e. vibrational excitation, dissociation and ionization) in a N_2/H_2 75/25 % mixture at 400 K, as a function of the reduced electric field, calculated using BOLSIG+ [93] from the corresponding cross sections. The ionization processes include direct and dissociative ionization of various molecules (N_2 , H_2 , NH , NH_2 and NH_3) as well as direct ionization of the atoms (N and H), not only from the ground levels, but also from the vibrationally and electronically excited levels of N_2 and H_2 . Vibrational excitation of H_2 is not plotted as it has an electron energy loss fraction less than 0.1 %. The mean electron energy, evaluated from the EEDF at each reduced electric field, is reported on the top x-axis. The cross sections used for vibrational excitation of N_2 and H_2 are the resonant vibrational excitation cross sections [101], [103], [104] taken from the Phys4Entry database, for which 38 and 9 levels are taken into account, respectively. The notations (X), (V) and (E) denote the ground state, vibrational levels and electronic excited levels, respectively.

In Figure 5.9, we plot the reduced electric field E/N and the vibrational temperature T_V as a function of time, before and after the 2nd and 3rd microdischarge pulse (conditions: 50 microdischarges per half cycle and $\gamma = 10^{-6}$). The vibrational temperature is calculated from the first vibrational level and the ground state, by

$$T_V = \frac{E_1 - E_0}{\ln(n_0/n_1)} \quad (5.1)$$

where E is the energy of the vibrational level and n the corresponding number density. The subscripts indicate the ground and first vibrationally excited state.

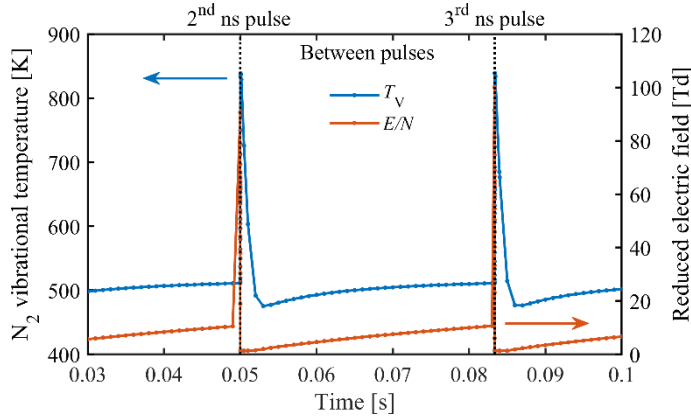


Figure 5.9. N_2 vibrational temperature (left y-axis) and reduced electric field (right y-axis) as a function of time, for the 2nd and 3rd microdischarge pulse, for 50 microdischarges per half cycle in the full model (i) and the most filamentary plasma ($\gamma = 10^{-6}$). The two microdischarges with ns pulse width are indicated, but are not resolved in detail on this long time scale.

Figure 5.9 shows that the reduced electric field peaks sharply during the microdischarge pulses, as expected. The vibrational temperature increases as well, but it decreases more slowly over a few milliseconds. From Figure 5.8 we can deduce that vibrational excitation is dominant in between the microdischarge peaks (where E/N is in the order of 1 to 10 Td), but also occurs during the microdischarges (with E/N around 100 Td; especially when considering that the maximum electric field is not reached instantaneously). Figure 5.6 also indicated a small rise in vibrationally excited N_2 density during the microdischarges, as mentioned before. The rising E/N in between the microdischarges can be understood from the constant power density, and the drop in electron density (due to recombination and lack of ionization, cf. Figure 5.6 and 5.8) and Eq. 4.6, from which follows $E/N \propto 1/\sqrt{n_e}$.

Figure 5.10 shows the maximum and minimum (steady state) reduced electric field (E/N) over the full range of filamentary to uniform plasma, for 50 microdischarges per half cycle, obtained from the full model. E/N is greater than 100 Td (i.e. ~ 140 Td) inside the microdischarges (maximum values), and 1 to 10 Td in between the microdischarge pulses (minimum values), in the filamentary plasma regime ($\gamma = 10^{-6} \dots 10^{-4}$), but the value inside the microdischarges drops upon increasing γ , because the power is more

evenly spread in the entire plasma reactor and not only concentrated in the microdischarges. Figure 5.10 further justifies our identification of $\gamma \geq \sim 10^{-3}$ as intermediate and uniform plasma, and $\gamma = 10^{-6} \dots 10^{-4}$ as filamentary plasma, which was based on Figures 5.2 – 5.4 (see section 5.3). In between the microdischarges the opposite trend occurs, showing a rise in E/N upon increasing γ , again because the power is more evenly spread in the entire plasma reactor, thus increasing the field strength of the uniform plasma component. The electric field is calculated from the power density (see Eq. 4.6), so the non-zero power density in between the microdischarges (when $\gamma > 0$) yields a non-zero electric field as well.

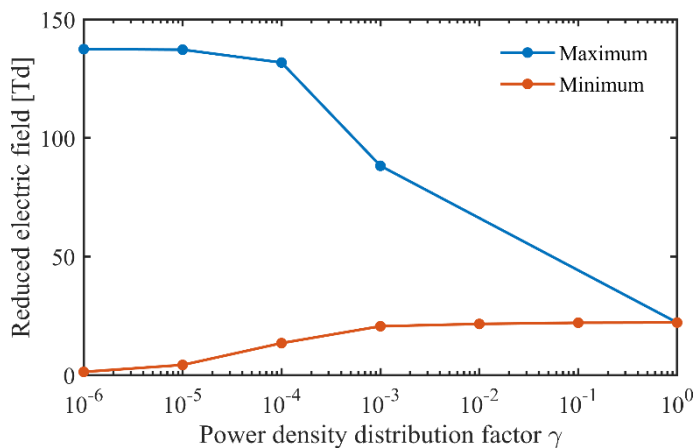


Figure 5.10. Maximum (i.e., during the microdischarges) and minimum (i.e., in between the microdischarges) reduced electric field, in steady state, as a function of γ , for 50 microdischarges per discharge half cycle, as calculated in the full model (model (i)).

Figure 5.11 shows the vibrational temperature, again as a function of the plasma uniformity (γ) for 50 microdischarges per half cycle, obtained from the full model. The values during and in between the microdischarges show a similar trend as a function of γ , but the vibrational temperature during the microdischarges is slightly higher. This indicates that vibrational excitation indeed occurs during the microdischarges. The maximum difference is 900 K (for $\gamma = 10^{-4}$). In the filamentary regime ($\gamma = 10^{-6} \dots 10^{-4}$) the vibrational temperature reaches values up to 2500 K. In literature, N_2 vibrational temperatures of experimental (PB) DBDs are reported in the order of 1750

to 3000 K [56], [57], hence in reasonable agreement with our calculations. However, as the modelling conditions are not exactly the same, the comparison is only quantitative.

The gas kinetic temperature in the DBD is assumed to be 400 K. Thus, Figures 5.8 – 5.11 indicate that vibrational excitation is generally strong enough to cause a significant vibrational-translational non-equilibrium, both inside the microdischarges and in the uniform plasma. At the same time, because of the low gas kinetic temperature, loss of the vibrational populations by VT relaxation is limited [105].

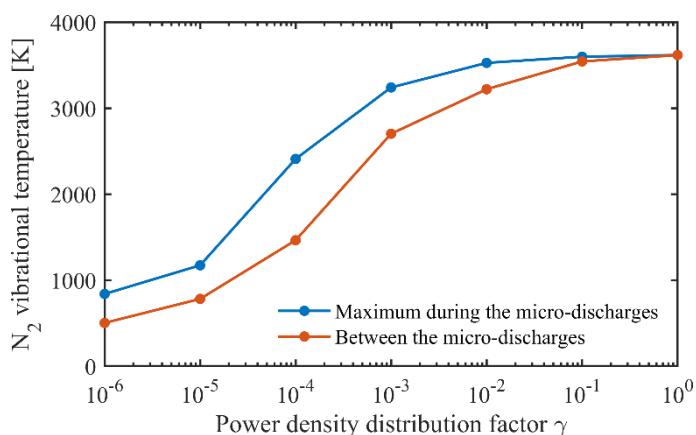


Figure 5.11. Maximum N_2 vibrational temperature during the microdischarges and vibrational temperature in between the microdischarge pulses (cf. Figure 5.9), as a function of γ , for 50 microdischarges per half cycle, as calculated in the full model (model (i)).

In general, we can conclude that the vibrational temperature is significant in both the microdischarges and the uniform plasma, as long as not all the power is assigned to the microdischarges, thus stressing again the importance of vibrational excitation for NH_3 synthesis in a (PB) DBD, both during the microdischarges and in between them.

5.5. Conclusions

We presented a new method for describing microdischarges in DBDs, including packed bed DBDs, in a zero-dimensional plasma kinetics model, by describing the spatial and temporal nature of these microdischarges or filaments in a more systematic way. This

approach allows capturing the properties of both packed bed and unpacked DBD reactors, mostly through the number of microdischarges taking place and the power considered in the model. Indeed, due to the spatial and temporal isolated nature of microdischarges in DBDs, molecules entering the plasma reactor cannot see all the microdischarges taking place during one discharge cycle within the full reactor, simply because the molecules do not traverse the whole reactor within this time period. Thus we did not automatically consider the total experimental plasma power in our model. We scaled our models over a wide range of plasmas, i.e. from filamentary to uniform plasmas, by redistributing the power. This was done by systematically changing the time-dependent power density function in our model. Due to the relatively short duration of the microdischarges, the considered power in the model is mostly determined by the power in the uniform plasma component.

When we included vibrational excitation, our calculated final NH_3 density did not vary to a large extent (i.e., within one order of magnitude), despite the fact that the power assumed in the model is not constant, mimicking the full range from filamentary to uniform plasma. Note that we only considered part of the experimental plasma power in a filamentary model, because individual molecules cannot see all the microdischarges taking place within their residence time in the reactor.

Models in the filamentary regime without vibrational excitation can show a very low steady state NH_3 density. We therefore identified that the microdischarges, the uniform plasma component and vibrational excitation (which actually can take place during both the microdischarges and the uniform plasma in between those microdischarges) all play an important role in enhancing the NH_3 yield, through the dissociation rate of N_2 .

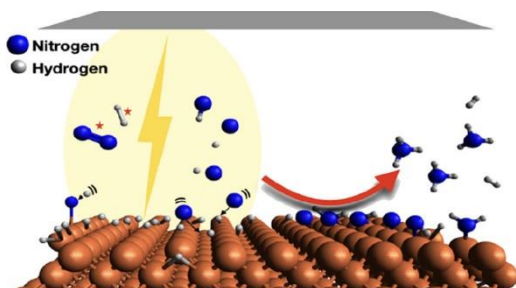
Our results are all consistent with commonly made assumptions in literature, like the strong reduced electric field found in filamentary DBDs and the assumption that all plasma power is being deposited by filaments. However, sophistication of the latter assumption has a major impact on the role of vibrational excitation in NH_3 synthesis in a DBD plasma. Indeed, our model reveals that, as soon as not all power is assigned to

the microdischarges, vibrational excitation is important for enhanced dissociation of N_2 in a (PB) DBD reactor, not only in the weaker uniform plasma but also during the strong microdischarges.

In the next chapter, we will investigate the reaction mechanisms in more detail.

Chapter 6.

Reaction mechanisms: Role of the microdischarges and their afterglows⁸



Abstract

We employ the plasma kinetics model to gain insights into the ammonia formation mechanisms, paying special attention to the role of the filamentary microdischarges and their afterglows. During the microdischarges the synthesized ammonia is actually decomposed, but the radicals created upon electron impact dissociation of N_2 and H_2 and the subsequent catalytic reactions cause a net ammonia gain in the afterglows of the microdischarges. Under our plasma conditions, electron impact dissociation of N_2 in the gas phase followed by the adsorption of N atoms is identified as rate-limiting step, instead of dissociative adsorption of N_2 at the catalyst surface. Both elementary Eley-Rideal and Langmuir-Hinshelwood reaction steps can be found important in plasma-catalytic NH_3 synthesis.

⁸ This chapter is based on:

Plasma-catalytic ammonia synthesis in a DBD plasma: Role of microdischarges and their afterglows.

K. van 't Veer, Y. Engelmann, F. Reniers and A. Bogaerts

J. Phys. Chem. C, 124, 22871–22883 (2020)

<https://doi.org/10.1021/acs.jpcc.0c05110>

6.1. Brief model description and model input

As discussed in the introduction (section 1.4.4), it is clear that the existing studies claim different processes to be important in plasma-catalytic ammonia synthesis, so there is a clear need for a more detailed understanding. The mentioned studies were all specific to DBDs, but the strong filamentary microdischarges and what happens in between them are typically not considered separately in the assessment of the reaction mechanisms.

Therefore, in this study, we present a reaction kinetics analysis, based on the OD plasma kinetics model explained in Chapter 4, in which we explicitly capture the filamentary behavior of an experimental PB DBD. In the assessment of the reaction mechanisms, we pay special attention to the separate notion of the filamentary microdischarges and their afterglows. We consider both elementary Eley-Rideal (ER) and Langmuir-Hinshelwood (LH) reaction steps. The LH reactions correspond to the classical (thermal) hydrogenations on the surface, while the ER reactions describe the interaction of plasma radicals with surface-adsorbed species. We will discuss the evolution of the species densities and reaction rates, as well as the overall NH_3 formation mechanisms.

We used the same time-dependent OD plasma kinetics model as in Chapter 5, called ZDPlasKin [93], [95], to investigate the plasma-catalytic synthesis of NH_3 from a $\text{N}_2:\text{H}_2$ 1:3 stoichiometric gas mixture in a PB DBD at 400 K and atmospheric pressure. As explained in Chapter 4, this plasma kinetics model uses rate coefficients from literature to describe the density evolution of various species, i.e. the precursor gases, various plasma radicals, the electrons, various ions, and electronically and vibrationally excited molecules, as well as surface-adsorbed atoms and molecules. The rate coefficients and the concentrations of these species provide the actual reaction rates, which in turn govern the time evolution of all these species.

The considered gas phase and surface kinetics are reported in Appendix A. The species included in the model were listed in Chapter 4 (Table 4.1). The surface kinetics use reaction rates based on sticking coefficients corresponding to a metal surface, which

could be related to iron [77], [80], [102], [106]–[108]. They describe the catalytic reactions leading to N, H and NH_x adsorption or hydrogenation and the eventual desorption of NH₃. Both elementary ER and LH reaction steps are included.

We assume a surface site density of 10¹⁵ cm⁻², which is generally representative of metal surfaces [102]. This value, together with the volume-to-surface area ratio of the reactor, is used to convert the rate coefficients of the catalytic reactions from s⁻¹ to cm³s⁻¹, or cm⁶s⁻¹ in case of dissociative adsorption. A volume-to-surface area ratio of 0.007 cm was used [80]. Any change in these parameters would cause an equal change in the rate coefficients of all surface reactions, i.e. the relative surface reaction rates remain the same. (See also Appendix C.3.)

The surface kinetics are subject to many assumptions and thus also to uncertainties. That includes the exact surface described, i.e. step or surface sites. We describe the surface as being representative of iron, merely for reference and context (see also Appendix C.3). A detailed description of the surface kinetics would require microkinetics models [57], [109], [110]. The latter type of model uses surface reaction rates more closely derived from density functional theory calculations and generally solves a system under steady state conditions, while not including a full gas phase chemistry.

We chose to only describe one surface in our model and neglect the wall effect [37] due to the electrodes or dielectric barrier, which represent different gas-surface interfaces. Indeed, those surfaces would require different kinetic parameters which are subject to the same uncertainties [106]. Furthermore, recent experimental insights show us that the NH₃ formation in an empty reactor is very low compared to a reactor packed with supports (Al₂O₃) and that both cases are significantly lower than when a (metal) catalyst is loaded onto the supports.

We derive the plasma conditions from experimentally measured current and voltage characteristics of a PB DBD (see Appendix B). The average plasma power was 68 W and a discharge frequency of 23.5 kHz was applied. The reactor volume was 20 ml. The flow

rate was 100 ml/min. The reactor was packed with 1.9-2.0 mm diameter Al₂O₃ beads. The measured electrical characteristics determine the plasma parameters during the calculations. Generally, we see no large difference in those characteristics between the Al₂O₃ supports alone and when a metallic coating (5 - 10 wt %) is on the beads. A detailed translation of the experimental conditions is given in Appendix B.

To summarize, we mimic the microdischarges by applying the experimentally measured plasma power over 50 triangular pulses with pulse duration of 200 ns (100 ns at FWHM), equally spaced over the residence time of 3.84 s. In practice, there will be millions of microdischarges in the reactor during this typical residence time, but individual gas molecules are never exposed to all microdischarges. Therefore, we consider that individual gas molecules see, on average, 50 microdischarges over their full gas residence time. This number is based on the average number of microdischarges that we counted during a single discharge cycle. Each microdischarge is followed by weaker plasma conditions, with 76.8 ms duration, which we refer to as the afterglow of a microdischarge. In addition, the first microdischarge in the model starts at 38.4 ms, to account for the gas that is already present in the plasma reactor before being exposed to an actual microdischarge. (See also section 4.2.)

The adopted maximum and minimum instantaneous plasma power (i.e., during the microdischarges and their afterglows) correspond to 332 W and 33 W, respectively, based on the typical experimentally measured instantaneous plasma power. These values are converted to a maximum and minimum power density of 3.4×10^6 W/cm³ and 12 W/cm³, for the microdischarges and their afterglows, respectively. The discharge volumes used in these conversions are based on the microdischarge and reactor volume, respectively, as described in detail in section 4.2.4. This power is used to heat the electrons, allowing us to also self-consistently calculate the reduced electric field in our model [82] (see section 4.1.2).

We studied the production and destruction mechanisms of NH₃ and its precursors during a single microdischarge and its afterglow. We evaluated the mechanisms in all

the successive microdischarge and afterglow pairs and found that the most important reactions are always the same. Therefore, in the following sections, we focus on the reaction kinetics in the first microdischarge and afterglow pair, as well as the overall NH_3 evolution during the full residence time.

6.2. Surface Coverages and Plasma Species Densities in the microdischarges and Their Afterglows

Our model predicts that the electrons, the plasma radicals and surface-adsorbed species (indicated with (s)) govern the most important reactions taking place, leading to NH_3 production. Some of these species are mainly important in the microdischarges, while others mainly in the afterglows. Figure 6.1(a) depicts the calculated surface coverage from the start of the plasma until the end of the first afterglow, while in Figure 6.1(b), the calculated concentrations of the gas phase species are plotted.

The first afterglow ends after approximately 115 ms. At this time scale, the 200 ns microdischarge pulse is not resolved in Figure 6.1. For the sake of completeness, we plot the time evolutions of the various species during the microdischarge alone in the SI (section C.1; Figure C.1). Typical densities of all species in Figure 6.1 are also summarized in Table C.1.

Figure 6.1 shows that all the adsorbed and gas phase species rise (either quickly or more gradually) during the first (few) ms, and reach a plateau after approximately 15 ms, i.e. well before the first microdischarge takes place, while the fraction of empty sites decreases over three orders of magnitude. H(s) is the main adsorbate, and both H(s) and N(s) reach their plateau within 0.3 ms. The coverages or concentrations of NH(s) , $\text{NH}_2(\text{s})$, H , N , the electrons, NH and NH_2 clearly increase due to the microdischarge (up to six orders of magnitude), after which they drop back smoothly to almost their original values over approximately 20 ms, but both NH and NH_2 rise slightly again in the late afterglow. The N(s) coverage stays almost constant during the microdischarge, but rises in the early afterglow, while H(s) is the main adsorbate throughout. The latter is initially

due to the dissociative adsorption, which has an initial high reaction rate, and then due to radical adsorption (which is discussed later and in Appendix C.3, Figure C.8). The NH_3 concentration decreases during the microdischarges (but only slightly in the first microdischarge where the NH_3 concentration is still low, see Figure C.1(b)), but rises in the early afterglow.

Figure 6.1(b) shows that radicals are already present in the gas phase before the first microdischarge. This is due to the non-zero power density outside of the microdischarges. Thus the electrons are already slightly heated by a small amount of power deposition, allowing for electron impact reactions that create the various plasma radicals. However, the reaction rates are of course small compared to the microdischarge itself.

It is also clear from Figure 6.1(b) that besides the H_2 and N_2 gas molecules (with concentrations of approximately 75 % and 25 %, or $1.4 \times 10^{19} \text{ cm}^{-3}$ and $4.6 \times 10^{18} \text{ cm}^{-3}$, respectively; not plotted in Figure 6.1), the H atoms have the highest density in the plasma ($1.2 \times 10^{17} \text{ cm}^{-3}$ and $1.0 \times 10^{14} \text{ cm}^{-3}$ in the microdischarge and afterglow, respectively; corresponding to an H_2 dissociation degree of 0.4 % and 0.0004 %, respectively), followed by NH_3 (up to 38 ppm or $6.9 \times 10^{14} \text{ cm}^{-3}$ after the first microdischarge and afterglow pair). The N atom density is two orders of magnitude lower than H, corresponding to a maximum concentration of $8.4 \times 10^{14} \text{ cm}^{-3}$ in the microdischarge and an N_2 dissociation degree of 0.01 %; attributed to the much higher bond strength of N_2 (9.8 eV) vs. H_2 (4.5 eV) [100]. The NH radical density ($1.5 \times 10^{11} \text{ cm}^{-3}$) is the same order of magnitude as the N atom density in the afterglow, while the NH_2 density is one order of magnitude higher ($1.9 \times 10^{12} \text{ cm}^{-3}$).

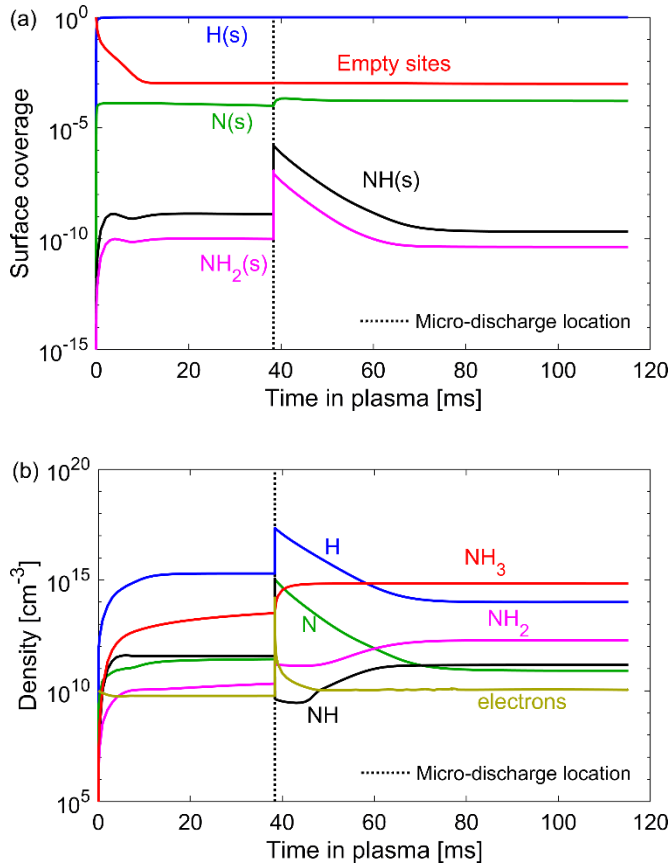


Figure 6.1. Surface coverages and fraction of empty surface sites (a), and number densities of the neutral gas phase species and electrons (b), as a function of time in the plasma, from the start of the plasma to the end of the first microdischarge and afterglow pair. The microdischarge with 200 ns duration takes place at 38.4 ms. The feed gas was $N_2:H_2$ 1:3 and the N_2 and H_2 densities were approximately $4.6 \times 10^{18} \text{ cm}^{-3}$ and $1.4 \times 10^{19} \text{ cm}^{-3}$, respectively.

Of course, this figure applies to the first pair of microdischarge and afterglow. The picture is a bit different after periodic steady state is reached, at least for the NH_3 concentration, because NH_3 will accumulate during successive microdischarge and afterglow pairs, while the other plasma species already reach periodic steady state after the first pair (see discussions in section 6.3).

Under the present DBD plasma conditions, the electron impact collisions with N_2 and H_2 typically involve the ground state, but also both the electronically and vibrationally excited molecules. In Figure 6.2 we show the time-evolution of the number densities of N_2 and H_2 in the ground state, as well as in the vibrationally and electronically excited

states, while in Figure 6.3 we plot the N_2 vibrational distribution function (VDF) in the microdischarges at various moments in time. The time-evolution of the number densities in the microdischarge is depicted in Appendix C (section C.1, Figure C.2), as well as the H_2 VDF, for completeness (Figure C.3).

Clearly, in the afterglows the vibrationally excited N_2 and H_2 molecules are higher in density than the electronically excited molecules, and this is most apparent for N_2 . The vibrational temperature is approximately 700 K in the afterglows (cf. Figure C.4(a)). Also, during the microdischarges, the vibrationally excited N_2 molecules have a higher density than the electronically excited states, and the vibrational temperature reaches 2100 K. On the other hand, the electronically excited H_2 molecules have a higher density than the vibrationally excited states during the microdischarges (cf. Figure C.2). The N_2 VDF shows a clear overpopulation compared to a Boltzmann distribution at the gas temperature, both at the start and especially during the microdischarges. Note that the start of a microdischarge corresponds to the end of the previous afterglow. An overpopulation is also observed in the afterglows, because of the non-zero power deposition between the microdischarges, which allows for continuous electron impact vibrational excitation, in turn causing a non-equilibrium compared to the gas temperature of 400 K.

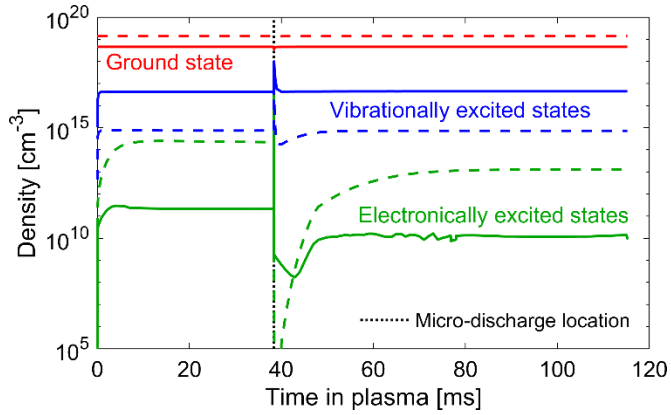


Figure 6.2. Number densities of the N_2 (solid lines) and H_2 (dashed lines) molecules in the ground state and the sum of the electronically and vibrationally excited states, as a function of time in the plasma, from the start of the plasma to the end of the first microdischarge and afterglow pair. The microdischarge with 200 ns duration takes place at 38.4 ms.

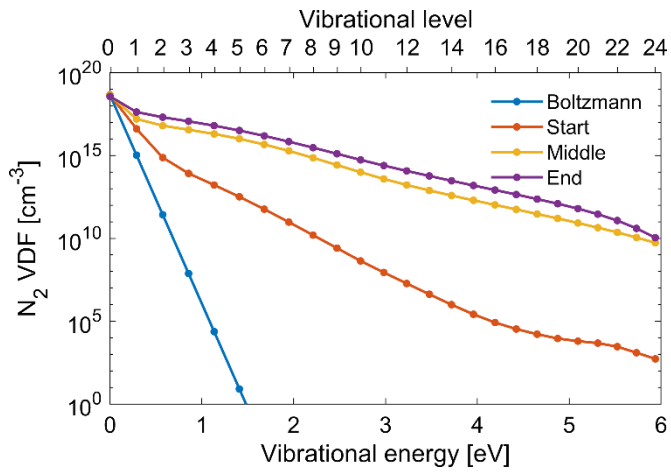


Figure 6.3. N_2 vibrational distribution function (VDF) at various moments in the microdischarge, as well as the Boltzmann distribution at the gas temperature (400 K).

6.3. Production and Destruction of Plasma Radicals, Adsorbed Species and NH₃ in the microdischarges and Their Afterglows

To illustrate more clearly whether species are being produced or destroyed during the microdischarges or the afterglows, we present in Figure 6.4 their time-averaged source terms, for a single microdischarge and its afterglow separately. As noted before, NH₂(s), NH(s), NH₂, N(s), and especially NH, H, N and the electrons are net produced during the microdischarges. For all these neutral species, the source term in the afterglows is destructive but small (compare red bar to gray background, and keeping in mind the log-scale), except for H, which is largely destroyed, and N(s), which is also produced in the afterglow, but again the net production is relatively small (cf. gray background). In other words, the actual production and destruction in the afterglows (grey bars) are nearly equal for all these species, which means that upon formation, the species are quickly converted into other species. For the electrons, the destruction far exceeds the production in the afterglows. This is attributed to the lack of electron impact ionization processes in the afterglows, where the plasma is significantly weaker compared to the microdischarges.

In contrast to the above species, NH₃ is largely destroyed during the microdischarges and produced in the afterglows. Likewise, the N₂ and H₂ ground state molecules also exhibit high loss rates during the microdischarges, because they are converted into reactive species by the electron impact reactions, but their population slightly increases again in the afterglows, due to recombination of these reactive species. This is also illustrated in Figure 6.5, showing the time-averaged source terms of the ground states and electronically and vibrationally excited molecules of both H₂ and N₂. During the microdischarges, the ground state H₂ and N₂ molecules get destroyed, while the electronically and vibrationally excited molecules are produced, and the opposite is true for the afterglows. The production of the N₂ vibrational levels in the microdischarges

and the subsequent depopulation in the afterglows is most pronounced, corresponding to their highest number density (cf. Figure 6.2).

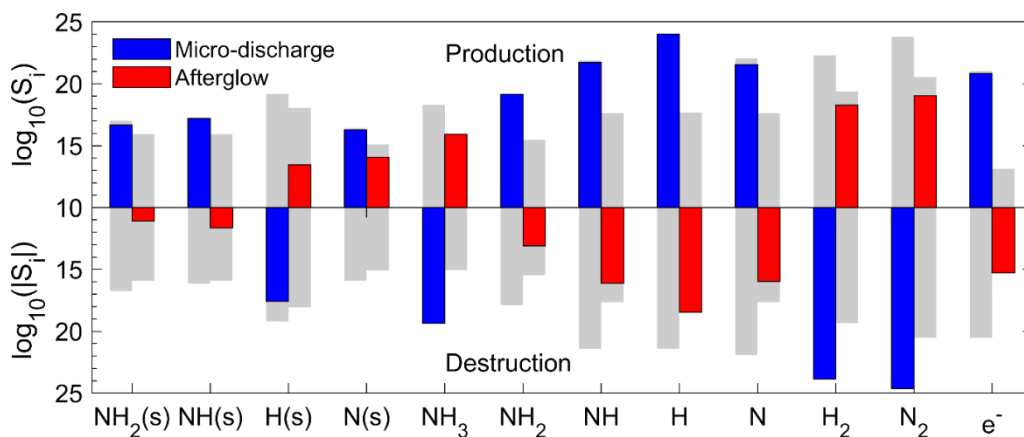


Figure 6.4. Time-averaged species source terms in the first microdischarge and its afterglow, of the surface-adsorbed and neutral gas-phase species and the electrons. The source term is either positive or negative, representing net production (top y-axis) and net destruction (bottom y-axis), respectively. The logarithm of the (absolute) source terms S_i is plotted. The grey bars indicate the total production and destruction source terms of the species i , $S_{i,p}$ and $S_{i,d}$, respectively. The net production or destruction $S_i = S_{i,p} - |S_{i,d}|$. Note: The units of S are in $\text{cm}^{-3} \text{s}^{-1}$. Comparing the blue or red bars with the grey background reveals whether production is much larger than destruction (or vice versa) (i.e., when the blue or red bar is as large as grey background), or whether they are nearly equal to each other (i.e., when the blue or red bar is smaller than the grey background). In other words, the colored bars correspond to the source terms S_i (cf. equation 1 and y axis labels) which can either be positive (production, upper panel) or negative (destruction, lower panel) and the grey background specifically corresponds to $S_{i,p}$ and $S_{i,d}$ in the microdischarge and the afterglow.

In general, the average production and destruction rates and thus the species source terms are much larger in the microdischarges than in the afterglows (i.e., typically $10^{16} - 10^{23} \text{ cm}^{-3}\text{s}^{-1}$ vs $10^{14} - 10^{18} \text{ cm}^{-3}\text{s}^{-1}$), attributed to the stronger plasma environment (cf. the difference in power density, mentioned in section 6.2) and the associated high radical and electron densities. However, the microdischarge lifetime is significantly shorter than the afterglow duration (i.e., 200 ns vs 76.8 ms).

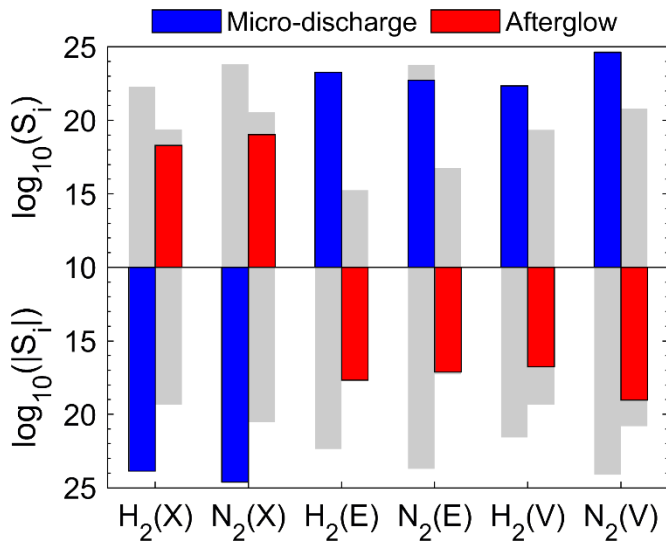


Figure 6.5. Time-averaged species source terms in the first microdischarge and its afterglow, of the ground state (X), electronically excited (E) and vibrationally excited (V) H₂ and N₂ molecules. Cf. caption of Figure 4 for more information.

Hence, to determine whether the various species accumulate or drop in consecutive microdischarge and afterglow pairs, we also need to account for the duration of the microdischarge and afterglow. We calculate the average production-to-destruction ratio across one pair with

$$\frac{P}{D} = \left| \frac{S_{afterglow} \times \tau_{afterglow}}{S_{microdischarge} \times \tau_{microdischarge}} \right|^{\alpha} \quad (6.1)$$

where S is the average source term (i.e., production minus destruction, red and blue bars in Figures 6.4 and 6.5) of a species in the afterglow or microdischarge, τ is the duration of the afterglow or microdischarge, and α is given by

$$\alpha = \begin{cases} 1, & S_{afterglow} > 0 \text{ and } S_{micro-discharge} < 0 \\ -1, & S_{afterglow} < 0 \text{ and } S_{micro-discharge} > 0 \end{cases} \quad (6.2)$$

For all gas phase and surface-adsorbed species, including electronically and vibrationally excited molecules, equation 6.1 yields a value of approximately 1, except for NH₃. This means that the surface coverages and gas phase concentrations of all species vary

quickly reach a periodic steady state, while NH_3 is able to accumulate by the consecutive microdischarges and afterglows, as shown in Figure 6.6.

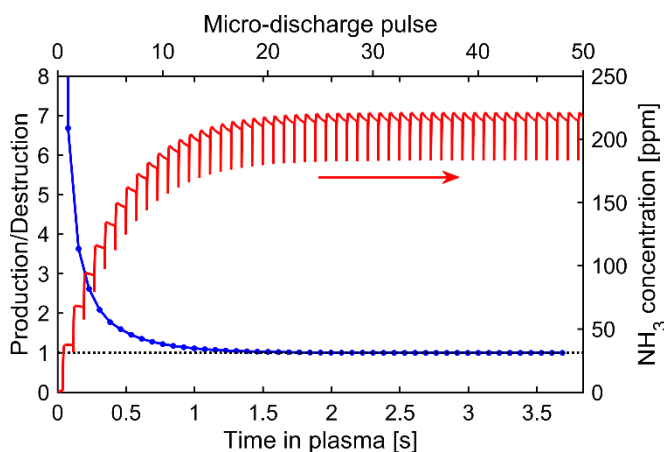


Figure 6.6. Production-to-destruction ratio of NH_3 based on the net production in the afterglows and net destruction in the microdischarges (equation 2, left y-axis), and NH_3 concentration (right y-axis), as a function of time (bottom x-axis) and microdischarge pulse number (top x-axis).

In this figure, the vertical lines in the NH_3 concentration correspond to the destruction of NH_3 in each microdischarge, followed by the strong rise in the beginning of each subsequent afterglow. Considering that the electron concentration immediately reaches periodic steady state, it is logical that the drop in each microdischarge increases with rising NH_3 concentration, as the electron impact dissociation rate is proportional to the NH_3 concentration. We identified this process as the main loss mechanism of NH_3 in the microdischarges. The NH_3 production in the afterglows has to overcome this dissociation in the microdischarges in order to increase the overall NH_3 concentration. Note that electron impact dissociation still occurs in the afterglows as well, despite a very low electron density. Hence, even in the afterglows, electron impact dissociation determines the eventual steady state NH_3 concentration.

The presented results are for a stoichiometric feed gas ratio (i.e. $\text{N}_2:\text{H}_2$ of 1:3), but our model predicts the NH_3 concentration to reach values up to 2000 ppm at higher N_2 contents (not shown). Indeed, for plasma-catalytic NH_3 synthesis, the optimal ratio does not necessary correspond to the stoichiometric gas ratio, among others because N_2

dissociation requires more energy than H_2 dissociation [100]. Furthermore, while we believe that the adopted plasma conditions in our model are representative for a PB DBD, the exact conditions, however, are subject to uncertainties. Therefore, higher NH_3 yields may be reached by using other input values, such as for the maximum and minimum instantaneous power, the microdischarge volumes and the number of microdischarges. However, we have generally observed no drastic differences in reaction mechanisms as a function of these model parameters (see also the species density evolution in section 5.4, where different conditions have been used). Therefore, while the exact species concentrations in Figure 6.1 and 6.6 must be considered with caution, as they depend on the conditions assumed in the model, the qualitative reaction mechanisms and the related discussions, presented in the next sections, should still contribute to a better insight.

6.4. NH_3 Formation: Reaction Rates and Determination of the Rate-Limiting Step

In reaction kinetics, the complete system can reach a steady state, meaning that the plasma parameters and the various species concentrations remain unchanged as a function of time, but reactions can still take place, with the total production and destruction rates of species being equal to each other. When in a chain of consecutive reactions, the reaction rate of the final reaction is equal to those of the preceding steps, the rate-limiting step can be determined. A DBD is a periodic discharge and thus such steady state is not evident. Instead, a periodic steady state might be reached, that is, each discharge period becomes identical.

Our calculations reveal that electron impact dissociation of N_2 in the plasma, followed by N adsorption at the catalyst surface, is the rate-limiting step for NH_3 synthesis at our conditions, and not dissociative adsorption of N_2 . This can be explained by the observation that shortly after a microdischarge, when NH_3 increases (cf. Figure 6.1(b)), multiple surface catalytic reaction rates are almost equal to each other. This is true for the formation of NH_3 as well as the NH_3 precursors. Hence, all intermediate surface

species, i.e., N(s), NH(s) and NH₂(s), created during the afterglows, are immediately converted towards NH₃ according to our model. In addition, electron impact dissociation of the feed gas becomes negligible during this period. The NH₃ formation rate was found to be equal to the various adsorption rates of N atoms, i.e. both direct adsorption and the ER reaction between N and H(s). As mentioned, in the early afterglow the N atom source (electron impact dissociation of N₂) is not present, and thus, the N atoms are consumed by adsorption, reducing the N density and thus also the N adsorption rate. Consequently, the rates of the further processes (i.e., hydrogenation steps) that exhibit the same rate as the N atom adsorption also drop, and thus also the densities of the NH₃ precursors (i.e. NH(s) and NH₂(s), cf. Figure 6.1(a)). We summarize this observation in Figure 6.7, while in Figure 6.8 we schematically depict the involved surface reaction mechanisms. A more detailed analysis is presented in Appendix C (section C.3). We note that the mechanisms in Figure 6.8 are in principle subject to the actual catalytic surface and the temperature at which the process takes place.

As part of our detailed analysis (cf. Appendix C.3) we saw a relatively large increase in NH₃ concentration when increasing the N atomic adsorption rates (i.e., $N + \text{Surface} \rightarrow N(s)$, $N + H(s) \rightarrow NH(s)$ and $N + N(s) \rightarrow N_2$) and an even larger increase when increasing the N₂ electron impact dissociation rate (cf. Figure C.10). We conclude that, among the surface reactions, the adsorption of N atoms is the rate-limiting step, both through the ER reaction between N and H(s) and direct adsorption of N, which leads to the other ER reaction, $H + N(s)$ (see Figure 6.8; blue and red arrows, respectively). This is attributed to both the relatively low N atom gas phase density and the large H(s) surface coverage. Note that the latter reaction is less significant to the formation of NH(s) (cf. Figure 6.7, group (2) compared to group (1)) under the conditions investigated. It is clear that the rate of those reactions can be increased by increasing the N atom density, i.e. by a higher N₂ gas phase dissociation. Thus, we conclude that electron impact N₂ dissociation in the plasma, followed by N adsorption at the surface, is the rate-limiting step determining the NH₃ yield in our DBD. In other words, we do not find that the

dissociative N₂ adsorption, from the ground state or vibrational levels, due to the surface itself, is rate limiting.

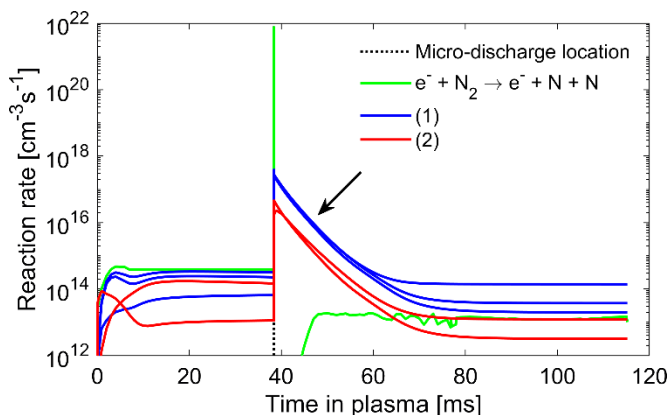


Figure 6.7. Graphical summary of the detailed analysis presented in the SI (section S.4), showing surface reaction rates that are identical shortly after the microdischarge (indicated with the arrow) and the N₂ electron impact dissociation rate in the plasma as a function of time, from the start of the plasma to the end of the first microdischarge and afterglow pair. The microdischarge with a 200 ns duration takes place at 38.4 ms. The electron impact N₂ dissociation rate, and thus the N atom source, becomes negligible after the microdischarge. The first group of overlapping reaction rates (1) consists of N + H(s) → NH(s), NH(s) + H(s) → NH₂(s) and NH₂(s) + H(s) → NH₃. The second group of overlapping reaction rates (2) consists of N + Surface → N(s) and H + N(s) → NH(s). The reactions are also depicted in Figure 6.8.

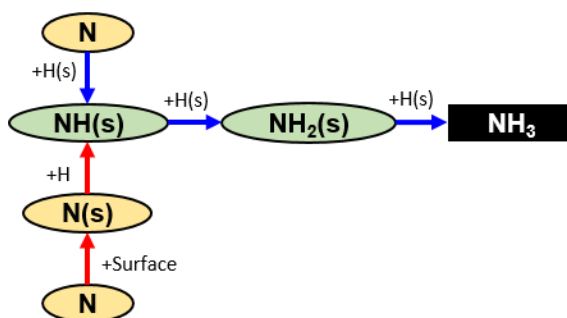


Figure 6.8. Schematic diagram of the various surface reactions, starting with N atoms, which form NH₃ shortly after a microdischarge. The blue and red arrows correspond to the reactions in group (1) and (2) in Figure 6.7, respectively.

6.5. N₂ Dissociation Rates in the Plasma

The dissociation of N₂ in the plasma occurs exclusively by electron impact collisions. In Figure 6.9, we show the various electron impact N₂ dissociation rates as a function of time. The dissociation is only significant in the microdischarges and consequently, the N atoms are consumed directly after the microdischarges. In Chapter 5 we showed that even in a filamentary DBD, vibrational excitation and thus dissociation from vibrational levels can be important. In experiments, high N₂ vibrational temperatures were also reported for PB DBDs [56], [57]. Colonna *et al.* showed the significance of the vibrational distribution function and electron energy distribution function in strong ns pulsed N₂ and H₂ discharges [74], [75]. As discussed before, our model predicts a maximum N₂ vibrational temperature slightly above 2100 K during the microdischarges, at the conditions under study, and it relaxes back to slightly above the gas temperature (700 K compared to 400 K) in the afterglows over approximately 1 ms (cf. Appendix C.2, Figure C.4(a)). Thus, vibrational excitation is quite prominent during the microdischarges. The reduced electric field (E/N) and electron temperature are also plotted as a function of time in Appendix C.2 (Figure C.4(b)). The maximum E/N was calculated to be 105 Td in each microdischarge and the maximum electron temperature (T_e) was 5.9 eV. In the afterglows, they reach constant values, around E/N = 6 Td and T_e = 0.7 eV.

When comparing the N₂ dissociation rates from the ground state, vibrational levels and electronically excited states in Figure 6.9, it is clear that ground state dissociation is always the highest, followed by dissociation from the vibrational levels in the afterglows, and from the electronically excited levels during the microdischarges. However, dissociation from the vibrational levels during the microdischarges is still high and contributes for 8 % to the total electron impact N₂ dissociation, while the contribution of the ground state and the electronically excited states is 73 % and 19 %, respectively. Compared to the microdischarges, the dissociation in the afterglows is much lower, and mainly due to the ground state (98.4 %), but dissociation from the

vibrational levels (1.6 %) is higher than from electronically excited levels (only 0.0001 %). Even if we account for the duration of the microdischarges (200 ns) and afterglows (76.8 ms), similar to before (cf. equation 6.1), we find that 99 % of all N₂ electron impact dissociation occurs during the microdischarges.

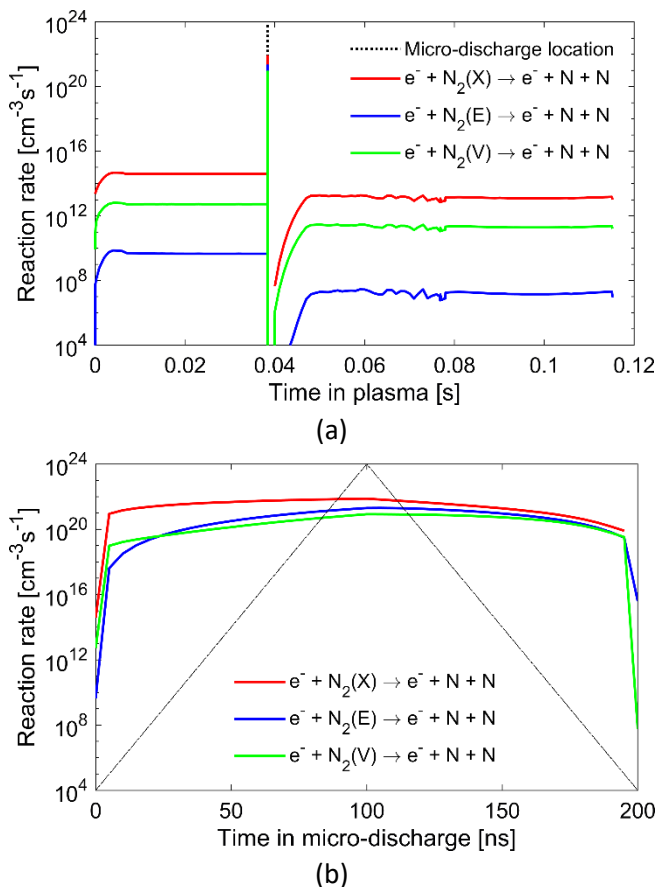


Figure 6.9. N₂ electron impact dissociation rates from the ground state (X), electronically (E) and vibrationally (V) excited states in the plasma, as a function of time, from the start of the plasma to the end of the first microdischarge and afterglow pair (a), and as a function of time in the first microdischarge (b). In (a), the microdischarge with a 200 ns duration takes place at 38.4 ms.

Many authors reported an increase in NH₃ yield upon increasing plasma power or applied voltage [35], [38], [43], [84], [85]. A higher plasma power or applied voltage leads to a stronger plasma, and thus higher electron densities and/or energies, and faster electron impact processes, including N₂ dissociation. Hence, these experimental

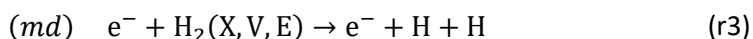
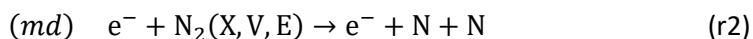
observations from literature qualitatively support our model prediction that electron impact N₂ dissociation in the plasma directly affects the NH₃ formation rate, or in other words, that it can be considered the rate-limiting step for NH₃ formation in DBD plasma.

6.6. NH₃ Formation Reaction Scheme for the microdischarges and Their Afterglows

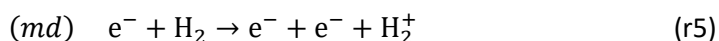
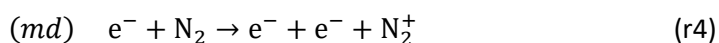
Based on the preceding sections, we can summarize the NH₃ formation mechanisms as follows, as revealed by our model. First, dissociative adsorption of H₂ covers the surface with H(s), before the first microdischarge occurs, due to the large number of free surface sites (cf. Figure 6.1(a) and Appendix C.1).



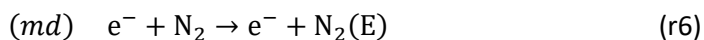
Subsequently, during the microdischarges (indicated with *md*), first electron impact dissociation of the feed gases takes place, from the ground state but also from the electronically and vibrationally excited states (cf. Figure 6.9).

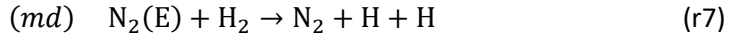


The dissociation is enhanced by the high electron density and high electron energy in the microdischarges (cf. Figure 6.1(b) and Figure C.4(b)). The high electron density is a result of ionization of the feed gases.

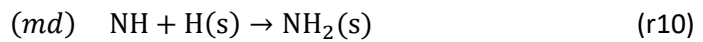
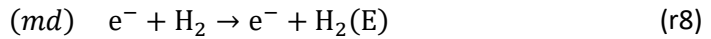


In addition, dissociation of H₂ also occurs upon collisions with electronically excited N₂ (contribution of 10 %).





During the microdischarges, the formation of NH₂(s) from NH and H(s) (ER reaction) is also significant, and even more, it only happens significantly during the microdischarges (cf. Figure C.5). The full pathway of this formation mechanism is as follows:



This causes some depletion of H(s) at the surface, but the latter is immediately compensated by the supply of fresh H(s) upon H atom adsorption in the afterglows (indicated with *ag*) (cf. Figure C.8 and C.9).

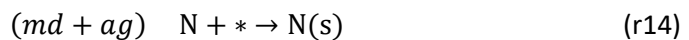


Note that during the microdischarges, H(s) is also consumed via the very large number of H atoms in the plasma (cf. Figure 6.1(b) and Appendix C.1).



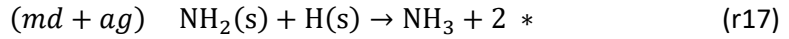
H atom recombination is also reported by Shah *et al.* to be more significant due to the surface in comparison with gas phase reactions [111].

Looking further to the NH₃ formation, the NH₃ precursors are formed according to the same reactions during both the microdischarges and afterglows, i.e., a combination of ER and LH reactions (cf. Figure 6.7 and 6.8).

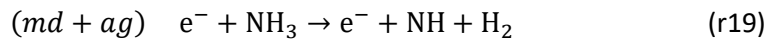
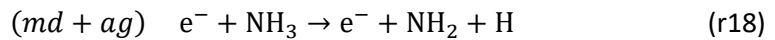




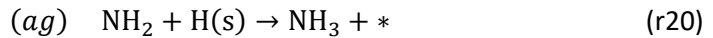
Finally, NH₃ is formed by the following LH reaction (cf. Figure 6.7 and 6.8).



This process takes place both during the microdischarges and the afterglows, but in the microdischarges a larger fraction of NH₃ is dissociated (cf. Figure 6.4) due to the high electron density.

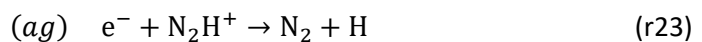
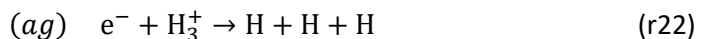


The same reactions govern the eventual NH₃ yield, i.e. in steady state, in the afterglows (cf. Figure 6.6). In other words, reactions r18 and r19 balance with the NH₃ formation in the late afterglow, due to the high NH₃ density, in spite of the low electron density in the afterglows (cf. Figure 6.1(b)). The most significant NH₃ formation in the late afterglow is actually the ER reaction with NH₂.

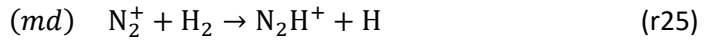
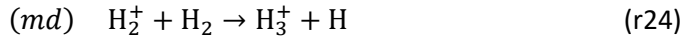


It should be noted however that this reaction does not contribute to the actual net NH₃ formation (cf. Figure 6.1 and Figure C.5(a)). NH₃ is mainly formed by reaction r17.

The electrons created in the microdischarges are lost in the afterglows due to recombination reactions.



The formation of these ions occurs in the microdischarges through the quick conversion of N₂⁺ and H₂⁺.



As mentioned, the electrons govern the NH₃ steady state yield (through reactions r18 and r19). They are produced upon ionization reactions r4 and r5, which are followed by charge transfer reactions r24 and r25, of which the products eventually recombine again with the electrons (reaction r21, r22 and r23). Thus, the electron source in the microdischarges is directly linked to the electron losses in the afterglows. This could explain why in literature, no saturation in NH₃ yield is observed upon increasing the plasma power or applied voltage [35], [38], [43], [84], [85]. Nevertheless, Mizushima *et al.* do speculate that NH₃ decomposition is promoted with increasing applied voltage [39].

Note that recombination reaction r23 is often mentioned in literature to be important for the formation of NH [41], [42], [112]. In our model, this is not the case. The latter is in agreement with Molek *et al.* who reports that only 5 % of this recombination leads to NH [113]. On the other hand, this NH formation mechanism may become important at different plasma conditions, such as low pressure [114]–[120].

Hong *et al.* performed a kinetic analysis based on a similar model as ours, but the plasma conditions, albeit derived from a PB DBD as well, were described as constants. Thus, their model did not explicitly capture the microdischarges. They also found that the surface is covered with H(s) under all plasma conditions due to dissociative adsorption (reaction r1), which they attribute to the low dissociation rates in the plasma [77]. This agrees with our model, up to the first microdischarge. Once a microdischarge occurs, the dissociation rate in the plasma increases, and our model predicts that direct adsorption of N and H atoms (reaction r11 and r14) are more important. In addition, instead of reaction r9, Hong *et al.* observed the formation of NH from vibrationally excited H₂ [77]. At our plasma conditions, however, the NH formation is only important during the microdischarges, which represent a stronger plasma than in reference [77],

thus it is logical that electronic excitation is more significant, explaining the difference in predicted NH precursors by both models. Furthermore, the subsequent ER reaction that forms $\text{NH}_2(\text{s})$ (reaction r10) was reported to be the main $\text{NH}_2(\text{s})$ source in reference [77], while in our study, this is again only true during the microdischarges. In the afterglows, the formation is attributed to an LH reaction instead (reaction r16). Finally, Hong *et al.* did not observe the ions to play an important role in the formation of NH or NH_3 [77], in agreement with our study, and they also found that gas phase NH_2 arises from the dissociation of NH_3 (reaction r18). However, they claimed that NH_2 is recirculated back to the desired products [77], which is in contrast to the conclusions of our model.

According to our reaction analysis, NH_2 only occurs as product of reaction r18, i.e. NH_3 electron impact dissociation, and it does not actively contribute towards NH_3 formation, despite $\text{NH}_2 + \text{H}(\text{s}) \rightarrow \text{NH}_3$ (reaction r20) having the highest NH_3 formation rate in the late afterglow (cf. Figure C.5(a)). Indeed, collisions with neutral species convert NH_2 into NH and back to the feed gas. Those collisions account for 71 % of the NH_2 destruction in the afterglow, while reaction r20 accounts for 10 % (cf. Appendix C.5, Table C.4). Furthermore, our model reveals that $\text{N}_2(\text{E})$, $\text{H}_2(\text{E})$ and NH radicals do not contribute towards NH_3 formation in the afterglows. Indeed, these three species are produced by electron impact collisions, which have a much lower rate in the afterglows than in the microdischarges (see for example Figure 6.6), and they are quenched back to the feed gas.

As mentioned above, at the DBD conditions under study, our calculations reveal that dissociative adsorption of N_2 does not play a significant role in the NH_3 synthesis. Furthermore, the surface is most significantly covered by H(s). Mehta *et al.* proposed that vibrational excitation of N_2 increases the NH_3 synthesis rate by an enhanced dissociative adsorption rate [57]. If we consider all N(s) sources, i.e. both direct adsorption of N atoms and dissociative adsorption from N_2 ground state and excited molecules, we find that only at the very beginning dissociative adsorption of N_2

molecules in the ground state or from vibrational levels causes the initial coverage with N(s) (96 % and 4 % contribution for ground state and vibrational levels, respectively). The same applies to the initial H(s) adsorption, i.e. due to the empty surface sites and the lack of other radicals. However, quickly thereafter, and already before the first microdischarge, the contribution from direct adsorption of N atoms is already 98 %, while dissociative adsorption accounts for the remainder of N(s) (i.e., 1.6 % from the ground state and 0.1 % from the vibrational levels). During the microdischarges, the contribution of dissociative adsorption does not rise, because the N atom density largely increases (cf. Figure 6.1(b)). After the microdischarges, the contribution of dissociative adsorption reduces further to only 0.28 % and 0.02 % for the ground state and vibrationally excited levels, respectively. Still the contribution of the vibrational levels in the afterglow is generally higher than that of the electronically excited molecules in dissociative adsorption; see also Figure C.12.

The above reaction mechanisms are summarized in Figure 6.10, in which we also distinguish between the microdischarges and their afterglows. During the microdischarges, electron impact excitation creates electronically excited levels ($H_2(E)$, $N_2(E)$), and vibrationally excited levels, while electron impact dissociation of H_2 and N_2 ground state and electronic and vibrationally excited molecules creates H and N atoms, and electron impact ionization creates H_2^+ and N_2^+ ions. The latter are converted into H_3^+ and N_2H^+ ions, which recombine with the electrons in the afterglows. These ions do not contribute to the NH_3 formation. The $N_2(E)$ molecules also contribute to H_2 dissociation. The collision between $H_2(E)$ molecules and N atoms yields NH radicals. In addition, the N atoms adsorb on the surface. Two types of ER reactions ($N(s) + H$, and $H(s) + N$) form NH(s). Both NH and NH(s) form $NH_2(s)$ upon reaction with H(s), i.e., in an ER and LH reaction, respectively. Finally, $NH_2(s)$ forms NH_3 , but the latter gets destroyed in the microdischarges upon electron impact dissociation.

In the afterglows, roughly the same processes occur as during the microdischarges, i.e., the two ER reactions ($N(s) + H$, and $H(s) + N$) form NH(s), which reacts further with H(s)

into $\text{NH}_2(\text{s})$ (LH). Note that the ER reaction ($\text{NH} + \text{H}(\text{s}) \rightarrow \text{NH}_2(\text{s})$) does not occur in the afterglows, because there are virtually no NH radicals present in the afterglows. The same is true for NH_2 radicals, which are actually quenched back to the feed gas (not shown). Finally, $\text{NH}_2(\text{s})$ reacts again with $\text{H}(\text{s})$ into NH_3 (LH), but in contrast to the microdischarges, NH_3 is virtually not consumed through electron impact dissociation (except by some residual electrons), so there is net NH_3 formation in the afterglows, until periodic steady state is reached (when NH_3 formation is balanced by dissociation due to the residual electrons at the high NH_3 density).

The data used in the assessment of the reaction mechanisms (reactions r1 through r25 and Figure 6.10) is presented in detail in Appendix C.5, where we comment on the sensitivity of the assessed mechanisms to possible uncertainties in the underlying reaction rate coefficients. The effect of the uncertainties in rate coefficients has been studied in the past by our group, for plasma-based CO_2 conversion and dry reforming of methane [121], [122]. While the absolute values of model outputs, e.g. conversion, were greatly affected by the uncertainties in reaction rate coefficients, the general plasma behavior and reaction pathways remained the same. Hence, we have to keep in mind that the present study aims at qualitatively clarifying the reaction mechanisms, rather than providing quantitative predictions.

Within the reaction mechanisms of Figure 6.10, we can thus identify four elementary ER reaction steps taking place during the microdischarges (i.e., $\text{N} + \text{H}(\text{s}) \rightarrow \text{NH}(\text{s})$; $\text{H} + \text{N}(\text{s}) \rightarrow \text{NH}(\text{s})$; $\text{NH} + \text{H}(\text{s}) \rightarrow \text{NH}_2(\text{s})$; and $\text{H} + \text{H}(\text{s}) \rightarrow \text{H}_2$; reaction r13, r15, r10 and r12 above). Two of these reactions (reaction r13 and r15) also play an important role in the afterglows. In addition, both in the microdischarges and afterglows, two elementary LH reaction steps occur (i.e., $\text{NH}(\text{s}) + \text{H}(\text{s}) \rightarrow \text{NH}_2(\text{s})$; and $\text{NH}_2(\text{s}) + \text{H}(\text{s}) \rightarrow \text{NH}_3$; reaction r16 and r17 above) but the ER reactions are mainly responsible for the formation of the precursor, $\text{NH}(\text{s})$ (reaction r13 and r15), indicating the overall importance of ER reactions in a DBD plasma.

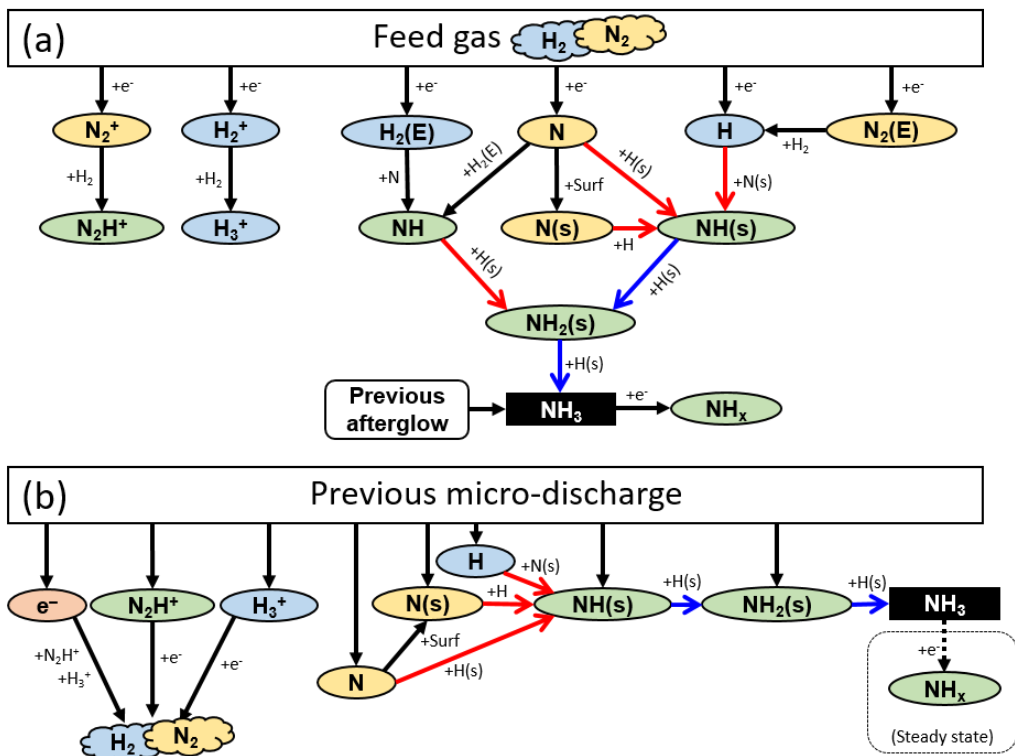


Figure 6.10. Reaction mechanisms governing the formation of NH_3 in a DBD during the microdischarges (a) and their afterglows (b). Elementary ER and LH reaction steps are drawn with red and blue arrows, respectively. In (a), the creation of reactive species during the microdischarges from electron impact collisions with the feed gas is shown, next to the further reactions of these species into NH_3 formation, as well as NH_3 destruction. In (b), the further reactions of these species, leading to a net production of NH_3 in the afterglows are shown, starting with the radicals produced in the previous microdischarge.

If we would only consider the gas phase reactions, the most significant NH_3 formation (in the afterglow) is due to $\text{H} + \text{NH}_2 + \text{M}$ and $\text{NH} + \text{H}_2 + \text{M}$, both with reaction rates in the order of $10^{14} \text{ cm}^{-3}\text{s}^{-1}$ to $10^{15} \text{ cm}^{-3}\text{s}^{-1}$. These reactions account for less than 10 % of the overall NH_3 formation rate. A calculation with only the gas phase reactions taken into account results in only 20 ppm of NH_3 formed, compared to 220 ppm with the catalytic reactions (cf. Figure 6.6).

The exact reaction mechanisms of course depend on the reaction and activation energies, and in turn, the latter can depend on the surface. For example, the activation

barriers for Langmuir-Hinshelwood reactions are different across different metals [57]. Our present model does not easily capture the properties of different metal surfaces, but we have seen that the reaction mechanisms beyond the formation of NH(s) indeed depend on the activation energies of Langmuir-Hinshelwood reactions and the overall available reactions in the chemistry description, and this should be subject to future studies. In the Appendix C.6 we provide a small analysis, which reveals that indeed with faster LH reactions, the results are unchanged and that with slower reactions other reactions will form NH₃ with the same reaction rate, resulting in the same NH₃ concentrations, due to the reactions being limited by the ER formation of NH(s). Based on these test cases, we found that NH₃ can also be formed in a single ER reaction (instead of reactions r16 and r17).



We acknowledge that this reaction appears to be a thermal-only process, but that it is generally not considered in typical thermal catalytic models of ammonia synthesis. When this reaction was not considered, we found that the stepwise ER hydrogenation reactions can form NH₃ instead.



In addition, the surface is quickly covered by H(s) due to dissociative adsorption due to the large presence of empty surface sites and the lack of radicals at the start of the plasma. The dissociative adsorption rates in principle also depend on the metal surface. This in combination with various feed gas mixtures, i.e. an excess of N₂, could change the (initial) surface coverage towards more N(s). Due to the high gas phase dissociation rate of H₂, the ER reaction between N(s) and H to form NH(s) is then expected to gain importance relative to H(s) + N → NH(s).

Our model reveals that radicals play an important role in the assessed reaction mechanisms, through direct adsorption and elementary ER reaction steps. Although the underlying rate coefficients suffer from large uncertainties, as there are no extensive (density functional theory calculation) reports on this type of reactions available yet, Engelmann et al. showed that for typical gas phase concentrations found in DBDs, the radical-surface interactions are important over a wide range of ER activation barriers (i.e. 0 eV to 1.5 eV) for this type of reactions [109].

Apart from NH_3 , which is created due to the presence of the catalytic reactions, the surface is most likely to influence the gas phase composition through the N and H atoms and NH_2 radicals. The former are the most significant gas phase precursors and undergo radical adsorption. The latter is a dissociation product of NH_3 and thus dependent on the formation of NH_3 , which happens mainly through the surface reactions. A change in the radical adsorption would either deplete the gas phase N and H atoms quicker or slower. A change in the NH_3 synthesis would result in more or less NH_3 dissociation and consequently NH_2 .

The gas phase concentrations would be more directly influenced by the plasma conditions themselves. Those conditions serve as model input (i.e. the power density) and are derived from experimental current and voltage characteristics of a PB DBD. Next to the catalytic reaction rates, the type of packing and the precise catalytic surface can also influence the current-voltage characteristics, which presents another way of the packing or catalytic surface to directly influence the gas phase reaction rates, e.g. dissociation. Indeed, the dielectric constant of the support is known to influence the discharge characteristics [61]. In addition, Patil et al. observed an effect of the (metal) catalyst on the discharge characteristics, but no clear explanation has yet been given [123].

In their recent paper [58], Rouwenhorst *et al.* proposed four plasma-catalytic NH_3 synthesis regimes, i.e. (1) NH_3 synthesis in the plasma phase only, (2) NH_3 formation in the plasma phase and at the catalytic surface, through direct adsorption of N and H

atoms, which are first formed in the plasma by electron impact dissociation, (3) the same as (2), but H_2 adsorbs dissociatively onto the catalytic surface, and (4) both H_2 and N_2 undergo dissociative adsorption on the catalytic surface and NH_3 formation occurs at the surface only. In the latter case, the dissociative adsorption of N_2 is promoted by vibrational excitation in the plasma, and this regime was claimed to be energetically most favourable [58]. Our model reveals that the conditions under study mostly give rise to the third proposed mechanism, except that in our case, NH_3 is not significantly formed in the gas phase and the adsorption of N atoms does not only occur onto free surface sites.

6.7. Conclusions

Using the same modeling approach as in the previous chapter, we determined the formation mechanisms that take place in the microdischarges and their afterglows, as well as how they are connected. Our findings can be summarized as follows.

- Initial surface coverage with H(s).
- Creation of plasma radicals (e.g., N, H, NH) by electron impact collisions in the microdischarges.
- Adsorption of these radicals onto the surface and subsequent hydrogenation until desorption of NH_3 .

The last step causes a net production of NH_3 in the afterglows, while during the microdischarges, the formed NH_3 is destroyed again by electron impact dissociation.

Specifically, we could identify electron impact dissociation of N_2 during the microdischarges and the subsequent adsorption of N atoms on the catalyst surface as rate-limiting reaction step for NH_3 formation in a DBD, and thus determining the eventual NH_3 yield. Despite the fact that a PB DBD is typically a filamentary plasma, electron impact dissociation from vibrationally excited N_2 levels still contributes for about 8 % to the overall N_2 dissociation rate in the plasma. The larger this contribution, the more energy efficient the overall NH_3 synthesis would be, as the required

dissociation energy is reduced by vibrational excitation. While vibrational excitation can also overcome the energy barrier of dissociative adsorption, within our reaction mechanisms we did not observe this process to play an important role. The N(s) formation is accounted for by the direct adsorption of N atoms for at least 98 %.

Overall, our model reveals that both elementary ER and LH reaction steps can play an important role in plasma-catalytic NH₃ synthesis. The ER reactions (involving N, H and NH) are mainly attributed to the large abundance of plasma radicals in the microdischarges, while in the afterglows, only the H and N atoms contribute to ER reactions, forming NH(s), but the subsequent NH₃ formation occurs by LH steps.

Chapter 7.

Microdischarges from the perspective of molecules⁹

Abstract

We use a Monte Carlo approach to determine the number of microdischarges to which a single molecule would be exposed, by means of particle tracing simulations through a full-scale packed bed DBD reactor, as well as an empty DBD reactor. We find that the fraction of microdischarges to which the molecules are exposed can be approximated as the microdischarge volume over the entire reactor gas volume. The use of this concept provides good agreement between a plasma-catalytic kinetics model and experiments for plasma-catalytic NH₃ synthesis. We also show that the concept of the fraction of microdischarges indicates the efficiency by which the plasma power is transferred to the gas molecules. This generalized concept is also applicable for other spatially and temporally non-uniform plasmas.

⁹ This chapter is based on:

Spatially and temporally non-uniform plasmas: Microdischarges from the perspective of molecules in a packed bed plasma reactor.

K. van 't Veer, S. van Alphen, A. Remy, Y. Gorbanev, N. De Geyter, R. Snyders, F. Reniers and A Bogaerts

J. Phys. D: Appl. Phys., 54, 174002 (2021)

<https://doi.org/10.1088/1361-6463/abe15b>

7.1. Methods

In this study we substantiate the concept of the fraction of microdischarges to which individual molecules are exposed. We employ a Monte Carlo approach to calculate this fraction of microdischarges. The Monte Carlo calculations consider particle trajectories through a reactor volume, based on a full-scale flow model of a packed bed and empty DBD reactor. Furthermore, we report ICCD images to substantiate the assumptions underlying our calculations and we use a plasma kinetic model and plasma catalysis experiments to validate our concept of the fraction of microdischarges. Finally, we discuss the general applicability of our findings. The fraction of microdischarges can be related to the efficiency by which the plasma power is transferred to the individual gas molecules in the plasma reactor.

7.1.1. Particle tracing¹⁰

To obtain realistic trajectories of gas molecules flowing through a typical plasma reactor, as input to our Monte Carlo calculations (section 7.1.2), we performed computational fluid dynamics (CFD) followed by particle tracing simulations.

The CFD model describes the behaviour of a pure N₂ gas flow in both an empty and a packed bed cylindrical DBD reactor. Modelling pure N₂, as opposed to a specific N₂-H₂ mixture, will deliver a general overview for N₂-containing gas flows, while avoiding the need for approximative theories for calculating gas mixture properties like the viscosity [124]. The CFD model solves the mass continuity and momentum continuity Navier-Stokes equations for an incompressible Newtonian fluid:

$$\rho \nabla \cdot \vec{u}_g = 0 \quad (7.1)$$

$$\rho (\vec{u}_g \cdot \nabla) \vec{u}_g = \nabla \cdot \left[-p \vec{I} + (\mu + \mu_T) (\nabla \vec{u}_g + \nabla (\vec{u}_g)^T) \right] + \vec{F} \quad (7.2)$$

¹⁰ The particle tracing calculations were performed by Senne van Alphen (University of Antwerp).

where ρ stands for the gas density, $\overline{u_g}$ is the gas flow velocity vector, superscript T stands for transposition, p is the gas pressure, μ is the dynamic viscosity and μ_T the turbulent viscosity of the fluid, \vec{I} is the unity tensor and \vec{F} is the body force vector.

In an empty reactor, the flow is expected to be highly laminar, which greatly reduces the complexity of Eq. 7.1 and 7.2, as we can consider $\mu_T = 0$.

To be prepared for any turbulence occurring when a packing is added to the reactor geometry, the turbulent properties of the flow were solved for in the packed bed DBD reactor. We achieved this by using a Reynolds-averaged-Navier-Stokes (RANS) turbulent model, which significantly reduces the computation time by averaging all fluctuating turbulent quantities (i.e., the turbulent kinetic energy and the turbulent dissipation rate) over time. We used the k- ω model, as this model is still applicable at low level of turbulence and is able to resolve the laminar boundary layer near the walls [125]. This is important for the flow inside a packed bed reactor, as contact with the beads will introduce a lot of these boundary layers.

To reduce the large computational time of the CFD calculations, especially regarding the complexity due to the introduction of 13,216 beads inside the geometry, several measures were taken to reduce the number of finite mesh elements in the modelled geometry. First, the axial symmetry allows us to consider only 1/8th of the reactor, reducing the complexity of the model to 1,652 beads. Secondly, to avoid the need for a very small finite element mesh to resolve the contact points between two beads, the radius of the beads was reduced by 5 % for the flow calculation.

After the CFD calculations, we performed particle tracing simulations, in which we computed the trajectory of gas molecules as they flow through the reactor. These trajectories are calculated based on Newton's law of motion, using the drag force imposed by the velocity fields that were previously computed:

$$\frac{d(m_p \overline{u_g})}{dt} = \overline{F_D} \quad (7.3)$$

where m_p is the particle's mass, \vec{u}_g is the gas flow velocity vector and \vec{F}_D the drag force.

We performed the trajectory calculations for 10,000 particles, i.e., gas molecules, to ensure statistically relevant results. This yields 10,000 possible trajectories which the gas molecules can follow when flowing through either the empty or the packed bed DBD reactor. However, the solver removes trajectories from the simulation when the particles get stuck on a wall, due to their velocity which can approximate 0 m/s upon collisions with the walls. This is especially quite significant in a packed bed DBD where the particles often collide with the beads, but more than 5,000 particle trajectories were still preserved in the simulation. Those remaining trajectories do also include collisions. The calculated trajectories served as input to our Monte Carlo calculations (section 7.1.2) from which we determined the fraction of microdischarges experienced by the gas molecules.

Both the CFD and the particle tracing calculations were solved using the CFD module of COMSOL version 5.5 [126]. We used the same residence time in the empty and packed bed reactor (see section 7.2.1).

The flow simulations do not account for plasma effects, because we consider a full scale packed bed reactor with approximately 13,000 beads in the reactor (see above), and the complexity of a plasma model on this scale would be too high.

7.1.2. Monte Carlo calculations

The Monte Carlo approach determines whether a particle along a specific trajectory through the reactor (see section 7.1.1) is hit by a microdischarge, which occurs randomly throughout the reactor.

The total number of microdischarge events that take place in a DBD reactor is typically in the order of a few millions. Because the microdischarges occur throughout the whole reactor and because single gas molecules can only be at one point in the reactor at any moment in time, we expect that they experience a reduced number of microdischarges.

For this reason, we employed a Monte Carlo approach to statistically determine the fraction of microdischarges to which the individual gas molecules are exposed. Hence, by the general Monte Carlo approach, we select random numbers between 0 and 1, which determine at which location a microdischarge occurs. We assume that the locations of the microdischarge events are uniformly distributed throughout the reactor gas volume (see next section for motivation), but their actual occurrence is determined randomly. We performed experimental diagnostics to show that a uniform distribution of the microdischarges throughout the reactor is indeed a good approximation (see section 7.1.3 and 7.4). For more details on the placement of the microdischarge events, we refer to section 7.3.

Furthermore, the microdischarge events are equally distributed over the gas residence time and the microdischarges stay active for a certain microdischarge lifetime. For each trajectory through the reactor we check whether or not a particle (i.e., gas molecule) is at the same location as a microdischarge at any moment in time during which the specific microdischarge is active. If this is the case, we define a hit for the microdischarge event. The total number of hits per trajectory over the total number of microdischarges that took place in the reactor will then define the fraction of microdischarges.

We acknowledge that we do not capture the actual physics of a microdischarge, and we do not consider an actual plasma, which could influence charged particles, especially in the microdischarges due to the presence of strong electric fields. Indeed, self-consistent modelling of a filamentary plasma is a difficult task, requiring e.g., particle-in-cell Monte Carlo methods [127]. As we consider millions of random microdischarges instead of individual microdischarges, a fully self-consistent filamentary plasma model is not feasible. However, we do apply this concept of the fraction of microdischarges in a 0D plasma kinetics model (section 7.1.4).

Finally, we note that the calculations in this specific study lead to general insights that are not necessary tied to a single experimental setup. As long as the assumption on the

uniform distribution of the microdischarges is valid, the findings will be unaltered. The conclusions are used in our OD plasma kinetics model.

7.1.3. Experiments¹¹

In the Monte Carlo calculations, we assume that the microdischarges are uniformly distributed throughout the plasma reactor. We verified this assumption by means of experimental diagnostics.

The reactor used to study the distribution of microdischarges by ICCD images is a closed parallel plate rectangular DBD reactor with two dielectrics. Each dielectric is a fused silica (quartz) piece of 118 x 68 x 3 mm³. A discharge gap of 2 mm is formed between them. On each outer side, the dielectrics are covered by a stainless-steel mesh acting as electrode. The structural parts of the reactor, i.e., the enclosure, are built in transparent polymethyl methacrylate (PMMA). This configuration allows to place a high-speed camera perpendicular to the dielectric surface and to have a clear view of the discharge (as illustrated in Figure 7.1).

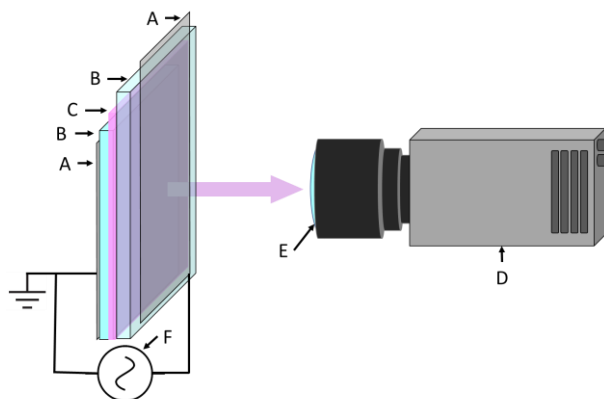


Figure 7.1. Schematic of the DBD setup used for ICCD imaging, showing the electrodes (A), dielectric barriers (B), discharge gap (C), camera body (D), lens (E) and high voltage generator (F).

¹¹ The ICCD experiments were performed by Antoine Remy (Université Libre de Bruxelles). The ammonia synthesis experiments were performed by Yury Gorbanov (University of Antwerp).

One of the electrodes is connected to a high voltage generator (AFS G10S-V) through a high frequency transformer (1-30 kHz), while the other electrode is grounded. The generator allows to control the operating frequency and the applied power in the plasma. The experiments were conducted at a frequency of 12 kHz and a power of 100 W. Approximately 60% of this power is effectively absorbed into the plasma. A constant flow rate of 1 L/min of a $N_2:O_2$ gas mixture with a ratio of 1:1 (500 mL/min each) is applied at atmospheric pressure. The high-speed camera used for ICCD imaging is a Photron Nova S2 working at 10,000 frames per second (fps) at a raw resolution of 1024 x 672 pixels. The final resolution is divided by two after application of a binning 2 x 2 to enhance the luminosity of the plasma, giving a final resolution of 512 x 336 pixels.

Furthermore, we studied the effect of the fraction of microdischarges in a plasma kinetics model (see section 7.1.4). We performed plasma-catalytic ammonia synthesis experiments to verify whether our plasma kinetics model is realistic. The ammonia synthesis experiments were performed in an axial cylindrical DBD reactor operated at atmospheric pressure, 23.5 kHz frequency and ca. 10 kV peak-to-peak voltage, and a gas mixture of $H_2:N_2$ with a ratio of 1:1. The applied voltage correspond to 100 W of supplied power of which approximately 70 % goes into the plasma. The catalyst was 10 wt% Co/ Al_2O_3 prepared via incipient wetness impregnation of commercial Al_2O_3 beads (diameter: 1.8 mm, Sasol). The production of NH_3 was monitored by mass spectrometry of the outlet gaseous mixture. The full description of the reactor, plasma discharge, experimental procedure, analytical techniques, and catalyst preparation and characterisation is found elsewhere [128].

In our experiments, the total gas flow rate was varied from 100 to 400 mL/min to allow different values of the gas residence time inside the plasma region (see section 7.5).

7.1.4. Plasma kinetics model

We use our previous 0D plasma chemistry model developed within ZDPlasKin (Chapter 4) and adopted a plasma-catalytic surface micro-kinetics model [109] to investigate the effect of using different fractions of microdischarges and we compare the results against experiments (see section 7.1.3).

Within the gas residence time in the reactor, we can approximate the total number of microdischarges in the reactor with:

$$N_{MD,total} = 2N_{MD,\frac{1}{2} cycle} f_D \tau_{res} \quad (7.4)$$

where N_{MD} is the number of microdischarges in the whole reactor, during the full residence time (subscript *total*) and during one discharge half cycle (subscript $\frac{1}{2} cycle$), f_D is the discharge frequency and τ_{res} is the residence time. This typically yields in the order of millions of microdischarges (i.e. by using typical values of $N_{MD,\frac{1}{2} cycle} = 25$, $f_D = 23.5$ kHz and $\tau_{res} = 4$ s [128]).

In plasma kinetics models of a DBD only a small fraction of those microdischarges are assumed to be experienced by the molecules [66], [67], [70]–[73], [81], [82]. The reduced number of microdischarges that are actually considered in the model can be described with:

$$N_{MD,reduced} = \eta_{MD} N_{MD,total} \quad (7.5)$$

which we determine in this study using a Monte Carlo approach (see section 7.1.2).

In the previous chapters (Chapter 5 and 6) we assumed that the fraction of microdischarges depends on the gas velocity and the amount of reactor volume passed through by the gas molecules during one discharge period. This caused the number of microdischarges in the model to be independent of the residence time [82]. In earlier literature, it was sometimes assumed that the fraction of microdischarges is given by the microdischarge volume over the reactor volume [67], [81]. (See also section 4.2.2.)

We will use the plasma kinetics model (Chapter 4) to investigate the effect of varying the fraction of microdischarges over a large range (section 7.5).

7.2. Particle tracing results

7.2.1. Particle trajectories through an axial cylindrical packed bed reactor

We calculated particle trajectories through both an empty and packed bed cylindrically symmetrical DBD reactor, as described in section 7.2.1. The flow rate in the empty DBD was adjusted relative to the one in the packed bed DBD, to account for the reduced volume due to the packing in the latter, and to obtain the same average residence time in both reactors. The empty reactor volume is approximately 9.42 cm^3 and the packing volume is approximately 5.93 cm^3 (i.e., 13,216 spheres with 1 mm diameter), yielding a packing factor of 63 %. This results in a flow rate of 270 ml/min for the empty reactor, based on a 100 ml/min flow rate in the packed bed reactor. Using those different flow rates, the average residence time in both reactors is then 2.1 s. In Figure 7.2 we show the packed bed reactor, the dimensions of the packing, as well as the simulated gas molecules and their velocity. The Figure shows that gas molecules flow through the reactor at a wide range of velocities, varying from 0.002 m/s to 0.1 m/s.

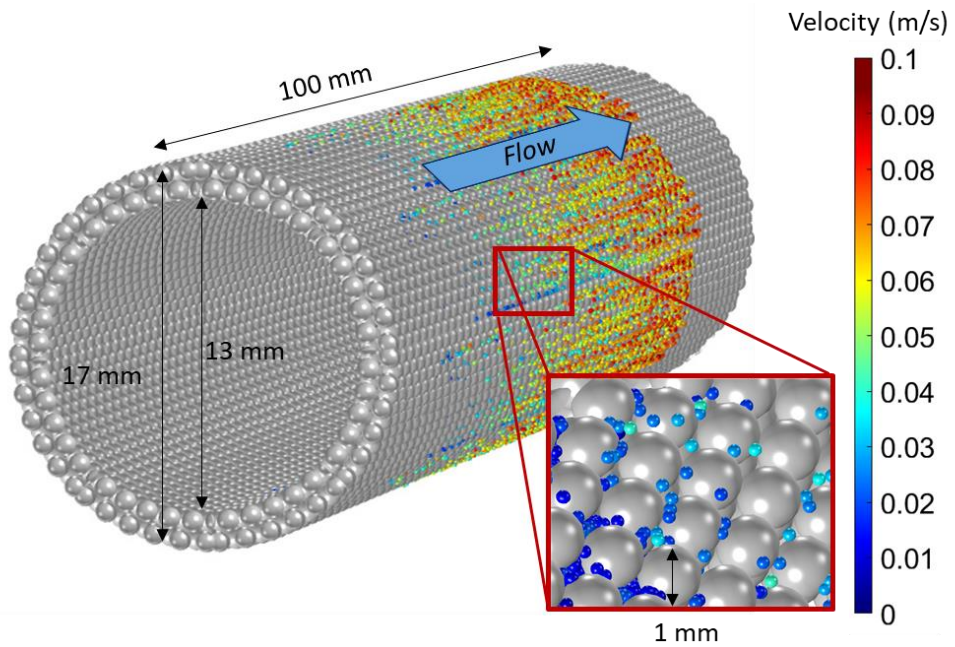


Figure 7.2. Illustration of the gas molecules flowing through a packed bed reactor consisting of two concentric cylinders. The reactor contains 13,216 spherical beads (1 mm in diameter) stacked into two layers in the gap between both concentric cylinders. Note that the reactor diameter and reactor length are not to scale, for clarity. The inner diameter of the large cylinder is 17 mm, while the outer diameter of the small cylinder is 13 mm, yielding a gaseous gap of 2 mm.

7.2.2. Residence time distribution in an empty and packed bed DBD reactor

In Figure 7.3a and 7.3b, we show the residence time distribution of the gas based on the particle tracing calculations for an empty and a packed bed DBD reactor, respectively. Besides the tail of the distribution, which is less smooth in case of the packed reactor, the distributions are quite similar. Indeed, the flow rate was chosen to yield the same average residence time in both reactors (see section 7.2.1).

The gas flow in an empty reactor follows a typical Poiseuille velocity profile, as illustrated in Figure 7.4a. As a result of the fluid viscosity, friction between the flowing gas and the reactor wall causes the gas to slow down close to the wall, creating a boundary layer that shapes the parabolic velocity profile. Hence, the molecules in vicinity to the reactor walls in the empty reactor are characterized by a longer residence time compared to the average. The molecules in the middle of the reactor have a high velocity and account for the shorter residence times, resulting in the distribution as shown in Figure 7.3a.

The gas flow in the packed reactor shows opposite behavior, as illustrated in Figure 7.4b. Fast molecules, with short residence times, now flow through the reactor in the vicinity of the wall, while the slow molecules, with long residence times, flow through the middle of the reactor. This effect is discussed in greater detail below (section 7.2.3).

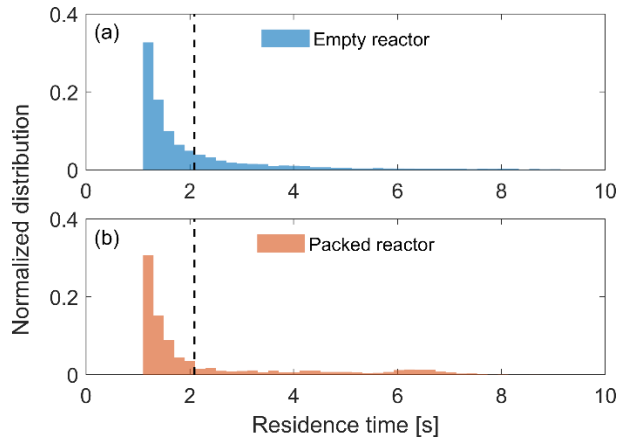


Figure 7.3. Residence time distribution in the empty (a) and packed bed (b) reactor. The average residence time is the same in both reactors, and is indicated with a vertical dashed line (approximately 2.1 s).

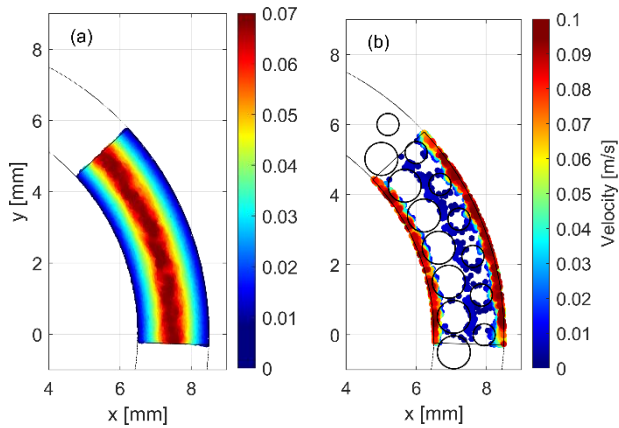


Figure 7.4. Top view of the axial velocity of each particle in the empty (a) and packed bed (b) reactor. The white space outside of the packing bead contours in (b) represents locations where the probability of finding a particle is so low that none of the simulated particles were found there. Note, both Figures show a cross section of the reactor made at a specific axial height ($z = 90$ mm, i.e., 10 mm before the reactor outlet). In (b) the intersection of this plane with the packing beads does not cut the beads equally because the two layers are not aligned in a closed packing of equal spheres, hence the outer layer of beads exhibits a smaller radius.

7.2.3. Gas distribution in an empty and packed bed DBD reactor

When a packed bed is introduced in the reactor, the incoming gas is forced to flow through the small gaps in between the beads of the packed bed, which drastically changes the distribution of the gas flow compared to an empty reactor. In Figure 7.5 we present the calculated gas distribution for an empty and a packed bed DBD reactor, as calculated by the particle tracing simulations. For an empty reactor, Figure 7.5a shows that most of the gas passes through the centre of the reactor, where the flow is undisturbed by the viscous boundary layer near the walls. As shown by Figure 7.5b, the introduction of a packed bed seemingly inverts this profile, as the flow is redistributed towards the reactor walls. The gas flow favours the path of least resistance and thus avoids the darkest blue zones around $r = 7.1$ mm and $r = 7.9$ mm, where the two bead layers are located (cf. Figure 7.4b). The small gaps between the beads only allow for small flow rates through the bed, so approximately 90% of the gas molecules flows towards the outer layer of the bed and the reactor wall, where the gaps are larger than in the perfectly packed centre. This value is based on integrating the probability distribution at the end of the reactor (Figure 7.5b at $z = 100$ mm) and comparing the outer layers to the middle section (between a radius of 6.9 and 7.9 mm), where the average probability of finding a gas molecule is 0.006 compared to 0.1 in the outer layers.

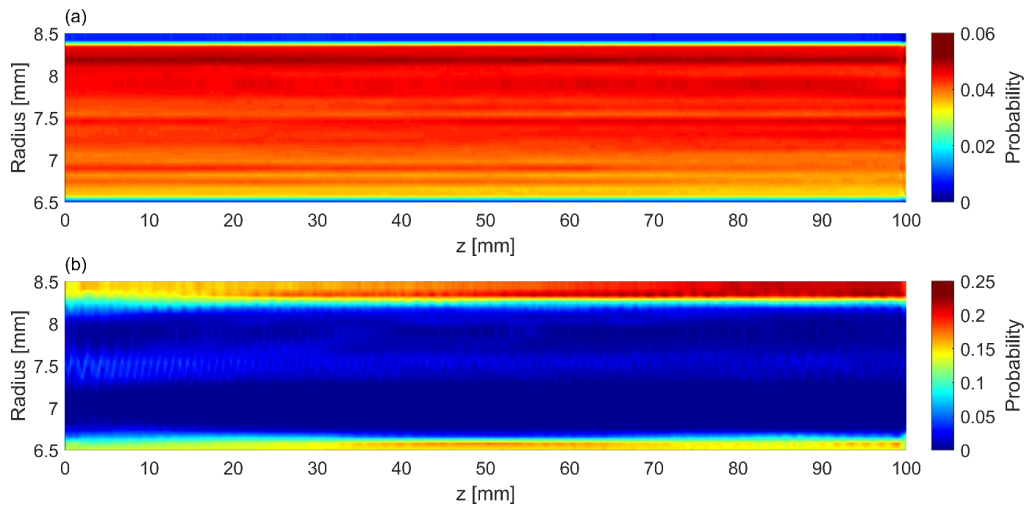


Figure 7.5. Radial gas distribution as a function of axial position in the reactor (i.e., along the reactor length) in the empty (a) and packed bed (b) reactor. The radial distribution was normalized at each axial position in the reactor, so integration along a vertical line in the Figure equals to 1.

Figure 7.5a and 7.5b both show that the gas density near the outer wall (towards 8.5 mm radius) is slightly higher than the gas density near the inner wall (6.5 mm radius). This is due to the curve of the cylindrical DBD reactor. Indeed, there can be more gas molecules at the larger radius due to the larger volume (or circumference). For the packed bed reactor this effect is larger, as also the packing configuration has to be considered. This is illustrated in Figure 7.6, which shows the close packing of equal spheres for a packed bed DBD reactor both with a straight and a curved electrode. The Figure demonstrates that a curved electrode introduces more space (highlighted in red) between the beads in the upper bead layer, allowing for more gas to flow through.

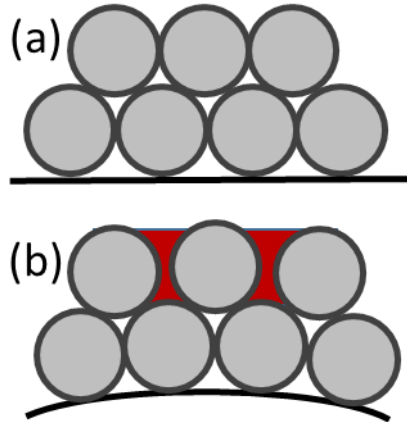


Figure 7.6. Close packing of equal spheres for a packed bed DBD reactor with a straight (a) and a curved (b) electrode surface.

The fact that the incoming gas is not evenly distributed over the reactor bed could be an important consideration for catalytic processes in packed bed DBD plasma reactors. Only a smaller portion of the gas will flow through the middle of the bed, i.e., in between the two bead layers, where there is more contact with the catalyst bed, and a longer residence time in the plasma (see previous section). However, in reality, the ideal packing assumed in this model is unlikely due to the bead shape and size and the filling of the reactor. Thus, in reality, gaps of various sizes can be formed throughout the packed bed, which can also allow more gas to flow through the center of the bed.

7.3. Monte Carlo calculations

7.3.1. Microdischarge distribution and “hits” in the empty and packed bed reactor

We calculated the fraction of microdischarges with the Monte Carlo approach explained in section 7.1.2, which we applied to the particle trajectories of the empty and packed bed DBD reactor (cf. section 7.2).

We assume 25 microdischarges per discharge half cycle, with a lifetime of 200 ns and a discharge frequency of 23.5 kHz [128]. With the maximum residence time of 9.41 s (corresponding to the empty reactor, cf. Figure 7.4a), this gives 10,739,500

microdischarges taking place throughout the whole reactor, during the entire gas residence time in the reactor. The maximum residence time in the packed reactor was 8.63 s, corresponding to 10,140,250 microdischarges.

In the empty reactor, we assumed the microdischarges to be small channels between the inner and outer electrode. For simplicity, the channels are actually very thin circle sectors, which allows us to use the cylindrical coordinate system throughout the Monte Carlo calculations. The azimuthal width of the microdischarges is 0.1 rad and the axial width is 0.1 mm. The channel length is approximately 2 mm, corresponding to an approximate microdischarge volume of 0.15 mm^3 . For clarity, the definition of the circle sector and the thin microdischarge channel is shown in Figure 7.7. The microdischarge events are placed randomly throughout the full reactor gas volume.

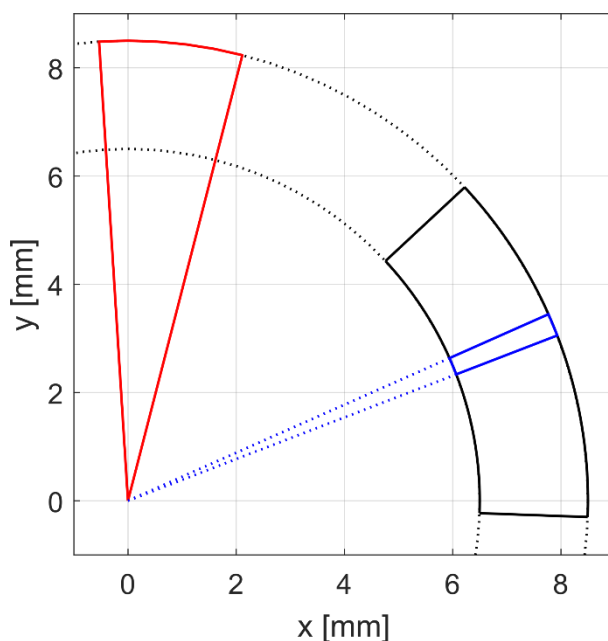


Figure 7.7. Schematic showing a top view of approximately $1/4^{\text{th}}$ of the cylindrical reactor (dashed black lines), the geometrical definition of a circle sector (red outline), the modelled reactor segment (black outline) and a thin circle sector representing a microdischarge channel in the empty reactor (blue outline).

In the packed bed reactor, the microdischarge events are defined as spheres with 0.3 mm radius, corresponding to an approximate microdischarge volume of 0.11 mm^3 . The

events are uniformly distributed throughout the packed bed reactor by randomly choosing a packing bead and then randomly choosing a point on the surface of this specific bead. Filamentary DBDs, especially with packed beds, are often characterized by point-to-point discharges, i.e., microdischarges between two beads, or surface discharges, i.e., microdischarges over the surface of a packing bead [61]. Our chosen spherical microdischarge volumes, which we center on the surface of the packing beads, can be considered a combination of both, as the chosen radius is also large enough to bridge the gaps between two close packing beads.

In Figure 7.8, we illustrate the locations of all the microdischarge events throughout the reactors. Note that this Figure only shows the locations and not the size (0.1 mm width and 0.3 mm radius in case of the empty and packed bed reactor, respectively) for the sake of clarity.

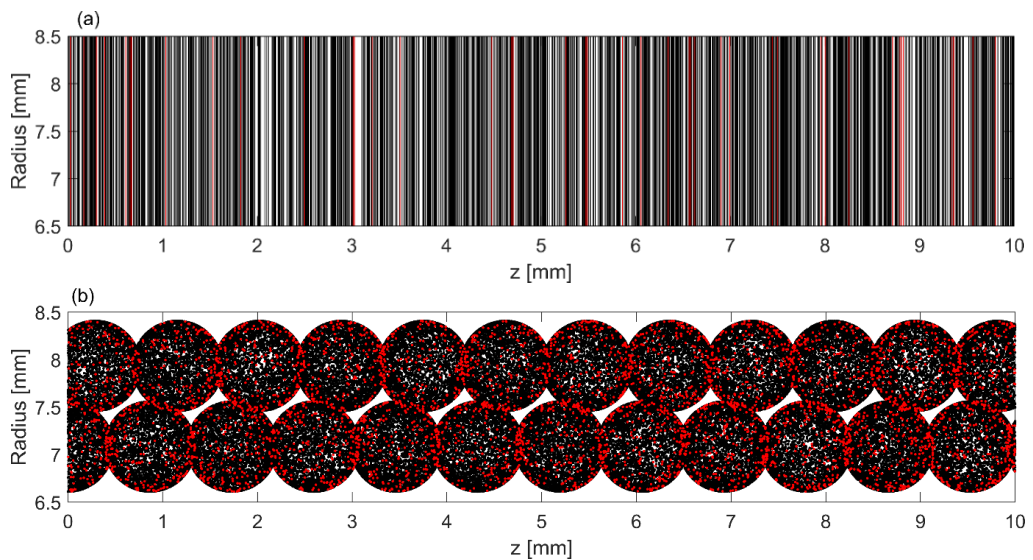


Figure 7.8. The microdischarge locations in both the empty (a) and the packed bed (b) DBD reactor. Only 1/10th of the reactor length is shown, with all of the microdischarges taking place (dark areas created by the overlapping and connecting individual vertical lines (a) or dots (b)). The red lines and dots indicate microdischarge events that have hit a particle trajectory. Note that in (a) only 1 % of all microdischarges are plotted for the sake of clarity. In addition, because in (b) the microdischarge events are placed on the surface of the packing beads, the shape of the packing beads is reflected back in this figure.

In Figure 7.9, we show five randomly selected particle trajectories and only the microdischarges to which they were exposed in the empty and packed reactor. It is clear that a particle trajectory can experience a microdischarge event anywhere along its trajectory. In case of the packed bed reactor (Figure 7.9b and 7.9c) particles (i.e., gas molecules) travelling near the walls are typically exposed to only a few microdischarges along their trajectory, while particles that travel through the center of the packed bed reactor experience more microdischarges. This is due to the longer residence time, as discussed in section 7.2, and because there are somewhat more microdischarge events in the middle of the reactor (at a radius of 7.5 mm), where the two packing bead layers are in contact with each other (cf. Figure 7.8b, which showed all microdischarges that took place, also including microdischarge events that did not hit any of the thousands of traced particles).

In Figure 7.10, we show that the hits between gas molecules and microdischarge events are also randomly distributed in time. We show this for the case of the packed bed, but it is also true for the empty reactor. Any gas molecule can have relatively short and long times between two microdischarges (cf. Figure 7.10 for the same trajectories as in Figure 7.9b). Note that the orange and yellow particle trajectories, which pass through the middle of the packed bed between $z = 10$ and 20 mm (cf. Figure 7.9b) have a longer residence time (3.12 s and 3.03 s) and experience more microdischarges.

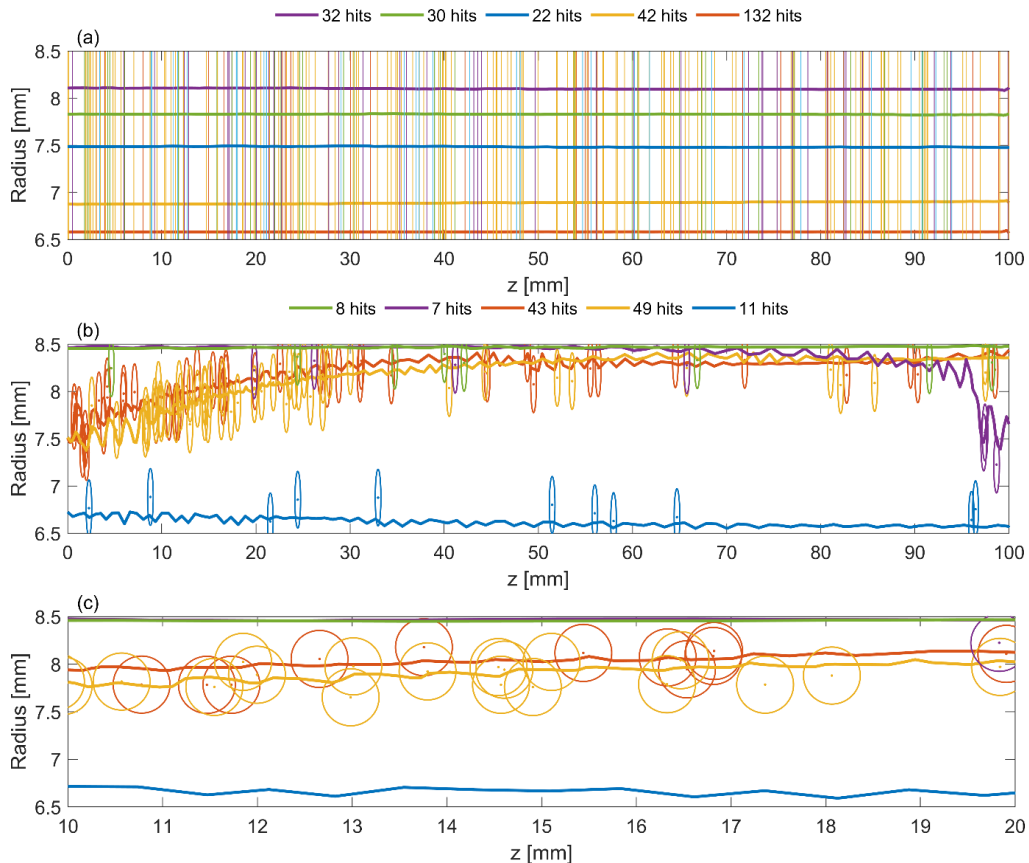


Figure 7.9. Five randomly selected particle trajectories flowing through the empty reactor (a) and the packed bed reactor (b, c), as well as the microdischarges to which they were exposed (vertical lines or spheres in the same color). In (a) and (b) the full reactor length is shown (reactor length and radius not to scale). In (c) $1/10^{\text{th}}$ of the reactor length is shown (with reactor length and radius to scale), i.e., between $z = 10$ and 20 mm, where most of the hits occur for the orange and yellow trajectory, because those particle trajectories go here through the middle of the packed bed, where they move more slowly (cf. Figure 7.4b), and there are slightly more microdischarge events.

In section 7.2.1 and 7.2.2 we explained that most of the particles travel through the packed bed reactor in the outer layers (cf. Figure 7.4b and 7.5b). Thus, only a few particles travel through the center of the reactor, and experience a large number of microdischarges (cf. orange and yellow particle trajectories in Figure 7.9b and 7.9c). Most particles will travel through the reactor near the electrode walls and experience only a few microdischarges.

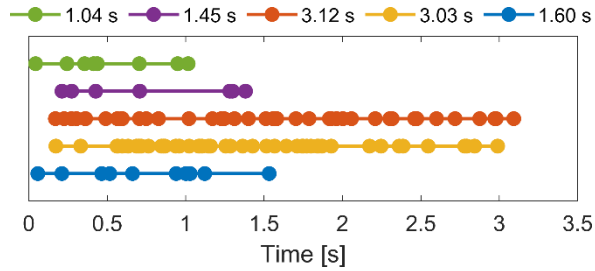


Figure 7.10. The moments in time at which the microdischarge event hits of Figure 9b occurred (dots on the line) for each of the five particle trajectories. The legend indicates the residence time of each displayed trajectory.

The distribution of the time between two microdischarge hits, based on all trajectories and all successful microdischarge events, is given in Figure 7.11. The median of this time distribution is 47 ms, the mode is 67 ms and the mean is 74 ms, the time between two microdischarge hits ranges from 68 μ s to 1.1 s.

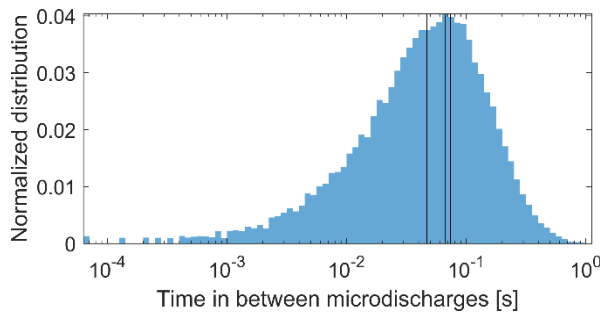


Figure 7.11. Distribution of the time between two microdischarge hits, when considering all trajectories. The vertical lines indicate, from left to right, the median (47 ms), mode (67 ms) and mean (74 ms), respectively.

7.3.2. Determination of the fraction of microdischarges to which the gas molecules are exposed

We use the results of each trajectory to determine the fraction of microdischarges to which the gas molecules are exposed, by fitting the Monte Carlo results of both the empty and packed bed reactor (see Figure 7.12) to:

$$\text{number of hits} = x_1 \times \tau_{res} \quad (7.6)$$

where x_1 is the slope of the fit, from which the fraction of microdischarges can be evaluated based on equation 4 and 5 above:

$$\eta_{MD} = \frac{x_1}{2N_{MD, \frac{1}{2} \text{ cycle}} f_D} \quad (7.7)$$

The fits are shown in Figure 7.12. For each of the particle trajectories, we plot the number of microdischarge hits and their residence time. Each cross in Figure 7.12 represents a particle trajectory. The slope of the fit through this plot of number of microdischarge hits vs the residence time gives us the value x_1 from Eq. 7.6 and from this slope we determine the fraction of microdischarges (Eq. 7.7).

Based on the slopes in Figure 7.12 (i.e., the values of x_1) and Eq. 7.7, we calculate the fraction of microdischarges to which the gas molecules are exposed, as $(1.548 \pm 0.003) \times 10^{-5}$ and $(1.306 \pm 0.006) \times 10^{-5}$, for the empty and packed bed reactor, respectively.

Note that the linear fits go through the origin of the graphs, based on the expected relationship (cf. Eq. 7.6), but at longer residence times the fit does not seem optimal when enforcing this intersection at (0,0) for the packed bed reactor (Figure 7.12b). Indeed, the points at longer residence time tend to lie above the fitted line. This is attributed to the fact that the slower particles move through the middle of the packed bed (cf. section 7.2), where there are slightly more microdischarge events, because the two packing bead layers are in contact with each other, hence explaining the slightly higher number of hits compared to the fitted line.

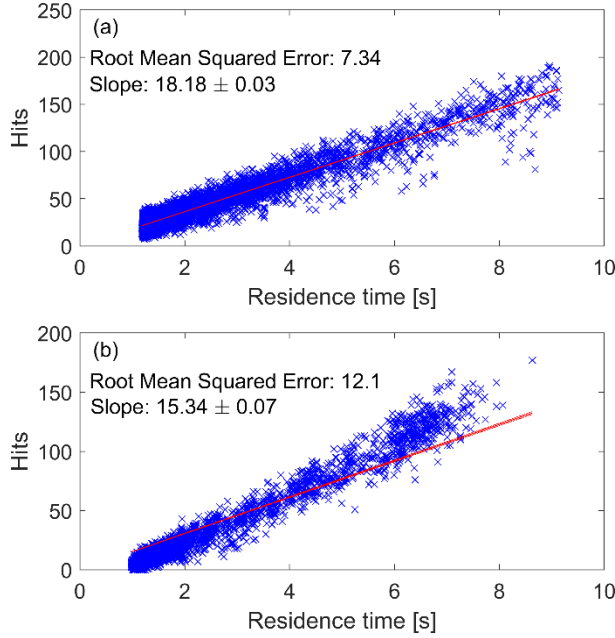


Figure 7.12. Number of microdischarge hits as a function of average residence time, for each of the particle trajectories, for the empty reactor (a) and the packed bed reactor (b). Each point corresponds to one trajectory. The data is fitted to Eq. 7.6, and the slope of the fit (x_1) is also indicated.

7.3.3. Empirical relationship for the fraction of microdischarges

As mentioned before, in earlier work from our group we assumed that the fraction of microdischarges to which the gas molecules are exposed, η_{MD} , is given by the ratio of microdischarge volume over the reactor volume [13], [14]. Based on the reactor volume $V_{reactor}$, the packing factor α and the microdischarge volume V_{MD} used in the COMSOL model and Monte Carlo calculations, we can also try to evaluate the fraction of microdischarges based on such volume-based relations:

$$\eta_{MD,empty} = \frac{V_{MD}}{V_{reactor}} \quad (7.8)$$

$$\eta_{MD,packed} = \frac{V_{MD}}{(1 - \alpha)V_{reactor}} \quad (7.9)$$

With the microdischarge volume of 0.15 mm^3 and 0.11 mm^3 for the empty and packed bed reactor, respectively, the reactor volume of 9.42 cm^3 and the packing factor of 63

%, Eq. 7.8 and 7.9 calculate the fraction of microdischarges as 1.6×10^{-5} and 3.2×10^{-5} for the empty and packed bed reactor, respectively.

Hence, using this method, the fraction of microdischarges for the empty reactor is in very good agreement with the Monte Carlo results (i.e., 1.6×10^{-5} vs. $(1.548 \pm 0.003) \times 10^{-5}$). On the other hand, the volume-based fraction of microdischarges for the packed bed reactor is somewhat overestimated compared to the Monte Carlo calculation (i.e., 3.2×10^{-5} vs $(1.306 \pm 0.006) \times 10^{-5}$). However, in this case we need to take into account that the effective microdischarge volume used in the Monte Carlo calculations is somewhat lower than 0.11 mm^3 , due to the placement of the spherical microdischarge events on the surface of the packing beads and because the assumed microdischarge radius is larger than the smallest distance between the packing beads. If we account for this in Eq. 7.9 (by assuming $V_{MD}/2$ instead of V_{MD}), we obtain a fraction of microdischarges of 1.6×10^{-5} , which shows a much better agreement with the Monte Carlo results. We note that the fraction $\frac{1}{2}$ is just an approximation. Indeed, in our Monte Carlo calculations for the packed bed reactor, we did place the spherical microdischarge events with an actual size of 0.11 mm^3 and the exact effective microdischarge volume is difficult to determine due to the complexity of the geometry of the packing beads and the stochastic nature of the calculation. The empty reactor (discussed above) is a much simpler case, as only the reactor walls give rise to a smaller effective microdischarge size.

It is clear that, in the case of a packed bed reactor, a direct comparison between the proposed simple relationship (of microdischarge volume over reactor volume) and the Monte Carlo calculations applied to a realistic reactor set-up is difficult, due to the definition of the microdischarge events, both in terms of their size and where they take place. However, the fact that the simple relationship predicts values close to the calculated result, especially for the empty reactor, is quite striking. Hence, we believe that the fraction of microdischarges to which the gas molecules are exposed, can be

properly approximated by the ratio of microdischarge volume over the reactor gas volume.

Such a relationship between the microdischarge volume, reactor gas volume and fraction of microdischarges experienced by the molecules can be understood by the following explanation. If the microdischarges can occur throughout the reactor with the same probability, we can consider that, on average, the microdischarges always take place in the same point of the reactor. This is true for any point in the reactor and thus also any point that will be crossed by a gas molecule.

Multiple microdischarges occurring at the same time would not increase the probability for gas molecules of being hit by a microdischarge. Indeed, when multiple microdischarges occur at the same time but at different places, it is clear that a molecule can only experience one of these microdischarges at most.

7.4. Experimentally observed microdischarge distributions

In the previous section, we calculated the fraction of microdischarges based on a Monte Carlo approach, assuming a uniform distribution of the microdischarges. Various authors have recorded DBD plasma in both empty reactors [65] and packed bed reactors [50], [61], [129], [130]. Wang et al. specifically reported their DBD plasma to become more uniform upon introducing a packing [112].

We made ICCD recording of a filamentary DBD plasma in an empty reactor. A transparent top electrode and dielectric allowed to record the microdischarges from above, as depicted in Figure 7.13. We show a standard photograph of the plasma (a), as well as the ICCD recording over a single frame (b) and multiple frames (c,d). We note that the microdischarge lifetime (in the order of 10 ns) is much smaller than the time window of a single frame (0.1 ms).

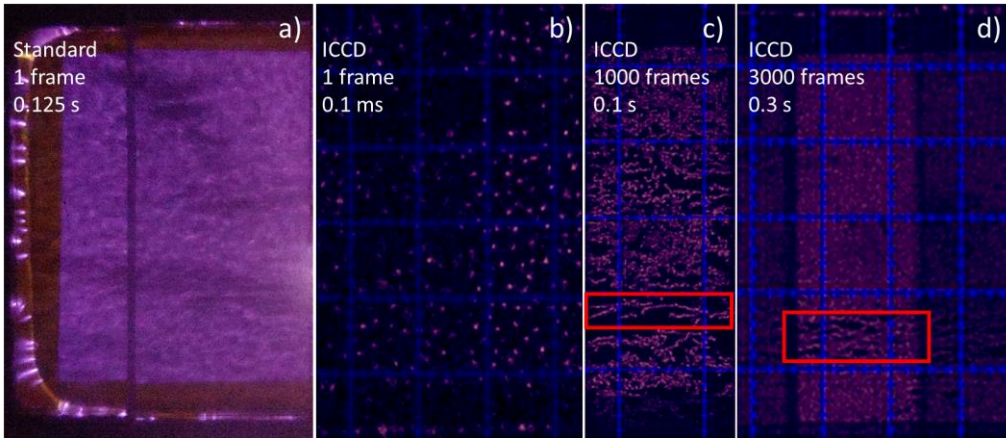


Figure 7.13. Photograph of a filamentary DBD plasma, driven at 12 kHz and 100 W (a), and ICCD recording of a single frame (0.1 ms, b) and multiple frames (i.e., 1,000 frames, 0.1 s (c) and 3,000 frames, 0.3 s (d)). The size of the grid is 10 x 10 mm².

From Figure 7.13 we can conclude that a uniform distribution of microdischarges is indeed an adequate assumption when considering typical time scales associated with the residence time (i.e., seconds). We note however that the exact behavior may depend on the discharge frequency, which will affect the randomness of the microdischarges due to the memory effect, leading to the self-organization of microdischarges as reported in literature [131], [132]. Those effects were also observed in our own experiments (not shown), but we note that such self-organized microdischarge distributions typically still cover the whole reactor volume, which means that this effect does not significantly impact the assumption behind our Monte Carlo calculations. Also the gas flow can influence the microdischarge location [132]. This can also be seen in Figures 7.13c and 7.13d, where microdischarges follow a path in the direction of the gas flow (from left to right) creating aligned dots instead of random dots (indicated in the red boxes). This effect was observed to be more pronounced at higher discharge frequencies, which is also attributed to the memory effect. The microdischarges moving with the gas flow, might be an effect that increases the total duration during which a gas molecule is exposed to the strong microdischarges. In general, we judge that our assumptions on the uniform distribution of microdischarges,

as used in the Monte Carlo calculations, is valid from 4 to 30 kHz, based on our experimental observations.

Finally, the operating pressure could influence the above observations and thus the assumptions behind the Monte Carlo calculations should be re-evaluated for such cases, i.e., low pressure conditions. However, low pressure plasmas are typically more homogeneous and thus do not exhibit the filamentary microdischarges of interest [133]. The memory effect is typically also a function of pressure due to the change in mean free path of the gas particles [134].

7.5. Experimental and calculated plasma-catalytic NH₃ yield

We now want to verify whether the concept of the fraction of microdischarges, as calculated in section 7.4, really has a physical meaning and whether the relationship (i.e., the fraction of microdischarges is the ratio of microdischarge volume over the reactor gas volume) provides a realistic value. Therefore, we applied this concept to plasma-catalytic NH₃ synthesis, using our previously developed plasma chemistry (see Chapter 4) and catalytic surface chemistry micro-kinetics models [109], by running them as a function of residence time, and comparing with plasma-catalytic NH₃ synthesis experiments in a packed bed DBD with Co catalyst on Al₂O₃ beads, at different residence times.

We now adopt an microdischarge volume of 0.088 mm³. The relevant reactor volume after packing was 6.4 cm³, which gives a fraction of microdischarges of 1.37×10⁻⁵. Again assuming 25 microdischarges per discharge half cycle and a discharge frequency of 23.5 kHz, following our experimental conditions, gives a microdischarge frequency of 1,175,000 s⁻¹ (i.e., $2N_{MD, \frac{1}{2} cycle} f_D$, cf. also Eq. 7.4) and 16 s⁻¹ after applying the above fraction of microdischarges (i.e., $\eta_{MD} 2N_{MD, \frac{1}{2} cycle} f_D$, cf. also Eq. 7.5). The simulation provides the NH₃ concentration as a function of time, for a total residence time of 3.84 s, which corresponds to 61 microdischarges that will be considered in the model, based

on the above fraction of microdischarges. The experiments were performed for different flow rates, ranging between 100 and 400 ml/min, thus yielding different residence times ranging from 1.0 to 3.8 s, which can directly be compared to the time dependence in the model.

In Figure 7.14, we compare the experimental results against the calculated results, obtained by performing a sensitivity analysis by varying the fraction of microdischarges over four orders of magnitude (between 10^{-6} and 10^{-2} , Figure 7.14a) and within the same order of magnitude (between 0.5×10^{-5} and 9.0×10^{-5} , Figure 7.14b).

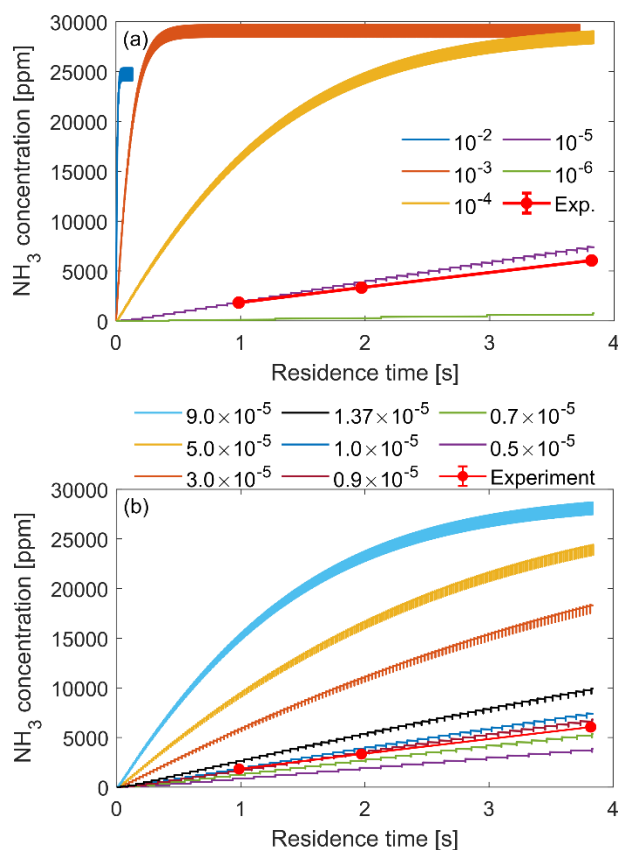


Figure 7.14. Calculated NH_3 concentration as a function of residence time, for different fractions of microdischarges, compared to experimentally obtained values (Exp.). The fraction of microdischarges is varied over four orders of magnitude in (a) and within the same order of magnitude in (b).

It is clear that a much larger or smaller fraction of microdischarges gives unrealistically fast and slow NH_3 synthesis rates (cf. Figure 7.14a). This confirms that the order of magnitude of the fraction of microdischarges, obtained in this study, appears realistic. Figure 7.14b shows that the results are quite sensitive to the assumption of the fraction of microdischarges, i.e., even a factor 2 makes a large difference. The experimental data agrees best with a fraction of microdischarges of 0.9×10^{-5} , which is slightly lower than the value of 1.37×10^{-5} , based on the assumed microdischarge volumes. However, we note that the chosen discharge volumes, the resulting power density and thus the plasma kinetics are subject to uncertainties. Nevertheless, the agreement is still very reasonable; the fraction of microdischarges yielding best agreement with the experiments is close to the value predicted by the empirical relationship (microdischarge volume over reactor gas volume) as discussed in section 7.4, and the value resulting from the combined particle tracing and Monte Carlo modelling approach. This indicates that our combined particle tracing and Monte Carlo simulations method can provide a realistic picture of the fraction of microdischarges experienced by the gas molecules.

In Figure 7.15 we plot the NH_3 concentration at the end of the reactor as a function of the fraction of microdischarges, with the latter both on a linear scale and logarithmic scale (inset, to cover a larger range). We can see that the NH_3 concentration increases with the fraction of microdischarges, but for a larger fraction of microdischarges (between 10^{-4} and 10^{-3}), it remains fairly constant, and for still larger fractions, it starts to drop (see inset in the figure). This is attributed to the interpulse time. When molecules experience more microdischarges (corresponding to a large fraction of microdischarges), the interpulse time is smaller (e.g., in the order of 100 ms and 100 μs for a fraction of microdischarges of 10^{-5} and 10^{-2} , respectively). In Chapter 6, we found that NH_3 is net produced in between the microdischarges and net destroyed during the microdischarges themselves. However, one so-called microdischarge and afterglow pair causes a net NH_3 gain, until a steady state is reached. Based on these considerations, we indeed expect that there is an optimal interpulse time, which we find between 1 and

10 ms (i.e., a microdischarge fraction between approximately 10^{-3} and 10^{-4} , respectively) based on Figure 7.15.

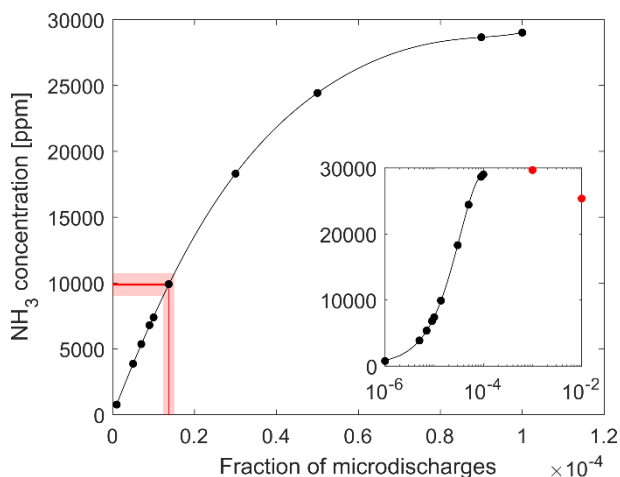


Figure 7.15. Calculated NH₃ concentration at the end of the reactor as a function of the fraction of microdischarges on both a linear scale and logarithmic scale (inset, with 2 extra data points (red dots)). A microdischarge fraction of 1.37×10^{-5} is indicated with a 1 % and 10 % spread (dark and light red areas, respectively).

The Monte Carlo calculations resulted in fractions of microdischarges with typical uncertainties, less than 1 %. However, we note that this is the average behavior and that the gas could also be described with a microdischarge fraction distribution, by evaluating the fraction of microdischarges for each particle trajectory individually. Assuming the average fraction of microdischarges of 1.37×10^{-5} and an uncertainty of 1 % gives an NH₃ concentration of 9880 ± 90 ppm (cf. Figure 7.15). A difference of 3, 5 or 10 %, which could be relevant when considering an actual microdischarge fraction distribution, would give a difference of 260, 430 and 870 ppm, respectively.

7.6. Generalization of the concept: Fraction of plasma power transferred to the gas molecules

The fraction of microdischarges experienced by the molecules can be considered as a plasma characteristic of a filamentary DBD. At the same time, however, this quantity directly represents the fact that not all power put into the plasma is equally transferred to each molecule [82]. In other words, gas molecules only see a fraction of the power put into the plasma. This is a direct consequence of the non-uniformity and stochastic behavior of the plasma. Gas molecules would only be able to experience all the plasma power if a plasma is perfectly uniform (i.e., constant plasma power density) in space and time, and if it occupies the entire reactor, such that all gas molecules passing through the reactor would effectively pass through the plasma region and experience the same plasma power. Either plasma non-uniformity or stochastic behavior of e.g., microdischarges will reduce the fraction of power transferred to the individual molecules, as these effects give rise to individual gas molecules being treated differently by the plasma.

As discussed above, the fraction of microdischarges can be generalized to the fraction of power transferred to each molecule, and this quantity can in principle be defined for any plasma and is related to both spatial and temporal plasma (non-)uniformity. It can be considered as a kind of “plasma reactor efficiency”. For instance, in a gliding arc (GA) plasma, only a limited fraction of the gas molecules actually passes through the active arc plasma, as the latter does not occupy the entire reactor volume, and this limits the “plasma reactor efficiency” [135]–[137]. The same was observed in an atmospheric pressure glow discharge (APGD) [138]. For a DBD, this fraction of power transferred would correspond to the fraction of microdischarges experienced by the molecules, giving rise to a very low “plasma reactor efficiency” (i.e., order of 0.001 %). However, this reasoning assumes that the entire applied plasma power is deposited in the microdischarges. In Chapter 6, we considered typical current-voltage characteristics of our packed bed DBD and found that a significant portion of the applied power still gives

rise to a uniform plasma power (related to surface discharges at the packing beads [61]). In other words, only part of the input power is transferred to the microdischarges. In that case, the “plasma reactor efficiency” can be even close to 50 %. This could explain the higher efficiency of a packed bed DBD (characterized by a combination of filamentary and surface microdischarges) compared to an empty DBD (characterized by only filamentary microdischarges), as often reported in plasma-catalytic experiments [139]–[143].

Finally, we note that a filamentary plasma, which, according to the above discussion, would have a lower “plasma reactor efficiency”, typically exhibits much stronger plasma conditions compared to uniform plasmas, which would correspond to higher “plasma reactor efficiencies”. This means that both types of plasmas are of interest in their own way, and warrant further investigation, due to completely different underlying mechanisms and chemical kinetics.

7.7. Conclusions

We performed particle tracing simulations through both an empty and packed bed DBD reactor, typically used for plasma catalysis. In the packed bed reactor, we placed approximately 13,000 hard sphere beads in the gap between two concentric cylinders. We discussed in detail the flow characteristics and residence time distribution of the gas molecules in both an empty and packed bed DBD. We showed that the addition of a packed bed creates viscous boundary layers that slow down the gas in the center of the packed bed where two packing bead layers are near to each other. Furthermore, we showed that nearly 90% of the gas is redistributed towards the wall of the reactor, where there is a relatively large distance between the reactor wall and the packing beads.

The calculated particle trajectories were used in a Monte Carlo calculation, mimicking a filamentary DBD, to determine the fraction of microdischarges experienced by a single gas molecule. The results provided evidence for an empirical expression of this fraction

of microdischarges, that is, the fraction of microdischarges is roughly equal to the microdischarge volume over the reactor gas volume.

To verify whether this proposed relationship (i.e., the fraction of microdischarges is the ratio of microdischarge volume over the reactor gas volume) provides a realistic value, we performed plasma and catalyst surface kinetics simulations for plasma-catalytic NH_3 synthesis, in which the fraction of microdischarges was used as input, and we compared the calculated NH_3 concentration as a function of time with experimental data. The experimental results could only be reproduced when the fraction of microdischarges was consistent with the definition based on microdischarge volume over reactor gas volume. The modelling results were highly sensitive to the assumed fraction of microdischarges, but a good agreement was obtained with the predicted value from the Monte Carlo simulations, which validates our concept of the fraction of microdischarges.

Finally, we can generalize the fraction of microdischarges, as it actually represents the fraction of plasma power transferred to the gas molecules. Indeed, not all power will be transferred to each molecule when the plasma is spatially and temporally non-uniform, and this principle is valid for other plasma types than DBDs as well, such as GA plasma or APGD. Based on these principles, we can define a “plasma reactor efficiency”, which in case of a DBD plasma can be directly related to the fraction of microdischarges.

Part IV.
Conclusion
&
Outlook

Chapter 8.

Overall conclusions

As modern society gains increasing awareness for the need of change towards a more sustainable future, science is tasked with finding more sustainable alternatives to energy-intensive and greenhouse gas emitting chemical processes. Specifically, one popular branch of technology to tackle the conversion of greenhouse gases and the synthesis of value-added chemicals is plasma technology.

Specifically, dielectric barrier discharge (DBD) plasmas receive a lot of scientific attention as a possible alternative for ammonia synthesis, which currently happens through the Haber-Bosch process – which is an industrial process with one of the largest environmental footprints.

DBDs for ammonia synthesis receive a lot of attention because a catalyst can easily be integrated in the plasma reactor. Furthermore, ammonia synthesis is an important case study for plasma-catalytic processes due to the relative simplicity of the reaction, which does not have many by-products.

While many studies have thus already been conducted on this subject, this thesis adds to the state-of-the-art through plasma kinetics zero-dimensional modelling of the plasma-catalytic ammonia synthesis in a DBD. This kind of models allows to focus on the plasma kinetics taking place. Various research questions were answered:

- *How can the differences between a packed bed DBD and an empty (non-packed) DBD be captured?*

While DBD plasmas have been studied greatly with zero-dimensional models, capturing a DBD plasma for a plasma-catalytic process was much less straightforward, due to the very distinct characteristics of an empty and packed bed DBD reactor.

A systematic approach has been developed to capture the characteristics of packed and unpacked DBD reactors as explained in Chapter 4. In this approach, the instantaneous power, fraction of microdischarges that are relevant to individual gas molecules and the discharge volume in which the plasma power is deposited was given special attention. Those specific considerations do in principle allow to describe the differences between a packed bed and empty reactor in the developed plasma kinetics model (see section 5.1.3).

- *What is the importance of vibrational excitation in packed bed DBDs in view of (experimental) reports in literature?*

The developed model was first used in Chapter 5 to investigate the role of vibrational excitation in DBDs. Due to the strong filamentary character of a DBD for gas conversion applications, vibrational excitation was always considered unimportant in literature, as such filamentary behavior is typically associated with a strong plasma, which is too energetic to efficiently populate vibrational levels. However, in literature sometimes high vibrational temperatures were reported in experimental studies.

Integral to the developed plasma kinetics model was the distribution of the dissipated power in the plasma to the filamentary microdischarges and a weaker uniform plasma throughout the whole reactor. Where in literature typically all plasma power was attributed to the microdischarges, we showed that considering a uniform plasma component could increase the contribution of vibrational excitation and result in significant vibrational temperatures.

- *What are the reaction mechanics of plasma-catalytic ammonia synthesis when considering the temporal plasma behavior?*

Various plasma conditions have been studied throughout this thesis. While a clear difference in reaction mechanics between those conditions was not easily observed, the overall observed reaction mechanisms still gave new insight. The description of filamentary DBD plasma in the developed zero-dimensional kinetics model allowed

capturing the temporal reaction mechanisms. In other words, not only the reactions that take place were elucidated in Chapter 6, but also explicitly the role of strong filamentary microdischarges and the role of weaker plasma (the afterglows of the microdischarges) in the reactor.

It was found that ammonia is readily destroyed during the strong microdischarges, but that the plasma species formed through dissociation, i.e. atoms and excited states, were able to recombine to ammonia in the weaker afterglows for a net ammonia gain.

In addition, while the surface kinetics were approximate, the model did indicate that elementary Eley-Rideal type reactions can be of importance in plasma catalysis. This stresses the need for more detailed plasma-catalytic surface kinetics studies that also focus on this type of reaction instead of only considering enhancement of conventional thermal catalysis pathways.

- *Can the concept of the fraction of microdischarges be substantiated?*

One of the key concepts introduced in the developed modelling approach is the fraction of microdischarges. This concept is very important in the determination of the plasma conditions that are effectively modelled, thus we investigated this property through computational and experimental methods in Chapter 7.

A combination of particle tracing and Monte Carlo type calculations allowed us to formally assess an empirical relationship for the fraction of microdischarges, which was sometimes used in literature. It was found that the fraction of microdischarges can be approximated as the ratio of microdischarge volume over the reactor (gas) volume, if the microdischarges are equally distributed over the whole plasma.

- *What are the implications of the (spatial and temporal) non-uniformity of a given plasma?*

Because we considered this concept in detail, we were also able to generalize this concept in Chapter 7. Dielectric barrier discharges are sometimes considered inefficient

because of its temporal and spatial non-uniformity. The fraction of microdischarges is a direct measure of this behavior and can directly be generalized to the efficiency with which the plasma power is deposited to the individual gas molecules. Moreover, it was argued that any plasma (reactor) that has some degree of non-uniformity (i.e. not filling the whole reactor or having some kind of periodicity) has such an associated efficiency. Those considerations can be of importance when considering the performance of a reactor, or when considering how to model the plasma.

Chapter 9.

Final thoughts and outlook

This thesis focused on plasma kinetics modelling of (dielectric barrier discharge) plasmas, specifically in a zero-dimensional or global modelling approach in which a (very) simplified form of the continuity equation is solved.

However, this simplicity is deceptive. The actual kinetics that occur in a plasma are of a complexity that, in a way, warrant this simplicity of the continuity equation. At the same time, this does mean that the kinetics itself should receive proper attention.

Kinetic data is often subject to large uncertainties and approximations, and while it is relatively straightforward to assess correct and expected behavior of a kinetics description under equilibrium conditions, the non-equilibrium conditions that can occur in plasma are more difficult, or nigh impossible, to benchmark. It is thus important, to be aware of the uncertainties in the kinetics data and its impact on the model outcome. This is especially true in application-driven modelling studies, where the model outcome is not only dictated by the kinetics data, but also in the approximations made to describe the specific plasma system (see Figure 3.2). There should thus be a clear order in kinetics plasma modelling, consisting of equilibrium benchmarks, followed by assessment of the non-equilibrium characteristics and finally application-driven modelling – especially if predictive models are the goal.

As acknowledged in the 2017 Plasma Roadmap on low temperature plasma science and technology [32], plasma research has become more and more application-driven. Effectively, this means that the building blocks – the kinetics data and its uncertainty – do not always receive the attention they deserve, such as the suggested assessment of the non-equilibrium characteristics. This can possibly also be attributed to the complexity of such analysis: The large number of reactions, and their possible

uncertainty, in a kinetics data set, correspond to a very large number of input parameters.

Still, a better distinction in plasma kinetics (zero-dimensional) modelling between 1) non-equilibrium benchmarks and assessments and 2) modelling of specific plasma systems/reactors, is considered an important step towards obtaining a better return from the latter studies (i.e. a quicker adoption of plasma chemistry applications).

Specifically, “plasma kinetics modelling” should focus on the kinetics data, their uncertainty and the partial chemical equilibrium that it reaches under (simple) non-equilibrium conditions of plasma. “Plasma kinetics reactor modelling” can then use this benchmarked data, in zero-dimensional or higher dimensional models, to describe specific plasma systems. The latter models would then typically introduce more complex species transport and/or more transient plasma conditions, which adds to the complexity of the modelling studies.

With those practices, the kinetics (and its uncertainties) itself will already be better understood and/or explained, which in turn provides more context behind application-driven models, increasing the impact of the latter, and enabling predictive studies of which the outcome can more easily be put into perspective. This will allow such modelling studies to steer further (experimental) research.

Appendix

Appendix A.

Kinetics¹²

A.1. Gas phase kinetics tables

Tables A.1 – A.4 list all rate coefficients of reactions between gas phase species in the model, except for the detailed interactions between the various vibrationally excited states. Those are described in Appendix A.2.

Table A.1. Electron impact collisions describing the plasma kinetics. The ground state, vibrational levels and electronically excited states are indicated with X, V and E, respectively. The temperatures are given in Kelvin unless otherwise noted. The units of the rate coefficients are in cm^3/s and cm^6/s for two-body and three-body reactions, respectively.

#	Reaction	Rate coefficient	Ref.
<u>Excitation and de-excitation</u>			
R1	$e^- + \text{H}_2(\text{X}, \text{V}) \leftrightarrow e^- + \text{H}_2(\text{E})$	$\sigma_{R1}(\mathcal{E})$	[144] ^{1,2,3}
R2	$e^- + \text{N}_2(\text{X}, \text{V}) \leftrightarrow e^- + \text{N}_2(\text{E})$	$\sigma_{R2}(\mathcal{E})$	[144] ^{1,2,3}
R3	$e^- + \text{N} \rightarrow e^- + \text{N}(\text{E})$	$\sigma_{R3}(\mathcal{E})$	[144] ¹
<u>Ionization</u>			
R4	$e^- + \text{N}_2(\text{X}, \text{V}, \text{E}) \rightarrow e^- + e^- + \text{N}_2^+$	$\sigma_{R4}(\mathcal{E})$	[145] ^{1,2}
R5	$e^- + \text{H}_2(\text{X}, \text{V}) \rightarrow e^- + e^- + \text{H}_2^+$	$\sigma_{R5}(\mathcal{E})$	[144] ^{1,2}
R6	$e^- + \text{N} \rightarrow e^- + e^- + \text{N}^+$	$\sigma_{R6}(\mathcal{E})$	[144] ¹
R7	$e^- + \text{H} \rightarrow e^- + e^- + \text{H}^+$	$\sigma_{R7}(\mathcal{E})$	[145] ¹
R8	$e^- + \text{NH} \rightarrow e^- + e^- + \text{NH}^+$	$\sigma_{R8}(\mathcal{E})$	[146] ¹
R9	$e^- + \text{NH}_2 \rightarrow e^- + e^- + \text{NH}_2^+$	$\sigma_{R9}(\mathcal{E})$	[146] ¹
R10	$e^- + \text{NH}_3 \rightarrow e^- + e^- + \text{NH}_3^+$	$\sigma_{R10}(\mathcal{E})$	[146] ¹
<u>Dissociative Ionization</u>			
R11	$e^- + \text{N}_2(\text{X}, \text{V}) \rightarrow e^- + e^- + \text{N}^+ + \text{N}$	$\sigma_{R11}(\mathcal{E})$	[147] ¹
R12	$e^- + \text{H}_2 \rightarrow e^- + e^- + \text{H} + \text{H}^+$	$\sigma_{R12}(\mathcal{E})$	[148] ¹
R13	$e^- + \text{NH} \rightarrow e^- + e^- + \text{H} + \text{N}^+$	$\sigma_{R13}(\mathcal{E})$	[146] ¹
R14	$e^- + \text{NH}_2 \rightarrow e^- + e^- + \text{H} + \text{NH}^+$	$\sigma_{R14}(\mathcal{E})$	[146] ¹
R15	$e^- + \text{NH}_3 \rightarrow e^- + e^- + \text{H} + \text{NH}_2^+$	$\sigma_{R15}(\mathcal{E})$	[146] ¹
<u>Dissociation</u>			
R16	$e^- + \text{H}_2 \rightarrow e^- + \text{H} + \text{H}$	$\sigma_{R16}(\mathcal{E})$	[148] ¹

¹² This appendix is based on K van 't Veer *et al* 2020 *Plasma Sources Sci. Technol.* **29** 045020 and K van 't Veer *et al* 2020 *J. Phys. Chem. C*, **124** 22871–22883.

R17	$e^- + N_2(X, V, E) \rightarrow e^- + N + N$	$\sigma_{R17}(\mathcal{E})$	[144]	^{1,2}
R18	$e^- + NH \rightarrow e^- + N + H$	$5.0 \times 10^{-8} T_e[\text{eV}]^{0.5} \exp(-8.6/T_e[\text{eV}])$	[102]	
R19	$e^- + NH_2 \rightarrow e^- + N + H_2$	$5.0 \times 10^{-8} T_e[\text{eV}]^{0.5} \exp(-7.6/T_e[\text{eV}])$	[102]	
R20	$e^- + NH_2 \rightarrow e^- + NH + H$	$5.0 \times 10^{-8} T_e[\text{eV}]^{0.5} \exp(-7.6/T_e[\text{eV}])$	[102]	
R21	$e^- + NH_3 \rightarrow e^- + NH_2 + H$	$5.0 \times 10^{-8} T_e[\text{eV}]^{0.5} \exp(-4.4/T_e[\text{eV}])$	[102]	
R22	$e^- + NH_3 \rightarrow e^- + NH + H_2$	$5.0 \times 10^{-8} T_e[\text{eV}]^{0.5} \exp(-5.5/T_e[\text{eV}])$	[102]	

(Dissociative) recombination

R23	$e^- + N_2^+ \rightarrow N + N$	$0.50 \times 1.8 \times 10^{-7} (300/T_e)^{0.39}$	[87]	
R24	$e^- + N_2^+ \rightarrow N + N(^2D^0)$	$0.45 \times 1.8 \times 10^{-7} (300/T_e)^{0.39}$	[87]	
R25	$e^- + N_2^+ \rightarrow N + N(^2P^0)$	$0.05 \times 1.8 \times 10^{-7} (300/T_e)^{0.39}$	[87]	
R26	$e^- + N_3^+ \rightarrow N_2 + N$	$2.0 \times 10^{-7} (300/T_e)^{0.5}$	[87]	
R27	$e^- + N_3^+ \rightarrow N_2(A^3) + N$	$6.91 \times 10^{-8} T_e[\text{eV}]^{-0.5}$	[149]	
R28	$e^- + N_3^+ \rightarrow N_2(B^3) + N$	$6.91 \times 10^{-8} T_e[\text{eV}]^{-0.5}$	[149]	
R29	$e^- + N_4^+ \rightarrow N_2 + N_2$	$2.3 \times 10^{-6} (300/T_e)^{0.53}$	[87]	
R30	$e^- + N_4^+ \rightarrow N_2 + N + N$	$3.13 \times 10^{-7} T_e[\text{eV}]^{-0.41}$	[149]	
R31	$e^- + H_2^+ \rightarrow H + H$	see footnote ⁴	[102]	⁴
R32	$e^- + H_3^+ \rightarrow H + H + H$	see footnote ⁵	[102]	⁵
R33	$e^- + H_3^+ \rightarrow H_2 + H$	see footnote ⁵	[102]	⁵
R34	$e^- + NH^+ \rightarrow N + H$	$4.30 \times 10^{-8} (0.026/T_e[\text{eV}])^{0.5}$	[102]	
R35	$e^- + NH_2^+ \rightarrow NH + H$	$1.02 \times 10^{-7} (0.026/T_e[\text{eV}])^{0.4}$	[102]	
R36	$e^- + NH_2^+ \rightarrow N + H + H$	$1.98 \times 10^{-7} (0.026/T_e[\text{eV}])^{0.4}$	[102]	
R37	$e^- + NH_3^+ \rightarrow NH + H + H$	$1.55 \times 10^{-7} (0.026/T_e[\text{eV}])^{0.5}$	[102]	
R38	$e^- + NH_3^+ \rightarrow NH_2 + H$	$1.55 \times 10^{-7} (0.026/T_e[\text{eV}])^{0.5}$	[102]	
R39	$e^- + NH_4^+ \rightarrow NH_3 + H$	$8.01 \times 10^{-7} (0.026/T_e[\text{eV}])^{0.605}$	[102]	
R40	$e^- + NH_4^+ \rightarrow NH_2 + H + H$	$1.23 \times 10^{-7} (0.026/T_e[\text{eV}])^{0.605}$	[102]	
R41	$e^- + N_2H^+ \rightarrow N_2 + H$	$7.1 \times 10^{-7} (0.026/T_e[\text{eV}])^{0.72}$	[102]	

Three-body recombination

R42	$e^- + N^+ + e^- \rightarrow N + e^-$	$7.0 \times 10^{-20} (300/T_e)^{4.5}$	[87]	
R43	$e^- + N^+ + M \rightarrow N + M$	$6.0 \times 10^{-27} (300/T_e)^{1.5}$	[150]	⁶
R44	$e^- + N_2^+ + e^- \rightarrow N_2 + e^-$	$1.0 \times 10^{-19} (T_e/300)^{-4.5}$	[150]	
R45	$e^- + N_2^+ + M \rightarrow N_2 + M$	$2.49 \times 10^{-29} T_e[\text{eV}]^{-1.5}$		¹² ⁶

Attachment

R46	$e^- + H_2(X, V) \rightarrow H + H^-$	$\sigma_{R46}(\mathcal{E})$	[101], [151]	^{1,7}
-----	---------------------------------------	-----------------------------	-----------------	----------------

¹ The rate coefficient is calculated from the electron impact cross section $\sigma(\mathcal{E})$ using BOLSIG+ [93]. The reference of the cross section is given.

² The cross section threshold energy is reduced when the reaction takes places from an excited state.

³ The rate coefficients for de-excitation processes are calculated using detailed balancing [93].

⁴ The rate coefficient is a fit as a function of the electron temperature, given by: $k = 7.51 \times 10^{-9} - 1.12 \times 10^{-9} T_e[\text{eV}]^1 + 1.03 \times 10^{-10} T_e[\text{eV}]^2 - 4.15 \times 10^{-12} T_e[\text{eV}]^3 + 5.86 \times 10^{-14} T_e[\text{eV}]^4$ [102].

⁵ The rate coefficient is a fit as a function of the electron temperature, given by: $k = 0.5 \times (8.39 \times 10^{-9} + 3.02 \times 10^{-9} T_e[\text{eV}]^1 - 3.80 \times 10^{-10} T_e[\text{eV}]^2 + 1.31 \times 10^{-11} T_e[\text{eV}]^3 + 2.42 \times 10^{-13} T_e[\text{eV}]^4 - 2.30 \times 10^{-14} T_e[\text{eV}]^5 + 3.55 \times 10^{-16} T_e[\text{eV}]^6)$ [102].

⁶The third body, M, is any neutral gas phase species.

⁷The cross section data is resolved for each individual vibrational state [101], [151].

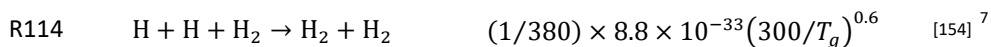
Table A.2. Neutral-neutral collisions describing the plasma kinetics. The ground state and vibrational levels are indicated with X and V, respectively. The temperatures are given in Kelvin. The units of the rate coefficients are in cm^3/s and cm^6/s for two-body and three-body reactions, respectively. The units of radiative decay processes are $1/\text{s}$.

#	Reaction	Rate coefficient	Ref.
<u>Neutral-neutral collisions</u>			
R47	$\text{N}_2(\text{X}, \text{V}) + \text{M} \rightarrow \text{N} + \text{N} + \text{M}$	$8.37 \times 10^{-4} (T_g/298)^{-3.50} \exp(-113710/T_g)$	[152] ^{1,2}
R48	$\text{N}(^2\text{D}^0) + \text{M} \rightarrow \text{N} + \text{M}$	2.4×10^{-14}	[153] ²
R49	$\text{N}(^2\text{P}^0) + \text{N} \rightarrow \text{N}(^2\text{D}^0) + \text{N}$	1.8×10^{-12}	[87]
R50	$\text{N}(^2\text{P}^0) + \text{N}_2 \rightarrow \text{N} + \text{N}_2$	2.0×10^{-18}	[87]
R51	$\text{N}_2(\text{a}^1) + \text{N} \rightarrow \text{N}_2 + \text{N}$	2.0×10^{-11}	[153]
R52	$\text{N}_2(\text{a}^1) + \text{N}_2 \rightarrow \text{N}_2 + \text{N}_2$	3.7×10^{-16}	[153]
R53	$\text{N}_2(\text{a}^1) + \text{N}_2 \rightarrow \text{N}_2(\text{B}^3) + \text{N}_2$	1.9×10^{-13}	[87]
R54	$\text{N}_2(\text{A}^3) + \text{N} \rightarrow \text{N}_2 + \text{N}(^2\text{P}^0)$	$4.0 \times 10^{-11} (300/T_g)^{0.667}$	[87]
R55	$\text{N}_2(\text{A}^3) + \text{N} \rightarrow \text{N}_2 + \text{N}$	2.0×10^{-12}	[87]
R56	$\text{N}_2(\text{A}^3) + \text{N}_2 \rightarrow \text{N}_2 + \text{N}_2$	3.0×10^{-16}	[87]
R57	$\text{N}_2(\text{A}^3) + \text{N}_2(\text{A}^3) \rightarrow \text{N}_2 + \text{N}_2(\text{A}^3)$	2.0×10^{-12}	[153]
R58	$\text{N}_2(\text{A}^3) + \text{N}_2(\text{A}^3) \rightarrow \text{N}_2 + \text{N}_2(\text{B}^3)$	3.0×10^{-10}	[87]
R59	$\text{N}_2(\text{A}^3) + \text{N}_2(\text{A}^3) \rightarrow \text{N}_2 + \text{N}_2(\text{C}^3)$	1.5×10^{-10}	[87]
R60	$\text{N}_2(\text{B}^3) + \text{N}_2 \rightarrow \text{N}_2 + \text{N}_2$	2.0×10^{-12}	[87]
R61	$\text{N}_2(\text{B}^3) + \text{N}_2 \rightarrow \text{N}_2(\text{A}^3) + \text{N}_2$	3.0×10^{-11}	[87]
R62	$\text{N}_2(\text{C}^3) + \text{N}_2 \rightarrow \text{N}_2(\text{a}^1) + \text{N}_2$	1.0×10^{-11}	[87]
R63	$\text{N} + \text{NH} \rightarrow \text{H} + \text{N}_2$	5×10^{-11}	[154]
R64	$\text{H} + \text{NH} \rightarrow \text{N} + \text{H}_2$	$5.4 \times 10^{-11} \exp(-165/T_g)$	[154]
R65	$\text{NH} + \text{NH} \rightarrow \text{H}_2 + \text{N}_2$	$5 \times 10^{-14} (T_g/300)$	[154] ³
R66	$\text{NH} + \text{NH} \rightarrow \text{N} + \text{NH}_2$	$1.7 \times 10^{-12} (T_g/300)^{1.5}$	[154] ³
R67	$\text{NH} + \text{NH} \rightarrow \text{N}_2 + \text{H} + \text{H}$	8.5×10^{-11}	[154] ³
R68	$\text{H} + \text{NH}_2 \rightarrow \text{H}_2 + \text{NH}$	$6.6 \times 10^{-11} \exp(-1840/T_g)$	[154]
R69	$\text{N} + \text{NH}_2 \rightarrow \text{N}_2 + \text{H} + \text{H}$	1.2×10^{-10}	[154]
R70	$\text{N} + \text{NH}_2 \rightarrow \text{N}_2 + \text{H}_2$	1.2×10^{-10}	[154]
R71	$\text{NH} + \text{NH}_2 \rightarrow \text{NH}_3 + \text{N}$	1.66×10^{-12}	[154] ⁴
R72	$\text{H}_2(\text{V}) + \text{N} \rightarrow \text{NH} + \text{H}$	$4.0 \times 10^{-10} (T_g/300)^{0.5} \exp(-16600/T_g)$	[154] ⁵
R73	$\text{H}_2 + \text{NH}_2 \rightarrow \text{NH}_3 + \text{H}$	$5.4 \times 10^{-11} \exp(-6492/T_g)$	[154]
R74	$\text{H} + \text{NH}_3 \rightarrow \text{NH}_2 + \text{H}_2$	$8.4 \times 10^{-14} (T_g/300)^{4.1} \exp(-4760/T_g)$	[154]
R75	$\text{N}_2(\text{A}^3) + \text{H} \rightarrow \text{N}_2 + \text{H}$	5×10^{-11}	[154]

R76	$N_2(A^3) + H_2 \rightarrow N_2 + H + H$	$2 \times 10^{-10} \exp(-3500/T_g)$	[154]
R77	$N_2(A^3) + NH_3 \rightarrow N_2 + NH_3$	1.6×10^{-10}	[154]
R78	$N_2(B^3) + H_2 \rightarrow N_2(A^3) + H_2$	2.5×10^{-11}	[154]
R79	$N_2(a^1) + H \rightarrow N_2 + H$	1.5×10^{-11}	[154]
R80	$N_2(a'^1) + H_2 \rightarrow N_2 + H + H$	2.6×10^{-11}	[154]
R81	$N + H_2(E) \rightarrow H + NH$	$4.0 \times 10^{-10} (T_g/300)^{0.5}$	[154]
R82	$N(^2D^0) + H_2 \rightarrow H + NH$	2.3×10^{-12}	[154]
R83	$N(^2D^0) + NH_3 \rightarrow NH + NH_2$	1.1×10^{-10}	[154]
R84	$N(^2P^0) + H_2 \rightarrow H + NH$	2.5×10^{-14}	[154]
R85	$N + NH \rightarrow H + N + N$	$4.02 \times 10^{-10} (T_g/298)^{-0.20} \exp(-27303/T_g)$	[155]
R86	$H_2 + NH \rightarrow H + NH_2$	$3.50 \times 10^{-11} \exp(-7758/T_g)$	[155]
R87	$N_2 + H \rightarrow NH + N$	$5.27 \times 10^{-10} (T_g/298)^{-0.50} \exp(-74453/T_g)$	[155]
R88	$NH_2 + N \rightarrow NH + NH$	$2.99 \times 10^{-13} \exp(-7600/T_g)$	[156]
R89	$NH_2 + NH_2 \rightarrow NH_3 + NH$	$5.07 \times 10^{-15} (T_g/298)^{-3.53} \exp(-278/T_g)$	[157]
R90	$NH_3 + NH \rightarrow NH_2 + NH_2$	$2.33 \times 10^{-14} (T_g/298)^{-3.41} \exp(-7350/T_g)$	[157]
R91	$H_2 + H \rightarrow H + H + H$	$2.54 \times 10^{-8} (T_g/298)^{-0.10} \exp(-52561/T_g)$	[158]
R92	$H_2 + N_2 \rightarrow H + H + N_2$	$2.61 \times 10^{-8} (T_g/298)^{-1.40} \exp(-52561/T_g)$	[158]
R93	$H_2 + H_2 \rightarrow H + H + H_2$	$2.61 \times 10^{-8} (T_g/298)^{-0.70} \exp(-52561/T_g)$	[158]
R94	$NH + M \rightarrow H + N + M$	$2.99 \times 10^{-10} \exp(-37647/T_g)$	[159]
R95	$NH_2 + M \rightarrow H + NH + M$	$1.99 \times 10^{-9} \exp(-38248/T_g)$	[159]
R96	$NH_3 + M \rightarrow H + NH_2 + M$	$4.17 \times 10^{-8} \exp(-47149/T_g)$	[160] ⁶
R97	$NH_3 + M \rightarrow H_2 + NH + M$	$1.05 \times 10^{-9} \exp(-47029/T_g)$	[160] ⁶

Three-body collisions

R98	$N + N + M \rightarrow N_2 + M$	$1.38 \times 10^{-33} \exp(502.978/T_g)$	[161] ²
R99	$N + N + N \rightarrow N_2(A^3) + N$	1.0×10^{-32}	[87]
R100	$N + N + N \rightarrow N_2(B^3) + N$	1.4×10^{-32}	[87]
R101	$N + N + N_2 \rightarrow N_2(A^3) + N_2$	1.7×10^{-33}	[87]
R102	$N + N + N_2 \rightarrow N_2(B^3) + N_2$	2.4×10^{-33}	[87]
R103	$N + N + H_2 \rightarrow N_2 + H_2$	$(1/380) \times 8.3 \times 10^{-34} \exp(500/T_g)$	[154] ⁷
R104	$H + H + N_2 \rightarrow H_2 + N_2$	$(1/380) \times 8.3 \times 10^{-33} (300/T_g)$	[154] ⁷
R105	$H + N + M \rightarrow NH + M$	$(1/380) \times 1.0 \times 10^{-33}$	[154] ^{7,8}
R106	$N + H_2 + M \rightarrow NH_2 + M$	$(1/380) \times 1.0 \times 10^{-34}$	[154] ^{7,8}
R107	$H + NH + M \rightarrow NH_2 + M$	$(1/380) \times 1.0 \times 10^{-32}$	[154] ^{7,8}
R108	$H + NH_2 + M \rightarrow NH_3 + M$	$(1/380) \times 5.5 \times 10^{-30}$	[154] ^{7,8}
R109	$NH + H_2 + M \rightarrow NH_3 + M$	$(1/380) \times 2.5 \times 10^{-35} (T_g/300) \exp(1700/T_g)$	[154] ^{7,8}
R110	$N + N + H_2 \rightarrow N_2(A^3) + H_2$	$(1/380) \times 1.7 \times 10^{-33}$	[154] ⁷
R111	$N + N + H \rightarrow N_2(A^3) + H$	$(1/380) \times 1.0 \times 10^{-32}$	[154] ⁷
R112	$N + N + H_2 \rightarrow N_2(B^3) + H_2$	$(1/380) \times 2.4 \times 10^{-33}$	[154] ⁷
R113	$N + N + H \rightarrow N_2(B^3) + H$	$(1/380) \times 1.4 \times 10^{-32}$	[154] ⁷



Ionization processes



Radiative decay



¹The rate coefficient is scaled according to the Fridmann-Macheret alpha-model [162] with $\alpha = 1$ [152].

²The third body, M, is any neutral gas phase species.

³R65, R66 and R67, are adopted from [154], however the product channel R65 can be considered very unlikely, as also reflected by the rate coefficients.

⁴A more likely reaction channel is $\text{NH} + \text{NH}_2 \rightarrow \text{N}_2\text{H}_2 + \text{H}$, however the N_2H_2 species is not described in our model.

⁵The reaction only occurs for the vibrational levels [154]. The reported rate coefficient is scaled according to the Fridmann-Macheret alpha-model [162] with $\alpha = 0.3$ [154].

⁶The adopted rate coefficients of R96 and R97 are related by $k_{R96}/k_{R97} \approx 40$, following the recommendations of Hanson et al [160].

⁷The rate coefficients of the three-body collisions are multiplied by (1/380) to account for the reaction taking place at atmospheric pressure [77], as opposed to low pressure [154].

⁸The third body, M, is $\text{N}_2(\text{X})$, $\text{N}_2(\text{V})$, $\text{H}_2(\text{X})$ or $\text{H}_2(\text{V})$.

Table A.3. Ion-neutral collisions describing the plasma kinetics. The ground state and vibrational levels are indicated with X and V, respectively. The effective ion temperature T_{ion} [87] is given in Kelvin.

#	Reaction	Rate coefficient	Ref.
<u>Ion-neutral collisions</u>			
R124	$N^+ + H_2 \rightarrow NH^+ + H$	5.0×10^{-10}	[163]
R125	$N^+ + NH_3 \rightarrow NH_2^+ + NH$	$0.20 \times 2.35 \times 10^{-9}$	[163]
R126	$N^+ + NH_3 \rightarrow NH_3^+ + N$	$0.71 \times 2.35 \times 10^{-9}$	[163]
R127	$N^+ + NH_3 \rightarrow N_2H^+ + H_2$	$0.09 \times 2.35 \times 10^{-9}$	[163]
R128	$N_2^+ + N \rightarrow N^+ + N_2$	$7.2 \times 10^{-13}(T_{ion}/300)$	[87]
R129	$N_2^+ + H_2 \rightarrow N_2H^+ + H$	2.00×10^{-9}	[102]
R130	$N_2^+ + N_2(A^3) \rightarrow N_3^+ + N$	3.0×10^{-10}	[164]
R131	$N_2^+ + NH_3 \rightarrow NH_3^+ + N_2$	1.95×10^{-9}	[102]
R132	$N_3^+ + N \rightarrow N_2^+ + N_2$	6.6×10^{-11}	[87]
R133	$N_4^+ + N \rightarrow N^+ + N_2 + N_2$	1.0×10^{-11}	[87]
R134	$N_4^+ + N_2 \rightarrow N_2^+ + N_2 + N_2$	$2.1 \times 10^{-16} \exp(T_{ion}/121)$	[87]
R135	$H^+ + NH_3 \rightarrow NH_3^+ + H$	5.20×10^{-9}	[163]
R136	$H_2^+ + H \rightarrow H^+ + H_2$	6.4×10^{-10}	[102]
R137	$H_2^+ + H_2 \rightarrow H_3^+ + H$	2.0×10^{-9}	[102]
R138	$H_2^+ + N_2 \rightarrow N_2H^+ + H$	2.00×10^{-9}	[163]
R139	$H_2^+ + NH_3 \rightarrow NH_3^+ + H_2$	5.70×10^{-9}	[163]
R140	$NH^+ + H_2 \rightarrow H_3^+ + N$	$0.15 \times 1.23 \times 10^{-9}$	[163]
R141	$NH^+ + H_2 \rightarrow NH_2^+ + H$	$0.85 \times 1.23 \times 10^{-9}$	[163]
R142	$NH^+ + NH_3 \rightarrow NH_3^+ + NH$	$0.75 \times 2.40 \times 10^{-9}$	[163]
R143	$NH^+ + NH_3 \rightarrow NH_4^+ + N$	$0.25 \times 2.40 \times 10^{-9}$	[163]
R144	$NH^+ + N_2 \rightarrow N_2H^+ + N$	6.50×10^{-10}	[163]
R145	$NH_2^+ + H_2 \rightarrow NH_3^+ + H$	1.95×10^{-10}	[163]
R146	$NH_2^+ + NH_3 \rightarrow NH_3^+ + NH_2$	$0.5 \times 2.30 \times 10^{-9}$	[163]
R147	$NH_2^+ + NH_3 \rightarrow NH_4^+ + NH$	$0.5 \times 2.30 \times 10^{-9}$	[163]
R148	$NH_3^+ + NH_3 \rightarrow NH_4^+ + NH_2$	2.10×10^{-9}	[163]
R149	$N_2H^+ + NH_3 \rightarrow NH_4^+ + N_2$	2.3×10^{-9}	[163]
<u>Ion-neutral three-body collisions</u>			
R150	$N_2^+ + N + N_2 \rightarrow N_3^+ + N_2$	$9.0 \times 10^{-30} \exp(400/T_{ion})$	[87]
R151	$N^+ + N_2 + N_2(X, V) \rightarrow N_3^+ + N_2$	$1.7 \times 10^{-29}(300/T_{ion})^{2.1}$	[87]
R152	$N_2^+ + N_2 + N_2(X, V) \rightarrow N_4^+ + N_2$	$5.2 \times 10^{-29}(300/T_{ion})^{2.2}$	[87]
R153	$N^+ + N + N_2 \rightarrow N_2^+ + N_2$	1.0×10^{-29}	[87]

Table A.4. Negative-positive ion recombination reactions describing the plasma kinetics. The ground state and vibrational levels are indicated with X and V, respectively. The temperatures are given in Kelvin.

#	Reaction	Rate coefficient	
<u>H⁻ recombination</u>			
R154	H ⁻ + H ₂ ⁺ → H + H + H	$2.0 \times 10^{-7}(300/T_g)$	[154]
R155	H ⁻ + H ₃ ⁺ → H ₂ + H + H	$2.0 \times 10^{-7}(300/T_g)$	[154]
R156	H ⁻ + N ₂ ⁺ → N ₂ + H	$2.0 \times 10^{-7}(300/T_g)$	[154]
R157	H ⁻ + N ₄ ⁺ → N ₂ + N ₂ + H	$2.0 \times 10^{-7}(300/T_g)$	[154]
R158	H ⁻ + N ₂ H ⁺ → H ₂ + N ₂	$2.0 \times 10^{-7}(300/T_g)$	[154]
<u>H⁻ three-body recombination</u>			
R159	H ⁻ + H ₂ ⁺ + M → H ₂ + H + N ₂	$(1/380) \times 2 \times 10^{-25}(300/T_g)^{2.5}$	[154] ^{1,2}
R160	H ⁻ + H ₃ ⁺ + M → H ₂ + H ₂ + M	$(1/380) \times 2 \times 10^{-25}(300/T_g)^{2.5}$	[154] ^{1,2}
R161	H ⁻ + N ₂ ⁺ + M → N ₂ + H + M	$(1/380) \times 2 \times 10^{-25}(300/T_g)^{2.5}$	[154] ^{1,2}
R162	H ⁻ + N ₄ ⁺ + M → N ₂ + N ₂ + H + M	$(1/380) \times 2 \times 10^{-25}(300/T_g)^{2.5}$	[154] ^{1,2}
R163	H ⁻ + N ₂ H ⁺ + M → H ₂ + N ₂ + M	$(1/380) \times 2 \times 10^{-25}(300/T_g)^{2.5}$	[154] ^{1,2}

¹The rate coefficients of the three-body collisions are multiplied by (1/380) to account for the reaction taking place at atmospheric pressure [77], as opposed to low pressure [154].

²The third body, M, is N₂(X), N₂(V), H₂(X) or H₂(V).

A.2. Gas phase: Vibrational kinetics

Tables A.1 – A.4 indicated some reactions (R1, R2, R4, R5, R11, R17, R46, R72, R151, R152) which are also considered for the vibrational levels. For reactions R1, R2, R4, R5 and R17, the corresponding cross section threshold energy is scaled according to the vibrational energy, while R11 assumes the same cross section. Reaction R46, i.e. dissociative attachment of H₂, uses a vibrationally resolved cross section set [151], [165]. The ground state rate coefficient expressions are used for the vibrational states in reactions R151 and R152. The ground state rate coefficient is also used for any reaction in which a vibrational level is the third body. Furthermore, Table A.2 includes H₂(V) + N → NH + H (R72), which only occurs for the vibrational levels [154]. The reported rate coefficient, in Table A.2, is scaled according to the Fridmann-Macheret alpha-model [162] with $\alpha = 0.3$ [154]. The same principle is applied to R47 (Table 7) with $\alpha = 1$ [152].

The remaining processes involving the vibrational levels are listed in Table A.5, with the detailed rate coefficient expressions, given in the respective references.

We included excitation and de-excitation of both $N_2(V)$ and $H_2(V)$ through the vibrationally resolved resonant vibrational excitation cross sections from the Phys4Entry database [101], [103], [104], see R164 and R165.

Similarly, for $H_2(V)$ we included the vibrationally resolved dissociative attachment, as already indicated in Table A.1 (R46) [151], [165].

Finally, we included various vibrational-translational (VT) and vibrational-vibrational (VV) relaxation processes. For the actual calculations or rate coefficient expressions we refer to the respective publications. N_2 -N VT relaxation (R166) is included using the rate coefficient calculated by Esposito et al. [88] which includes all the individual single and multi-quantum jumps.

The N_2 - N_2 VT relaxation (R167) and the N_2 - N_2 VV relaxation (R174) are adopted from the work of Adamovich et al. [89]. They are fitted, as a function of temperature, to an appropriate rate coefficient expression.

The H_2 - H_2 VT relaxation (R168) and the H_2 - H_2 VV relaxation (175) are implemented using the SSH (Schwartz, Slawsky and Herzfeld) theory [87], [166]. The SSH theory rates are also fitted to an appropriate temperature-dependent expression.

The SSH theory is also used for H_2 -H VT relaxation, adopted from Gordiets et al. [154]. Only the individual one-quantum transitions are included (R169). Multi-quantum processes use a rate coefficient that represents the effective sum of all the transitions (R170) [154].

The relaxations between nitrogen and hydrogen are also adopted from Gordiets et al., using the SSH theory. N_2 - H_2 VT (R171), N_2 -H VT (R171 and R172, with similar treatment of one- and multi-quantum jumps to H_2 -H VT relaxation, i.e. processes R169 and R170) and H_2 - N_2 VV relaxation (R176), are included.

H₂-N₂ VT relaxation is insignificant compared to the other processes, while two-quantum N₂-H₂ VV relaxations (R177) are included [154].

Table A.5. Vibrational processes describing the plasma kinetics. The calculations of the rate coefficients can be found in the listed references.

#	Reaction	
<u>Excitation and de-excitation</u>		
R164	$e + N_2(v) \leftrightarrow N_2(v' > v) + e$	[101]
R165	$e + H_2(v) \leftrightarrow H_2(v' > v) + e$	[103], [104]
<u>Vibrational-translational relaxation</u>		
R166	$N_2(v) + N \leftrightarrow N_2(v' < v) + N$	[88]
R167	$N_2(v) + N_2 \leftrightarrow N_2(v - 1) + N_2$	[89]
R168	$H_2(v) + H_2 \leftrightarrow H_2(v - 1) + H_2$	[87]
R169	$H_2(v) + H \leftrightarrow H_2(v - 1) + H$	[154] ¹
R170	$H_2(v) + H \leftrightarrow H_2 + H$	[154] ¹
R171	$N_2(v) + H_2 \leftrightarrow N_2(v - 1) + H_2$	[154]
R172	$N_2(v) + H \leftrightarrow N_2(v - 1) + H$	[154] ¹
R173	$N_2(v) + H \leftrightarrow N_2 + H$	[154] ¹
<u>Vibrational-vibrational relaxation</u>		
R174	$N_2(v + 1) + N_2(w) \leftrightarrow N_2(v) + N_2(w + 1)$	[89]
R175	$H_2(v + 1) + H_2(w) \leftrightarrow H_2(v) + H_2(w + 1)$	[87]
R176	$H_2(v) + N_2(w - 1) \leftrightarrow H_2(v - 1) + N_2(w)$	[154]
R177	$N_2(v) + H_2(w - 1) \leftrightarrow N_2(v - 2) + H_2(w)$	[154]

¹ Only the single quantum processes are included separately (R169 and R172), the multi-quantum processes are included by an effective sum (R170 and R173).

A.3. Surface kinetics

We adopted the surface kinetics module from Hong et al. [77] and Shah et al. [80] and we adopted their sticking probability values for metal surfaces. The rate coefficients are calculated using Chantry's formula [102], [167].

Table A.6 lists the reactions included in the surface model, together with the relevant parameters to calculate their rate coefficients. Wall relaxation (wall), direct adsorption (ads), Eley-Rideal (ER), Langmuir-Hinshelwood (LH) and dissociative adsorption (dads) processes are taken into account.

Table A.61. Surface reactions included in the plasma kinetics model. The ground state, vibrational levels and electronically excited states are indicated with X, V and E, respectively. The sticking coefficients, γ , diffusion energy barrier, E_d , and the activation energy, E_a , are given. The rate coefficients are given in Eq. A.1 – A.5.

#	Reaction		
<u>Wall relaxation</u>			
R178	$N_2(A^3) \rightarrow N_2$	$\gamma = 1 \times 10^{-3}$	[154]
R179	$N_2(A^1) \rightarrow N_2(B^3)$	$\gamma = 1 \times 10^{-3}$	[154]
R180	$H_2(E) \rightarrow H_2$	$\gamma = 1 \times 10^{-3}$	[154]
R181	$N_2(V) \rightarrow N_2(V-1)$	$\gamma = 4.5 \times 10^{-4}$	[154]
R182	$H_2(V) \rightarrow H_2(V-1)$	$\gamma = 1 \times 10^{-4}$	[154]
<u>Direct adsorption</u>			
R183	$N(X, E) + \text{Surface} \rightarrow N(s)$	$\gamma = 1$	[102]
R184	$H + \text{Surface} \rightarrow H(s)$	$\gamma = 1$	[102]
R185	$NH + \text{Surface} \rightarrow NH(s)$	$\gamma = 1$	[102]
R186	$NH_2 + \text{Surface} \rightarrow NH_2(s)$	$\gamma = 1$	[102]
<u>Eley-Rideal</u>			
R187	$N(X, E) + N(s) \rightarrow N_2$	$\gamma = 6 \times 10^{-3}$	[102]
R188	$H + H(s) \rightarrow H_2$	$\gamma = 1.5 \times 10^{-3}$	[102]
R189	$N(X, E) + H(s) \rightarrow NH(s)$	$\gamma = 1 \times 10^{-2}$	[102]
R190	$NH + H(s) \rightarrow NH_2(s)$	$\gamma = 1 \times 10^{-2}$	[102]
R191	$H + N(s) \rightarrow NH(s)$	$\gamma = 8 \times 10^{-3}$	[102]
R192	$H + NH(s) \rightarrow NH_2(s)$	$\gamma = 8 \times 10^{-3}$	[102]
<u>Eley-Rideal: NH₃ formation</u>			
R193	$NH_2 + H(s) \rightarrow NH_3$	$\gamma = 1 \times 10^{-2}$	[102]
R194	$H + NH_2(s) \rightarrow NH_3$	$\gamma = 8 \times 10^{-3}$	[102]
R195	$H_2(X, V) + NH(s) \rightarrow NH_3$	$\gamma = 8 \times 10^{-4}$	[102]
<u>Langmuir-Hinshelwood</u>			
R196	$N(s) + H(s) \rightarrow NH(s)$	$E_a = 1.099 \text{ eV}, E_d = 0.2 \text{ eV}$	[77]
R197	$NH(s) + H(s) \rightarrow NH_2(s)$	$E_a = 0.3 \text{ eV}, E_d = 0.2 \text{ eV}$	[102]
R198	$NH_2(s) + H(s) \rightarrow NH_3$	$E_a = 0.2 \text{ eV}, E_d = 0.2 \text{ eV}$	[102]
<u>Dissociative adsorption</u>			

R199	$N_2(X, V) + \text{Surface}$	$\rightarrow N(s) + N(s)$	See Eq. A.6 – A.8	[106], [107]
R200	$N_2(E) + \text{Surface}$	$\rightarrow N(s) + N(s)$	$\gamma = 1 \times 10^{-1}$	[77]
R201	$H_2(X) + \text{Surface}$	$\rightarrow H(s) + H(s)$	$\gamma = 1 \times 10^{-3}$	[77]
R202	$H_2(v = 1) + \text{Surface}$	$\rightarrow H(s) + H(s)$	$\gamma = 1 \times 10^{-2}$	[77]
R203	$H_2(v = 2) + \text{Surface}$	$\rightarrow H(s) + H(s)$	$\gamma = 5 \times 10^{-2}$	[77]
R204	$H_2(v \geq 3) + \text{Surface}$	$\rightarrow H(s) + H(s)$	$\gamma = 1 \times 10^{-1}$	[77]
R205	$H_2(E) + \text{Surface}$	$\rightarrow H(s) + H(s)$	$\gamma = 1$	[77]

The rate coefficients are calculated with Eq. A.1 – A.5, for the various processes. In those equations, γ is the sticking probability, $\bar{v} = \sqrt{8k_B T / \pi m}$ is the average velocity of the gas phase species in the reaction, (V/A) is the volume to surface area ratio of the reactor, Λ is the diffusion length, D is the diffusion coefficient, $\nu \approx 10^{-13} \text{ s}^{-1}$ is the surface diffusional jump frequency [168], E_d is the diffusion energy barrier and E_a is the activation energy. We assume the wall temperature T_{wall} equal to the gas temperature T_g and k_B is the Boltzmann constant. The total surface site density S_T in cm^{-2} is used to convert the rate coefficients from s^{-1} to cm^2s^{-1} or to cm^4s^{-1} where appropriate. Subsequently, this rate is multiplied by (V/A) to convert the rate coefficients to cm^3s^{-1} and cm^6s^{-1} , respectively – as already included in the equations. The volume to surface area ratio of the reactor (V/A) and the total surface site density (S_T) are adopted from [80].

$$k_{wall} = \left[\frac{\Lambda^2}{D} + \left(\frac{V}{A} \right) \frac{2(2 - \gamma_{wall})}{\bar{v}\gamma_{wall}} \right]^{-1} \quad (\text{A.1})$$

$$k_{ads} = \left[\frac{\Lambda^2}{D} + \left(\frac{V}{A} \right) \frac{2(2 - \gamma_{ads})}{\bar{v}\gamma_{ads}} \right]^{-1} \times S_T^{-1} \times \left(\frac{V}{A} \right) \quad (\text{A.2})$$

$$k_{ER} = \left[\frac{\Lambda^2}{D} + \left(\frac{V}{A} \right) \frac{2(2 - \gamma_{ER})}{\bar{v}\gamma_{ER}} \right]^{-1} \times S_T^{-1} \times \left(\frac{V}{A} \right) \quad (\text{A.3})$$

$$k_{LH} = \frac{\nu}{4} \exp\left(-\frac{E_a + E_d}{k_B T_{wall}}\right) \times S_T^{-1} \times \left(\frac{V}{A} \right) \quad (\text{A.4})$$

$$k_{dad} = \left[\frac{\Lambda^2}{D} + \left(\frac{V}{A} \right) \frac{2(2 - \gamma_{dad})}{\bar{v}\gamma_{dad}} \right]^{-1} \times S_T^{-2} \times \left(\frac{V}{A} \right)^2 \quad (\text{A.5})$$

The diffusion length is given by $\Lambda = R/2.405$, with R the radius of the reactor. For a packed bed reactor we assume a reduced diffusion length $\Lambda = 0.2 \times R/2.405$ [80].

The diffusion coefficients for N, H, N₂, H₂, NH and NH₂ in both N₂ and H₂, were calculated from collision integrals [169]. The collision integrals used are the same as adopted by Murphy in [170]. In addition, the NH₂-NH₂ interaction was calculated in a similar fashion as the NH-NH interaction, as described in [170] – using the force constants of NH and H instead of N and H. For any missing interaction, a combination rule was assumed [171]. The actual diffusion coefficient for the actual mixing ratio of N₂ and H₂ is calculated using Blanc's law [172].

The sticking coefficients (γ) for the wall relaxation of the vibrationally excited molecules were adopted from Gordiets et al. [154]. The authors assumed $\gamma = 4.5 \times 10^{-4}$ for N₂(V) (Reaction R181) based on Black et al., who performed a detailed study on the deactivation coefficient of N₂(V=1) upon collisions with various surfaces, including stainless steel [173]. The value of $\gamma = 1 \times 10^{-4}$ for H₂(V) (R182) is based on Heidner et al., who considered multiple de-excitation channels in flow tube experiments [174]. The relaxation of N₂(E) (specifically metastable N₂, R178 and R179) was estimated by Gordiets et al. upon comparison between their predictions and experiments [154]. Relaxation of H₂(E) (R180) is assumed equal, following Hong et al [77].

Direct adsorption sticking coefficients (R183-R186) are adopted from Carrasco et al. who selected $\gamma = 1$ as a generally high value representing transition metals [102].

The Eley-Rideal (ER) sticking probability of $\gamma = 1.5 \times 10^{-3}$ between H and H(s) (R188) was adopted from Carrasco et al. who used the value yielding best agreement in their earlier experimental study, in which the apparatus had stainless steel walls [102], [175]. The value of $\gamma = 6 \times 10^{-3}$ for N₂ (R187) was estimated by Carrasco et al. [102]. The

remaining sticking probabilities of ER type reactions (R189-R195) were adopted from the same study, where the values were chosen based on agreement with experimental data, due to a lack of reported values. Specifically, the ER reaction with H₂ as the gas phase reactant (R195) was chosen as significantly lower (order of magnitude 10⁻⁴ compared to 10⁻² ... 10⁻³). Note that Hong et al. reported three unique sets of sticking probabilities for three types of surfaces (aluminium oxide, nanodiamond coated alumina and metal) [77].

The diffusion energy barrier of 0.2 eV for Langmuir-Hinshelwood (LH) type reactions (R196-R198) is adopted from Carrasco et al. who assumed this value based on the typical characteristics of chemisorbed H atoms on Fe [77], [102], [176]. The activation barrier for NH₂(s) formation (R197) was taken as 0.3 eV based on detailed surface kinetics studies [108], [177], while for the production of NH₃, a barrier of 0.2 eV was adopted [102]. For the elementary LH step between N(s) and H(s) (R196), an activation energy of 1.099 eV is used, after Hong et al. [77], [108]. They used the H atom diffusion barrier because the N atom diffusion barrier was reported as significantly higher (0.9 eV compared to 0.2 eV) [77].

The sticking coefficients for N₂ dissociative adsorption (R199) are resolved for the vibrational levels based on the studies by Hansen et al. Their calculations generally represent metallic surfaces [106], [107]. The sticking probability is given by $\gamma_{dads} = \bar{\gamma}_{dads, N_2}(V)$, which is the average sticking probability, with $V = 0 \dots 10$ ($V = 0$ corresponds to X, i.e. the ground state in process R199 [Table 11]). We calculated this average value with

$$\bar{\gamma}_{dads}(V) = \frac{\int P(E_z) \times \gamma_{dads}(E_z, V) dE_z}{\int P(E_z) dE_z} \quad (\text{A.6})$$

where E_z is the kinetic energy of a species hitting the surface, perpendicular to the surface itself and $P(E_z)$ is the probability distribution function, proportional to those species hitting the surface, given by [106], [107]

$$P(E_z) = \frac{1}{\sqrt{2\pi M k_B T_g}} \times \sqrt{\frac{E_z}{k_B T_g}} \times \exp\left(-\frac{E_z}{k_B T_g}\right) \quad (\text{A.7})$$

where M is the mass of N_2 . The sticking probability, $\gamma_{dads}(E_z, V)$, as a function of the kinetic energy and vibrational level of the incoming species, is given by [106], [107]

$$\log_{10}[\gamma_{dads}(E_z, V)] = a_V + b_V \times [1 - \exp(-c_V E_z)] + [1 - \exp(-d_V E_z)] \quad (\text{A.8})$$

where a_V , b_V , c_V and d_V are fit parameters, given in Table 1 of [106]. We assume the parameters of $V = 10$ for all vibrational levels higher than 10.

The sticking probabilities of the dissociative adsorption of electronically excited N_2 and all H_2 molecules (R200-R205) were adopted from Hong et al., following their assumptions [77]. We assumed their $\text{H}_2(v = 3)$ sticking probability also for any higher level (R204).

From the above, it is clear that the surface kinetics are subject to many assumptions and thus also to uncertainties. That includes the exact surface described. We summarize the above as a metal surface, most representative of iron, merely for reference and context. The exact surface characteristics, such as a distinction between step or surface sites, are not captured. This would require a more detailed model, such as micro-kinetics models [57], [109], [110]. This type of model uses surface reaction rates derived from density functional theory calculations and generally solves those reaction rates in steady state conditions and does not include a full gas phase chemistry. To our knowledge, such micro-kinetics models have not yet been combined with a full time-dependent plasma kinetics model. The present study, albeit with a less accurate surface description, focusses mainly on giving novel insight in the temporal discharge behavior (i.e. the role of the microdischarges and their afterglows). This study thus allows to better demarcate future studies, considering the increased number of degrees of freedom in a combined model (i.e. surface kinetics + plasma kinetics, introducing the exact surface, described by the surface binding energy) [109].

Appendix B.

Plasma current, gas voltage and instantaneous power¹³

Experimental charge-voltage characteristics, i.e. Lissajous figures, were measured¹⁴, to (1) calculate the actual plasma current and gas voltage from the measured current and applied voltage, and (2) determine the partial discharging [98]. The Lissajous figures of the N₂/H₂ plasma are given in Figure B.1(a). In addition, in Figure B.1(b), the Lissajous Figure for a measurement in pure argon is plotted, for which it is assumed that the plasma reactor is fully discharging [62]. With those figures, we can determine the dissipated plasma power, P_{diss} , and the partial discharging factor, β , using the following equations [98].

$$P_{diss} = W f_D \quad (\text{B.1})$$

$$W = 2U_b \Delta Q_D \quad (\text{B.2})$$

$$\Delta Q_D = \frac{Q_0}{1 - C_{cell}/C_{diel}} \quad (\text{B.3})$$

$$U_b = \left(1 + \frac{\alpha C_{cell}}{\beta C_{diel}}\right) \Delta U \quad (\text{B.4})$$

$$\alpha + \beta = 1 \quad (\text{B.5})$$

$$\alpha = \frac{C_{diel} - \zeta_{diel}}{C_{diel} - C_{cell}} \quad (\text{B.6})$$

where W is the work done by the plasma, f_D is the discharge frequency, U_b is the burning voltage, ΔQ_D is the charge transferred by the discharge, Q_0 is the measured charge transferred, ΔU is the measured burning voltage, C_{diel} is the capacitance of the

¹³ This appendix is based on K van 't Veer *et al* 2020 *J. Phys. Chem. C*, 124 **42** 22871–22883.

¹⁴ The experiments were performed by Yury Gorbanov (University of Antwerp).

dielectric, C_{cell} is the capacitance of the reactor and ζ_{diel} is the effective dielectric capacitance.

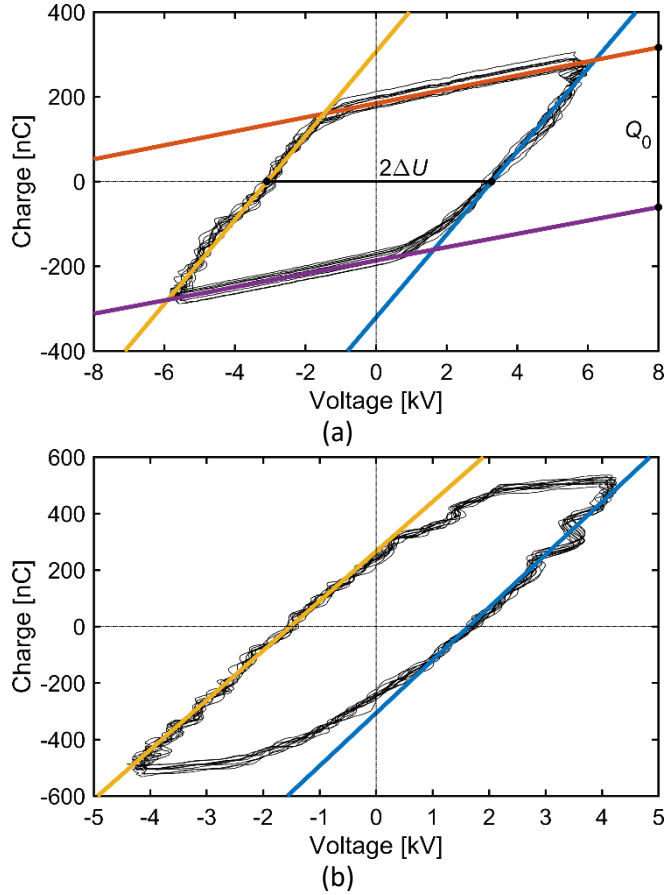


Figure B.1. Lissajous Figure measured in our packed bed dielectric barrier discharge for a 1:3 N₂:H₂ gas mixture (a) and operated with argon only (b). From those measurements, $\Delta U = 3066.7$ V and $Q_0 = 385.72$ nC are determined (a). The capacitances $\zeta_{diel} = 88.87$ pF and $C_{cell} = 16.468$ pF are determined from the two steepest and the two slighter slopes in (a), respectively. In addition $C_{diel} = 181.28$ pF is determined according to the plotted slopes in (b).

The plasma current i_{plasma} and gas voltage U_{gas} are given in Figure B.2, calculated with [98]:

$$i_{plasma}(t) = \frac{1}{1 - C_{cell}/C_{diel}} \left[\frac{dQ(t)}{dt} - C_{cell} \frac{dV(t)}{dt} \right] \quad (B.7)$$

$$U_{gas}(t) = \left(1 + \frac{\alpha C_{cell}}{\beta C_{diel}} \right) V(t) - \frac{1}{\beta C_{diel}} Q(t) \quad (B.8)$$

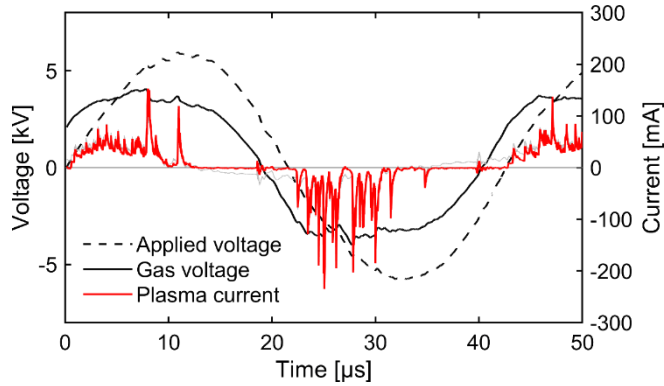


Figure B.2. Plasma current and gas voltage, as well as the actual applied voltage, in our packed bed dielectric barrier discharge for a 1:3 $N_2:H_2$ gas mixture. The discharge frequency is 23.5 kHz.

The plasma current and gas voltage are used to calculate the instantaneous plasma power, which is shown in Figure B.3. Based on this Figure (black line), we define the average life-time of the microdischarges as 200 ns (100 ns at FWHM), and we assume 25 microdischarge per discharge half cycle.

Figure B.3 represents all the microdischarges (red line) over a time of 50 μs . In our model we consider an interpulse time of 76.8 ms, because the gas molecules do not feel all the microdischarges when they travel through the reactor (see section 4.2.2).

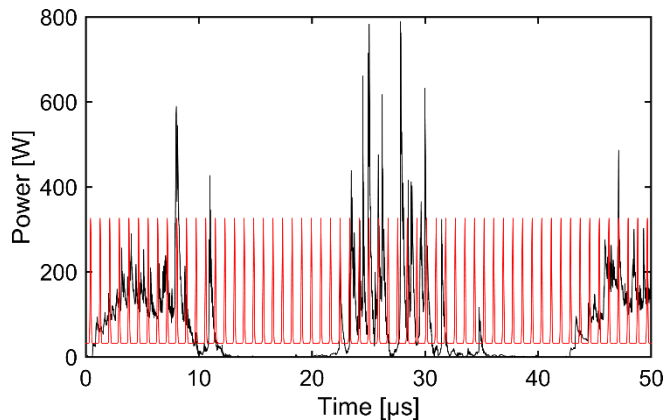


Figure B.3. Instantaneous plasma power measured in our PB DBD for a 1:3 $N_2:H_2$ gas mixture, as well as the model representation of the instantaneous plasma power (red line). We chose $\gamma = 0.1$, such that the average P_{max} is in reasonable agreement with the experimental measurement. Lower γ values would result in very high P_{max} , i.e. 540 W for $\gamma = 0.01$.

Appendix C.

Supplementary Information of Chapter 6

C.1. Surface Coverages and Gas Phase Concentrations in the microdischarge

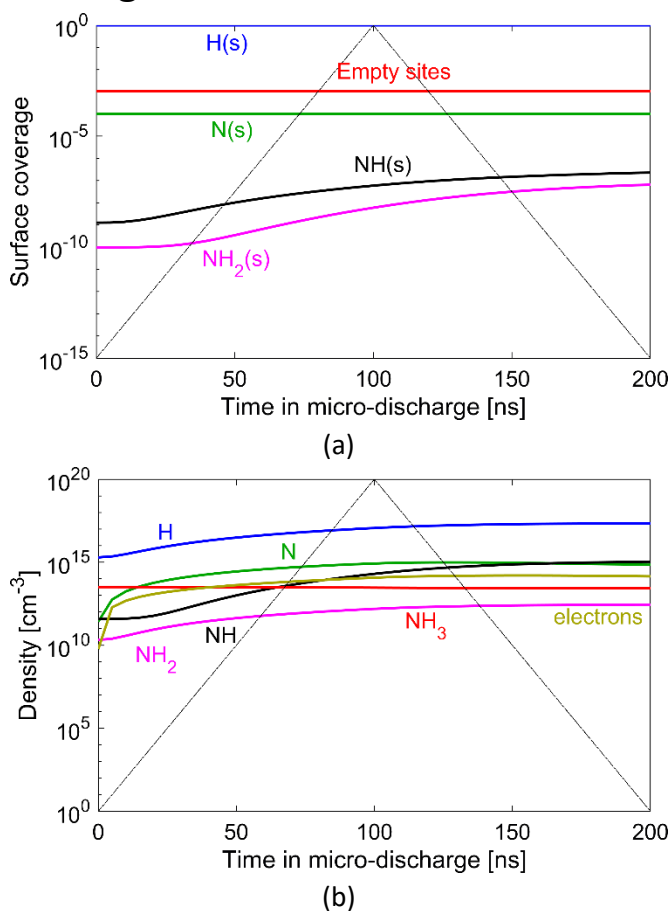


Figure C.1. Surface coverages and fraction of empty surface sites (a), and concentrations of the neutral gas phase species and electrons (b), as a function of time in the first microdischarge. This Figure corresponds to Figure 6.1 in Chapter 6.

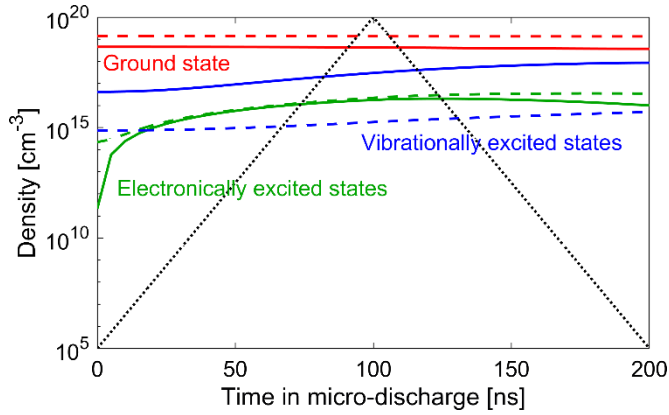


Figure C.2. Number densities of the N₂ (solid lines) and H₂ (dashed lines) molecules in the ground state and the sum of the electronically and vibrationally excited states, as a function of time in the first microdischarge. This Figure corresponds to Figure 6.2 in Chapter 6.

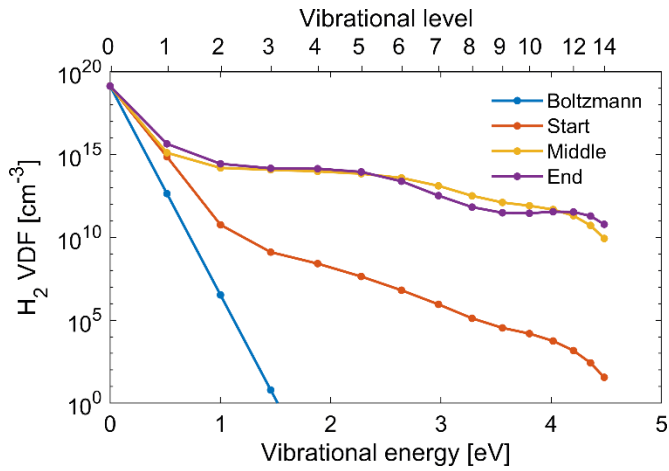


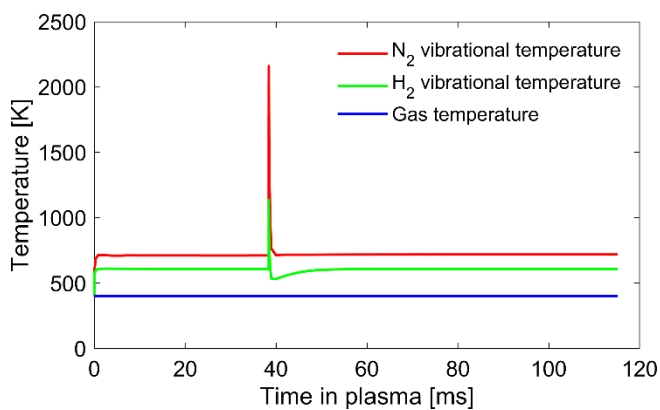
Figure C.3. H₂ vibrational distribution function (VDF) at various moments in the microdischarge, as well as the Boltzmann distribution at the gas temperature (400 K).

Table C.1. Typical species densities in cm⁻³ of the various surface-adsorbed species and plasma radicals in both the microdischarge and afterglow. The equivalent coverages are given between brackets.

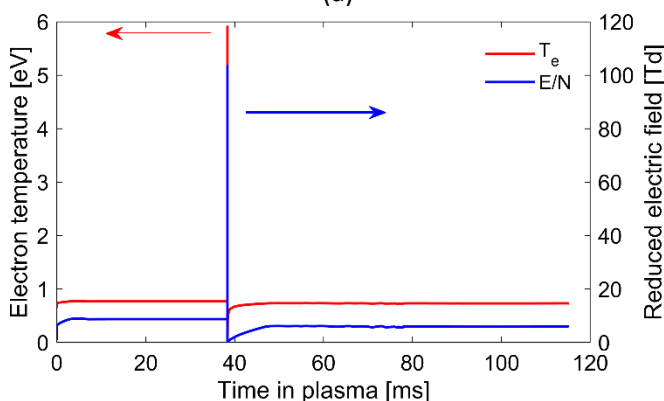
Species	Microdischarge (at maximum power density)	Afterglow (end)
NH ₂ (s)	8.6 × 10 ⁸ (6.0 × 10 ⁻⁹)	6.1 × 10 ⁶ (4.3 × 10 ⁻¹¹)
NH(s)	8.5 × 10 ⁹ (5.9 × 10 ⁻⁸)	3.0 × 10 ⁷ (2.1 × 10 ⁻¹⁰)
H(s)	1.4 × 10 ¹⁷ (1.0)	1.4 × 10 ¹⁷ (1.0)
N(s)	1.5 × 10 ¹³ (1.0 × 10 ⁻⁴)	2.4 × 10 ¹³ (1.7 × 10 ⁻⁴)
Surface	1.5 × 10 ¹⁴ (1.1 × 10 ⁻³)	1.4 × 10 ¹⁴ (9.9 × 10 ⁻⁴)
NH ₃	2.9 × 10 ¹³	6.9 × 10 ¹⁴
NH ₂	1.6 × 10 ¹²	1.9 × 10 ¹²
NH	2.0 × 10 ¹⁴	1.5 × 10 ¹¹
H	1.2 × 10 ¹⁷	1.0 × 10 ¹⁴
N	8.4 × 10 ¹⁴	8.1 × 10 ¹⁰
H ₂	1.4 × 10 ¹⁹	1.4 × 10 ¹⁹
N ₂	4.3 × 10 ¹⁸	4.6 × 10 ¹⁸
e ⁻	1.2 × 10 ¹⁴	1.2 × 10 ¹⁰

C.2. Calculated Plasma Parameters

The N₂ vibrational temperature (Figure C.4(a)) is calculated to be slightly above 2100 K during the microdischarges, and it relaxes back to above the gas temperature (700 K compared to 400 K) over approximately 1 ms. The H₂ vibrational temperature behaves similarly but reaches lower values, i.e. 600 K and 1100 K in the afterglow and microdischarge, respectively. Figure C.4(b) illustrates the calculated reduced electric field (E/N) and electron temperature (T_e), as a function of time. The maximum E/N was calculated to be 105 Td in each microdischarge (and the maximum electron temperature was 5.9 eV. After the microdischarges, both values significantly drop to virtually zero, but then rise again, and reach constant values in the entire afterglows, around E/N = 6 Td and T_e = 0.7 eV.



(a)



(b)

Figure C.4. N_2 and H_2 vibrational temperature (a) and reduced electric field and electron temperature (b) as a function of time in the plasma, from the start of the plasma to the end of the first microdischarge and afterglow pair. The maximum values of the reduced electric field and electron temperature are 105 Td and 5.9 eV, respectively. The microdischarge with a 200 ns duration takes place at 38.4 ms.

C.3. NH_3 Formation: Detailed Analysis of the Reaction Rates and Determination of the Rate-Limiting Step

Figure C.5(a) depicts the actual reaction rates of the main NH_3 (and precursor) formation reactions as a function of time from the start of the plasma until the end of the first afterglow. The main NH_3 formation reaction is the elementary LH step of $\text{NH}_2(\text{s})$ with $\text{H}(\text{s})$; blue curve. Similarly, $\text{NH}_2(\text{s})$ is mainly formed from the LH reaction of $\text{NH}(\text{s})$ with $\text{H}(\text{s})$; red curve. $\text{NH}(\text{s})$, however, is formed from elementary ER steps, either by gas phase N with $\text{H}(\text{s})$, or by gas phase H with $\text{N}(\text{s})$; black curve in Figure C.5(a). This process is predominant in the microdischarges (cf. Figure C.5(b)). In addition, we also plot the

formation rate of $\text{NH}_2(\text{s})$ from gas phase NH and $\text{H}(\text{s})$ (ER mechanism; green curve), as it is also important in the microdischarges (cf. Figure C.5(b)). Similarly, the ER formation of NH_3 by NH_2 and $\text{H}(\text{s})$ is also plotted (dark yellow curve), becoming important in the late afterglow.

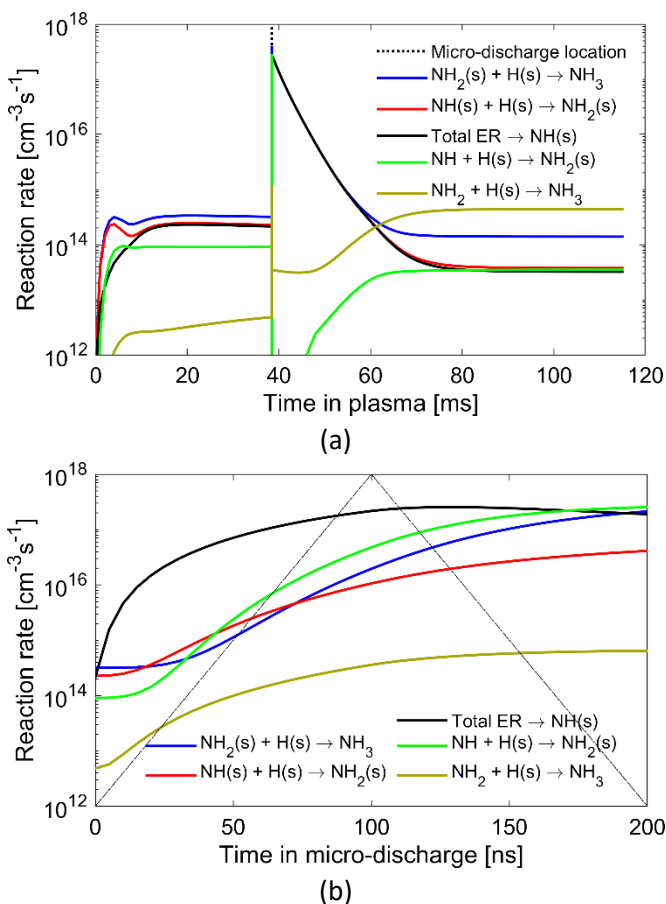


Figure C.5. Main reaction rates for the formation of NH_3 , $\text{NH}_2(\text{s})$ and $\text{NH}(\text{s})$ as a function of time in the plasma, from the start of the plasma to the end of the first microdischarge and afterglow pair (a), and as a function of time in the first microdischarge (b). “Total ER $\rightarrow \text{NH}(\text{s})$ ” stands for the sum of both reactions $\text{N} + \text{H}(\text{s})$ and $\text{H} + \text{N}(\text{s})$ reactions. In (a) the blue, red and black curve mostly overlap with each other. In (a), the microdischarge with a 200 ns duration takes place at 38.4 ms.

Directly after the microdischarge, we see in Figure C.5(a) a complete overlap between the reactions forming NH_3 , $\text{NH}_2(\text{s})$ and $\text{NH}(\text{s})$ (blue, red and black curves). This means that the intermediate products, $\text{NH}(\text{s})$ and $\text{NH}_2(\text{s})$, are immediately converted towards

NH₃. During the microdischarges, there is no overlap between the various reaction rates, and the earlier products are generally formed at a higher rate (black and green curves are higher than blue curve). Note that in addition to the reactions in Figure c.5(b), NH₃ is net destroyed during the microdischarges due to electron impact dissociation (cf. Figure 6.2 in Chapter 6). Towards the end of the afterglow, the NH₃ formation is faster than the NH₂(s) formation, and the latter is slightly faster than NH(s) formation, meaning that both NH₂(s) and NH(s) are slightly being depleted in the afterglow, as discussed in section 6.4 in Chapter 6.

To find the rate-limiting step, we further investigate the formation of NH(s) in Figure C.6, where we plot the rates of the individual ER reaction steps as a function of time, again from the start of the plasma until the end of the first afterglow (Figure C.6(a)) and in the microdischarge (Figure C.6(b)). The ER reaction of N with H(s) is generally faster, especially in the microdischarges, and generally determines the total NH(s) formation, except before the first microdischarge, where the ER reaction of H with N(s) seems more important. This is attributed to the relatively high dissociation of H₂ at the very beginning (see Figure C.9 below).

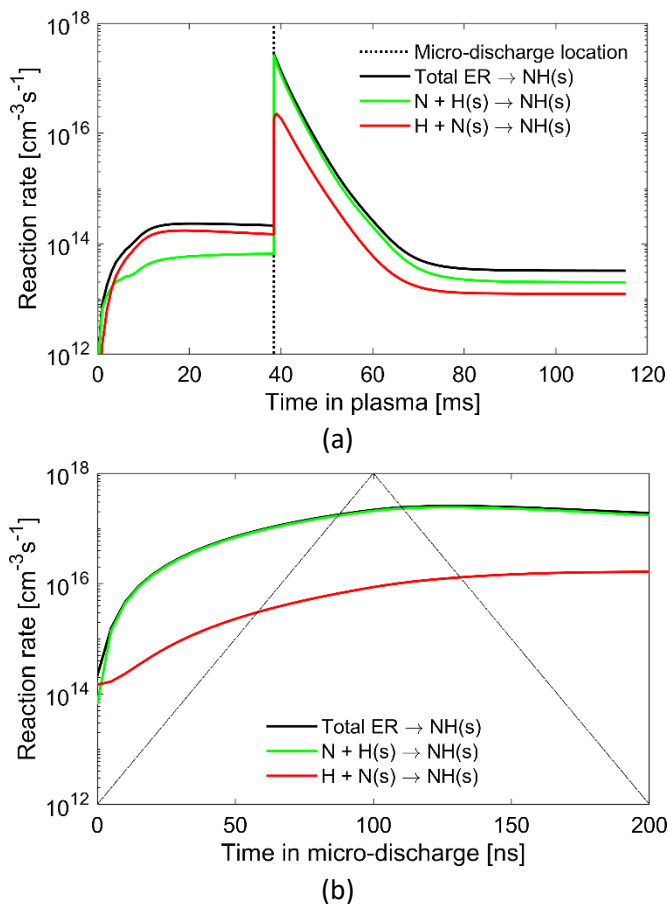


Figure C.6. Reaction rates for the formation of NH(s) as a function of time in the plasma, from the start of the plasma to the end of the first microdischarge and afterglow pair (a), and as a function of time in the first microdischarge (b). In (a), the microdischarge with a 200 ns duration takes place at 38.4 ms.

Based on Figures C.5 and C.6, we can identify the elementary ER reaction step between N and H(s) as the limiting reaction in NH_3 formation, i.e. N_2 dissociation in the plasma and H_2 or H (dissociative) adsorption are required for this. Similarly, the alternative ER reaction requires N(s). In Figure C.7, we show that the rate of this reaction overlaps with the direct adsorption of N, shortly after the microdischarge. Thus, N atoms are required in both NH(s) formation pathways.

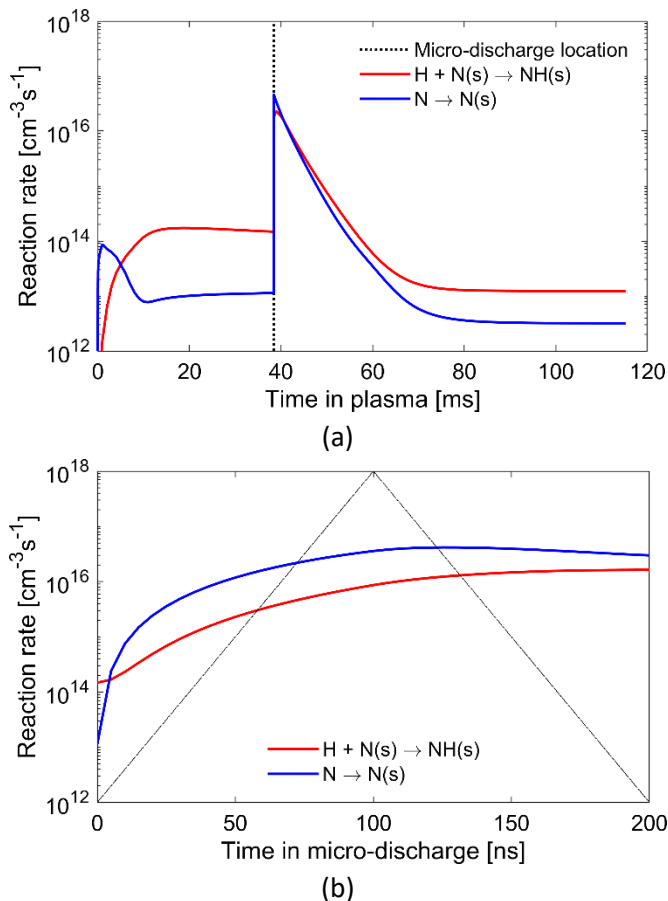


Figure C.7. Reaction rates for the formation and consumption of N(s) as a function of time in the plasma, from the start of the plasma to the end of the first microdischarge and afterglow pair (a), and as a function of time in the first microdischarge (b). In (a), the microdischarge with a 200 ns duration takes place at 38.4 ms.

Unlike N(s) , which is only significantly formed by direct adsorption and only reacts further to the desired products (NH(s)), the formation and consumption of H(s) is more complex. In the afterglow, we found that the net H(s) formation rate, attributed to direct adsorption (red curve in Figure C.8) overlaps in the afterglow with the total H(s) consumption rate to the desired products (blue curve). The contributions of individual processes to the net H(s) formation is given in Figure C.9

During the microdischarges (Figure C.8(b) and C.9(b)), more H(s) is destroyed than formed. Indeed, this is due to the importance of $\text{H} + \text{H(s)} \rightarrow \text{H}_2$. The dissociative

adsorption ($H_2 \rightarrow 2 H(s)$) has the lowest reaction rate once a microdischarge occurred and the net formation of H_2 is then always higher, this means that the net $H(s)$ formation is not determined by the dissociative adsorption anymore. However, the $H(s)$ coverage is never significantly influenced after the initial coverage, due to the predominant dissociative adsorption before the first microdischarge, and it is always nearly 1 (cf. Figure 6.1(a) in Chapter 6 and Figure C.1(a)).

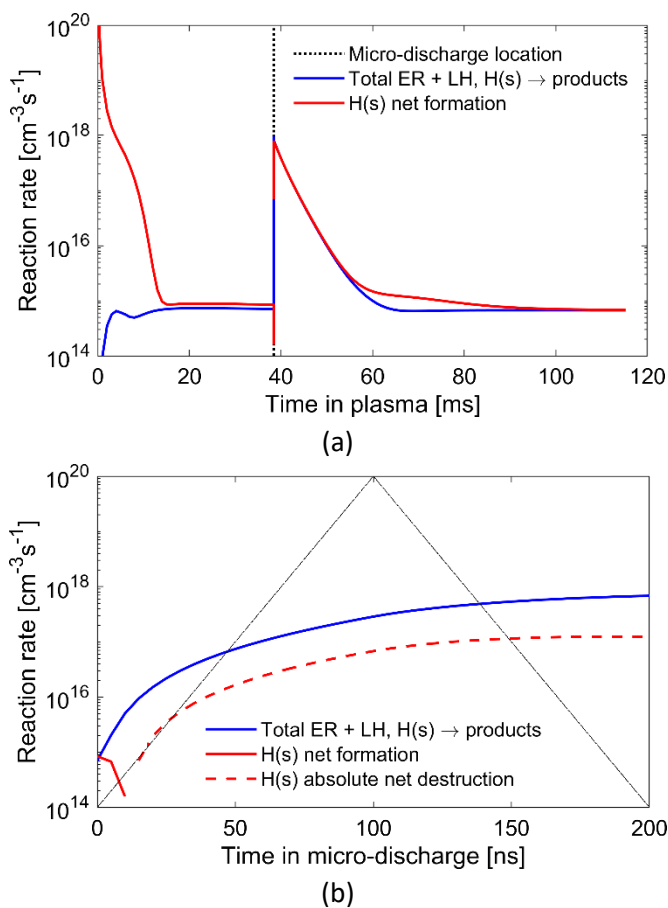


Figure C.8. Total and net reaction rates for the formation and consumption of $H(s)$ as a function of time in the plasma, from the start of the plasma to the end of the first microdischarge and afterglow pair (a), and as a function of time in the first microdischarge (b). In (a), the microdischarge with a 200 ns duration takes place at 38.4 ms.

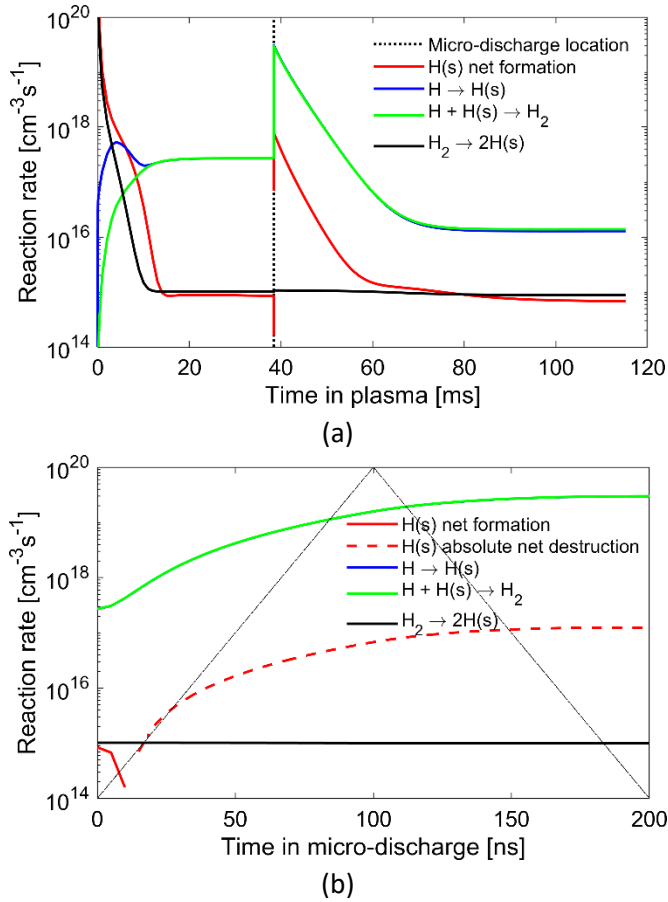


Figure C.9. Net formation of H(s) and the individual reactions that determine the net formation as a function of time in the plasma, from the start of the plasma to the end of the first microdischarge and afterglow pair (a), and as a function of time in the first microdischarge (b). The green and blue curves generally overlap (i.e., H \rightarrow H(s) and H + H(s) \rightarrow H₂). In (a), the microdischarge with a 200 ns duration takes place at 38.4 ms.

We show in Figure C.10 the rates of direct adsorption of N and H atoms and compare it to the dissociation rates of N₂ and H₂. The dissociation rates of both N₂ and H₂ (i.e., upon electron impact) exhibit a sharp peak in the microdischarge (red curves), followed by a pronounced drop, because the electric field reduces to near 0 directly after the microdischarge (cf. section C.2 above). In the microdischarges, the H₂ dissociation rate is 3 orders of magnitude higher, and consequently H adsorption is also 3 orders of magnitude faster than N adsorption. Directly after the microdischarges, the ER reaction between H and N(s) (green dashed curve) clearly overlaps with direct adsorption of N

(blue solid line). The dissociation of H_2 eventually overlaps with the direct adsorption of H in the afterglows (red and blue dashed lines), while the N_2 dissociation overlaps more with the ER reaction between N and H(s) (red and green solid lines). However, due to the quenching of H(s) back to H_2 , we need to consider the net formation of H(s). This reaction rate is higher than for the ER reaction between N and H(s) (green curve). Instead, the net H(s) formation overlaps with the sum of all the ER and LH reactions that lead towards NH_3 and which require H(s) (cf. Figure C.8(a)).

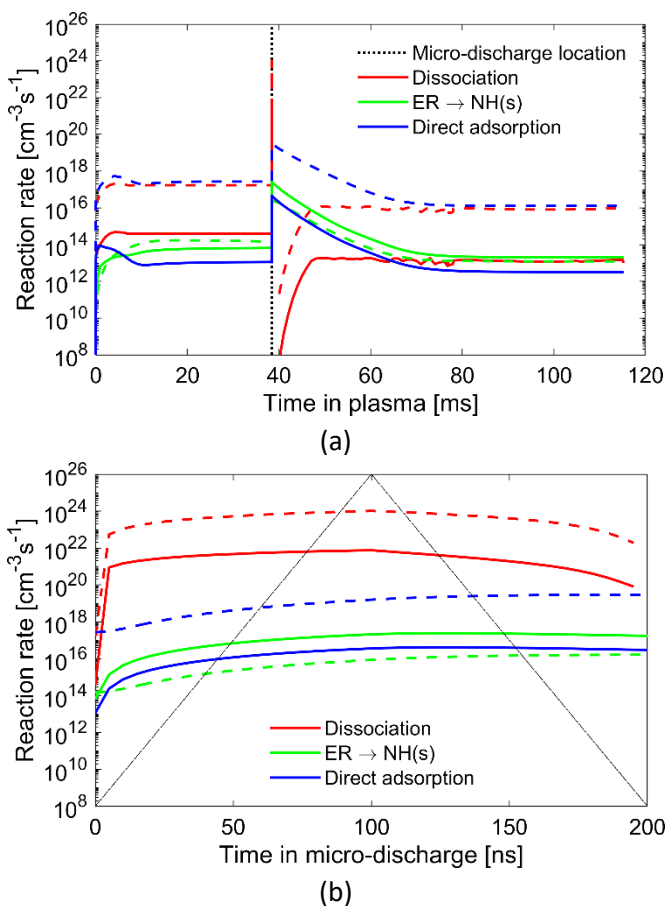
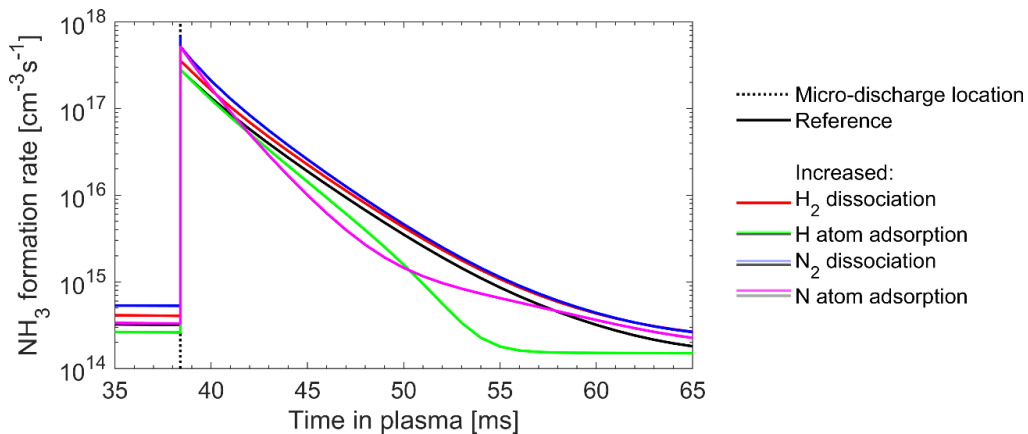


Figure C.10. Gas phase dissociation and atomic adsorption reaction rates for nitrogen (solid lines) and hydrogen (dashed lines) as a function of time in the plasma, from the start of the plasma to the end of the first microdischarge and afterglow pair. The curves of “ER \rightarrow NH(s)” are defined according to the gas phase atom, i.e. $N + H(s)$ is the solid curve and $H + N(s)$ is the dashed curve. In (a), the microdischarge with a 200 ns duration takes place at 38.4 ms.

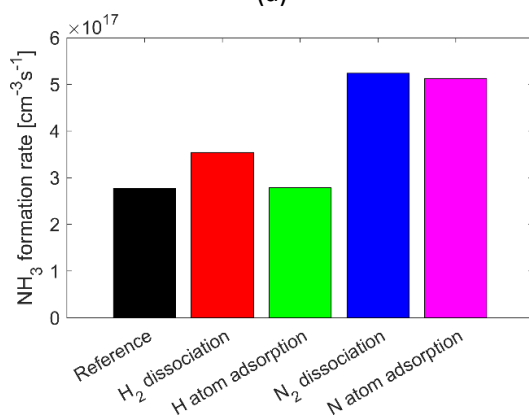
Based on the above, we identify the adsorption of N and H atoms, both in ER reactions and direct adsorption, as rate-limiting. Consequently, electron impact dissociation of N₂ or H₂ in the plasma can be the overall rate-limiting step. In order to further specify the rate-limiting step, we performed calculations in which the rate coefficients for the atomic adsorption processes or for electron impact gas phase dissociation are multiplied by a factor 2. The adjusted reactions are listed in Table C.2 and the results are compared in Figure C.11.

Table C.2. The test cases to confirm the rate-limiting reaction step. In each case the rate coefficient of the listed reactions was multiplied by a factor two.

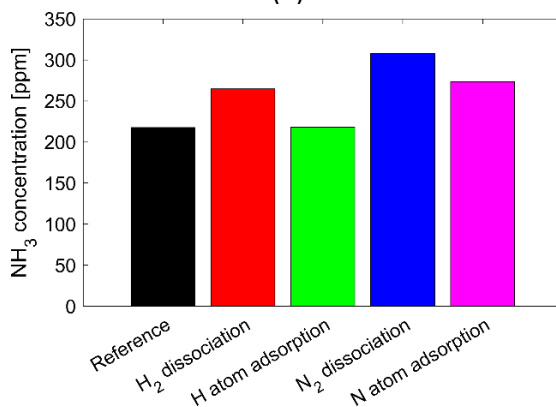
Case	Modified reactions
Reference	None
Increased H ₂ dissociation	$e^- + H_2(X, V) \rightarrow e^- + H + H$
Increased H atom adsorption	$H + \text{Surface} \rightarrow H(s)$
	$H + H(s) \rightarrow H_2$
	$H + N(s) \rightarrow NH(s)$
	$H + NH(s) \rightarrow NH_2(s)$
Increased N ₂ dissociation	$e^- + N_2(X, E, V) \rightarrow e^- + N + N$
	$N + \text{Surface} \rightarrow N(s)$
Increased N atom adsorption	$N + H(s) \rightarrow NH(s)$
	$N + N(s) \rightarrow N_2$



(a)



(b)



(c)

Figure C.11. Comparisons of the various test cases presented in Table C.2 in which we increase the rate coefficients of specific reactions by a factor 2 (cf. Table S8), showing the effect on the NH_3 formation rate, i.e. the reaction rate of $\text{NH}_2(\text{s}) + \text{H}(\text{s}) \rightarrow \text{NH}_3$, as a function of time (a), and 15 μs after the microdischarge (b), and the eventual NH_3 concentration (c). In (a), the microdischarge with a 200 ns duration takes place at 38.4 ms.

It is clear from Figure C.11(a) that the increased rate coefficient of the feed gas dissociation and of the atomic adsorption influences the final NH₃ synthesis reaction step (NH₂(s) + H(s) → NH₃). Most notably, the slope of the increased N adsorption is steeper, due to faster depletion of gas phase N atoms. Only an increased H atom adsorption does not increase the NH₃ formation rate throughout the afterglow, which is attributed to the faster H atom recombination rate by H + H(s) → H₂.

In Figure C.11(b) the NH₃ formation rates are compared shortly after the microdischarge. Clearly both an increase in N₂ dissociation and N atom adsorption by a factor 2 effectively enhance the NH₃ formation rate by the same factor 2, directly after the microdischarge. However, as noted before, the NH₃ formation rate with increased N atom adsorption rates will fall below the reference, due to the faster depletion of N atoms in the gas. An increase in the H₂ dissociation by a factor 2 also enhances the NH₃ formation rate, but only by a factor 1.3, due to a slight increase in H(s), and thus all further hydrogenation processes on the surface (N + H(s) → NH(s), NH(s) + H(s) → NH₂(s) and NH₂(s) → NH₃). The increase by a factor 1.3, instead of 2, approximately follows by considering all these three hydrogenation processes (i.e., $\sqrt[3]{2} = 1.26$).

In Figure C.11(c) the eventual NH₃ concentration is shown. Here the factor 2 increase is not directly reflected, due to how steady state is reached, i.e. because the overall system is non-linear in time. An increased gas phase H₂ dissociation enhances the NH₃ concentration by a factor 1.22. N atom adsorption increases the NH₃ concentration slightly more (factor 1.27), mainly due to an increase in N + H(s) → NH(s). H atom adsorption does not increase the NH₃ formation rate and the eventual NH₃ concentration is equal. The largest benefit is seen from an increased electron impact N₂ dissociation in the gas phase, enhancing the NH₃ concentration by a factor 1.41.

Based on the above analysis, electron impact N₂ dissociation in the plasma, followed by N atom adsorption at the surface, is identified as the rate-limiting step determining the NH₃ yield. H₂ dissociation in the plasma can also increase the formed NH₃, but to a lesser extent, as the H(s) precursor is required in multiple reaction steps. In addition, the

surface is always generally covered with H(s) (see Figure 6.1(a) in the main paper) and H₂ is easier to dissociate than N₂ (i.e. a dissociation threshold of 4.5 eV and 9.8 eV, respectively), thus the rate-limiting behaviour of the NH₃ synthesis in a DBD is attributed to nitrogen.

C.4. N₂ Dissociative Adsorption Compared Against N Atom Direct Adsorption

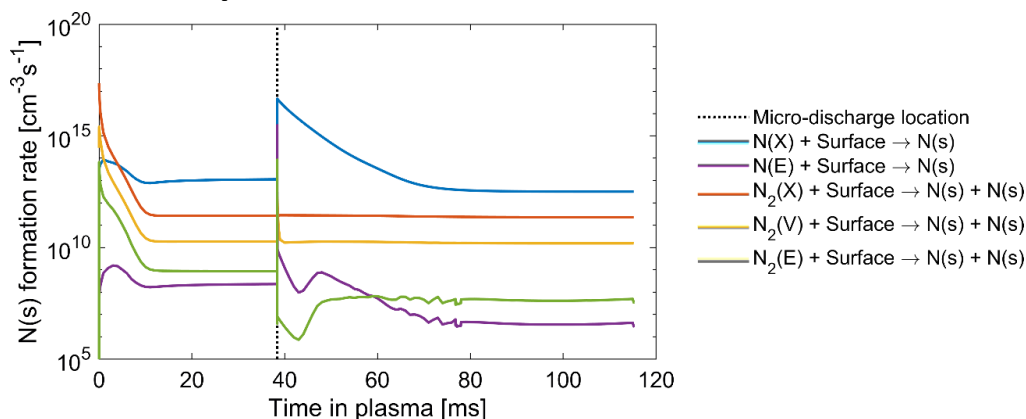


Figure C.12. Comparison of N(s) formation rates from the various atomic adsorption and dissociative adsorption processes, resolved for the ground state species (X), electronically excited states (E) and vibrational levels (V), as a function of time in the plasma, from the start of the plasma to the end of the first microdischarge and afterglow pair. The microdischarge with a 200 ns duration takes place at 38.4 ms.

C.5. Data Used in the Assessment of the Reaction Mechanisms

We present the data based on which we assessed the reaction mechanisms presented in Chapter 6. We based ourselves on the N_xH_y gas phase species (i.e. N, H, NH, NH₂ and NH₃), the surface adsorbed and related species (i.e. Surface (free sites), N(s), H(s), NH(s) and NH₂(s)) and the electrons and feed gas (i.e. e⁻ and H₂ and N₂, respectively). In addition, any other relevant species that is dictated by the significant reactions are also presented (i.e. electronically excited molecules: H₂(E) and N₂(E) and ions: N₂⁺, H₂⁺, N₂H⁺ and H₃⁺). We first considered separately whether or not the species is produced or destroyed during the microdischarge and during the afterglow (cf. also Figure 6.4). The

reaction rates, source terms and the reactions themselves were carefully inspected to determine whether or not the single reaction could be considered, and if indeed only the production or destruction had to be considered during a single phase of the discharge (i.e. the microdischarges and their afterglows).

The above analysis was based on the relative information instead of the absolute rates, i.e. the production-to-destruction ratio and the contribution of a reaction to either the production or destruction of a specific species. This is because the total source terms, and thus the typical reaction rates, can differ by orders of magnitude between the various species (cf. Figure 6.4 and 6.5). In Table C.3 and C.4 we present the reactions and their contribution to either the production or destruction of a species during the microdischarge and the afterglow, respectively. In addition we note how we considered the species, based on the production-to-destruction ratio. The (individual) vibrational levels of both the N_2 and H_2 molecules, as well as the N_2 electronic states, $N_2(E)$, are not resolved in Table C.3 of the microdischarges, as those species typically show fast excitation and de-excitation processes between the various levels or states. Similarly, in addition in the afterglow (Table C.4), the $H_2(X)$ and $N_2(X)$ ground states are populated (and depopulated) by the various vibrational interactions and (de-)excitation processes and $H_2(E)$ is mainly quenched back to the feed gas. Those interactions were not considered in detail, however typical vibrational distribution functions were shown in Figure 6.3 and C.2 for N_2 and H_2 , respectively.

For context, we provide the reaction rates of the listed reactions in Table C.5, time averaged over the first microdischarge and over the afterglow. Some reactions were not explicitly mentioned in the main paper (numbered in the tables with n.a.), those reactions typically quench any desired product back to the feed gas or indicate the population of electronically excited states or vibrational levels, which lead to the subsequent interactions between those states or levels.

Table C.3. The various species considered in the assessment of the reaction mechanisms and the most significant reactions and their contribution to the production (+) and/or destruction (–) of this species in the microdischarges. Either the production, destruction or both are given, depending on the specific consideration made, which is based on the production-to-destruction ratio (P/D).

Species	Consideration	(# Chapter 6) Reaction	Contribution
NH ₂ (s)	Most significantly produced (P/D = 1.8)	(10) NH + H(s) → NH ₂ (s)	0.86 (+)
		(16) NH(s) + H(s) → NH ₂ (s)	0.14 (+)
NH(s)	Most significantly produced (P/D = 12)	(13) N + H(s) → NH(s)	0.84 (+)
H(s)	Produced and destroyed (P/D = 0.98)	(11) H + Surface → H(s)	1.00 (+)
		(12) H + H(s) → H ₂	0.98 (–)
N(s)	Most significantly produced (P/D = 3.2)	(14) N + Surface → N(s)	0.96 (+)
Surface	Produced and destroyed (P/D = 1.01)	(12) H + H(s) → H ₂ + Surface	0.99 (+)
		(11) H + Surface → H(s)	1.00 (–)
NH ₃	Most significantly destroyed (P/D = 0.08)	(18) e [–] + NH ₃ → e [–] + NH ₂ + H	0.56 (–)
		(19) e [–] + NH ₃ → e [–] + NH + H ₂	0.32 (–)
NH ₂	Produced and destroyed (P/D = 18)	(18) e [–] + NH ₃ → e [–] + NH ₂ + H	0.92 (+)
NH	Most significantly produced (P/D = 3.1)	(9) N + H ₂ (E) → H + NH	0.99 (+)
H	Most significantly produced (P/D = 421)	(3) e [–] + H ₂ (X, V, E) → e [–] + H + H	0.89 (+)
		(7) N ₂ (E) + H ₂ → N ₂ + H + H	0.10 (+)
N	Most significantly produced (P/D = 1.4)	(2) e [–] + N ₂ (X, V, E) → e [–] + N + N	0.78 (+)
H ₂ (X)	Most significantly destroyed (P/D = 0.03)	(3) e [–] + H ₂ (X) → e [–] + H + H	0.63 (–)
		(8) e [–] + H ₂ → e [–] + H ₂ (E)	0.27 (–)
H ₂ (E)	Most significantly produced (P/D = 6.0)	(8) e [–] + H ₂ → e [–] + H ₂ (E)	1.00 (+)
N ₂ (X)	Most significantly destroyed (P/D = 0.13)	(n. a.) e [–] + N ₂ (X) → e [–] + N ₂ (V)	0.94 (–)
e [–]	Most significantly produced (P/D = 3.1)	(4) e [–] + N ₂ → e [–] + e [–] + N ₂ ⁺	0.65 (+)
		(5) e [–] + H ₂ → e [–] + e [–] + H ₂ ⁺	0.17 (+)
N ₂ ⁺	Produced and destroyed (P/D = 1.00)	(4) e [–] + N ₂ → e [–] + e [–] + N ₂ ⁺	0.52 (+)
		(n. a.) e [–] + N ₂ (E) → e [–] + e [–] + N ₂ ⁺	0.44 (+)
		(25) N ₂ ⁺ + H ₂ → N ₂ H ⁺ + H	0.98 (–)
H ₂ ⁺	Produced and destroyed (P/D = 1.00)	(5) e [–] + H ₂ → e [–] + e [–] + H ₂ ⁺	1.00 (+)
		(24) H ₂ ⁺ + H ₂ → H ₃ ⁺ + H	0.76 (–)
		(n. a.) H ₂ ⁺ + N ₂ → N ₂ H ⁺ + H	0.24 (–)
H ₃ ⁺	Most significantly produced (P/D = 5.8)	(24) H ₂ ⁺ + H ₂ → H ₃ ⁺ + H	1.00 (+)
N ₂ H ⁺	Most significantly produced (P/D = 2.1)	(25) N ₂ ⁺ + H ₂ → N ₂ H ⁺ + H	0.67 (+)
		(n. a.) H ₂ ⁺ + N ₂ → N ₂ H ⁺ + H	0.33 (+)

Table C.4. The various species considered in the assessment of the reaction mechanisms and the most significant reactions and their contribution to the production (+) and/or destruction (–) of this species in the afterglows of the microdischarges. Either the production, destruction or both are given, depending on the specific consideration made which is based on the production-to-destruction ratio (P/D).

Species	Consideration	(# Chapter 6) Reaction	Contribution
NH ₂ (s)	Produced and destroyed (P/D = 1.00)	(16) NH(s) + H(s) → NH ₂ (s)	0.99 (+)
		(17) NH ₂ (s) + H(s) → NH ₃	1.00 (–)
NH(s)	Produced and destroyed (P/D = 1.00)	(13) N + H(s) → NH(s)	0.86 (+)
		(15) H + N(s) → NH(s)	0.14 (+)
		(16) NH(s) + H(s) → NH ₂ (s)	1.00 (–)
H(s)	Produced and destroyed (P/D = 1.00)	(11) H + Surface → H(s)	1.00 (+)
		(12) H + H(s) → H ₂	0.98 (–)
N(s)	Produced and destroyed (P/D = 1.1)	(14) N + Surface → N(s)	1.00 (+)
		(15) H + N(s) → NH(s)	1.00 (–)
Surface	Produced and destroyed (P/D = 1.00)	(12) H + H(s) → H ₂ + Surface	0.98 (+)
		(11) H + Surface → H(s)	1.00 (–)
NH ₃	Most significantly produced (P/D = 8.7)	(17) NH ₂ (s) + H(s) → NH ₃	0.88 (+)
NH ₂	Produced and destroyed (P/D = 1.00)	(18) e [–] + NH ₃ → e [–] + NH ₂ + H	0.29 (+)
		(n. a.) N + H ₂ + M → NH ₂ + M	0.66 (+)
		(n. a.) H + NH ₂ → H ₂ + NH	0.33 (–)
		(n. a.) N + NH ₂ → N ₂ + H ₂	0.19 (–)
		(n. a.) N + NH ₂ → N ₂ + H + H	0.19 (–)
NH	Produced and destroyed (P/D = 0.97)	(20) NH ₂ + H(s) → NH ₃	0.10 (–)
		(9) N + H ₂ (E) → H + NH	0.99 (+)
H	Most significantly destroyed (P/D = 0.14)	(n. a.) H + NH → N + H ₂	0.98 (–)
		(11) H + Surface → H(s)	0.35 (–)
		(12) H + H(s) → H ₂	0.35 (–)
		(n. a.) H + H + H ₂ → H ₂ + H ₂	0.13 (–)
N	Produced and destroyed (P/D = 0.98)	(n. a.) H + NH → N + H ₂	0.13 (–)
		(n. a.) H + NH → N + H ₂	1.00 (+)
		(9) N + H ₂ (E) → H + NH	0.96 (–)
e [–]	Most significantly destroyed (P/D = 0.008)	(21) e [–] + H ₃ ⁺ → H ₂ + H	0.30 (–)
		(22) e [–] + H ₃ ⁺ → H + H + H	0.30 (–)
		(23) e [–] + N ₂ H ⁺ → N ₂ + H	0.37 (–)
N ₂ ⁺	Produced and destroyed (P/D = 0.98)	(n. a.) N ₂ (E) + N ₂ (E) → N ₂ ⁺ + N ₂ + e [–]	1.00 (+)
		(25) N ₂ ⁺ + H ₂ → N ₂ H ⁺ + H	0.98 (–)
H ₂ ⁺	Most significantly destroyed (P/D = 0.008)	(24) H ₂ ⁺ + H ₂ → H ₃ ⁺ + H	0.78 (–)
		(n. a.) H ₂ ⁺ + N ₂ → N ₂ H ⁺ + H	0.21 (–)
H ₃ ⁺	Most significantly destroyed (P/D = 3×10 ^{–6})	(21) e [–] + H ₃ ⁺ → H ₂ + H	0.50 (–)
		(22) e [–] + H ₃ ⁺ → H + H + H	0.50 (–)
N ₂ H ⁺	Most significantly destroyed (P/D = 0.0002)	(23) e [–] + N ₂ H ⁺ → N ₂ + H	1.00 (–)

Table C.5. The time averaged reaction rates, of the reactions in Table S10 and S11, during a microdischarge and its afterglow.

(# main paper) Reaction	Reaction rate (cm ⁻³ s ⁻¹), time averaged over the:	
	Microdischarge	Afterglow
(4) H ₂ + Surface → H(s) + H(s)	1.01 × 10 ¹⁵	9.46 × 10 ¹⁴
(5) e ⁻ + N ₂ (X, V, E) → e ⁻ + N + N	4.63 × 10 ²¹	1.19 × 10 ¹³
(6) e ⁻ + H ₂ (X, V, E) → e ⁻ + H + H	4.81 × 10 ²³	7.72 × 10 ¹⁵
(7) e ⁻ + N ₂ → e ⁻ + e ⁻ + N ₂ ⁺	1.78 × 10 ²⁰	7.80 × 10 ⁶
(8) e ⁻ + H ₂ → e ⁻ + e ⁻ + H ₂ ⁺	6.84 × 10 ²⁰	3.65 × 10 ⁷
(9) e ⁻ + N ₂ → e ⁻ + N ₂ (E)	2.45 × 10 ²³	6.41 × 10 ¹⁵
(10) N ₂ (E) + H ₂ → N ₂ + H + H	5.59 × 10 ²²	1.64 × 10 ¹⁶
(11) e ⁻ + H ₂ → e ⁻ + H ₂ (E)	2.04 × 10 ²³	1.81 × 10 ¹⁵
(12) N + H ₂ (E) → H + NH	7.81 × 10 ²¹	4.17 × 10 ¹⁷
(13) NH + H(s) → NH ₂ (s)	8.77 × 10 ¹⁶	3.89 × 10 ¹³
(14) H + Surface → H(s)	1.55 × 10 ¹⁹	1.17 × 10 ¹⁸
(15) H + H(s) → H ₂	1.55 × 10 ¹⁹	1.15 × 10 ¹⁸
(16) N + H(s) → NH(s)	1.49 × 10 ¹⁷	7.36 × 10 ¹⁵
(17) N + Surface → N(s)	2.57 × 10 ¹⁶	1.30 × 10 ¹⁵
(18) H + N(s) → NH(s)	8.46 × 10 ¹⁵	1.18 × 10 ¹⁵
(19) NH(s) + H(s) → NH ₂ (s)	1.47 × 10 ¹⁶	8.51 × 10 ¹⁵
(20) NH ₂ (s) + H(s) → NH ₃	5.57 × 10 ¹⁶	8.60 × 10 ¹⁵
(21) e ⁻ + NH ₃ → e ⁻ + NH ₂ + H	1.36 × 10 ¹⁹	8.54 × 10 ¹⁴
(22) e ⁻ + NH ₃ → e ⁻ + NH + H ₂	7.73 × 10 ¹⁸	1.88 × 10 ¹⁴
(23) NH ₂ + H(s) → NH ₃	3.40 × 10 ¹⁴	3.09 × 10 ¹⁴
(24) e ⁻ + H ₃ ⁺ → H ₂ + H	4.29 × 10 ¹⁹	5.53 × 10 ¹⁴
(25) e ⁻ + H ₃ ⁺ → H + H + H	4.29 × 10 ¹⁹	5.53 × 10 ¹⁴
(26) e ⁻ + N ₂ H ⁺ → N ₂ + H	2.30 × 10 ²⁰	6.85 × 10 ¹⁴
(27) H ₂ ⁺ + H ₂ → H ₃ ⁺ + H	5.19 × 10 ²⁰	3.36 × 10 ⁹
(28) N ₂ ⁺ + H ₂ → N ₂ H ⁺ + H	3.38 × 10 ²⁰	1.38 × 10 ¹¹
(n. a.) H + NH ₂ → H ₂ + NH	1.63 × 10 ¹⁷	9.67 × 10 ¹⁴
(n. a.) N + NH ₂ → N ₂ + H ₂	1.43 × 10 ¹⁷	5.75 × 10 ¹⁴
(n. a.) N + NH ₂ → N ₂ + H + H	1.43 × 10 ¹⁷	5.75 × 10 ¹⁴
(n. a.) e ⁻ + N ₂ (E) → e ⁻ + e ⁻ + N ₂ ⁺	1.53 × 10 ²⁰	4.98 × 10 ⁸
(n. a.) H ₂ ⁺ + N ₂ → N ₂ H ⁺ + H	1.64 × 10 ²⁰	9.23 × 10 ⁸
(n. a.) N + H ₂ + M → NH ₂ + M	1.06 × 10 ¹⁵	1.94 × 10 ¹⁵
(n. a.) H + NH → N + H ₂	2.51 × 10 ²¹	4.25 × 10 ¹⁷
(n. a.) H + H + H ₂ → H ₂ + H ₂	5.03 × 10 ¹⁸	2.23 × 10 ¹⁷

The data presented in Table C.3 and C.4 also gives some insight in the sensitivity of the overall assessed reaction mechanisms to changes in the underlying rate coefficients of either the involved reactions themselves or of other reactions also present in the chemistry set (cf. Appendix A). Indeed, reaction rate coefficients always have an uncertainty, typically in the order of 30% [121], [122]. In general, if we concluded that

there is only one significant reaction relevant to the production or destruction of one species, while the contribution of this reaction is just slightly above 0.5 (i.e. 50%), then it is clear that a slight change in this or other reactions could change the actual main reaction taking place. On the other hand, if we find a large contribution to the overall production or destruction (i.e. contributions of 0.8, or 80%, and up), then it is less likely that other reactions that were not part of our assessed reaction mechanisms (which thus have very low contributions) would become the most important, even when the uncertainties in the rate coefficients are considered. In Table C.3 and C.4, the lowest considered contribution to the production or destruction of a species, for determining the reaction mechanisms, is 0.81, i.e. 81%, which is the sum of the four reactions (0.33 + 0.19 + 0.19 + 0.1) accounting for the destruction of NH₂ in the afterglow (cf. Table C.4).

C.6. Influence of Langmuir-Hinshelwood Reactions and Alternative Reaction Mechanisms

Because the adopted Langmuir-Hinshelwood activation energies are subject to uncertainties, we calculate several hypothetical cases in which we change the activation energy and thus the rate coefficients governing the reactions, as shown in Table C.6. The diffusion barrier is kept constant, as reported in Appendix A.3. We cover cases in which the reactions are slower and faster. Results are given in Table C.7.

Table C.6. Summary of the calculations performed to investigate the influence of the LH reactions.

Case	Reaction	Activation energy	Rate coefficient	
			cm ³ s ⁻¹	s ⁻¹
Adopted chemistry	H(s) + N(s) → NH(s)	$E_a = 1.099 \text{ eV}$	7.5×10^{-22}	1.1×10^{-4}
	H(s) + NH(s) → NH ₂ (s)	$E_a = 0.3 \text{ eV}$	8.8×10^{-12}	1.3×10^6
	H(s) + NH ₂ (s) → NH ₃	$E_a = 0.2 \text{ eV}$	1.6×10^{-10}	2.3×10^7
Equal barriers	H(s) + N(s) → NH(s)	$E_a = 1.0 \text{ eV}$	1.3×10^{-20}	1.9×10^{-3}
	H(s) + NH(s) → NH ₂ (s)	$E_a = 1.0 \text{ eV}$	1.3×10^{-20}	1.9×10^{-3}
	H(s) + NH ₂ (s) → NH ₃	$E_a = 1.0 \text{ eV}$	1.3×10^{-20}	1.9×10^{-3}
Increased barriers	H(s) + N(s) → NH(s)	$E_a = 2.0 \text{ eV}$	3.3×10^{-33}	4.8×10^{-16}
	H(s) + NH(s) → NH ₂ (s)	$E_a = 2.0 \text{ eV}$	3.3×10^{-33}	4.8×10^{-16}
	H(s) + NH ₂ (s) → NH ₃	$E_a = 2.0 \text{ eV}$	3.3×10^{-33}	4.8×10^{-16}
Barrierless	H(s) + N(s) → NH(s)	$E_a = 0.0 \text{ eV}$	5.3×10^{-8}	7.6×10^9
	H(s) + NH(s) → NH ₂ (s)	$E_a = 0.0 \text{ eV}$	5.3×10^{-8}	7.6×10^9
	H(s) + NH ₂ (s) → NH ₃	$E_a = 0.0 \text{ eV}$	5.3×10^{-8}	7.6×10^9

Table C.7. Calculated steady state NH₃ concentration and NH₃ formation rate through the LH pathway (H(s) + NH₂(s) → NH₃) for the various test cases.

Case	NH ₃ concentration (ppm)	LH NH ₃ formation rate (cm ⁻³ s ⁻¹) in the first afterglow
Basic chemistry	223	<u>8.6 × 10¹⁵</u>
Equal barriers	224	2.4 × 10 ¹⁰
Increased barriers	224	6.0 × 10 ⁻³
Barrierless	223	<u>8.7 × 10¹⁵</u>

Table C.7 lists the calculated steady-state NH₃ concentration for the basic model and the additional calculations. It can be seen that all additional calculations give the same concentration as the basic chemistry which was used to assess the reaction mechanisms in detail. In the basic chemistry model we found that the eventual formation of NH₃ is through the LH reaction: H(s) + NH₂(s) → NH₃. Table C.7 also reports the corresponding reaction rate of this LH reaction. Despite the same NH₃ concentration, we do see different LH reaction rates when increasing the activation energy (i.e. for barriers of 1.0 eV and 2.0 eV in the case of equal barriers and increased barriers, respectively). This means that reactions other than this LH reaction should be responsible for the formation of NH₃. When the LH reactions were barrierless, the eventual rate is the same, despite a significantly higher rate coefficient (cf. Table C.6), thus indicating a preceding step as rate limiting, i.e. the formation of NH(s) by ER reactions. Indeed, also when the LH formation of NH(s) is increased, i.e. the barrierless case, the formation rate is still the same, indicating that the same ER NH(s) formation is still faster than the LH alternative.

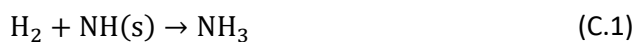
In addition, when the LH reactions are slower (increased barriers), we don't see a change in the main formation of NH(s) by the ER reactions, but we do see other NH₃ formation reactions taking place in the final step, with the same rate as when the formation was due to LH reactions, as shown in Table C.8.

Table C.8. Comparison of the NH₃ formation rate by the most important reactions for the various test cases.

Case	NH ₃ formation rate (cm ⁻³ s ⁻¹) in the first afterglow		
	H(s) + NH ₂ (s) → NH ₃	H ₂ + NH(s) → NH ₃	H + NH ₂ (s) → NH ₃
Basic chemistry	<u>8.6 × 10¹⁵</u>	3.4 × 10 ¹³	2.2 × 10 ¹¹
Equal barriers	2.4 × 10 ¹⁰	<u>7.7 × 10¹⁵</u>	7.6 × 10 ¹⁴
Increased barriers	6.0 × 10 ⁻³	<u>7.7 × 10¹⁵</u>	7.6 × 10 ¹⁴
Barrier-less	<u>8.7 × 10¹⁵</u>	6.8 × 10 ⁸	6.8 × 10 ⁸

The reaction H₂ + NH(s) → NH₃ is dominant when the LH reaction (H(s) + NH₂(s) → NH₃) is not fast enough, and is characterized by a nearly equal rate (underlined in Table C.8). We also list H + NH₂(s) → NH₃ which has the highest reaction rate after the LH reaction and the H₂ ER reaction in the basic chemistry case. Indeed, we also found that the stepwise ER hydrogenations with H are fast enough to account for the same NH₃ formation rates if the H₂ ER reaction is absent.

Based on the above we can present two alternative NH₃ formation paths as revealed by our model. After the ER formation of NH(s), a single reaction step might form NH₃:



Alternatively, stepwise ER hydrogenation reactions might form NH₃:



Bibliography

- [1] M. Roser, H. Ritchie and E. Ortiz-Ospina, “World Population Growth,” *Published online at OurWorldInData.org*, 2013, <https://ourworldindata.org/world-population-growth>.
- [2] P. L. Pingali, “Green Revolution: Impacts, limits, and the path ahead,” *Proc. Natl. Acad. Sci.*, vol. 109, no. 31, pp. 12302–12308, Jul. 2012, doi: 10.1073/pnas.0912953109.
- [3] A. P. Kinzig and R. H. Socolow, “Human Impacts on the Nitrogen Cycle,” *Phys. Today*, vol. 47, no. 11, pp. 24–31, Nov. 1994, doi: 10.1063/1.881423.
- [4] L. Y. Stein and M. G. Klotz, “The nitrogen cycle,” *Curr. Biol.*, vol. 26, no. 3, pp. R94–R98, Feb. 2016, doi: 10.1016/j.cub.2015.12.021.
- [5] A. Adel, “Atmospheric Nitrous Oxide and the Nitrogen Cycle,” *Science*, vol. 113, no. 2944, pp. 624–625, Jun. 1951, doi: 10.1126/science.113.2944.624.
- [6] D. A. Lashof and D. R. Ahuja, “Relative contributions of greenhouse gas emissions to global warming,” *Nature*, vol. 344, no. 6266, pp. 529–531, Apr. 1990, doi: 10.1038/344529a0.
- [7] C. Muñoz, L. Paulino, C. Monreal, and E. Zagal, “Greenhouse Gas (CO₂ and N₂O) Emissions from Soils: A Review,” *Chil. J. Agric. Res.*, vol. 70, no. 3, Sep. 2010, doi: 10.4067/S0718-58392010000300016.
- [8] K. Butterbach-Bahl, E. M. Baggs, M. Dannenmann, R. Kiese, and S. Zechmeister-Boltenstern, “Nitrous oxide emissions from soils: how well do we understand the processes and their controls?,” *Philos. Trans. R. Soc. B Biol. Sci.*, vol. 368, no. 1621, p. 20130122, Jul. 2013, doi: 10.1098/rstb.2013.0122.
- [9] C. O. Dimkpa, J. Fugice, U. Singh, and T. D. Lewis, “Development of fertilizers for enhanced nitrogen use efficiency – Trends and perspectives,” *Sci. Total Environ.*, vol. 731, p. 139113, Aug. 2020, doi: 10.1016/j.scitotenv.2020.139113.
- [10] P. M. Vitousek *et al.*, “Human alteration of the global nitrogen cycle: sources and consequences,” *Ecol. Appl.*, vol. 7, no. 3, pp. 737–750, 1997, doi: [https://doi.org/10.1890/1051-0761\(1997\)007\[0737:HAOTGN\]2.0.CO;2](https://doi.org/10.1890/1051-0761(1997)007[0737:HAOTGN]2.0.CO;2).
- [11] K. H. R. Rouwenhorst, F. Jardali, A. Bogaerts, and L. Lefferts, “From the Birkeland–Eyde process towards energy-efficient plasma-based NO_x synthesis: a techno-economic analysis,” *Energy Environ. Sci.*, vol. 14, no. 5, pp. 2520–2534, 2021, doi: 10.1039/D0EE03763J.
- [12] T. Kandemir, M. E. Schuster, A. Senyshyn, M. Behrens, and R. Schlögl, “The Haber-Bosch Process Revisited: On the Real Structure and Stability of

- 'Ammonia Iron' under Working Conditions," *Angew. Chemie Int. Ed.*, vol. 52, no. 48, pp. 12723–12726, Nov. 2013, doi: 10.1002/anie.201305812.
- [13] S. Ghavam, M. Vahdati, I. A. G. Wilson, and P. Styring, "Sustainable Ammonia Production Processes," *Front. Energy Res.*, vol. 9, Mar. 2021, doi: 10.3389/fenrg.2021.580808.
- [14] C. Lal Pandey, "The limits of climate change agreements: from past to present," *Int. J. Clim. Chang. Strateg. Manag.*, vol. 6, no. 4, pp. 376–390, Nov. 2014, doi: 10.1108/IJCCSM-03-2013-0026.
- [15] A. Savaresi, "The Paris Agreement: a new beginning?," *J. Energy Nat. Resour. Law*, vol. 34, no. 1, pp. 16–26, Jan. 2016, doi: 10.1080/02646811.2016.1133983.
- [16] N. K. Arora and I. Mishra, "COP26: more challenges than achievements," *Environ. Sustain.*, vol. 4, no. 4, pp. 585–588, Dec. 2021, doi: 10.1007/s42398-021-00212-7.
- [17] A. Dzebo, H. Janetschek, C. Brandi and G. Iacobuta, "Connections between the Paris Agreement and the 2030 Agenda: the case for policy coherence," *SEI Working Paper*, 2019, <https://www.sei.org/publications/connections-between-the-paris-agreement-and-the-2030-agenda/>.
- [18] W. Colglazier, "Sustainable development agenda: 2030," *Science*, vol. 349, no. 6252, pp. 1048–1050, Sep. 2015, doi: 10.1126/science.aad2333.
- [19] C. Smith and L. Torrente-Murciano, "Guidance for targeted development of ammonia synthesis catalysts from a holistic process approach," *Chem Catal.*, vol. 1, no. 6, pp. 1163–1172, Nov. 2021, doi: 10.1016/j.checat.2021.09.015.
- [20] M. Osaki, "Science for sustainable agriculture," in *Sustainability Science*, United Nations, pp. 272–293, 2013, doi: <https://doi.org/10.18356/47e32247-en>.
- [21] "Symposium MF01—Cutting-Edge Plasma Processes Contributing to Sustainable Development Goals," Materials Research Society and Japan Society of Applied Physics, Call for Papers, 2022, https://www.mrs.org/meetings-events/spring-meetings-exhibits/2022-mrs-spring-meeting/call-for-papers/detail/2022_mrs_spring_meeting/mf01/Symposium_MF01.
- [22] S. M. Thagard, M. Sankaran, and M. J. Kushner, "Science Challenges in Low Temperature Plasma Science and Engineering: Enabling a Future Based on Electricity through Non-Equilibrium Plasma Chemistry." 2019, <https://arxiv.org/abs/1911.07076>.
- [23] K. H. R. Rouwenhorst, Y. Engelmann, K. van 't Veer, R. S. Postma, A. Bogaerts, and L. Lefferts, "Plasma-driven catalysis: green ammonia synthesis with

intermittent electricity," *Green Chem.*, vol. 22, no. 19, pp. 6258–6287, 2020, doi: 10.1039/D0GC02058C.

- [24] N. K. Kaushik, S. Bekeschus, H. Tanaka, A. Lin, and E. H. Choi, "Plasma Medicine Technologies," *Appl. Sci.*, vol. 11, no. 10, p. 4584, May 2021, doi: 10.3390/app11104584.
- [25] M. Laroussi *et al.*, "Low-Temperature Plasma for Biology, Hygiene, and Medicine: Perspective and Roadmap," *IEEE Trans. Radiat. Plasma Med. Sci.*, vol. 6, no. 2, pp. 127–157, Feb. 2022, doi: 10.1109/TRPMS.2021.3135118.
- [26] K. Weltmann *et al.*, "The future for plasma science and technology," *Plasma Process. Polym.*, vol. 16, no. 1, p. 1800118, Jan. 2019, doi: 10.1002/ppap.201800118.
- [27] "Perspective on Plasmas – What are plasmas?," *plasma.org*, <http://www.plasmas.org/what-are-plasmas.htm>.
- [28] "Plasma classification (types of plasma)," *plasma-universe.com*, <https://www.plasma-universe.com/plasma-classification-types-of-plasma/>.
- [29] B. S. Patil, Q. Wang, V. Hessel, and J. Lang, "Plasma N₂-fixation: 1900–2014," *Catal. Today*, vol. 256, pp. 49–66, Nov. 2015, doi: 10.1016/j.cattod.2015.05.005.
- [30] N. Cherkasov, A. O. Ibhadon, and P. Fitzpatrick, "A review of the existing and alternative methods for greener nitrogen fixation," *Chem. Eng. Process. Process Intensif.*, vol. 90, pp. 24–33, Apr. 2015, doi: 10.1016/j.cep.2015.02.004.
- [31] S. Samukawa *et al.*, "The 2012 Plasma Roadmap," *J. Phys. D. Appl. Phys.*, vol. 45, no. 25, p. 253001, Jun. 2012, doi: 10.1088/0022-3727/45/25/253001.
- [32] I. Adamovich *et al.*, "The 2017 Plasma Roadmap: Low temperature plasma science and technology," *J. Phys. D. Appl. Phys.*, vol. 50, no. 32, p. 323001, Aug. 2017, doi: 10.1088/1361-6463/aa76f5.
- [33] A. Bogaerts and E. C. Neyts, "Plasma Technology: An Emerging Technology for Energy Storage," *ACS Energy Lett.*, vol. 3, no. 4, pp. 1013–1027, Apr. 2018, doi: 10.1021/acsenenergylett.8b00184.
- [34] P. Peng *et al.*, "A review on the non-thermal plasma-assisted ammonia synthesis technologies," *J. Clean. Prod.*, vol. 177, pp. 597–609, Mar. 2018, doi: 10.1016/j.jclepro.2017.12.229.
- [35] G. Akay and K. Zhang, "Process Intensification in Ammonia Synthesis Using Novel Coassembled Supported Microporous Catalysts Promoted by

- Nonthermal Plasma," *Ind. Eng. Chem. Res.*, vol. 56, no. 2, pp. 457–468, Jan. 2017, doi: 10.1021/acs.iecr.6b02053.
- [36] B. Mingdong, B. Xiyao, Z. Zhitao, and B. Mindi, "Synthesis of Ammonia in a Strong Electric Field Discharge at Ambient Pressure," *Plasma Chem. Plasma Process.*, vol. 20, no. 4, pp. 511–520, 2000, doi: 10.1023/A:1007031906589.
- [37] M. L. Carreon, "Plasma catalytic ammonia synthesis: state of the art and future directions," *J. Phys. D. Appl. Phys.*, vol. 52, no. 48, p. 483001, Nov. 2019, doi: 10.1088/1361-6463/ab3b2c.
- [38] Mindong Bai, Zhitao Zhang, Xiyao Bai, Mindi Bai, and Wang Ning, "Plasma synthesis of ammonia with a microgap dielectric barrier discharge at ambient pressure," *IEEE Trans. Plasma Sci.*, vol. 31, no. 6, pp. 1285–1291, Dec. 2003, doi: 10.1109/TPS.2003.818761.
- [39] T. Mizushima, K. Matsumoto, J. Sugoh, H. Ohkita, and N. Kakuta, "Tubular membrane-like catalyst for reactor with dielectric-barrier-discharge plasma and its performance in ammonia synthesis," *Appl. Catal. A Gen.*, vol. 265, no. 1, pp. 53–59, Jun. 2004, doi: 10.1016/j.apcata.2004.01.002.
- [40] T. Mizushima, K. Matsumoto, H. Ohkita, and N. Kakuta, "Catalytic Effects of Metal-loaded Membrane-like Alumina Tubes on Ammonia Synthesis in Atmospheric Pressure Plasma by Dielectric Barrier Discharge," *Plasma Chem. Plasma Process.*, vol. 27, no. 1, pp. 1–11, Feb. 2007, doi: 10.1007/s11090-006-9034-2.
- [41] A. Gómez-Ramírez, J. Cotrino, R. M. Lambert, and A. R. González-Elipe, "Efficient synthesis of ammonia from N₂ and H₂ alone in a ferroelectric packed-bed DBD reactor," *Plasma Sources Sci. Technol.*, vol. 24, no. 6, p. 065011, Nov. 2015, doi: 10.1088/0963-0252/24/6/065011.
- [42] A. Gómez-Ramírez, A. M. Montoro-Damas, J. Cotrino, R. M. Lambert, and A. R. González-Elipe, "About the enhancement of chemical yield during the atmospheric plasma synthesis of ammonia in a ferroelectric packed bed reactor," *Plasma Process. Polym.*, vol. 14, no. 6, p. 1600081, Jun. 2017, doi: 10.1002/ppap.201600081.
- [43] P. Barboun, P. Mehta, F. A. Herrera, D. B. Go, W. F. Schneider, and J. C. Hicks, "Distinguishing Plasma Contributions to Catalyst Performance in Plasma-Assisted Ammonia Synthesis," *ACS Sustain. Chem. Eng.*, vol. 7, no. 9, pp. 8621–8630, May 2019, doi: 10.1021/acssuschemeng.9b00406.
- [44] P. Peng, Y. Li, Y. Cheng, S. Deng, P. Chen, and R. Ruan, "Atmospheric Pressure Ammonia Synthesis Using Non-thermal Plasma Assisted Catalysis," *Plasma Chem. Plasma Process.*, vol. 36, no. 5, pp. 1201–1210, Sep. 2016, doi: 10.1007/s11090-016-9713-6.

- [45] K. Van Laer and A. Bogaerts, "How bead size and dielectric constant affect the plasma behaviour in a packed bed plasma reactor: a modelling study," *Plasma Sources Sci. Technol.*, vol. 26, no. 8, p. 085007, Jul. 2017, doi: 10.1088/1361-6595/aa7c59.
- [46] N. Y. Babaeva and M. J. Kushner, "Effect of inhomogeneities on streamer propagation: I. Intersection with isolated bubbles and particles," *Plasma Sources Sci. Technol.*, vol. 18, no. 3, p. 035009, Aug. 2009, doi: 10.1088/0963-0252/18/3/035009.
- [47] N. Y. Babaeva and M. J. Kushner, "Effect of inhomogeneities on streamer propagation: II. Streamer dynamics in high pressure humid air with bubbles," *Plasma Sources Sci. Technol.*, vol. 18, no. 3, p. 035010, Aug. 2009, doi: 10.1088/0963-0252/18/3/035010.
- [48] N. Y. Babaeva, A. N. Bhoj, and M. J. Kushner, "Streamer dynamics in gases containing dust particles," *Plasma Sources Sci. Technol.*, vol. 15, no. 4, pp. 591–602, Nov. 2006, doi: 10.1088/0963-0252/15/4/001.
- [49] R. Dorai and M. J. Kushner, "A model for plasma modification of polypropylene using atmospheric pressure discharges," *J. Phys. D. Appl. Phys.*, vol. 36, no. 6, pp. 666–685, Mar. 2003, doi: 10.1088/0022-3727/36/6/309.
- [50] J. Kruszelnicki, K. W. Engeling, J. E. Foster, Z. Xiong, and M. J. Kushner, "Propagation of negative electrical discharges through 2-dimensional packed bed reactors," *J. Phys. D. Appl. Phys.*, vol. 50, no. 2, p. 025203, Jan. 2017, doi: 10.1088/1361-6463/50/2/025203.
- [51] Woo Seok Kang, Jin Myung Park, Yongho Kim, and Sang Hee Hong, "Numerical study on influences of barrier arrangements on dielectric barrier discharge characteristics," *IEEE Trans. Plasma Sci.*, vol. 31, no. 4, pp. 504–510, Aug. 2003, doi: 10.1109/TPS.2003.815469.
- [52] A. A. Kulikovskiy, "Positive streamer between parallel plate electrodes in atmospheric pressure air," *J. Phys. D. Appl. Phys.*, vol. 30, no. 3, pp. 441–450, Feb. 1997, doi: 10.1088/0022-3727/30/3/017.
- [53] H. Russ, M. Neiger, and J. E. Lang, "Simulation of micro discharges for the optimization of energy requirements for removal of NO_x from exhaust gases," *IEEE Trans. Plasma Sci.*, vol. 27, no. 1, pp. 38–39, 1999, doi: 10.1109/27.763019.
- [54] Jen-Shih Chang *et al.*, "Removal of NF₃ from semiconductor-process flue gases by tandem packed-bed plasma and adsorbent hybrid systems," *IEEE Trans. Ind. Appl.*, vol. 36, no. 5, pp. 1251–1259, 2000, doi: 10.1109/28.871272.
- [55] K. Takaki, J.-S. Chang, and K. G. Kostov, "Atmospheric pressure of nitrogen

plasmas in a ferro-electric packed bed barrier discharge reactor part I: modeling," *IEEE Trans. Dielectr. Electr. Insul.*, vol. 11, no. 3, pp. 281–290, Jun. 2004, doi: 10.1109/TDEI.2004.1306726.

- [56] Y. Uchida, K. Takaki, K. Urashima, and Jen-Shih Chang, "Atmospheric pressure of nitrogen plasmas in a ferro-electric packed-bed barrier discharge reactor part II: spectroscopic measurements of excited nitrogen molecule density and its vibrational temperature," *IEEE Trans. Dielectr. Electr. Insul.*, vol. 11, no. 3, pp. 291–297, Jun. 2004, doi: 10.1109/TDEI.2004.1306727.
- [57] P. Mehta *et al.*, "Overcoming ammonia synthesis scaling relations with plasma-enabled catalysis," *Nat. Catal.*, vol. 1, no. 4, pp. 269–275, Apr. 2018, doi: 10.1038/s41929-018-0045-1.
- [58] K. H. R. Rouwenhorst, H.-H. Kim, and L. Lefferts, "Vibrationally Excited Activation of N₂ in Plasma-Enhanced Catalytic Ammonia Synthesis: A Kinetic Analysis," *ACS Sustain. Chem. Eng.*, vol. 7, no. 20, pp. 17515–17522, Oct. 2019, doi: 10.1021/acssuschemeng.9b04997.
- [59] K. Van Laer and A. Bogaerts, "Fluid modelling of a packed bed dielectric barrier discharge plasma reactor," *Plasma Sources Sci. Technol.*, vol. 25, no. 1, p. 015002, Feb. 2016, doi: 10.1088/0963-0252/25/1/015002.
- [60] K. Van Laer and A. Bogaerts, "Influence of Gap Size and Dielectric Constant of the Packing Material on the Plasma Behaviour in a Packed Bed DBD Reactor: A Fluid Modelling Study," *Plasma Process. Polym.*, vol. 14, no. 4–5, p. 1600129, Apr. 2017, doi: 10.1002/ppap.201600129.
- [61] W. Wang, H.-H. Kim, K. Van Laer, and A. Bogaerts, "Streamer propagation in a packed bed plasma reactor for plasma catalysis applications," *Chem. Eng. J.*, vol. 334, pp. 2467–2479, Feb. 2018, doi: 10.1016/j.cej.2017.11.139.
- [62] Y. Uytendhouwen, S. Van Alphen, I. Michielsen, V. Meynen, P. Cool, and A. Bogaerts, "A packed-bed DBD micro plasma reactor for CO₂ dissociation: Does size matter?," *Chem. Eng. J.*, vol. 348, pp. 557–568, Sep. 2018, doi: 10.1016/j.cej.2018.04.210.
- [63] A. Ozkan *et al.*, "The influence of power and frequency on the filamentary behavior of a flowing DBD—application to the splitting of CO₂," *Plasma Sources Sci. Technol.*, vol. 25, no. 2, p. 025013, Apr. 2016, doi: 10.1088/0963-0252/25/2/025013.
- [64] A. Ozkan, A. Bogaerts, and F. Reniers, "Routes to increase the conversion and the energy efficiency in the splitting of CO₂ by a dielectric barrier discharge," *J. Phys. D: Appl. Phys.*, vol. 50, no. 8, p. 084004, Mar. 2017, doi: 10.1088/1361-6463/aa562c.

- [65] A. Ozkan, T. Dufour, A. Bogaerts, and F. Reniers, "How do the barrier thickness and dielectric material influence the filamentary mode and CO₂ conversion in a flowing DBD?," *Plasma Sources Sci. Technol.*, vol. 25, no. 4, p. 045016, Aug. 2016, doi: 10.1088/0963-0252/25/4/045016.
- [66] R. Snoeckx, R. Aerts, X. Tu, and A. Bogaerts, "Plasma-Based Dry Reforming: A Computational Study Ranging from the Nanoseconds to Seconds Time Scale," *J. Phys. Chem. C*, vol. 117, no. 10, pp. 4957–4970, Mar. 2013, doi: 10.1021/jp311912b.
- [67] R. Snoeckx, A. Ozkan, F. Reniers, and A. Bogaerts, "The Quest for Value-Added Products from Carbon Dioxide and Water in a Dielectric Barrier Discharge: A Chemical Kinetics Study," *ChemSusChem*, vol. 10, no. 2, pp. 409–424, Jan. 2017, doi: 10.1002/cssc.201601234.
- [68] R. Snoeckx, S. Heijkers, K. Van Wesenbeeck, S. Lenaerts, and A. Bogaerts, "CO₂ conversion in a dielectric barrier discharge plasma: N₂ in the mix as a helping hand or problematic impurity?," *Energy Environ. Sci.*, vol. 9, no. 3, pp. 999–1011, 2016, doi: 10.1039/C5EE03304G.
- [69] R. Snoeckx, Y. X. Zeng, X. Tu, and A. Bogaerts, "Plasma-based dry reforming: improving the conversion and energy efficiency in a dielectric barrier discharge," *RSC Adv.*, vol. 5, no. 38, pp. 29799–29808, 2015, doi: 10.1039/C5RA01100K.
- [70] R. Snoeckx, M. Setareh, R. Aerts, P. Simon, A. Maghari, and A. Bogaerts, "Influence of N₂ concentration in a CH₄/N₂ dielectric barrier discharge used for CH₄ conversion into H₂," *Int. J. Hydrogen Energy*, vol. 38, no. 36, pp. 16098–16120, Dec. 2013, doi: 10.1016/j.ijhydene.2013.09.136.
- [71] R. Aerts, W. Somers, and A. Bogaerts, "Carbon Dioxide Splitting in a Dielectric Barrier Discharge Plasma: A Combined Experimental and Computational Study," *ChemSusChem*, vol. 8, no. 4, pp. 702–716, Feb. 2015, doi: 10.1002/cssc.201402818.
- [72] R. Aerts, T. Martens, and A. Bogaerts, "Influence of Vibrational States on CO₂ Splitting by Dielectric Barrier Discharges," *J. Phys. Chem. C*, vol. 116, no. 44, pp. 23257–23273, Nov. 2012, doi: 10.1021/jp307525t.
- [73] T. Kozák and A. Bogaerts, "Splitting of CO₂ by vibrational excitation in non-equilibrium plasmas: a reaction kinetics model," *Plasma Sources Sci. Technol.*, vol. 23, no. 4, p. 045004, Jun. 2014, doi: 10.1088/0963-0252/23/4/045004.
- [74] G. Colonna, L. D. Pietanza, G. D'Ammando, R. Celiberto, M. Capitelli, and A. Laricchiuta, "Vibrational kinetics of electronically excited states in H₂ discharges," *Eur. Phys. J. D*, vol. 71, no. 11, p. 279, Nov. 2017, doi: 10.1140/epjd/e2017-80080-3.

- [75] G. Colonna, A. Laricchiuta, and L. D. Pietanza, "Time dependent selfconsistent electron energy distribution functions during nano-second repetitive discharges in reacting N_2/H_2 mixtures," *Plasma Phys. Control. Fusion*, vol. 62, no. 1, p. 014003, Jan. 2020, doi: 10.1088/1361-6587/ab469e.
- [76] Y. Teramoto and H.-H. Kim, "Effect of vibrationally excited $N_2(v)$ on atomic nitrogen generation using two consecutive pulse corona discharges under atmospheric pressure N_2 ," *J. Phys. D. Appl. Phys.*, vol. 52, no. 49, p. 494003, Dec. 2019, doi: 10.1088/1361-6463/ab3f83.
- [77] J. Hong, S. Pancheshnyi, E. Tam, J. J. Lowke, S. Prawer, and A. B. Murphy, "Kinetic modelling of NH_3 production in N_2-H_2 non-equilibrium atmospheric-pressure plasma catalysis," *J. Phys. D. Appl. Phys.*, vol. 50, no. 15, p. 154005, Apr. 2017, doi: 10.1088/1361-6463/aa6229
- [78] J. Hong *et al.*, "Plasma Catalytic Synthesis of Ammonia Using Functionalized-Carbon Coatings in an Atmospheric-Pressure Non-equilibrium Discharge," *Plasma Chem. Plasma Process.*, vol. 36, no. 4, pp. 917–940, Jul. 2016, doi: 10.1007/s11090-016-9711-8.
- [79] H.-E. Wagner, R. Brandenburg, K. V. Kozlov, A. Sonnenfeld, P. Michel, and J. F. Behnke, "The barrier discharge: basic properties and applications to surface treatment," *Vacuum*, vol. 71, no. 3, pp. 417–436, May 2003, doi: 10.1016/S0042-207X(02)00765-0.
- [80] J. Shah, W. Wang, A. Bogaerts, and M. L. Carreon, "Ammonia Synthesis by Radio Frequency Plasma Catalysis: Revealing the Underlying Mechanisms," *ACS Appl. Energy Mater.*, vol. 1, no. 9, pp. 4824–4839, Sep. 2018, doi: 10.1021/acsaem.8b00898.
- [81] A. Bogaerts, W. Wang, A. Berthelot, and V. Guerra, "Modeling plasma-based CO_2 conversion: crucial role of the dissociation cross section," *Plasma Sources Sci. Technol.*, vol. 25, no. 5, p. 055016, Aug. 2016, doi: 10.1088/0963-0252/25/5/055016.
- [82] K. van 't Veer, F. Reniers, and A. Bogaerts, "Zero-dimensional modeling of unpacked and packed bed dielectric barrier discharges: the role of vibrational kinetics in ammonia synthesis," *Plasma Sources Sci. Technol.*, vol. 29, no. 4, p. 045020, Apr. 2020, doi: 10.1088/1361-6595/ab7a8a.
- [83] E. C. Neyts, K. Ostrikov, M. K. Sunkara, and A. Bogaerts, "Plasma Catalysis: Synergistic Effects at the Nanoscale," *Chem. Rev.*, vol. 115, no. 24, pp. 13408–13446, Dec. 2015, doi: 10.1021/acs.chemrev.5b00362.
- [84] K. Aihara, M. Akiyama, T. Deguchi, M. Tanaka, R. Hagiwara, and M. Iwamoto, "Remarkable catalysis of a wool-like copper electrode for NH_3 synthesis from N_2 and H_2 in non-thermal atmospheric plasma," *Chem. Commun.*, vol. 52, no. 93,

pp. 13560–13563, 2016, doi: 10.1039/C6CC06752B.

- [85] P. Peng *et al.*, “Ru-based multifunctional mesoporous catalyst for low-pressure and non-thermal plasma synthesis of ammonia,” *Int. J. Hydrogen Energy*, vol. 42, no. 30, pp. 19056–19066, Jul. 2017, doi: 10.1016/j.ijhydene.2017.06.118.
- [86] X. Zhu, X. Hu, X. Wu, Y. Cai, H. Zhang, and X. Tu, “Ammonia synthesis over γ - Al_2O_3 pellets in a packed-bed dielectric barrier discharge reactor,” *J. Phys. D: Appl. Phys.*, vol. 53, no. 16, p. 164002, Apr. 2020, doi: 10.1088/1361-6463/ab6cd1.
- [87] M. Capitelli, C. M. Ferreira, B. F. Gordiets, and A. I. Osipov, *Plasma Kinetics in Atmospheric Gases*, Berlin, Heidelberg: Springer Berlin Heidelberg, 2000.
- [88] F. Esposito, I. Armenise, and M. Capitelli, “N– N_2 state to state vibrational-relaxation and dissociation rates based on quasiclassical calculations,” *Chem. Phys.*, vol. 331, no. 1, pp. 1–8, Dec. 2006, doi: 10.1016/j.chemphys.2006.09.035.
- [89] I. V. Adamovich, S. O. Macheret, J. W. Rich, and C. E. Treanor, “Vibrational Energy Transfer Rates Using a Forced Harmonic Oscillator Model,” *J. Thermophys. Heat Transf.*, vol. 12, no. 1, pp. 57–65, Jan. 1998, doi: 10.2514/2.6302.
- [90] F. R. Gilmore, “Potential energy curves for N_2 , NO, O_2 and corresponding ions,” *J. Quant. Spectrosc. Radiat. Transf.*, vol. 5, no. 2, pp. 369–IN3, Mar. 1965, doi: 10.1016/0022-4073(65)90072-5.
- [91] Y. Uytendhouwen, K. M. Bal, E. C. Neyts, V. Meynen, P. Cool, and A. Bogaerts, “On the kinetics and equilibria of plasma-based dry reforming of methane,” *Chem. Eng. J.*, vol. 405, p. 126630, Feb. 2021, doi: 10.1016/j.cej.2020.126630.
- [92] M. A. Lieberman and A. J. Lichtenberg, *Principles of Plasma Discharges and Materials Processing*. Hoboken, NJ, USA: John Wiley & Sons, Inc., 2005.
- [93] G. J. M. Hagelaar and L. C. Pitchford, “Solving the Boltzmann equation to obtain electron transport coefficients and rate coefficients for fluid models,” *Plasma Sources Sci. Technol.*, vol. 14, no. 4, pp. 722–733, Nov. 2005, doi: 10.1088/0963-0252/14/4/011.
- [94] P. Viegas, M. C. M. van de Sanden, S. Longo, and P. Diomedede, “Validation of the Fokker–Planck Approach to Vibrational Kinetics in CO_2 Plasma,” *J. Phys. Chem. C*, vol. 123, no. 37, pp. 22823–22831, Sep. 2019, doi: 10.1021/acs.jpcc.9b06576.
- [95] S. Pancheshnyi, B. Eismann, G. J. M. Hagelaar and L. C. Pitchford, “Computer code ZDPlasKin,” University of Toulouse, LAPLACE, CNRS-UPS-INP, Toulouse, France, 2008, <http://www.zdplaskin.laplace.univ-tlse.fr>

- [96] N. Jidenko, E. Bourgeois, and J.-P. Borra, "Temperature profiles in filamentary dielectric barrier discharges at atmospheric pressure," *J. Phys. D. Appl. Phys.*, vol. 43, no. 29, p. 295203, Jul. 2010, doi: 10.1088/0022-3727/43/29/295203.
- [97] F. Peeters and T. Butterworth, "Electrical Diagnostics of Dielectric Barrier Discharges," in *Atmospheric Pressure Plasma, IntechOpen*, 2019, doi: 10.5772/intechopen.80433.
- [98] F. J. J. Peeters and M. C. M. van de Sanden, "The influence of partial surface discharging on the electrical characterization of DBDs," *Plasma Sources Sci. Technol.*, vol. 24, no. 1, p. 015016, Dec. 2014, doi: 10.1088/0963-0252/24/1/015016.
- [99] Y. Uytendhouwen *et al.*, "How process parameters and packing materials tune chemical equilibrium and kinetics in plasma-based CO₂ conversion," *Chem. Eng. J.*, vol. 372, pp. 1253–1264, Sep. 2019, doi: 10.1016/j.cej.2019.05.008.
- [100] H.-H. Kim, Y. Teramoto, A. Ogata, H. Takagi, and T. Nanba, "Atmospheric-pressure nonthermal plasma synthesis of ammonia over ruthenium catalysts," *Plasma Process. Polym.*, vol. 14, no. 6, p. 1600157, Jun. 2017, doi: 10.1002/ppap.201600157.
- [101] V. Laporta, D. A. Little, R. Celiberto, and J. Tennyson, "Electron-impact resonant vibrational excitation and dissociation processes involving vibrationally excited N₂ molecules," *Plasma Sources Sci. Technol.*, vol. 23, no. 6, p. 065002, Aug. 2014, doi: 10.1088/0963-0252/23/6/065002.
- [102] E. Carrasco, M. Jiménez-Redondo, I. Tanarro, and V. J. Herrero, "Neutral and ion chemistry in low pressure dc plasmas of H₂/N₂ mixtures: routes for the efficient production of NH₃ and NH₄⁺," *Phys. Chem. Chem. Phys.*, vol. 13, no. 43, p. 19561, 2011, doi: 10.1039/c1cp22284h.
- [103] R. Celiberto, R. K. Janev, J. M. Wadehra, and A. Laricchiuta, "Cross sections for 11–14-eV e-H₂ resonant collisions: Vibrational excitation," *Phys. Rev. A*, vol. 77, no. 1, p. 012714, Jan. 2008, doi: 10.1103/PhysRevA.77.012714.
- [104] R. Celiberto, R. K. Janev, V. Laporta, J. Tennyson, and J. M. Wadehra, "Electron-impact vibrational excitation of vibrationally excited H₂ molecules involving the resonant ²Σ_g⁺ Rydberg-excited electronic state," *Phys. Rev. A*, vol. 88, no. 6, p. 062701, Dec. 2013, doi: 10.1103/PhysRevA.88.062701.
- [105] S. Van Alphen, V. Vermeiren, T. Butterworth, D. C. M. van den Bekerom, G. J. van Rooij, and A. Bogaerts, "Power Pulsing To Maximize Vibrational Excitation Efficiency in N₂ Microwave Plasma: A Combined Experimental and Computational Study," *J. Phys. Chem. C*, vol. 124, no. 3, pp. 1765–1779, Jan. 2020, doi: 10.1021/acs.jpcc.9b06053.

- [106] F. Y. Hansen, N. E. Henriksen, G. D. Billing, and A. Guldborg, "Catalytic synthesis of ammonia using vibrationally excited nitrogen molecules: theoretical calculation of equilibrium and rate constants," *Surf. Sci.*, vol. 264, no. 1–2, pp. 225–234, Mar. 1992, doi: 10.1016/0039-6028(92)90180-E.
- [107] G. D. Billing, A. Guldborg, N. E. Henriksen, and F. Y. Hansen, "Dissociative chemisorption of N₂ on rhenium: Dynamics at low impact energies," *Chem. Phys.*, vol. 147, no. 1, pp. 1–11, Oct. 1990, doi: 10.1016/0301-0104(90)85015-O.
- [108] G. Ertl, "Surface Science and Catalysis—Studies on the Mechanism of Ammonia Synthesis: The P. H. Emmett Award Address," *Catal. Rev.*, vol. 21, no. 2, pp. 201–223, Jan. 1980, doi: 10.1080/03602458008067533.
- [109] Y. Engelmann, K. van 't Veer, Y. Gorbaney, E. C. Neyts, W. F. Schneider, and A. Bogaerts, "Plasma Catalysis for Ammonia Synthesis: A Microkinetic Modeling Study on the Contributions of Eley–Rideal Reactions," *ACS Sustain. Chem. Eng.*, vol. 9, no. 39, pp. 13151–13163, Oct. 2021, doi: 10.1021/acssuschemeng.1c02713.
- [110] Y. Engelmann, P. Mehta, E. C. Neyts, W. F. Schneider, and A. Bogaerts, "Predicted Influence of Plasma Activation on Nonoxidative Coupling of Methane on Transition Metal Catalysts," *ACS Sustain. Chem. Eng.*, vol. 8, no. 15, pp. 6043–6054, Apr. 2020, doi: 10.1021/acssuschemeng.0c00906.
- [111] J. Shah, F. Gorky, P. Psarras, B. Seong, D. A. Gómez-Gualdrón, and M. L. Carreon, "Enhancement of the Yield of Ammonia by Hydrogen-Sink Effect during Plasma Catalysis," *ChemCatChem*, vol. 12, no. 4, pp. 1200–1211, Feb. 2020, doi: 10.1002/cctc.201901769.
- [112] Y. Wang *et al.*, "Plasma-Enhanced Catalytic Synthesis of Ammonia over a Ni/Al₂O₃ Catalyst at Near-Room Temperature: Insights into the Importance of the Catalyst Surface on the Reaction Mechanism," *ACS Catal.*, vol. 9, no. 12, pp. 10780–10793, Dec. 2019, doi: 10.1021/acscatal.9b02538.
- [113] C. D. Molek, J. L. McLain, V. Poterya, and N. G. Adams, "A Remeasurement of the Products for Electron Recombination of N₂H⁺ Using a New Technique: No Significant NH + N Production," *J. Phys. Chem. A*, vol. 111, no. 29, pp. 6760–6765, Jul. 2007, doi: 10.1021/jp068965d.
- [114] A. K. Brewer and J. W. Westhaver, "The Synthesis of Ammonia in the Glow Discharge," *J. Phys. Chem.*, vol. 33, no. 6, pp. 883–895, Jun. 1929, doi: 10.1021/j150300a008.
- [115] A. K. Brewer and J. W. Westhaver, "Chemical Action in the Glow Discharge II. Further Investigation on the Synthesis of Ammonia," *J. Phys. Chem.*, vol. 34, no. 1, pp. 153–164, Jan. 1930, doi: 10.1021/j150307a010.

- [116] G. Y. Botchway and M. Venugopalan, "Plasma Synthesis of Ammonia in Presence of an Iron Catalyst," *Zeitschrift für Phys. Chemie*, vol. 120, no. 1, pp. 103–110, Jan. 1980, doi: 10.1524/zpch.1980.120.1.103.
- [117] K. S. Yin and M. Venugopalan, "Plasma chemical synthesis. I. Effect of electrode material on the synthesis of ammonia," *Plasma Chem. Plasma Process.*, vol. 3, no. 3, pp. 343–350, Sep. 1983, doi: 10.1007/BF00564632.
- [118] M. Touvelle, J. L. M. Licea, and M. Venugopalan, "Plasma chemical synthesis. II. Effect of wall surface on the synthesis of ammonia," *Plasma Chem. Plasma Process.*, vol. 7, no. 1, pp. 101–108, Mar. 1987, doi: 10.1007/BF01016001.
- [119] H. Uyama and O. Matsumoto, "Synthesis of ammonia in high-frequency discharges," *Plasma Chem. Plasma Process.*, vol. 9, no. 1, pp. 13–24, Mar. 1989, doi: 10.1007/BF01015824.
- [120] H. Uyama and O. Matsumoto, "Synthesis of ammonia in high-frequency discharges. II. Synthesis of ammonia in a microwave discharge under various conditions," *Plasma Chem. Plasma Process.*, vol. 9, no. 3, pp. 421–432, Sep. 1989, doi: 10.1007/BF01083676.
- [121] A. Berthelot and A. Bogaerts, "Modeling of CO₂ plasma: effect of uncertainties in the plasma chemistry," *Plasma Sources Sci. Technol.*, vol. 26, no. 11, p. 115002, Oct. 2017, doi: 10.1088/1361-6595/aa8ffb.
- [122] W. Wang, A. Berthelot, Q. Zhang, and A. Bogaerts, "Modelling of plasma-based dry reforming: how do uncertainties in the input data affect the calculation results?," *J. Phys. D. Appl. Phys.*, vol. 51, no. 20, p. 204003, May 2018, doi: 10.1088/1361-6463/aab97a.
- [123] B. S. Patil *et al.*, "The role of heterogeneous catalysts in the plasma-catalytic ammonia synthesis," *Catal. Today*, vol. 362, pp. 2–10, Feb. 2021, doi: 10.1016/j.cattod.2020.06.074.
- [124] B. E. Poling, J. M. Prausnitz and J. P. O'Connell, "The Properties of Gases and Liquids," 5th edn, *New York: McGraw-Hill*, 2000
- [125] F. Menter, "Zonal Two Equation k-w Turbulence Models For Aerodynamic Flows," Jul. 1993, doi: 10.2514/6.1993-2906.
- [126] COMSOL Multiphysics® v. 5.5. www.comsol.com. COMSOL AB, Stockholm, Sweden.
- [127] M. Gao, Y. Zhang, H. Wang, B. Guo, Q. Zhang, and A. Bogaerts, "Mode Transition of Filaments in Packed-Bed Dielectric Barrier Discharges," *Catalysts*, vol. 8, no. 6, p. 248, Jun. 2018, doi: 10.3390/catal8060248.
- [128] Y. Gorbanev *et al.*, "Al₂O₃-Supported Transition Metals for Plasma-Catalytic NH₃

Synthesis in a DBD Plasma: Metal Activity and Insights into Mechanisms," *Catalysts*, vol. 11, no. 10, p. 1230, Oct. 2021, doi: 10.3390/catal11101230.

- [129] K. W. Engeling, J. Kruszelnicki, M. J. Kushner, and J. E. Foster, "Time-resolved evolution of micro-discharges, surface ionization waves and plasma propagation in a two-dimensional packed bed reactor," *Plasma Sources Sci. Technol.*, vol. 27, no. 8, p. 085002, Aug. 2018, doi: 10.1088/1361-6595/aad2c5.
- [130] Z.-I. Mujahid, J. Kruszelnicki, A. Hala, and M. J. Kushner, "Formation of surface ionization waves in a plasma enhanced packed bed reactor for catalysis applications," *Chem. Eng. J.*, vol. 382, p. 123038, Feb. 2020, doi: 10.1016/j.cej.2019.123038.
- [131] H. Itoh, K. Kobayashi, K. Teranishi, N. Shimomura, and S. Suzuki, "Time-Resolved Observation of Self-Organized Filaments Formed in a Helium-Dielectric Barrier Discharge," *IEEE Trans. Plasma Sci.*, vol. 39, no. 11, pp. 2204–2205, Nov. 2011, doi: 10.1109/TPS.2011.2160568.
- [132] Yong Yang, Y. I. Cho, G. Friedman, A. Fridman, and G. Fridman, "Self-Organization and Migration of Dielectric Barrier Discharge Filaments in Argon Gas Flow," *IEEE Trans. Plasma Sci.*, vol. 39, no. 11, pp. 2060–2061, Nov. 2011, doi: 10.1109/TPS.2011.2129599.
- [133] B. Eliasson and U. Kogelschatz, "Modeling and applications of silent discharge plasmas," *IEEE Trans. Plasma Sci.*, vol. 19, no. 2, pp. 309–323, Apr. 1991, doi: 10.1109/27.106829.
- [134] F. Massines, N. Gherardi, N. Naudé, and P. Ségur, "Recent advances in the understanding of homogeneous dielectric barrier discharges," *Eur. Phys. J. Appl. Phys.*, vol. 47, no. 2, p. 22805, Aug. 2009, doi: 10.1051/epjap/2009064.
- [135] M. Ramakers, G. Trenchev, S. Heijkers, W. Wang, and A. Bogaerts, "Gliding Arc Plasmatron: Providing an Alternative Method for Carbon Dioxide Conversion," *ChemSusChem*, vol. 10, no. 12, pp. 2642–2652, Jun. 2017, doi: 10.1002/cssc.201700589.
- [136] S. Heijkers and A. Bogaerts, "CO₂ Conversion in a Gliding Arc Plasmatron: Elucidating the Chemistry through Kinetic Modeling," *J. Phys. Chem. C*, vol. 121, no. 41, pp. 22644–22655, Oct. 2017, doi: 10.1021/acs.jpcc.7b06524.
- [137] S. R. Sun, H. X. Wang, D. H. Mei, X. Tu, and A. Bogaerts, "CO₂ conversion in a gliding arc plasma: Performance improvement based on chemical reaction modeling," *J. CO₂ Util.*, vol. 17, pp. 220–234, Jan. 2017, doi: 10.1016/j.jcou.2016.12.009.
- [138] G. Trenchev, A. Nikiforov, W. Wang, S. Kolev, and A. Bogaerts, "Atmospheric pressure glow discharge for CO₂ conversion: Model-based exploration of the

- optimum reactor configuration," *Chem. Eng. J.*, vol. 362, pp. 830–841, Apr. 2019, doi: 10.1016/j.cej.2019.01.091.
- [139] X. Duan, Z. Hu, Y. Li, and B. Wang, "Effect of dielectric packing materials on the decomposition of carbon dioxide using DBD microplasma reactor," *AIChE J.*, vol. 61, no. 3, pp. 898–903, Mar. 2015, doi: 10.1002/aic.14682.
- [140] K. Van Laer and A. Bogaerts, "Improving the Conversion and Energy Efficiency of Carbon Dioxide Splitting in a Zirconia-Packed Dielectric Barrier Discharge Reactor," *Energy Technol.*, vol. 3, no. 10, pp. 1038–1044, Oct. 2015, doi: 10.1002/ente.201500127.
- [141] Y. Zeng, X. Zhu, D. Mei, B. Ashford, and X. Tu, "Plasma-catalytic dry reforming of methane over γ -Al₂O₃ supported metal catalysts," *Catal. Today*, vol. 256, pp. 80–87, Nov. 2015, doi: 10.1016/j.cattod.2015.02.007.
- [142] I. Michielsen *et al.*, "CO₂ dissociation in a packed bed DBD reactor: First steps towards a better understanding of plasma catalysis," *Chem. Eng. J.*, vol. 326, pp. 477–488, Oct. 2017, doi: 10.1016/j.cej.2017.05.177.
- [143] Y. Uytdenhouten, V. Meynen, P. Cool, and A. Bogaerts, "The Potential Use of Core-Shell Structured Spheres in a Packed-Bed DBD Plasma Reactor for CO₂ Conversion," *Catalysts*, vol. 10, no. 5, p. 530, May 2020, doi: 10.3390/catal10050530.
- [144] L. L. Alves, "The IST-LISBON database on LXCat," *J. Phys. Conf. Ser.*, vol. 565, p. 012007, Dec. 2014, doi: 10.1088/1742-6596/565/1/012007.
- [145] W. Lowell Morgan, Morgan (Kinema Research & Software), scattering cross sections, www.lxcat.net/Morgan
- [146] V. Tarnovsky, H. Deutsch, and K. Becker, "Cross-sections for the electron impact ionization of ND_x (x = 1–3)," *Int. J. Mass Spectrom. Ion Process.*, vol. 167–168, pp. 69–78, Nov. 1997, doi: 10.1016/S0168-1176(97)00033-5.
- [147] Y. Itikawa, "Cross Sections for Electron Collisions with Nitrogen Molecules," *J. Phys. Chem. Ref. Data*, vol. 35, no. 1, pp. 31–53, Mar. 2006, doi: 10.1063/1.1937426.
- [148] J.-S. Yoon *et al.*, "Cross Sections for Electron Collisions with Hydrogen Molecules," *J. Phys. Chem. Ref. Data*, vol. 37, no. 2, pp. 913–931, Jun. 2008, doi: 10.1063/1.2838023.
- [149] W. L. Nighan, "Electron Energy Distributions and Collision Rates in Electrically Excited N₂, CO, and CO₂," *Phys. Rev. A*, vol. 2, no. 5, pp. 1989–2000, Nov. 1970, doi: 10.1103/PhysRevA.2.1989.
- [150] I. A. Kossyi, A. Y. Kostinsky, A. A. Matveyev, and V. P. Silakov, "Kinetic scheme

- of the non-equilibrium discharge in nitrogen-oxygen mixtures," *Plasma Sources Sci. Technol.*, vol. 1, no. 3, pp. 207–220, Aug. 1992, doi: 10.1088/0963-0252/1/3/011.
- [151] R. Celiberto, R. K. Janev, J. M. Wadehra, and A. Laricchiuta, "Cross sections for 14-eV e-H₂ resonant collisions: Dissociative electron attachment," *Phys. Rev. A*, vol. 80, no. 1, p. 012712, Jul. 2009, doi: 10.1103/PhysRevA.80.012712.
- [152] D. J. Kewley and H. G. Hornung, "Free-piston shock-tube study of nitrogen dissociation," *Chem. Phys. Lett.*, vol. 25, no. 4, pp. 531–536, Apr. 1974, doi: 10.1016/0009-2614(74)85360-1.
- [153] W. Van Gaens and A. Bogaerts, "Kinetic modelling for an atmospheric pressure argon plasma jet in humid air," *J. Phys. D. Appl. Phys.*, vol. 46, no. 27, p. 275201, Jul. 2013, doi: 10.1088/0022-3727/46/27/275201.
- [154] B. Gordiets, C. M. Ferreira, M. J. Pinheiro, and A. Ricard, "Self-consistent kinetic model of low-pressure - flowing discharges: I. Volume processes," *Plasma Sources Sci. Technol.*, vol. 7, no. 3, pp. 363–378, Aug. 1998, doi: 10.1088/0963-0252/7/3/015.
- [155] A. Fontijn, S. M. Shamsuddin, D. Crammond, P. Marshall, and W. R. Anderson, "Kinetics of the NH reaction with H₂ and reassessment of HNO formation from NH + CO₂, H₂O," *Combust. Flame*, vol. 145, no. 3, pp. 543–551, May 2006, doi: 10.1016/j.combustflame.2005.12.012.
- [156] S. W. Mayer, L. Schieler, and H. S. Johnston, "Computation of high-temperature rate constants for bimolecular reactions of combustion products," *Symp. Combust.*, vol. 11, no. 1, pp. 837–844, Jan. 1967, doi: 10.1016/S0082-0784(67)80209-1.
- [157] S. J. Klippenstein *et al.*, "Thermal Decomposition of NH₂OH and Subsequent Reactions: Ab Initio Transition State Theory and Reflected Shock Tube Experiments," *J. Phys. Chem. A*, vol. 113, no. 38, pp. 10241–10259, Sep. 2009, doi: 10.1021/jp905454k.
- [158] N. Cohen and K. R. Westberg, "Chemical Kinetic Data Sheets for High-Temperature Chemical Reactions," *J. Phys. Chem. Ref. Data*, vol. 12, no. 3, pp. 531–590, Jul. 1983, doi: 10.1063/1.555692.
- [159] J. Deppe, G. Friedrichs, A. Ibrahim, H.-J. Römmling, and H. G. Wagner, "The Thermal Decomposition of NH₂ and NH Radicals," *Berichte der Bunsengesellschaft für Phys. Chemie*, vol. 102, no. 10, pp. 1474–1485, Oct. 1998, doi: 10.1002/bbpc.199800016.
- [160] R. K. Hanson and S. Salimian, "Survey of Rate Constants in the N/H/O System," in *Combustion Chemistry*, New York, NY: Springer New York, 1984, pp. 361–

421.

- [161] M. A. A. Clyne and D. H. Stedman, "Rate of recombination of nitrogen atoms," *J. Phys. Chem.*, vol. 71, no. 9, pp. 3071–3073, Aug. 1967, doi: 10.1021/j100868a056.
- [162] A. Fridman, *Plasma Chemistry*. Cambridge: Cambridge University Press, 2008.
- [163] V. G. Anicich, "Evaluated Bimolecular Ion-Molecule Gas Phase Kinetics of Positive Ions for Use in Modeling Planetary Atmospheres, Cometary Comae, and Interstellar Clouds," *J. Phys. Chem. Ref. Data*, vol. 22, no. 6, pp. 1469–1569, Nov. 1993, doi: 10.1063/1.555940.
- [164] W. Wang, R. Snoeckx, X. Zhang, M. S. Cha, and A. Bogaerts, "Modeling Plasma-based CO₂ and CH₄ Conversion in Mixtures with N₂, O₂, and H₂O: The Bigger Plasma Chemistry Picture," *J. Phys. Chem. C*, vol. 122, no. 16, pp. 8704–8723, Apr. 2018, doi: 10.1021/acs.jpcc.7b10619.
- [165] R. Celiberto, R. K. Janev, J. M. Wadehra, and J. Tennyson, "Dissociative electron attachment to vibrationally excited H₂ molecules involving the resonant Rydberg electronic state," *Chem. Phys.*, vol. 398, pp. 206–213, Apr. 2012, doi: 10.1016/j.chemphys.2011.05.004.
- [166] R. N. Schwartz, Z. I. Slawsky, and K. F. Herzfeld, "Calculation of Vibrational Relaxation Times in Gases," *J. Chem. Phys.*, vol. 20, no. 10, pp. 1591–1599, Oct. 1952, doi: 10.1063/1.1700221.
- [167] P. J. Chantry, "A simple formula for diffusion calculations involving wall reflection and low density," *J. Appl. Phys.*, vol. 62, no. 4, pp. 1141–1148, Aug. 1987, doi: 10.1063/1.339662.
- [168] V. P. Zhdanov, "Arrhenius parameters for rate processes on solid surfaces," *Surf. Sci. Rep.*, vol. 12, no. 5, pp. 185–242, May 1991, doi: 10.1016/0167-5729(91)90011-L.
- [169] J. O. Hirschfelder, C. F. Curtiss and R. B. Bird, "Molecular Theory of Gases and Liquids," 1954, New York: Wiley.
- [170] A. B. Murphy, "Transport coefficients of plasmas in mixtures of nitrogen and hydrogen," *Chem. Phys.*, vol. 398, pp. 64–72, Apr. 2012, doi: 10.1016/j.chemphys.2011.06.017.
- [171] R. A. Svehla and B. J. McBride, "FORTRAN 4 computer program for calculation of thermodynamic and transport properties of complex chemical systems," *NASA Report*, NASA-TN-D-7056, E-6514, 1973.
- [172] Z. Lj Petrovic, "The Application of Blanc's Law to the Determination of the Diffusion Coefficients for Thermal Electrons in Gases," *Aust. J. Phys.*, vol. 39, no.

2, p. 237, 1986, doi: 10.1071/PH860237.

- [173] G. Black, H. Wise, S. Schechter, and R. L. Sharpless, "Measurements of vibrationally excited molecules by Raman scattering. II. Surface deactivation of vibrationally excited N_2 ," *J. Chem. Phys.*, vol. 60, no. 9, pp. 3526–3536, May 1974, doi: 10.1063/1.1681570.
- [174] R. F. Heidner and J. V. V. Kasper, "An experimental rate constant for $H + H_2(v'' = 1) \rightarrow H + H_2(v'' = 0)$," *Chem. Phys. Lett.*, vol. 15, no. 2, pp. 179–184, Aug. 1972, doi: 10.1016/0009-2614(72)80144-1.
- [175] M. Jiménez-Redondo, E. Carrasco, V. J. Herrero, and I. Tanarro, "Isotopic exchange processes in cold plasmas of H_2/D_2 mixtures," *Phys. Chem. Chem. Phys.*, vol. 13, no. 20, p. 9655, 2011, doi: 10.1039/c1cp20426b.
- [176] J. Barth, "Transport of adsorbates at metal surfaces: from thermal migration to hot precursors," *Surf. Sci. Rep.*, vol. 40, no. 3–5, pp. 75–149, Oct. 2000, doi: 10.1016/S0167-5729(00)00002-9.
- [177] J. Dumesic, "Kinetic simulation of ammonia synthesis catalysis," *J. Catal.*, vol. 116, no. 1, pp. 119–129, Mar. 1989, doi: 10.1016/0021-9517(89)90080-8.
- [178] D. Manthey, "Atomic Orbitals", Orbital Viewer computer program, <https://www.orbitals.com/orb/index.html>.
- [179] The Bodner Group, "Molecular Orbital Theory," Purdue University, <https://chemed.chem.purdue.edu/genchem/topicreview/bp/ch8/mo.php>.
- [180] "Orbital Filling," *Chemistry LibreTexts*, 2020, <https://chem.libretexts.org/@go/page/226590>
- [181] H. S. Fogler, "Elements of chemical reaction engineering," Prentice Hall, 2016

List of publications and conference contributions

First author peer-reviewed publications

Spatially and temporally non-uniform plasmas: Microdischarges from the perspective of molecules in a packed bed plasma reactor.

K. van 't Veer, S. van Alphen, A. Remy, Y. Gorbanev, N. De Geyter, R. Snyders, F. Reniers and A Bogaerts

J. Phys. D: Appl. Phys., 54, 174002 (2021)

Plasma-catalytic ammonia synthesis in a DBD plasma: Role of microdischarges and their afterglows.

K. van 't Veer, Y. Engelmann, F. Reniers and A. Bogaerts

J. Phys. Chem. C, 124, 22871–22883 (2020)

Zero-dimensional modelling of unpacked and packed bed dielectric barrier discharges: The role of vibrational kinetics in ammonia synthesis.

K. van 't Veer, F. Reniers and A. Bogaerts

Plasma Sources Sci. Technol., 29, 045020 (2020)

Other peer-reviewed publications

Al₂O₃-supported transition metals for plasma-catalytic NH₃ synthesis in a DBD plasma: Metal activity and insights into mechanisms.

Y. Gorbanev, Y. Engelmann, **K. van 't Veer**, E. Vlasov, C. Ndayirinde, Y. Yi, S. Bals and A. Bogaerts

Catalysts, 11, 1230 (2021)

Plasma catalysis for ammonia synthesis: A microkinetic modeling study on the contributions of Eley–Rideal reactions.

Y. Engelmann, **K. van 't Veer**, Y. Gorbanev, E.C. Neyts, W. F. Schneider and A. Bogaerts

ACS Sust. Chem. Eng., 9, 13151–13163 (2021)

Plasma-driven catalysis: green ammonia synthesis with intermittent electricity.

K.H.R. Rouwenhorst, Y. Engelmann, **K. van 't Veer**, R.S. Postma, A. Bogaerts and L. Lefferts

Green Chem., 22, 6258 (2020)

Numerical simulation of atmospheric-pressure 200 kHz/13.56 MHz dual-frequency dielectric barrier discharges

Y. Liu, **K. van 't Veer**, F. J. J. Peeters, D. B. Mihailova, J. van Dijk, S. A. Starostin, M. C. M. van de Sanden and H. W. de Vries

Plasma Sources Sci. Technol., 27, 105016 (2018)

Techno-economic Analysis of Methane-to-Hydrogen-to-Ammonia Conversion by Integration of High-Temperature Plasma and Non-Thermal Plasma Processes

V. Hessel, **K. van 't Veer**, N. Van Duc Long, J. L. Osorio-Tejada, N. Tran, L. Fulcheri, B. Patil, A. Bogaerts

Submitted to ACS Sustain. Chem. Eng.

The 2021 release of the Quantemol database (QDB) of plasma chemistries and reactions

J. Tennyson, S. Mohr, M. Hanicinec, A. Dzarasova, C. Smith, S. Waddington, B. Liu, L. L. Alves, K. Bartschat, A. Bogaerts, S. U. Engelmann, T. Gans, A. R. Gibson, S. Hamaguchi, K. R. Hamilton, C. Hill, D. O'Connell S. Rauf, **K. van 't Veer**, O. Zatsarinny

Submitted to Plasma Sources Sci. Technol.

Invited talks

Solvay Workshop on "Plasma Technology and Other Green Methods for Nitrogen Fixation", Brussels, Belgium, 15th-17th November, 2021

"Plasma-catalytic NH₃ production in DBD plasma: Chemical kinetics modeling"

Other conference/workshop contributions

1st Frontiers in Low-Temperature Plasma (FLTPS) Workshop, Bad Honnef, Germany, 13th-16th May, 2019

"Modelling for NH₃ synthesis in dielectric barrier discharges with catalysts"

(Poster presentation)

Workshop Twente-Eindhoven-Antwerpen-Amsterdam on Plasma Catalysis, DIFFER, Eindhoven, The Netherlands, 8th July, 2019

"Plasma kinetic modelling for catalytic NH₃ synthesis in (packed bed) DBD: On modelling, experiments and vibrational kinetics"

(Oral Presentation)

ERC SCOPE Workshop, online, 18th February, 2021

"Plasma kinetic modeling of plasma-catalytic NH₃ synthesis"

(Oral Presentation)

The image shows a musical score for the piece 'Gnomus' from Modest Mussorgsky's 'Pictures at an Exhibition'. The score is written for piano and violin. The piano part is in the lower register, and the violin part is in the upper register. The key signature is three flats (B-flat major or D-flat minor), and the time signature is 3/4. The tempo marking is 'velocissimo' and the dynamic marking is 'con tutta forza'. The score consists of five measures. The piano part starts with a whole rest in the first measure, followed by a series of eighth and sixteenth notes. The violin part starts with a whole rest in the first measure, followed by a series of eighth and sixteenth notes. The piece ends with a double bar line and repeat dots.

Excerpt from Modest Mussorgsky's *Pictures at an Exhibition* – 1. *Gnomus* (1874)

International Music Score Library Project (imslp.org)

Acknowledgements

I want to thank my promotors prof. Annemie Bogaerts and prof. François Reniers. You have supported me throughout my PhD and have been available whenever I needed you; to provide assurance or a new point of view both within and outside the world of science.

I also would like to thank my colleagues and friends at ChemSIN who I have been able to meet due to my joint PhD. Antoine, Nicolas, Cédric and Nepal, thank you for the enthusiastic scientific discussions and the often new experimental insight and ideas.

Despite the pandemic covering half of my doctorate, during my PhD I have had the great pleasure to meet many people and friends. Some of whom have been rather successful at getting me out of my comfort zone. However, of course I have never left my comfort zone at all, it merely expanded: A special thank you to Hamid, Shooka, Colin, KT, Ivan, Ed, Josh and Edgar.

I also want to thank Claudia, Elise, Senne and Eline, who were there to receive me on my first day of this adventure we have in common.

Xiaoyan, Shangkun and Yuxiang; thank you for the dinner invitation and the introduction to the real Chinese cuisine, it was very delicious.

In addition, I would like to thank Joachim, Björn, Callie, Greg, Omar, Sean, Yury, Pepijn, Rani, and all other PLASMANT members. You all make working here very enjoyable. Amin, Yannick and Maryam and Saeid, I am very grateful that we were around at the same time.

Finally, als laatste, wil ik mijn moeder, vader en broer bedanken, waar ik weet dat ik altijd terecht kan.